Tsunamis: Non-Breaking and Breaking Solitary Wave Run-Up

Thesis by

Ying Li

In Partial Fulfillment of the Requirements

for the Degree of

Doctor of Philosophy

California Institute of Technology

Pasadena, California

2000

(Submitted May, 2000)

Acknowledgments

I would like to take this opportunity to express the warmest thanks to several people:

Dr. Fredric Raichlen, my advisor, for your intellectual inspiration and great guidance and for arranging my financial support during my five year investigation at Caltech. I appreciate your assistance and patience which showed me the way to become an independent researcher, and enjoy answering your endless questions.

Dr. Theodore Yao-tsu Wu, Dr. Christopher E. Brennen, Dr. Tim Colonius, for kindly serving on my Ph.D. committee and for valuable discussions of the theoretical and numerical results. I appreciate the time and helpful suggestions given to my investigation. Dr. Thomas Yizhao Hou, I benefit from your knowledge and intuition of the numerical analysis.

Dr. Costas Synolakis, Dr. Phillip Liu and Dr. Phil Watts, for the brief discussions we have had during various occasions.

Rich Eastvedt, for helping me set up and clean the experiment equipment and for teaching me how to use them. Hai Vu, Russ Green, and Mike Vodus, for the great knowledgeable assistance with the design and construction of the mechanical and electrical equipment used during the study. Without your skillful work this doctoral research would not be possible.

Fran Matzen, Linda Scott, Irene Loera, for the help and support during the daily work.

Sueanne Lee, Hilla Shaviv, for providing much needed assistance with my experiments.

Xiangjun Li, Ruxia Wang, my parents, for the encouragement and emotional support that accompany me in every step of my life.

Caltech C Soccer Team, Caltech Badminton Club, and "Card Game Gang" for refreshing me during the exhausting life at Caltech.

Most important of all, Jie Yu, my fiancee, not only for typing and proofreading this thesis, but also for your unconditional support, love, and smile everyday.

This material is based upon work supported by the National Science Foundation under Award CMS-9523414. Any opinions, findings, and conclusions or recommendations expressed in this publication are those of the author and do not necessarily reflect the views of the National Science Foundation.

Abstract

This study considers the run-up of non-breaking and breaking solitary waves on a smooth sloping beach. A non-linear theory and a numerical model solving the non-linear shallow water equations (NLSW) were developed to model this physical process. Various experiments to obtain wave amplitude time-histories, water particle velocities, wave free-surface profiles, and maximum run-up were conducted and the results were compared with the analytical and numerical models.

A higher order theoretical solution to the non-linear shallow water equations, which describes the non-breaking wave characteristics on the beach, was sought and presented in this study. The solution was obtained analytically by using the Carrier and Greenspan (1958) hodograph transformation. It was found that the non-linear theory agreed well with experimental results. The maximum run-up predicted by the non-linear theory is larger than that predicted by Synolakis (1986) at the order of the offshore relative wave height for a given slope. This correction for non-breaking waves on beach decreases as the beach slope steepens, and increases as the relative incident solitary wave height increases.

A unique run-up gage that consists of a laser and a photodiode camera was developed in connection with this study to measure the time-history of the tip of the run-up tongue of a non-breaking solitary wave as it progresses up the slope. The results obtained with this run-up gage agree well with other measurements and provides a simple and reliable way of measuring run-up time histories.

The run-up of breaking solitary waves was studied experimentally and numerically

since no fully theoretical approach is possible. The wave characteristics such as wave shape and shoaling characteristics, and, for plunging breakers, the shape of the jet produced are presented. The experimental results show that wave breaking is such a complicated process that even sophisticated numerical models cannot adequately model its details.

Two different plunging wave breaking and resultant run-up were found from the experiments. The point where the tip of the incident jet produced by the plunging breaking wave impinges determines the characteristics of the resulting splash-up. If the jet impinges on a dry slope, no splash-up occurs and the plunging breaker simply collapses. If the impingement point is located on the free-surface, splash-up including a reflected jet is formed, which further increases the turbulence and energy dissipation associated with wave breaking. It is hypothesized that both clockwise and counter-clockwise vortices may be generated by the impinging plunging jet and the reflected jet associated with the splash-up when the jet impinges on the front face of a breaking wave or on the still water surface in front of the wave.

If only the run-up process and maximum run-up are of interest, the wave and the water flow produced after breaking can be simplified as a propagating bore, which is analogous to a shock wave in gas dynamics. A numerical model using this bore structure to treat the process of wave breaking and propagation was developed. The non-linear shallow water equations were solved using the weighted essentially non-oscillatory (WENO) shock capturing scheme employed in gas dynamics. Wave breaking and propagation is handled automatically by this scheme and no ad-hoc term is required. A computational domain mapping technique proposed by Zhang (1996) is used in the numerical scheme to model the shoreline movement. This numerical scheme is found to provide a somewhat simple and reasonably good prediction of various aspects of the run-up process. The numerical results agree well with the ex-

periments corresponding to the run-up on a relatively steep slope (1:2.08) as well as on a more gentle slope (1:19.85).

A simple empirical estimate of maximum run-up based on energy conservation considerations is also presented where the energy dissipation associated with wave breaking was estimated using the results from the numerical model. This approach appears to be useful and the maximum run-up predicted agrees reasonably well with the experimental results.

The splash-up of a solitary wave on a vertical wall positioned at different locations on a gentle slope was also investigated in this study to understand the degree of protection from tsunamis afforded by seawalls. It was found that the effect of breaking wave kinematics offshore of the vertical wall on the splash-up is of critical importance to the maximum splash-up. The maximum slope of the front face of the wave upon impingement of the wave on the wall, which represents the maximum water particle acceleration, was important in defining the maximum sheet splash-up as well as the trend for splash-up composed of drops and spray.

Contents

List of Figures

List of Tables

Nomenclature

The following symbols are used in this paper:

a	a measurement of the non-linear effect
a_0	the upstream vertical plane location of the control volume
a_1	the downstream vertical plane location of the control volume
A_i	incident wave amplitude
A_r	reflected wave amplitude
B	transmitted wave amplitude
c	wave celerity
c_1	constant in the domain mapping of the numerical model
c_2	constant in the domain mapping of the numerical model
c_{rj}	coefficient of the polynomial interpolation
d	total water depth; equals $h + \eta$
D	energy dissipation rate
E	wave energy
E_B	energy dissipation associated with wave breaking

E_D	energy dissipation
E_{FB}	energy dissipation by the bottom friction
E_{FF}	energy dissipation by the free surface friction
E_I	wave energy associated with incident solitary wave
E_K	wave kinetic energy
E_P	wave potential energy
F	boundary condition for shallow water wave equations
$\vec{F}$	numerical flux vector
g	the acceleration of gravity
h	water depth
h_0	water depth at the constant depth region
H	the incident solitary wave height at the constant depth region
H'	local wave height
H_b	maximum wave height at breaking
i	the square root of -1
J_n	Bessel function of order n
k	wave number
l	horizontal scale of the problem
L	a measure of the horizontal extent of a solitary wave

L_0	wavelength
L_1	horizontal length of the plunging jet
L_2	thickness of the plunging jet at the wave vertical plane
L_3	thickness of the plunging jet at half length of L_1
m	mass flux across a bore
p	water pressure
$\bar{p}$	analogous pressure of water wave
R	the maximum wave run-up
R_s	the maximum wave run-up from linear theory
R_{cr}	the difference between the non-linear and linear maximum run-up
$\vec{S}$	numerical source vector
s	tangent of the slope angle β
t	time coordinate
T	wave period
T_c	bore collapse time
u	dimensionless water particle velocity of the wave
U_r	Ursell number
u_s	the shoreline velocity
v_0	relative upstream water velocity with respect to the bore propagation speed

v_1	relative downstream water velocity with respect to the bore propagation speed
V	volume of the wave
$\vec{V}$	numerical velocity vector
V_m	impact velocity of the plunging jet
x	horizontal coordinate
x_b	the x coordinate of the wave breaking point
x_s	the x coordinate of the shoreline
x_t	the x coordinate of the tip of the plunging jet
x_{t0}	the initial x coordinate of the tip of the plunging jet
x_{th}	the theoretical x coordinate of the tip of the plunging jet by free-falling assumption
x_w	the x coordinate of the vertical wall
X	the shoreline location
X_0	the location of the toe of the slope
X_1	the dimensionless x-location where the initial solitary wave is defined
y	vertical coordinate
y_t	the y coordinate of the tip of the plunging jet
y_{t0}	the initial y coordinate of the tip of the plunging jet

y_{th}	the theoretical y coordinate of the tip of the plunging jet by free-falling assumption
α	shape factor
α	a dimensionless solitary wave parameter
α_1	calibration coefficient in energy balance model
β	the angle of the slope
δt	time increment step of the numerical model
δx	grid size of the numerical model
ϵ	a measurement of the dispersive effect
ϵ	a small quantity used in WENO scheme ($\epsilon = 1e-6$)
η	wave amplitude
Γ	the initial length of the computational domain of the numerical model
γ	dimensionless wave number
λ	Carrier-Greenspan transformation coordinate
ν	water kinematic viscosity
ρ	density of water
$\bar{\rho}$	analogous density of water wave
σ	Carrier-Greenspan transformation coordinate

σ_0 the location where the boundary condition is imposed to solve the transformed shallow water equation

θ_m impact angle of the plunging jet

Ψ the Carrier-Greenspan function

π 3.14159265

$\dot{\xi}$ bore propagation speed

ζ surf similarity parameter

Superscripts:

* non-dimensional

$'$ transformation in computational domain mapping technique

Chapter 1 Introduction

1.1 Tsunamis

Tsunamis are ocean waves generated by movements of the earth's crust. Several geophysical events can lead to this kind of catastrophe: earthquakes, landslides, volcano eruptions, and other mechanisms such as underwater explosions. Once this event happens the local rise and/or depression of the water surface will generate waves that propagate in all directions and a tsunami is produced. At generation and as the wave propagates away from the source, the wave amplitude is small (perhaps less than 1 m $\sim$ 2 m) but the wavelength is large compared to the local water depth (less than 3 km $\sim$ 10 km) and usually of the order of 100 km. Thus, the energy associated with a tsunami can be very large. As tsunamis propagate shoreward they undergo changes induced by the nearshore bathymetry and increase significantly in height. Upon reaching the shoreline, the waves generated run up the shore and can travel inland for relatively large distances with the potential for causing large property damage and loss of life.

Tsunamis have a long history around the Pacific Basin, where earthquakes are frequent. Over the past one hundred years there has been approximately one destructive tsunami per year, which has caused loss of life or serious property damage in the world (Zelt (1986)). Only a few of them are mentioned here. On June 15, 1896, a tsunami resulting from an earthquake attacked Sanriku, Japan, and more than 27,000 people died and over 10,000 buildings were destroyed. One of the most

severe historical tsunamis occured in Indonesia, generated by the eruption of the Krakatoa volcano, resulting in the loss of 36,000 people on August 27, 1883. A recent earthquake in Turkey on August 17, 1999, generated a tsunami with a maximum run-up on the coast of 2.5 m (Synolakis (1999)). Indeed most of the damage associated with tsunamis is related to their run-up at the shoreline. Therefore, understanding and being able to predict this run-up is an important aspect of any seismic sea wave mitigation effort.

Solitary waves or combinations of negative and positive solitary-like waves are often used to simulate the run-up and shoreward inundation of these catastrophic waves, e.g., Synolakis (1986, 1987), Zelt (1991a, 1991b) and Tadepalli and Synolakis (1994). Such waves can model many of the characteristics of tsunamis. Using a simple plane beach, important characteristics of the run-up tongue can be obtained both analytically and experimentally. This information, for the simple two-dimensional case of a solitary wave propagating in a constant depth and impinging on a plane sloping beach, can yield results applicable to three-dimensional numerical models of coastal sites.

The characteristics of non-breaking and breaking waves have been observed by tsunami victims, as revealed by field investigations. For example, the tsunami in Papua New Guinea in July 1998 resulted in wide destruction and more than 2,000 deaths. From eye-witness accounts it appears that the waves, some about 15 m high at the shoreline, were breaking (Synolakis (1999)). This research was motivated by these observations.

1.2 Objective and Scope

The objective of this study was to investigate theoretically, experimentally, and numerically solitary wave run-up on a sloping beach. Of particular importance was evaluating the maximum run-up. Both non-breaking and breaking waves were considered. Special attention was given to the interaction between the breaking wave and the slope.

For non-breaking solitary waves a higher order theoretical solution for non-linear shallow water equations was sought. This solution was based on the transformation proposed by Carrier and Greenspan (1958). Experiments were also performed in a wave tank where solitary waves run up on relatively steep and gentle smooth slopes. The incident wave profile, the maximum run-up, and the water particle velocities were measured to validate the non-linear theory presented.

The wave breaking process is so complicated that no fully theoretical approach is possible. Figure 1.1 shows the wave breaking and the splash-up process afterwards. (These photographs were taken by a still camera at different locations and times of the wave breaking process and then rearranged sequentially according to the nature of the breaking process. The experiments were repeated until the complete wave breaking process was covered.) The complexity of the problem, as well as its theoretical intractability, is obvious in Figure 1.1. Thus, the investigation for breaking solitary wave run-up presented herein is only experimental and numerical.

A breaking wave on a smooth slope of 1:15 was studied to define several characteristics of the plunging jet produced by the breaker. Such results of wave breaking kinematics can provide information relating to the study of the air entrainment and energy dissipation associated with the plunging jet produced at the crest of the breaking waves.

A numerical model using a bore structure similar to a shock in gas dynamics to treat the process of wave breaking and propagation was developed. The non-linear shallow water equations were solved using the weighted essentially non-oscillatory (WENO) shock capturing scheme employed in gas dynamics. Wave breaking and propagation is treated automatically by the scheme and no ad-hoc term is required to keep the scheme stable such as the artificial viscosity term used in Boussinesq models. It was found that the numerical scheme can predict the wave profile on the slope and maximum run-up very well.

Maximum run-up, defined as the highest position the wave can reach on a slope, is one of the most important parameters needed to estimate tsunami destruction. Theoretical results obtained from non-breaking wave considerations could be used to predict it. However, since wave breaking is not considered in such theories, the prediction is much higher than actual because of the energy dissipation associated with the breaking process. As mentioned earlier, numerical simulations incorporating simulated breaking effects can give a reasonable estimate of the maximum run-up. However it usually involves time-consuming computations and intensive computing resources. A second approach taken in this investigation was a simple empirical estimation based on energy conservation principles using both the experimental results and numerical simulations.

Coastal-sited protective structures such as seawalls have been used in some locations to reduce inland inundation associated with tsunamis. The rate of overtopping of seawalls exposed to periodic and random storm waves has been studied experimentally by numerous investigators generally for specific engineering problems using physical models. Goda et al. (1975) synthesized some of these results into generalized overtopping volume predictions for periodic waves. For periodic waves, reflections from the structure significantly affect the overtopping of subsequent waves in a

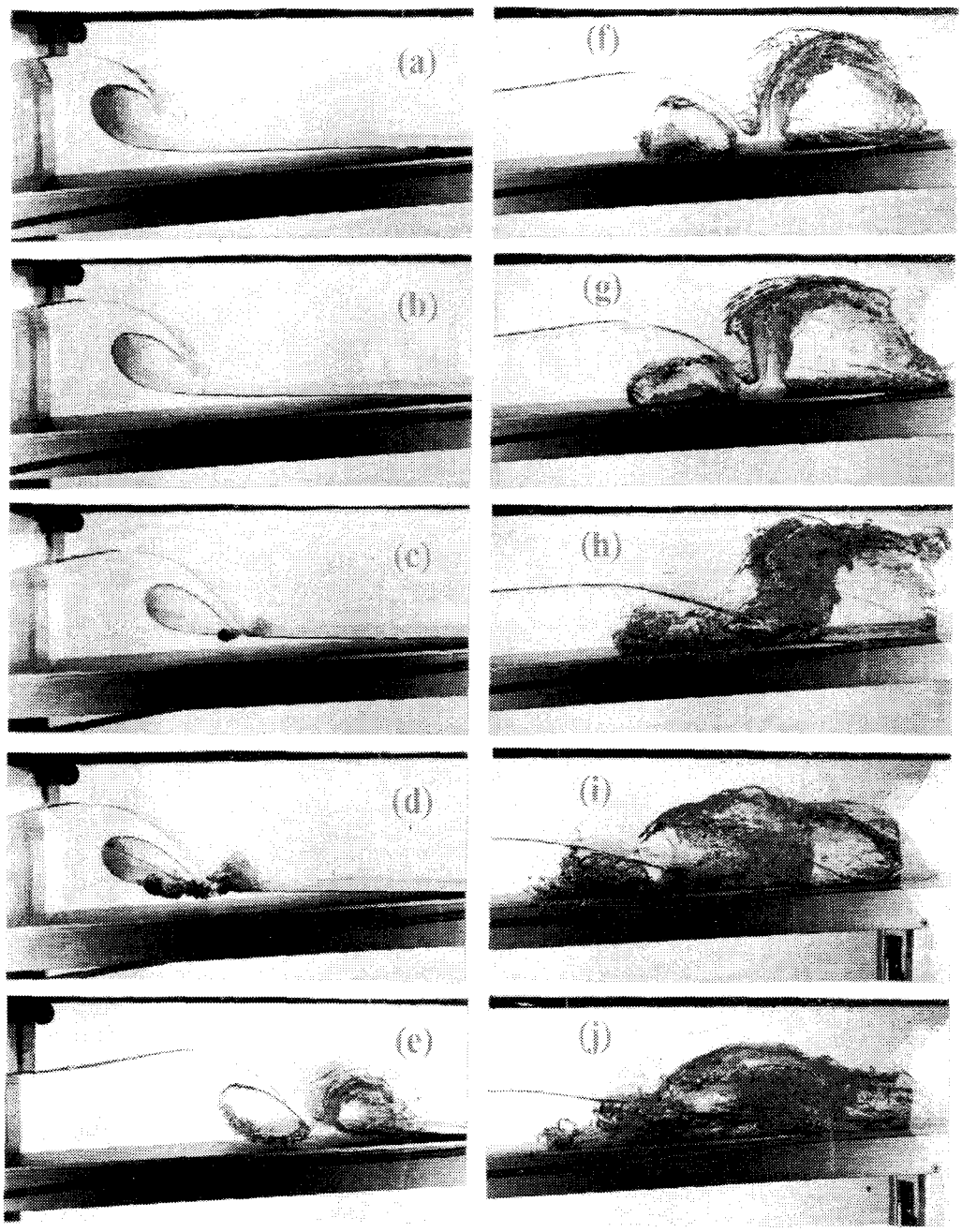

Figure 1.1: Photographs of the solitary wave splash-up on 1:15 slope for incident wave height $H/h_0 = 0.40$.

wave train. Comparable attention has not been given to the overtopping of seawalls by "tsunami-like" waves which consist more of groups of "isolated" waves (solitary waves) as contrasted with periodic storm waves. One objective of the present study was to investigate the splash-up (or the run-up) of such waves on vertical walls to understand the degree of protection from tsunamis afforded by seawalls. However, attention will not be given to the rate of overtopping of solitary waves. Experimental and numerical studies were conducted to investigate various aspects of this problem. Of special interest was the effect of breaking wave kinematics offshore of the vertical wall on the splash-up.

1.3 Thesis Outline

This chapter has introduced several general aspects of tsunamis and provides some historical data relating the destructive features as well as stating the objective and scope of this study. Chapter 2 summarizes the literature relating to solitary wave run-up and wave breaking characteristics, including theoretical analyses, experimental research, and numerical modeling. A new theoretical solution to the non-linear shallow water equations is presented in Chapter 3, along with a comparison to previous theoretical analyses. A numerical method to solve the non-linear shallow water wave equations and a special treatment of the wave breaking process and the moving shoreline are also described. Chapter 4 discusses the experimental equipment and the procedures used in this investigation. The results from the theoretical analysis, experiments, and numerical simulations are presented and discussed in Chapter 5 along with a discussion of the conservation of energy approach to breaking wave run-up. Chapter 6 summarizes the major conclusions of the thesis and suggests several directions for future work. The experimental results of maximum run-up measured

in the present study were listed in Appendix I.

Chapter 2 Literature Review

The study of the wave propagation, breaking, and the run-up process has been the subject of numerous analytical, numerical, and experimental studies in recent years. Since the objective of this investigation is focused on solitary wave run-up and the breaking process of the wave on run-up, only the literature related to these two topics is reviewed here. General reviews of tsunamis can be found in Lander and Lockridge (1989).

2.1 Theoretical Analyses

Various simplified models have been used to describe the wave run-up process, which is a strongly non-linear and dispersive wave phenomenon, e.g., the Boussinesq equations and the non-linear shallow water wave equations. In theory, the non-linear effects and the dispersive effects can be estimated by two parameters respectively:

$$a = \frac{H}{h} \qquad \epsilon = \frac{h}{l} \tag{2.1}$$

where H is the offshore wave height, h is the depth, and l is a characteristic horizontal length. For the propagation of long waves such as tsunamis, the Ursell number, U_r defined as:

$$U_r = \frac{a}{\epsilon^2} \tag{2.2}$$

is important in this process to measure the relative importance of non-linear effects and frequency dispersion. When $H/h \ll 1$ and $h/l \ll 1$, both non-linear effects and

frequency dispersion can be neglected and the linearized shallow water equations can adequately describe the wave propagation (Mei (1983)). As these long waves approach the coast the wave height increases and at some point the effects of non-linearity cannot be neglected. In that case, the fully non-linear shallow water equations are the suitable model if one can neglect the effects of frequency dispersion.

Keller and Keller (1964) studied periodic wave propagation over a constant depth and with the waves running up a sloping beach by matching the solutions for wave amplitude and velocities from the linear non-dispersive shallow water equations for both regions at the toe of the beach; the theoretical prediction of the maximum run-up of the wave on the slope was presented. Carrier and Greenspan (1958) studied the non-linear shallow water equations and proposed a method to transform these equations into a set of linear equations that can be solved analytically. It is still one of the few analytical solutions available for non-linear wave dynamics. They investigated the run-up of periodic waves with several different initial shapes on a plane slope using this theory. Tuck and Hwang (1972) and Spielvogel (1976) extended the Carrier and Greenspan (1958) transformation and used it to solve long wave run-up also under prescribed initial water-surface configurations. Tuck and Hwang (1972) investigated the problem of the generation of waves on a slope due to a bottom disturbance. Spielvogel (1976) extended the Carrier and Greenspan (1958) transformation and used it inversely to determine initial wave conditions offshore from the long wave run-up assuming a logarithmic initial surface profile on the slope at the instant of the maximum run-up.

Synolakis (1986, 1987) simplified the Carrier and Greenspan (1958) transformation, and applied it to the problem of a solitary wave propagating in a constant depth and running up a simple plane beach. His analytical results agreed well with laboratory experiments for non-breaking waves on the slope. Based on his simplification,

Synolakis (1986) drew the conclusion that the maximum run-up predicted by the linear shallow water equations was the same as that predicted by the non-linear shallow water equations, although the behavior of the wave on the slope such as the wave amplitude and the water particle velocities were quite different. Both this statement and his assumptions will be revisited in this investigation. Kanoglu and Synolakis (1998) studied long wave evolution and run-up on piecewise linear two and three-dimensional bathymetries using the linear shallow water equations. In addition, they defined the amplification factors of different ocean bathymetry to study the evolution of solitary waves over various bathymetries.

The three-dimensional run-up problem has received comparatively less attention. Zhang (1996) investigated the run-up associated with a solitary wave obliquely incident to a plane beach. A linear solution was found for the three-dimensional run-up using Fourier synthesis. Zhang (1996) also investigated both the non-linear problem and the effect of frequency dispersion. Brocchini (1998) investigated non-breaking solitary pulses incident and reflecting on an inclined plane beach by means of a weakly three-dimensional extension of the solution proposed by Synolakis (1986).

All of the simplified models above deal with non-breaking solitary wave run-up. If the wave breaks during the run-up or run-down process, the basic physics of the run-up is complicated and far from being completely understood. Most of the previous work on breaking wave run-up consists of experimental studies or numerical simulations. It has been found from field and laboratory studies that after a wave breaks, the form of the propagating wave is similar to a propagating bore in terms of appearance. Thus, the study of bore propagation and bore run-up may provide valuable information about breaking wave run-up. Ho and Meyer (1962) and Shen and Meyer (1963) proposed an analytical theory for bore run-up using the non-linear shallow water equations. From this derivation, they found that when the bore arrived at the initial

shoreline, the height of the bore became zero and, thus, the bore collapsed at the shoreline. After that, the fluid motion entered another stage in the form of a thin sheet of water propagating up the slope. The maximum run-up predicted by Shen and Meyer (1963) was:

$$R_b = \frac{u^{*2}}{2g} \tag{2.3}$$

which was independent of the beach slope, and u^* was the horizontal velocity of the bore at the instant it reached the initial shoreline. Miller (1968) experimentally measured the maximum run-up of a bore on four beaches with different angles and compared those results with the prediction, i.e., Eq. 2.3. He found that the beach angle and the bottom roughness of the slope were important factors in determining the run-up of bore, and the experimental results differed from the theoretical predictions significantly. Yeh (1991) also investigated the bore-like tsunami run-up in the laboratory and reported that bore collapse did not occur in his experiments. The transition process that took place when the bore approached the initial shoreline was more of a "momentum exchange" (Yeh (1991)) between the incident bore and the small wedge-shaped water that was initially still ahead of the bore along the shore. The maximum run-up, however, seemed to be predicted from the initial offshore condition by Eq. 2.3 by reducing the value of u^*. Thus, it appears that the bore run-up theory can give qualitative information about the physical process, and it is one of few analytical solutions available to describe the process of wave propagation after wave breaking.

2.2 Laboratory Experiments

The early experiments reported by Hall and Watts (1953) and Camfield and Street (1969) have been used in the past to verify analytical results and the accuracy of

numerical models. Hall and Watts (1953) measured the maximum run-up of solitary waves on five different beaches. The slopes of the beaches were: 1:1, 1:2.14, 1:2.75, 1:3.73, 1:5.67 and 1:11.43. The empirical formula of maximum run-up as a function of beach slope and incident wave height was given based on the laboratory measurements in the form:

$$\frac{R}{h_0} = k(\beta)[(\frac{H}{h_0})^{a(\beta)}, (\beta)^{c(\beta)}] \tag{2.4}$$

where k, a, and c are empirical parameters as a function of the beach slope β. The experiments of Hall and Watts (1953) were performed for a variety of water depths ranging from 15.24 cm to 68.58 cm. The waves were generated by what is now considered to be a crude process, i.e., by pushing the original still water horizontally with a vertical plate. The shape of the incident solitary wave was not described in these experiments. Using a different generation mechanism, Camfield and Street (1969) confirmed Hall and Watts's (1953) experimental results.

Battjes (1974) used dimensional analysis to analyze the characteristics of periodic wave breaking and run-up on plane slopes, and showed that breaking criterion, breaker type, breaker height-to-depth ratio, and the maximum run-up were approximately governed by only one parameter referred to as the surf similarity parameter:

$$\zeta = \frac{tan\beta}{(H/L_0)^{1/2}} \tag{2.5}$$

where L_0 is the deep-water wavelength of the incident periodic wave. Battjes (1974) summarized published experimental data to present empirical formulas of several wave characteristics as a function of the surf similarity parameter, ζ. For example, the maximum run-up normalized by the incident wave height was written as:

$$\frac{R}{H} = \zeta \qquad for \quad 0.1 < \zeta < 2.3 \tag{2.6}$$

The more recent experiments of Synolakis (1986) and Zelt (1991a) are of importance in confirming analytical and numerical models of the run-up process due to the precision of their experimental techniques compared to those of earlier studies. Synolakis (1986) measured the maximum run-up of non-breaking and breaking solitary waves on a 1:19.85 slope, and the following expressions were obtained:

$$\begin{aligned} non-breaking: & \\ \frac{R}{h_0} &= 2.831\sqrt{cot\beta}(\frac{H}{h_0})^{\frac{5}{4}} \qquad (2.7) \\ breaking: & \\ \frac{R}{h_0} &= 0.918(\frac{H}{h_0})^{0.606} \qquad (2.8) \end{aligned}$$

The non-breaking formula was obtained from his approximate non-linear theory and reasonably confirmed by experimental data, and the breaking formula was obtained empirically for the slope investigated, which was 1:19.85. Synolakis (1986) also measured the time history and the spatial wave shape for breaking solitary waves.

Kobayashi and Karjadi (1994) extended the surf similarity parameters proposed by Battjes (1974) for solitary wave run-up. The wavelength of the solitary wave L_0 in Eq. 2.5 was defined as:

$$L_0 = \frac{gT^2}{2\pi} \qquad (2.9)$$

where T was the representative time period of solitary waves and selected as the duration that the wave amplitude of the solitary wave was greater than some predefined small number δ_i ($\eta(t) > \delta_i$). Kobayashi and Karjadi (1995) fitted the breaking data of Synolakis (1986) and the numerical data from their own model and proposed an empirical expression for the maximum run-up normalized by the incident wave height as:

$$\frac{R}{H} = 2.955\zeta^{0.395} \qquad (2.10)$$

The laboratory work cited to this point dealt with two-dimensional wave run-up, i.e., the wave was generated and propagated along a narrow water channel or tank. Briggs et al. (1994) conducted solitary wave run-up experiments using a three-dimensional 30 m wide by 25 m long wave basin 30 cm deep and compared their results with those using a narrow wave tank. They found that the run-up of non-breaking waves in a basin was smaller than in a tank. They proposed an explanation that in the flume experiments, the walls were reflective and contained the wave energy, while in the basin, energy was leaked from the end of the wave front by diffraction, thereby reducing the wave height. The difference in flume and basin experiments was negligible for breaking wave run-up because the primary energy loss was due to wave breaking. The effect of the wave generation source was also investigated in their experiments.

Run-up of solitary waves on a circular island were reported by Liu et al. (1995). Surface displacement and maximum run-up were measured and compared with a numerical model based on three-dimensional shallow water equations. It was found that maximum run-up was largest in front of the island (facing the wave attack direction), and decreased gradually as the wave moved toward the lee side of the island. However, if the length of the wave generator or the crest length of the wave was much larger than the base diameter of the island, a dramatic increase in the run-up was found on the lee side of the island.

There is large body of literature on the process of solitary wave breaking. Only the most pertinent work will be discussed here. The general review of the various aspects of waves at and after breaking can be found in Peregrine (1983) and Battjes (1988). Ippen and Kulin (1955) studied the shoaling and breaking behavior of solitary waves on slopes of 1:15.38, 1:20, and 1:43.48. Based on their experimental results they concluded that the breaking height-to-depth ratio was practically constant at 1.2

for all incident solitary wave heights on gentle slopes, which was different from the theoretical value usually quoted of 0.78 for solitary waves in water of constant depth. For a steep slope, this ratio increases with the slope and with decreasing relative incident wave height, and the breaking amplitude and breaking depth increase with decreasing slope. These results are still used on occasion to compare to theoretical analyses and numerical models.

Skjelbreia (1987) used a unique laser Doppler velocimeter (LDV) to determine the kinematic characteristics of breaking solitary waves. Water particle velocities were measured under spilling and plunging breaking waves close to the free surface and to the bottom both near breaking and after breaking. From these measurements vector diagrams for the water particle velocities and accelerations under breaking waves were constructed. However, no clear mechanism was found that would define the initiation of breaking which showed the extreme complexity of the wave breaking process. Skjelbreia (1987) also measured the evolution of the wave amplitude during wave breaking and defined four regions according to the behavior of the wave amplitude on the beach: zones of gradual shoaling, rapid shoaling, rapid decay, and gradual decay. Different power laws of growth and decay rate appeared to define these zones. Skjelbreia (1987) noted from his measurements that the vortices generated from breaking appeared to be counter-rotating, and their size was on the order of the undisturbed depth at breaking. In the present discussion, a possible generation mechanism for these counter-rotating vortices will be proposed.

Papanicolaou and Raichlen (1987a, 1987b) investigated the breaking wave kinematics by visual observation of the changes in the breaking process using high-speed movies. They noted that plunging breaking differed from spilling breaking primarily in the rate of change of the properties, not in the overall characteristics of the waves. The variation of the breaking wave height-to-depth ratio with distance for solitary

waves was presented and compared with that of cnoidal waves. Other aspects of the breaking, such as bubble mass, which was defined as the area of the roller generated by the air entrainment in the breaking wave, were also measured from the images. Similar changes were found in wave height and bubble mass for solitary and cnoidal waves for each type of breaking, indicating that the effects of bubbles on the breaking waves were similar for translatory and oscillatory waves.

Measurements of the characteristics of the plunging jet generated by periodic breaking waves on slopes were reported by Chanson and Lee (1997). They found that the location of the plunging jet impact with the free surface was always above the still water level, and the impact angle of the plunging jet with the free surface was about 31°. The energy dissipation associated with the plunging jet was also estimated; they suggested that the ratio of the energy dissipation to the incident wave energy was about 20% to 60%, and it increased with the bubble penetration depth and with the characteristic length of the plunging jet.

Stansby, Chegini, and Barnes (1998) investigated the flow induced by "dam-breaking" with different ratios of the upstream depth to the downstream depth. An interesting observation was the generation of a "mushroom like" jet similar to the plunging jet of a breaking wave with the resultant splash-up as was seen in Figure 1.1. While the structure and the evolution of the jet and the splash-up were complex and difficult to define, the overall surface profiles at different times agreed remarkly well with exact solutions of the non-linear shallow water equations. These results suggested that the same non-linear shallow water equations also may be applicable to breaking wave run-up if the details of plunging jet are not included in the analysis.

2.3 Numerical Simulations

There have been a number of numerical solutions relating to the run-up of non-breaking waves and breaking waves using different simplified models. For example, an early study by Brennen and Whitney (1970) used the inviscid dynamical equations of motion in Lagrangian coordinates to investigate run-up of waves, their calculation was reasonable for non-breaking waves, but computation stopped when the wave was breaking.

The non-linear shallow water equations have been widely employed to model long wave propagation and the run-up process. If provision is made in the numerical model to account for the energy dissipation associated with wave breaking, they may also be used to simulate the breaking wave run-up.

Two basic types of numerical methods have been used to solve the shallow water equations: (i) the method of characteristics and (ii) finite-difference methods. The characteristics method has the advantage that the line of characteristics has clear physical meaning, and the path of the shoreline is always a characteristic line, thus, the position of the shoreline can be obtained directly from the computation. Freeman and Le Mehaute (1964) used this method to study wave breaking and surging on a dry bed. However, when using the method to investigate run-up, "*the line of characteristics become very near parallel and this leads to a large uncertainty in finding their point of intersection*" (Hibbert and Peregrine (1979)). Finite difference methods have been used more successfully to compute the shallow water equations. Hibbert and Peregrine (1979) solved these equations in conservative form using the Lax-Wendroff scheme, and applied the scheme to calculate the evolution and run-up of a uniform bore on a slope. The moving shoreline was treated by adding new grid points during run-up, and, if necessary, subtracting the points that were not covered by water during run-

down. A predictor-corrector-smoothing procedure was presented to predict whether the grid points needed to be adjusted. This numerical treatment was not robust, as pointed out by Titov and Synolakis (1995). Nevertheless, Hibbert and Peregrine (1979) gave the first quantitative and realistic solution of the uniform bore behavior during the run-up process.

Titov and Synolakis (1995) solved the characteristic form of the shallow water equations using finite difference methods and used it to model the propagation and run-up of solitary waves. The characteristic equation was solved using the Godunov scheme to avoid the numerical instabilities problem associated with wave breaking. The moving shoreline was treated the same as that of Hibbert and Peregrine (1979) by adding and subtracting grid points according to the shoreline position, except the boundary conditions imposed on the shoreline were modified as the following to avoid stability problems:

$$\eta(x_s) + h(x_s) = 0 \qquad \frac{dx_s}{dt} = 0 \quad at \quad x = x_s(t) \tag{2.11}$$

where x_s is the location of the shoreline, η is the wave amplitude measured from the initial water level, and h is the water depth. The wave amplitude evolution and maximum run-up for non-breaking and breaking solitary waves were computed and compared with experimental results. However, small oscillations can still be found around the breaking point in their simulations, and the second boundary conditions in Eq.2.11 was wrong (see Zhang (1996)) and need to be corrected to provide good prediction of run-up.

Zhang (1996) developed a finite-difference scheme for the shallow water equations using the Lax-Wendroff scheme to investigate non-breaking solitary wave run-up. The run-up was modeled by remapping the grid points at the surface according to the

instant shoreline position. Based on his numerical simulations, Zhang (1996) found that *"the maximum run-up of a solitary wave predicted by the shallow water equations was dependent on the initial location of the solitary wave and its value was not unique because the wave became increasely steepened given long time to travel in the absence of the dispersive effects."* Zhang (1996) also investigated the frequency dispersion and three-dimensional wave run-up upon a vertical wall using his numerical scheme. The computing domain mapping technique proposed by Zhang (1996) apparently treats the shoreline movement well and will be used in the numerical scheme developed in the present study.

Dodd (1998) investigated wave run-up, overtopping, and regeneration by solving the non-linear shallow water equations using a Roe-type Riemann solver, which was developed in gas dynamics to track shock waves. An energy dissipative term representing bottom friction was included in the model. In the scheme, a minimum local depth d_{min} was defined to treat the moving shoreline. When the water depth in the cell is less than d_{min}, the cell was considered "dry", otherwise, the cell was occupied by water ("wet"). The shoreline was defined as the separation line between the "dry" cell and the "wet" cell. Dodd (1998) conducted simulations of wave propagation and overtopping including random waves and compared them with experimental results, good agreements were found from his investigation.

In summary, the models utilizing non-linear shallow water wave equations, although having the limitation of failing to provide depthwise variations in velocity and omitting frequency dispersive effects, appear to have the ability to model aspects of the wave breaking process and the corresponding run-up for solitary waves. *"The well-documented but unexplained ability of the shallow water equations to provide quantitatively correct runup results even in parameter ranges where the underlying assumptions of the governing equations are violated"* (Titov and Synolakis (1995))

need further investigation and will be given attention in this thesis.

Boussinesq type models have also been used widely to simulate wave breaking and run-up. They can represent the non-linear effects and dispersive effects theoretically to any degree of accuracy and can describe most wave phenomena. However, a special breaking term has to be included in the momentum conservation equation to model the dissipation associated with wave breaking. The term must incorporate coefficients that need to be calibrated by field or experimental data. This drawback limits the application of the Boussinesq models. Pedersen and Gjevik (1983) developed a finite-difference scheme for the Boussinesq equations using a Lagrangian description, which can predict the non-breaking run-up process and also the possibility of wave breaking during run-down. The maximum run-up predicted using this numerical model was larger than the experimental data of Hall and Watts (1953). Peterson and Gjevik (1983) suggested that this difference was due to surface tension and friction effects that were neglected in the numerical model. It was also found that the friction effects became less important as the depth in the channel increases.

Zelt and Raichlen (1990) developed a Lagrangian representation of the Boussinesq equations and used a finite-element model to investigate non-breaking solitary wave run-up on two-dimensional and three-dimensional bathymetry. Zelt (1991a) applied this model to the case of the run-up of both non-breaking and breaking waves on a plane beach. Wave breaking was parameterized with an artificial viscosity term in the momentum equation, and the bottom friction was also modeled as a term quadratic in the horizontal water velocity. Zelt (1991a) found that non-hydrostatic effects associated with the frequency dispersion term in the Boussinesq equations reduced the tendency of waves to break and improved the agreement of the numerical results with the laboratory run-up data. When calibrated with laboratory data, the model of Zelt (1991a) could provide reasonable predictions of the wave run-up process.

In addition, Zelt (1991b) studied the landward inundation of non-breaking solitary waves that propagate up a non-planar slope.

Numerical solutions of the Laplace equations and the Navier-Stokes equations also have been used in wave run-up investigations as the computer power has increased and the algorithms used to solve complex systems have been developed. Grilli, Svendsen, and Subramanya (1997) solved a fully non-linear potential flow model (the Laplace equation) using the boundary element techniques (BEM), and used it to calculate various characteristics of breaking solitary propagation and run-up. In contrast to the depth-averaged models like the shallow water equations and the Boussinesq models, the vertical structure of the water particle velocities could be treated by the numerical model. The detailed wave breaking information including the shape of the plunging jet generated by the wave breaking, the celerity, and water particle velocity as well as the wave shoaling and overall wave profile were reported. However, this numerical model cannot predict maximum run-up since the computation stops when the plunging jet impinges the free surface. In Chapter 5, the numerical results of Grilli et al. (1997) will be compared to experimental results obtained from the present investigation.

Lin, Chang and Liu (1999) developed a numerical model solving the Reynolds equations for the mean flow field and the $k - \epsilon$ equations for the turbulent kinetic energy, k, and the turbulence dissipation rate, ϵ, and applied the model to wave breaking and run-up problems. The free-surface locations and movement were tracked by the volume-of-fluid (VOF) method proposed by Hirt and Nichols (1981). Their numerical results agreed with the experimental results in terms of the wave profile and velocities, but fail to provide the jet and splash-up information, which may be due to the inaccuracy of the free surface tracking techniques used.

Chapter 3 Theoretical Analysis

3.1 Non-Breaking Solitary Wave Run-Up

In this section the run-up of non-breaking solitary waves on a uniform plane beach connected to an open ocean of constant depth is considered. The waves are non-breaking during the run-up and run-down process. A non-linear solution to the classical shallow water equation, which describes the wave characteristics on the beach, is obtained analytically by using the Carrier and Greenspan (1958) hodograph transformation. It was found that the non-linear theory agreed well with experimental results. The maximum run-up predicted by the non-linear theory is larger than that predicted by the approximate non-linear theory of Synolakis (1986) at the order of the relative incident wave height. The validity of this non-linear theory also is discussed.

3.1.1 Governing Equations and Basic Assumptions

Consider the specific case of the run-up of two-dimensional long waves incident upon a uniform sloping beach connected to an open ocean of uniform depth, as shown in Figure 3.1. The classical shallow water equations are:

$$\eta_t + (u(h+\eta))_x = 0 \tag{3.1}$$

$$u_t + uu_x + g\eta_x = 0 \tag{3.2}$$

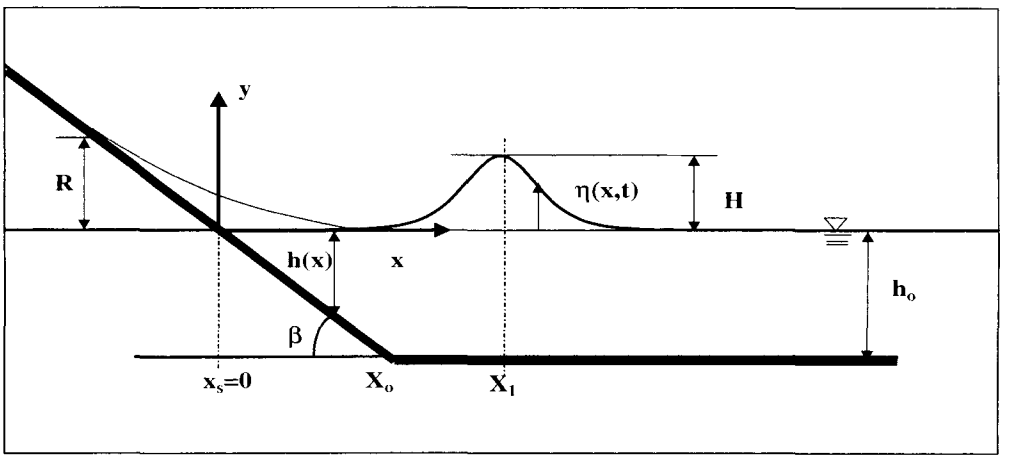

Figure 3.1: Definition sketch of the solitary wave run-up

where the subscripts denote differentiation, h is the wave amplitude, u is the depth-averaged velocity, and g is the acceleration of gravity. By introducing the following non-dimensional variables in Eqs. 3.1 and 3.2:

$$x^* = \frac{x}{h_0} \qquad h^* = \frac{h}{h_0} \qquad \eta^* = \frac{\eta}{h_0} \qquad t^* = t\sqrt{\frac{g}{h_0}} \tag{3.3}$$

where h_0 is the constant water depth in front of the slope, the non-dimensionalized non-linear shallow water equations (NLSW) are obtained:

$$\eta^*_{t^*} + (u^*(h^* + \eta^*))_{x^*} = 0 \tag{3.4}$$

$$u^*_{t^*} + u^* u^*_{x^*} + \eta^*_{x^*} = 0 \tag{3.5}$$

For convenience, the asterisk will be dropped in the following developments; therefore, all equations presented subsequently in this section are non-dimensionalized.

The depth variations in the model to be used, i.e., Figure 3.1, are:

$$h(x) = \begin{cases} 1 & x \geq X_0 \\ x \tan\beta & x < X_0 \end{cases}$$

where β is the angle of the slope shown in Figure 3.1. Eqs. 3.4 and 3.5 are the governing equations we will investigate in this study.

3.1.2 Theoretical Considerations – Existing Theories

In this section the earlier work of Synolakis (1986), Tuck and Hwang (1972), and Zhang (1996) will be summarized along with a brief discussion of the linear approach that can be taken to this problem.

Neglecting non-linear effects, Eqs. 3.4 and 3.5 can be linearized to obtain the traditional small amplitude long wave equation:

$$\eta_{tt} - (\eta_x h)_x = 0 \tag{3.6}$$

For constant depth ($h_0 = 1$) the general solution to Eq. 3.6 is:

$$\eta(x,t) = A_i e^{-ik(x+ct)} + A_r e^{ik(x-ct)} \tag{3.7}$$

where A_i, A_r are the amplitudes of the incident and reflected wave, respectively, c is the non-dimensional wave celerity at constant depth region ($c = 1$) and k is the wave number ($2\pi/L$ where L is the wave length). For a linearly varying depth the general

linear solution to Eq. 3.6 can be written as:

$$\eta(x,t) = B(k,\beta)J_0(2k\sqrt{x\cot\beta})e^{-ikct} \tag{3.8}$$

By matching Eqs. 3.7 and 3.8 at the toe of the slope, i.e., at X_0, Camfield and Street (1969) gave the solution for $A_r(k,\beta)$ and $B(k,\beta)$ in terms of $A_i(k,\beta)$ for the combined bathymetry as:

$$A_r(k,\beta) = A_i \exp(-2ik\cot\beta + 2i\arctan[\frac{J_0(2kX_0)}{J_1(2kX_0)}]) \tag{3.9}$$

$$B(k,\beta) = \frac{2\exp(-ikX_0)A_i}{J_0(2kX_0) - iJ_1(2kX_0)} \tag{3.10}$$

Superimposing a number of linear incident waves at $x = X_0$ one obtains the following expression for the wave amplitude at the toe of the slope:

$$\eta(X_0,t) = \int_{-\infty}^{\infty} A_i(k)e^{-ikct}dk \tag{3.11}$$

The wave amplitude in the region of positive depth on the slope ($0 < x < X_0$) can be determined as:

$$\eta(x,t) = 2\int_{-\infty}^{\infty} A_i(k)\frac{J_0(2k\sqrt{xX_0})e^{-ik(X_0+ct)}}{J_0(2kX_0) - iJ_1(2kX_0)}dk \tag{3.12}$$

This solution is valid only for the region $0 < x < X_0$. However, near the initial shoreline non-linear effects cannot be neglected. Therefore, one cannot solve the run-up as a linear problem, but non-linear effects must be considered and the non-linear equations, Eqs. 3.4 and 3.5, must be solved to obtain a solution for the run-up subject to various assumptions and /or approximations.

Carrier and Greenspan (1958) introduced the following transformations considering Riemann invariants of this hyperbolic system of equations to obtain the solution of Eqs. 3.4 and 3.5 for periodic waves:

$$u = \frac{\Psi_\sigma}{\sigma} \tag{3.13}$$

$$x = (\frac{\sigma^2}{16} - \frac{\Psi_\lambda}{4} + \frac{u^2}{2}) \cot\beta \tag{3.14}$$

$$t = (\frac{\Psi_\sigma}{\sigma} - \frac{\lambda}{2}) \cot\beta \tag{3.15}$$

$$\eta = \frac{\Psi_\lambda}{4} - \frac{u^2}{2} \tag{3.16}$$

where (σ, λ) are variables in the transformed plane.

Note that in the development of the transformations of Carrier and Greenspan (1958), the normalized depth variation is defined essentially in terms of the beach slope and the characteristic horizontal length of the wave. For the application of this approach to solitary waves this characteristic length is a function of the offshore depth, and for non-breaking waves it remains relatively unchanged throughout the run-up process. Thus, with decreasing depth, as the wave propagates up the slope one would not expect the shallow water wave assumption to be compromised by the slope. Therefore, the application of this approach for a steeply sloping beach should be as reasonable as for a gentle sloping beach.

Eqs. 3.4 and 3.5 are then reduced to the following simple linear equation:

$$(\sigma\Psi_\sigma)_\sigma = \sigma\Psi_{\lambda\lambda} \tag{3.17}$$

From Eq. 3.14 it can be seen that the shoreline position is always at $\sigma = 0$. Using Fourier transforms, Eq. 3.17 can be solved from the boundary condition that

at $\sigma = \sigma_0$, $\Psi(\sigma_0, k) = F(k)$; the solution bounded at $\sigma = 0$ and $\sigma = \infty$ is :

$$\Psi(\sigma, \lambda) = \frac{1}{2\pi} \int_{-\infty}^{\infty} F(k) \frac{J_0(k\sigma)}{J_0(k\sigma_0)} e^{ik\lambda} dk \tag{3.18}$$

The difficulties in determining a solution to Eq. 3.17 lies in specifying the boundary conditions and transferring the boundary conditions from (x, t) space to (σ, λ) space. To circumvent this, Synolakis (1986) simplified the Carrier and Greenspan transformations (Eq. 3.13 to 3.16) as follows under the assumption that $\Psi_\lambda \ll \sigma^2/16$ and $\Psi_\sigma/\sigma \ll \lambda/2$:

$$u = \frac{\Psi_\sigma}{\sigma} \tag{3.19}$$

$$x = \frac{\sigma^2}{16} \cot\beta \tag{3.20}$$

$$t = -\frac{\lambda}{2} \cot\beta \tag{3.21}$$

$$\eta = \frac{\Psi_\lambda}{4} \tag{3.22}$$

These approximate transformation equations are uncoupled, and make the transformation from (x, t) space to (σ, λ) space significantly easier. Synolakis (1986) chose the seaward boundary condition at the toe of slope, i.e., $x = X_0$, which corresponds to $\sigma = \sigma_0 = 4$ in (σ, λ) space. The boundary condition $F(k)$ in the (σ, λ) plane is determined from Eqs. 3.18 and 3.22 to finally yield the wave amplitude at the shoreline, $\eta(x_s, t)$ where x_s defines the shoreline path and corresponds to $\sigma = 0$. For u_s defined as the velocity of the shoreline, Synolakis (1986) obtains the following expression for the amplitude at the shoreline:

$$\eta(x_s, t) = \int_{-\infty}^{\infty} \frac{A_i(k) exp(-ik(X_0 + ct))}{J_0(2kX_0) - iJ_1(2kX_0)} dk - \frac{u_s^2}{2} \tag{3.23}$$

It is noted that the maximum run-up is reached when the shoreline velocity u_s, becomes zero. Using a solitary wave whose wave crest is located at $x = X_1$ when $t = 0$, the surface profile is defined as:

$$\eta(x,0) = \frac{H}{h_0} sech^2(\sqrt{\frac{3}{4}\frac{H}{h_0}}(x - X_1)) \tag{3.24}$$

where H is the wave height in the constant depth region ($h = h_0$), and X_1 (see Figure 3.1) is defined as the distance seaward from the toe of the slope where $X_1 = L/2$, and L is a characteristic length of the wave defined here for the solitary wave as:

$$L = \frac{2}{\sqrt{3H/4h_0}}[arccosh(\sqrt{\frac{1}{0.05}})] \tag{3.25}$$

Synolakis (1986) obtained for the solitary wave, after considerable effort, the following expression for the maximum run-up normalized by the constant offshore depth:

$$\frac{R_s}{h_0} = 2.831\sqrt{\cot\beta}(\frac{H}{h_0})^{\frac{5}{4}} \tag{3.26}$$

Comparing the simplified transformation of Synolakis (1986) to the original transformation of Carrier and Greenspan (1958), both advantages and disadvantages in using the simplified approach are apparent. The advantages are that the approach can uncouple the transformation equations, can transpose boundary conditions and initial conditions easily from (x, t) space to (σ, λ) space, and can facilitate the calculation of the wave characteristics beyond the initial shoreline position. This was a significant step past the application of the classical linear wave theory. However, the major disadvantages of the approximate non-linear theory, which the present approach attempts to eliminate, is that the simplified transformation neglects not only the terms η^2 and $u^2/2$, but also the terms Ψ_σ/σ and $\Psi_\lambda/4$, which are both of the

order of η and u. This affects both the accuracy of the wave characteristics during the run-up and run-down process and the predicted maximum run-up height. That these terms can be neglected compared to the other terms in the transformation equations has to be justified so that the simplified non-linear theory of Synolakis (1986) can be used. We will discuss the extent and significance of the effects of this approximation in Section 3.1.3.

Tuck and Hwang (1972) have proposed another method to transform the non-linear shallow water wave equations to linear form; their transformation equations are:

$$\tilde{\eta} = \eta + \frac{u^2}{2} \tag{3.27}$$

$$\tilde{u} = u \tag{3.28}$$

$$\tilde{x} = x + \eta \tag{3.29}$$

$$\tilde{t} = t + u \tag{3.30}$$

Using Eqs. 3.27 to 3.30, the shallow water equations, i.e., Eqs. 3.4 and 3.5, become:

$$\tilde{\eta}_{\tilde{t}} + (\tilde{x}\tilde{u})_{\tilde{x}} = 0 \tag{3.31}$$

$$\tilde{u}_{\tilde{t}} + \tilde{\eta}_{\tilde{x}} = 0 \tag{3.32}$$

Zhang (1996) pointed out that using the simplified transformation proposed by Synolakis (1986) is equivalent to solving the linear equations Eqs. 3.31 and 3.32, since by combining Eqs 3.13 to 3.16 and 3.27 to 3.30 we can obtain:

$$\eta = \tilde{\eta} = \frac{\Psi_\lambda}{4} \tag{3.33}$$

$$u = \tilde{u} = \frac{\Psi_\sigma}{\sigma} \tag{3.34}$$

$$x = \tilde{x} = \frac{\sigma^2}{16}\cot\beta \tag{3.35}$$

$$t = \tilde{t} = -\frac{\lambda}{2}\cot\beta \tag{3.36}$$

Thus, the approximate non-linear theory of Synolakis (1986) must have the same accuracy as the linear solution. Hence, in a sense it can be viewed as an extension of the linear theory.

3.1.3 Theoretical Considerations – The Non-Linear Theory

As mentioned earlier, the transformation of Carrier and Greenspan (1958) reduces the shallow water wave equations (Eqs. 3.4 and 3.5) to a single linear equation, i.e., Eq. 3.17, which can be solved using standard methods. The major difficulty is to determine accurate boundary conditions or initial conditions in the (σ, λ) space. Here we propose a method to obtain the boundary condition, which is one order higher than that used by Synolakis (1986). Thus, the associated solution of Eq. 3.17 using this higher-order boundary condition should be more accurate than both the linear and the approximate non-linear solutions. The validity of this method will be verified with experiments and discussed later.

Carrier (1966) pointed out that far seaward from the shoreline, non-linear effects can be neglected. Therefore, we assume the linear solution presented in Eq. 3.8 is still valid in the region near the toe of the slope, $x = X_0$, i.e., the furthest point on the slope from the initial shoreline. When we substitute the transformations (Eqs.

3.14 and 3.15) into Eq. 3.8, we obtain:

$$\eta(\sigma,\lambda) = B(k,\beta)J_0(2kX_0\sqrt{\frac{\sigma^2}{16}-\eta})e^{-ikX_0(u-\frac{\lambda}{2})} \tag{3.37}$$

Since the wave amplitude, η, and the velocity, u, are small quantities near the toe of the slope, we can expand Eq. 3.37 in a Taylor's series and retain terms less than those of the order of h^2 and u^2. Thus, we obtain for the amplitude:

$$\eta(\sigma,\lambda) = B(k,\beta)(J_0(\frac{kX_0}{2}\sigma) + \frac{4kX_0}{\sigma}J_1(\frac{kX_0}{2}\sigma)\eta)(1-ikX_0u) \tag{3.38}$$

The general linear solution for the wave amplitude presented in Eq. 3.8 can be substituted back into the original linearized shallow water equation, and the linear solution for the wave velocity u can be found. The relation between u and η, obtained in this manner is:

$$u = i\frac{J_1(2kX_0)}{J_0(2kX_0)}\eta \tag{3.39}$$

After substituting Eq. 3.39 into Eq. 3.38, we obtain one algebraic equation for the wave height η near the toe of the slope ($x = X_0$), i.e., $\sigma = 4$:

$$\eta(4,\lambda) = B(k,\beta)e^{ikX_0\frac{\lambda}{2}}(J_0(2kX_0) + 2kX_0J_1(2kX_0)\eta) \tag{3.40}$$

Eq. 3.40 can be solved easily, and the result can be used as the boundary condition to solve Eq. 3.17. Thus, the boundary condition at $\sigma = 4$ is:

$$\eta(4,\lambda) = \frac{B(k,\beta)e^{ikX_0\frac{\lambda}{2}}J_0(2kX_0)}{1-2kX_0J_1(2kX_0)B(k,\beta)e^{ikX_0\frac{\lambda}{2}}} \tag{3.41}$$

Since the denominator in Eq. 3.41 is less than unity for any value of the wave

number k, we can use the approximation $(1-x)^{-1} = 1 + x + x^2 + O(x^3)$ and expand the boundary condition around the toe of the slope as:

$$\eta(4,\lambda) = [B(k,\beta)e^{ikX_0\frac{\lambda}{2}}J_0(2kX_0)] + [2kX_0B(k,\beta)^2e^{ikX_0\lambda}J_0(2kX_0)J_1(2kX_0)] \quad (3.42)$$

Finally for an arbitrary incident wave as given by Eq. 3.11, the boundary condition at $\sigma = 4$, Eq. 3.42, becomes:

$$\begin{aligned}\eta(4,\lambda) &= \int_{-\infty}^{\infty} B(k,\beta)e^{ikX_0\frac{\lambda}{2}}J_0(2kX_0)dk \\ &+ \int_{-\infty}^{\infty} 2kX_0B(k,\beta)^2e^{ikX_0\lambda}J_0(2kX_0)J_1(2kX_0)dk \end{aligned} \quad (3.43)$$

The first integral in Eq. 3.43 is the boundary condition used in the approximate non-linear theory of Synolakis (1986). The second integral that results from the present study can be viewed as a correction to this approximate non-linear theory. Since the governing equation, Eq. 3.17, is linear in σ and λ, we can solve the complete problem by superposing the solutions for Eq. 3.17 using the first term and second term in Eq. 3.43 as the boundary condition. The solution using the first integral in Eq. 3.43 as the boundary condition is the same as the approximate non-linear solution of Synolakis (1986), and the solution using the second integral in Eq. 3.43 as the boundary condition is:

$$\frac{\psi_\lambda(\sigma,\lambda)}{4} = \int_{-\infty}^{\infty} \frac{2kX_0B(k,\beta)^2e^{i2kX_0\frac{\lambda}{2}}J_0(2kX_0)J_1(2kX_0)J_0(kX_0\sigma)}{J_0(4kX_0)}dk \quad (3.44)$$

Adding the two solutions, we obtain the final solution for the non-linear problem

subject to the approximations discussed earlier:

$$\begin{aligned}
\frac{\psi_\lambda(\sigma,\lambda)}{4} &= \int_{-\infty}^{\infty} B(k,\beta)e^{ikX_0\frac{\lambda}{2}}J_0(kX_0\frac{\sigma}{2})dk \\
&+ \int_{-\infty}^{\infty} \frac{2kX_0B(k,\beta)^2e^{i2kX_0\frac{\lambda}{2}}J_0(2kX_0)J_1(2kX_0)J_0(kX_0\sigma)}{J_0(4kX_0)}dk \qquad (3.45)\\
u &= \frac{\psi_\sigma(\sigma,\lambda)}{\sigma} \\
&= \int_{-\infty}^{\infty} iB(k,\beta)e^{ikX_0\frac{\lambda}{2}}J_0(kX_0\frac{\sigma}{2})dk \\
&+ \int_{-\infty}^{\infty} \frac{2kX_0B(k,\beta)^2e^{i2kX_0\frac{\lambda}{2}}J_1(2kX_0)^2J_0(kX_0\sigma)}{J_1(4kX_0)}dk \qquad (3.46)\\
\eta &= \frac{\psi_\lambda}{4} - \frac{u^2}{2} \qquad (3.47)\\
x &= cot\beta(\frac{\sigma^2}{16} - \eta) \qquad (3.48)\\
t &= cot\beta(u - \frac{\lambda}{2}) \qquad (3.49)
\end{aligned}$$

where $B(k,\beta)$ is given in Eq. 3.10.

Once the incident wave profile is known in terms of the Fourier components $A_i(k)$, we can calculate all the wave characteristics in the sloping region including the maximum run-up from Eqs. 3.45 to 3.49. The asymptotic form of the Bessel function is used to simplify the calculations.

For an incident solitary wave centered at $x = X_1$, the Fourier form of this wave is:

$$A(k) = \frac{2}{3}k[csch(\alpha k)e^{ikX_1}] \qquad (3.50)$$

where $\alpha = \pi/\gamma$ and $\gamma = (3H/4h_0)^{1/2}$.

Now we are in a position to compare the solitary wave run-up predicted by the approximate non-linear theory and the present non-linear theory. The non-linear run-

up is given by the value of the wave height at shoreline position, i.e., $\sigma = 0$. From Eqs. 3.45 to 3.49, we obtain:

$$\begin{aligned}\eta(0,\lambda) &= \frac{4}{3}\int_{-\infty}^{\infty}\frac{kcsch(\alpha k)e^{ik(X_1-X_0+X_0\frac{\lambda}{2})}}{J_0(2kX_0)-iJ_1(2kX_0)}dk \\ &+ \frac{32X_0}{9}\int_{-\infty}^{\infty}\frac{k^3csch(\alpha k)^2e^{i2k(X_1-X_0+X_0\frac{\lambda}{2})}J_0(2kX_0)J_1(2kX_0)}{(J_0(2kX_0)-iJ_1(2kX_0))^2J_0(4kX_0)}dk \\ &- \frac{u_s^2}{2} \end{aligned} \tag{3.51}$$

where as before u_s is the velocity of the shoreline tip, i.e., the tip of the run-up tongue.

At the maximum run-up, the shoreline velocity is zero. (It is noted that in Eq. 3.51 the first integral is identical to Eq. 3.23, i.e., the maximum run-up predicted by the linear theory and the approximate non-linear theory.) The two integrals can be calculated using the method proposed by Synolakis (1986). Thus, the maximum run-up obtained from the present non-linear theory is obtained as:

$$\frac{R}{h_0} = \frac{R_s}{h_0} + \frac{R_{cr}}{h_0} = \frac{R_s}{h_0}(1 + \frac{R_{cr}}{R_s}) \tag{3.52}$$

with

$$\frac{R_s}{h_0} = 2.831\sqrt{cot\beta}(\frac{H}{h_0})^{\frac{5}{4}} \tag{3.53}$$

$$\frac{R_{cr}}{h_0} = 0.293(cot\beta)^{\frac{3}{2}}(\frac{H}{h_0})^{\frac{9}{4}} \tag{3.54}$$

$$\frac{R_{cr}}{R_s} = 0.104cot\beta(\frac{H}{h_0}) \tag{3.55}$$

In Eq. 3.52 R_s/h_0 is the run-up obtained by Synolakis (1986) and R_{cr}/h_0 is the correction to the approximate theory based on the non-linear approach presented here. Thus, the non-linear run-up is different from the linear run-up by an extra term

that is a function of the initial relative incident wave height and beach slope. The significance of the non-linear correction term, R_{cr}/R_s, can be seen easily from Eq. 3.55. This will be discussed later along with the influence of wave breaking on the non-breaking correction term.

3.2 Numerical Simulation of Breaking Solitary Wave Run-Up - WENO Scheme

The higher-order non-linear theory presented in the previous section is applied to non-breaking solitary waves run-up only. As the incident wave height increases or the slope investigated becomes gentler, the non-linear effects and the dispersive effects cannot be balanced during the wave propagation process, and the wave height and water particle velocity in the wave increase. The increase rate is so large that when the water particle velocity equals the wave speed, wave breaking occurs. "*The physical significance of this wave breaking process arises from the fluid motion associated with breaking that absorbs most of the energy transmitted with the wave.*" (Galvin (1983)). This energy dissipation process not only changes the wave kinematics of the propagation process but also decreases the maximum wave run-up dramatically. From recent field observations, it appears that the run-up associated with many tsunamis may be caused by breaking waves. As mentioned earlier, one recent event in Papua New Guinea in July 1998 resulted in wide destruction and more than 2,000 deaths. From eye-witness accounts it appears that the waves, some about 15 m high at the shoreline, were breaking. Thus, the development of an applicable theory to predict run-up due to breaking waves is desirable and important for the tsunami research.

Due to the mathematical difficulties in dealing with the complexities of the fluid motion in the wave breaking process, most of the previous studies on breaking wave run-up are experimental and focus on breaking wave effects on beaches. In the present study, a numerical model based on the weighted essentially non-oscillatory (WENO) scheme used in gas dynamics is developed to simulate the process of wave breaking and run-up. However, since breaking was only modeled as a propagating bore by the numerical model, the details of wave breaking, such as the plunging jet, splash-up,

etc., cannot be provided.

A depth-averaged numerical model that solves the non-linear shallow water equations is implemented here. As mentioned earlier, the shock-capturing method of Weighted Essentially Non-Oscillatory Scheme(WENO) developed in gas dynamics is used to capture the wave breaking process. The wave breaking process is modeled and captured automatically by the numerical scheme without introducing any ad-hoc breaking term to suppress the numerical oscillation that is very common in other numerical models. The energy dissipation associated with breaking and the maximum wave run-up on the slope during the wave breaking process will be investigated by this numerical method.

3.2.1 Mathematical Formulation

We consider the run-up problem defined in the last section of two-dimensional long waves incident upon a uniform sloping beach connected to an open ocean of constant depth (see Figure 3.1).

The difficulties associated with the numerical study of wave breaking and the resulting run-up process lie in how to choose a suitable mathematical model to simulate wave breaking. The classical nonlinear shallow water equations (NLSW):

$$\eta_t + (u(h+\eta))_x = 0 \tag{3.56}$$

$$u_t + uu_x + g\eta_x = 0 \tag{3.57}$$

were found to be a suitable model to describe the run-up process of non-breaking solitary waves in Section 3.1.3. These equations are very similar in terms of the mathematical structure to the Eulër equations in gas dynamics, which can admit

discontinuous solutions if written in conservative form. The discontinuities are interpreted as shocks and found to be good mathematical representations of the real flow. Similarly, if we write the NLSW equations in conservative form, a discontinuity in the solution is also possible and it can be used as a simplified mathematical model for a breaking wave or a bore.

When written in conservative form, the shallow water equations become:

$$(h+\eta)_t + (u(h+\eta))_x = 0 \tag{3.58}$$

$$(u(h+\eta))_t + [(h+\eta)u^2 + \frac{1}{2}g(h+\eta)^2]_x = g(h+\eta)h_x \tag{3.59}$$

Let $d = h + \eta$ and introduce the following non-dimensional variables in Eqs. (2.3) and (2.4):

$$x^* = \frac{x}{h_0} \qquad h^* = \frac{h}{h_0} \qquad \eta^* = \frac{\eta}{h_0} \qquad t^* = t\sqrt{\frac{g}{h_0}} \tag{3.60}$$

where h_0 is the constant depth seaward of the slope, as shown in Figure 3.1. The non-dimensional conservative shallow water equations are then obtained as:

$$d_t + (ud)_x = 0 \tag{3.61}$$

$$(du)_t + [du^2 + \frac{1}{2}d^2]_x = dh_x \tag{3.62}$$

For convenience, the asterisk (*) indicating non-dimensionality has been dropped in the above equations and the remaining discussion.

3.2.2 Numerical Model and Treatment of a Moving Shoreline

When using Eqs. 3.61 and 3.62 on wave run-up problems, difficulties arise from treating the shoreline position, since the shoreline changes as the water swashes

up the slope during the run-up process. Therefore a special treatment has to be included in the numerical model to define the shoreline. The most commonly used technique to model the run-up is using Eulërian models with fixed numerical meshes covering both the wet and the dry regions. The shoreline position is then defined as the interface between the "wet cell" and the "dry cell". Examples of this treatment can be seen in Lin, Chang, and Liu (1999). These methods can be implemented easily, but can cause inaccuracy in determing the shoreline position and numerical instabilities if not treated carefully. Also the "dry" region has to be covered in the computing domain, which affects the computational efficiency of the numerical scheme. Another approach is using a Lagrangian model for the governing equations instead of the Eulërian model. In this method the shoreline position is automatically defined. Zelt (1991b) used a Lagrangian Boussinesq finite-element wave model to study the run-up of non-breaking and breaking solitary waves. The Lagrangian methods do not need special treatment at the shoreline, but the governing equations become complicated and these methods are rarely used in wave studies.

In this development we use the computational domain mapping technique proposed by Zhang (1996) to model the shoreline movement. This method retains the simplicity of the Eulër method, but uses the simplified Lagrangian approach for the shoreline position. The technique is summarized below. (The following description is from Zhang (1996).)

For the computational domain $(-\Gamma, 0)$ of the numerical calculation the following transformation on (x, t) plane is introduced:

$$x = (1 + \frac{X}{\Gamma})x' + X \tag{3.63}$$

$$t = t' \tag{3.64}$$

where $x = X(t)$ is the shoreline position defined in the coordinate system as a function of time t, Γ is the total initial length of the computational domain, (x', t') is the new computing plane. Notice that under this transformation, the water shoreline position $x = X(t)$ is always located at $x' = 0$, and the seaward boundary of the computational domain, $x = -\Gamma$, is always located at $x' = -\Gamma$ in the transformed computational domain (x', t'). Therefore, the length of the computational domain and the number of mesh points do not change with time during the shoreline movement process in the new (x', t') plane. Only the actual location for each grid in (x, t) plane is changed at each calculation cycle, but this actual location for each mesh point can be calculated from Eqs. 3.63, 3.64 after every computing cycle. The moving boundary problem is then changed to a fixed boundary problem and the shoreline and its associated boundary conditions can be treated using standard techniques.

From Eqs. 3.63 and 3.64 the relationship between the derivatives in the two systems are obtained as:

$$\frac{\partial}{\partial t} = \frac{\partial}{\partial t'} - \frac{1 + x'/\Gamma}{1 + X/\Gamma} U \frac{\partial}{\partial x'} \tag{3.65}$$

$$\frac{\partial}{\partial x} = \frac{1}{1 + X/\Gamma} \frac{\partial}{\partial x'} \tag{3.66}$$

where $U = dX/dt$ is the shoreline velocity along the slope. Substituting these relations into the original equations, i.e., Eqs. 3.61 and 3.62, the governing equations in the new coordinate system are obtained (the primes are dropped for convenience):

$$d_t + (-c_1 U d + c_2 u d)_x = -\frac{c_2}{\Gamma} U d \tag{3.67}$$

$$(du)_t + [-c_1 U du + c_2 d u^2 + \frac{1}{2} c_2 d^2]_x = c_2 d h_x - \frac{c_2}{\Gamma} U du \tag{3.68}$$

where c_1, c_2 are defined as:

$$c_1 = c_1(x,t) = \frac{1 + x/\Gamma}{1 + X/\Gamma} \qquad c_2 = c_2(t) = \frac{1}{1 + X/\Gamma} \tag{3.69}$$

Eqs. 3.67, 3.68 can be written in standard vector form as:

$$\vec{V}_t + \vec{F}_x = \vec{S} \tag{3.70}$$

where $\vec{V}$ is the calculating variable, $\vec{F}$ is the numerical flux, and $\vec{S}$ is the source term. These vectors are defined as:

$$\vec{V} = \begin{bmatrix} d \\ du \end{bmatrix} \quad \vec{F} = \begin{bmatrix} -c_1 U d + c_2 u d \\ -c_1 U d u + c_2 d u^2 + \frac{1}{2} c_2 d^2 \end{bmatrix} \quad \vec{S} = \begin{bmatrix} -c_2 U d/\Gamma \\ c_2 d h_x - c_2 U d u/\Gamma \end{bmatrix} \tag{3.71}$$

Eq. 3.70 is a system of hyperbolic conservation laws, and can be discretized on uniform grids by the standard finite difference method with conservative form:

$$\frac{\vec{V}_i^{n+1} - \vec{V}_i^n}{\delta t} = -\frac{\vec{F}_{i+\frac{1}{2}}^n - \vec{F}_{i-\frac{1}{2}}^n}{\delta x} + \vec{S}_i^n \tag{3.72}$$

where δt is the computing time step, δx is the grid size. $\vec{F}(\vec{V})$ is the numerical flux function:

$$\vec{F}_{i+\frac{1}{2}}^n = f(\vec{V}_{i-r}^n, \vec{V}_{i-r+1}^n, \cdots, \vec{V}_{i+s}^n) \tag{3.73}$$

The quantity f is a Lipschitz continuous function in all the arguments, and consistent with the physical flux F. These conditions assure that if the solution to the conservative scheme Eq. 3.72 converges, it will converge to a weak solution of original partial differential equation, i.e., Eq. 3.70. $(i-r, i-r+1, \cdots, i+s)$ is the stencil of the present numerical scheme.

3.2.3 Weighted Essentially Non-Oscillatory (WENO) Shock-Capturing Scheme

The differences between various numerical methods applied to the general conservation laws, Eq. 3.70, lie in the choice of the computational stencils and the numerical flux functions. Traditional numerical methods like the Lax-Wendroff method and the MacCormack method use fixed stencils for each computing point and interpolate the numerical flux function inside the stencil to get the flux values at the cell boundaries $i + 1/2$, $i - 1/2$. These methods work well for most problems with continuous solutions. For example, Zhang (1996) used the Lax-Wendroff scheme to compute the non-breaking solitary wave run-up on steep slopes. However, when applying the fixed stencil method to a problem with discontinuities within the computing domain, such as breaking wave cases, a well-known numerical problem called the "Gibbs phenomenon" arises. This is when the numerical solution oscillates near the discontinuities, and does not decay when the grid is refined. The oscillations often lead to numerical instabilities, which are the challenge that must be faced when numerically simulating breaking waves. Various remedies have been used to eliminate or reduce the spurious oscillations. The most successful methods that have been used in the past are the artificial viscosity method and the limit flux or slope method. These methods introduce some ad-hoc "breaking terms" to increase the numerical dissipation in the original equations or reduce the order of accuracy. These are very problem dependent. The coefficient in the ad-hoc term must be calibrated according to prior experimental data before being applied to actual numerical calculations. Besides, since the numerical dissipation has been increased, the discontinuities will be smeared and the numerical scheme will lose accuracy.

The essentially non-oscillatory (ENO) scheme developed by Harten, Engquist, Os-

her, and Chakravarthy (1987) is the first successful method that achieves no oscillations near the discontinuities and retains high-order accuracy to solve the conservative laws (Eq. 3.70). The difference between the ENO scheme and other methods lies in how to choose the cells used in the reconstructing the numerical flux. These cells together are called the stencil for the numerical method. The basic idea of the ENO scheme is instead of using a fixed stencil to interpolate the numerical flux function, an adaptive stencil is chosen based on the local smoothness of the solutions. The measurement of the local smoothness, the hierarchy to choose the stencil points, and the extension to higher-order schemes have been developed by Harten et al. (1987) to ensure the efficiency and accuracy for the numerical methods. The ENO scheme has been used successfully in gas dynamics to simulate shock behavior and in channel flows to simulate bores. The results have been very satisfactory. For example, Yang and Shu (1993) used a second-order ENO scheme to simulate bore impingement on a circular cylinder and the propagation of a bore through a channel with a contraction and an expansion.

Recently Liu, Osher, and Chan (1994) and Jiang and Shu (1996) have developed the weighted essentially non-oscillatory scheme (WENO) based on the original ENO scheme. The WENO scheme provides several improvements compared to the ENO scheme, and it can achieve a higher accuracy of the numerical flux on the same number of stencil points by exploring all the local smoothness information provided by the ENO method. Applications of WENO scheme to gas dynamics have been reported recently, see Shu (1998). However the application to breaking waves and bore problems has not been reported. This study is the first to attempt to implement this scheme in simulating the breaking wave run-up process. A detailed description of the WENO scheme can be found in Shu (1998); below is the summary of the fifth-order WENO scheme used with Eq. 3.70.

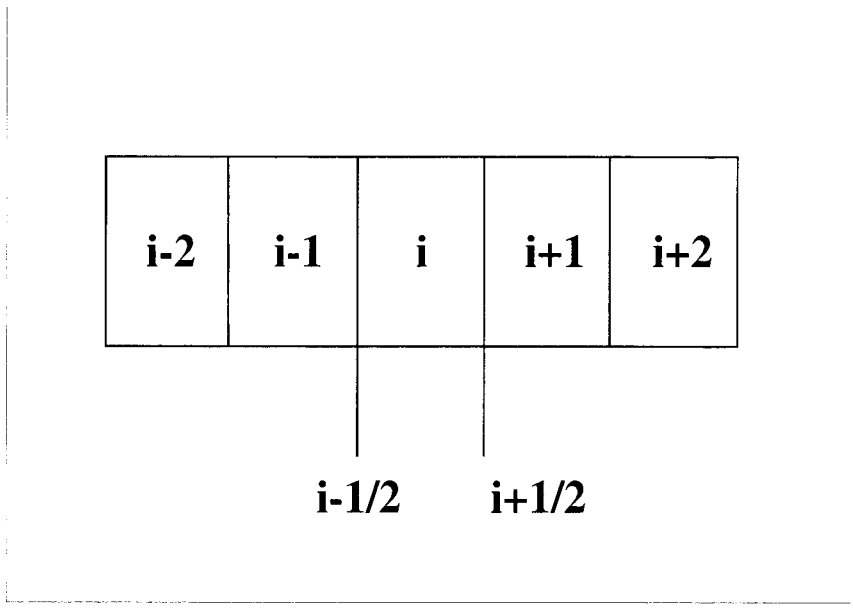

Figure 3.2: Sketch of the stencil used in WENO scheme

Consider the possible stencils used for calculation for point i $(i-2, i-1, \cdots, i+2)$ shown in Figure 3.2. The value of the numerical flux $\vec{F}$ is known from Eq. 3.71. To assure the numerical stability and convergence to a physical possible solution for Eq. 3.70, the Lax-Friedrichs flux splitting is used on the numerical flux:

$$\vec{F}(\vec{V}) = \vec{F}^{+}(\vec{V}) + \vec{F}^{-}(\vec{V}) \tag{3.74}$$

where

$$\vec{F}^{\pm}(\vec{V}) = \frac{1}{2}(\vec{F}(\vec{V}) \pm \alpha \vec{V}) \qquad \alpha = \max_{\vec{V}} |\vec{F}'(\vec{V})|$$

note $\vec{F}'(\vec{V})$ is the derivative matrix and can be obtained easily from Eq. 3.71.

From numerical analysis, a polynomial with third-order accuracy can be con-

structed from point-wise values $\vec{F}_i^{\pm}(\vec{V})$ for the candidate stencils and the value $\vec{F}_{i+1/2}^{\pm}(\vec{V})$ in Eq. 3.72 can be obtained from this polynomial. This will give us three different reconstructions for the stencils above:

$$F_{i+\frac{1}{2}}^{\pm(r)} = \Sigma_{j=0}^{2} c_{rj} F_{i-r+j}^{\pm} \quad r = 0, 1, 2 \tag{3.75}$$

where c_{rj} is the interpolation coefficient and can be found in Shu (1998) and has the value:

$$c_{rj} = \sum_{m=j+1}^{k} \frac{\sum_{l=0, l\neq m}^{k} \prod_{q=0, q\neq m, l}^{k} (r-q+1)}{\prod_{l=0, l\neq m}^{k} (m-l)} \tag{3.76}$$

The WENO scheme gives a new approximation to the numerical flux at the boundaries as the combinations of these reconstructions:

$$F_{i+\frac{1}{2}}^{\pm} = \Sigma_{r=0}^{2} \omega_r F_{i+\frac{1}{2}}^{\pm(r)} \tag{3.77}$$

where ω_r can be obtained as:

$$\omega_r = \frac{\alpha_r}{\Sigma_{s=0}^{2} \alpha_s} \qquad \alpha_r = \frac{d_r}{(\epsilon + \beta_r)^2} \tag{3.78}$$

ϵ is a small number introduced to make sure the denominator in above equation does not become zero; one usually chooses $\epsilon = 10^{-6}$. The quantities d_r, β_r are determined as:

$$d_0 = \frac{3}{10} \quad d_1 = \frac{3}{5} \quad d_2 = \frac{1}{10} \tag{3.79}$$

and

$$\beta_0 = \frac{13}{12}(F_i^{\pm} - 2F_{i+1}^{\pm} + F_{i+2}^{\pm})^2 + \frac{1}{4}(3F_i^{\pm} - 4F_{i+1}^{\pm} + F_{i+2}^{\pm})^2 \tag{3.80}$$

$$\beta_1 = \frac{13}{12}(F_{i-1}^{\pm} - 2F_i^{\pm} + F_{i+1}^{\pm})^2 + \frac{1}{4}(F_{i-1}^{\pm} - F_{i-1}^{\pm})^2 \tag{3.81}$$

$$\beta_2 = \frac{13}{12}(F^{\pm}_{i-2} - 2F^{\pm}_{i-1} + F^{\pm}_{i})^2 + \frac{1}{4}(F^{\pm}_{i-2} - 4F^{\pm}_{i-1} + 3F^{\pm}_{i})^2 \quad (3.82)$$

By applying the above procedure on $\vec{F}_i^{+}(\vec{V})$ and $\vec{F}_i^{-}(\vec{V})$ separately for both the left boundary numerical flux $\vec{F}^n_{i-\frac{1}{2}}$ and the right boundary numerical flux $\vec{F}^n_{i+\frac{1}{2}}$ at each computing point i, we can get the total flux for the cell. From Eq. 3.72, the solutions at the new time level $n+1$ can be found explicitly from the values at time level n. By numerical analyses of Shu (1998), the above numerical scheme is stable and has accuracy up to fifth-order at smooth regions and obtains sharp discontinuities without spurious oscillation nearby.

3.2.4 Boundary Conditions

It is necessary to apply boundary conditions to the computational domain. To efficiently impose different boundary conditions, "ghost cells" have been added to the left and right boundary. When choosing the computing stencil in the numerical scheme described above to calculate the numerical flux, only real cells are chosen during the calculation.

For the totally reflective boundary conditions (vertical wall located at the boundary between first cell (ghost cell) and the second cell (the real cell)) at the seaward boundary, the velocity of the wave at the vertical wall must be zero: $u_{\frac{1}{2}} = 0$. The following boundary conditions can be derived from the Eq. 3.70:

$$d_0 = d_1 \quad (3.83)$$

$$(du)_0 = -(du)_1 \quad (3.84)$$

where the cell with index 0 is the ghost cell added in the computation domain. (This

boundary conditions will also be used in this thesis to model the vertical wall in the case of the splash-up of a non-breaking or breaking wave on a vertical wall.)

No special treatment has to be imposed on the boundary for the non-reflective boundary conditions at the seaward boundary since the WENO scheme is a conservative scheme: this conditions are automatically satisfied when calculating the numerical flux at the boundary cells.

For the shoreline boundary conditions, Zhang (1996) has proposed the following conditions in the transformed computing domain:

$$h(X(t)) + \eta(X(t).t) = 0 \tag{3.85}$$

$$\frac{dX}{dt} = U(t) \tag{3.86}$$

$$\frac{dU}{dt} = -\eta_x \tag{3.87}$$

Eqs. 3.85 and 3.86 are obviously true for shoreline position, and 3.87 is identical to Eq. 3.57. It is the Lagrangian description of the shoreline movement.

The Beam-Warming scheme and trapezoidal integration are used when discretizing Eqs. 3.85 to 3.87 following Zhang (1996). These schemes are second-order in space and time:

$$U_N^{n+1} = U_N^n - \frac{\delta t}{\delta x}(3\eta_N^n - 4\eta_{N-1}^n + \eta_{N-2}^n) + \frac{\delta t^2}{2\delta x^2}(3\eta_N^n - 2\eta_{N-1}^n + \eta_{N-2}^n) \tag{3.88}$$

$$X_N^{n+1} = X_N^n + \frac{1}{2}\delta t(U_N^{n+1} + U_N^n) \tag{3.89}$$

where N is the last grid index of the transformed computing domain, and always corresponds to the shoreline position.

3.2.5 Test Cases

In this section the numerical scheme including the boundary conditions described above is verified by several numerical experiments.

A Solitary Wave Propagating on a Constant Water Depth This test case models the single solitary wave propagating on a constant water depth and is used to verify both the accuracy of the numerical scheme when solving wave problems and the conservation laws of the physical parameters like total mass and total energy of the computing domain.

We use the first-order solitary wave theory for the initial wave shape and wave velocity, i.e.:

$$\eta = H sech^2(\sqrt{\frac{3H}{4h_0^3}}(x - X_1) \tag{3.90}$$

$$u = \frac{c\eta}{1+\eta} \tag{3.91}$$

$$c = \sqrt{g(H+h_0)} \tag{3.92}$$

where H is the initial relative wave height for the solitary wave, X_1 is the position of the initial wave crest in the computing domain as shown in Figure 3.1 , and c is the wave celerity.

The comparison between numerical results and theoretical results is presented in Figure 3.3 for wave shape. It has been pointed out by other researchers that any disturbance with a positive hump like the solitary wave propagating into still water of constant depth under shallow water equations will ultimately be discontinuous and break, see Stoker (1957). This can be proved by analyzing the characteristic curves for the simple wave case. Thus, the dispersive effects cannot be neglected and the

balance between the non-linear effects and dispersive effects is very important when simulating the solitary wave propagation on a constant water depth. To include the dispersive effect in the numerical scheme, we include the dispersive term of the general Boussinesq model (Wu (1979)) into our numerical scheme. The treatment of this dispersive term is the same as that of Zhang (1996). It can be seen that the solitary wave keeps the original shape when propagating and that the agreement between the theoretical prediction and numerical results is very good. The amplitude of the solitary wave is almost constant during the calculation with numerical error less than 0.1%. This shows the WENO scheme has high-order accuracy in smooth regions. Note the discretization of the Boussinesq term here is still using a fixed stencil, this will cause numerical stability when simulating the wave breaking process and hence cannot be used in the breaking wave run-up simulation. However, as pointed out before, for the wave run-up process, the dispersive term is very small compared to the non-linear term and thus can be neglected.

The mass and energy conservation properties are investigated in this numerical experiment. Mass conservation is guaranteed by the governing Eq. 3.58. For continuous solutions, the mass conservation of Eq. 3.58 and momentum conservation of Eq. 3.59 are equivalent to the energy conservation, thus mass and energy should be conserved for solitary wave propagation. The calculated mass and energy in the computing domain as a function of time are presented in Figure 3.4. We can see that the mass and energy are indeed preserved during the calculation process. The method to calculate the mass and energy will be discussed in Chapter 5. For solutions with discontinuities, the energy will not be conserved but decrease across the shock. This can be interpreted as the energy dissipation during the wave breaking process.

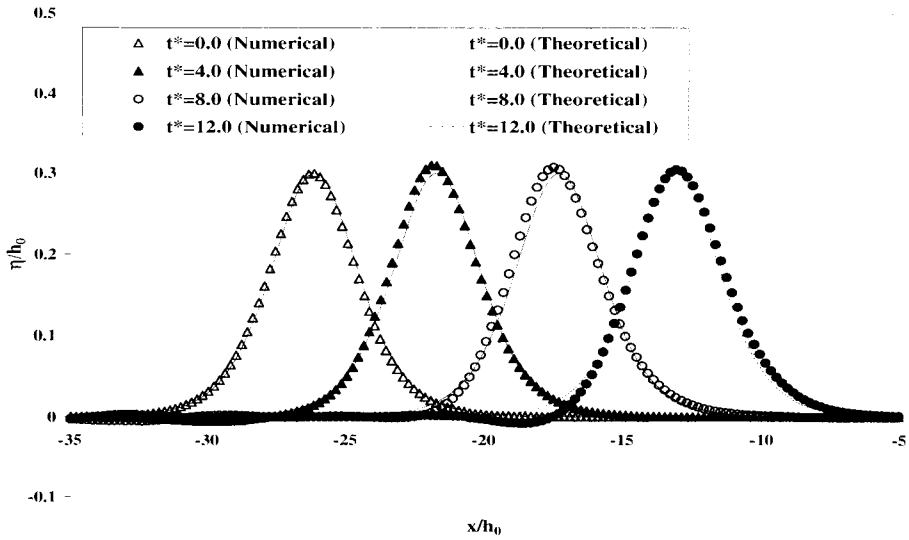

Figure 3.3: Numerical simulation of propagation of a solitary wave with $H/h_0 = 0.30$ over constant water depth. Shapes of the wave at different times

Dam-Break Problem The dam-break problem is an interesting theoretical and practical problem in civil engineering. Various theoretical and experimental investigations have been conducted in the past to study this particular flow. Here we use the numerical scheme described to simulate the flow. The numerical results will be compared to the theoretical results presented by Stoker (1957).

The initial water is still and separated by a thin plate with left (upstream) water depth $h_1 = 1.5$, and right (downstream) water depth $h_2 = 1.0$, as shown in Figure 3.5. At $t^* = 0$ the plate is removed and the water flows freely. By theory, after the plate is removed an expansion wave propagates upstream and a bore (discontinuity) travels downstream. The comparison between the theoretical solutions and the numerical results for water free-surface at $t^* = 0$, $t^* = 5.0$, $t^* = 10.0$ is shown in Figure 3.5.

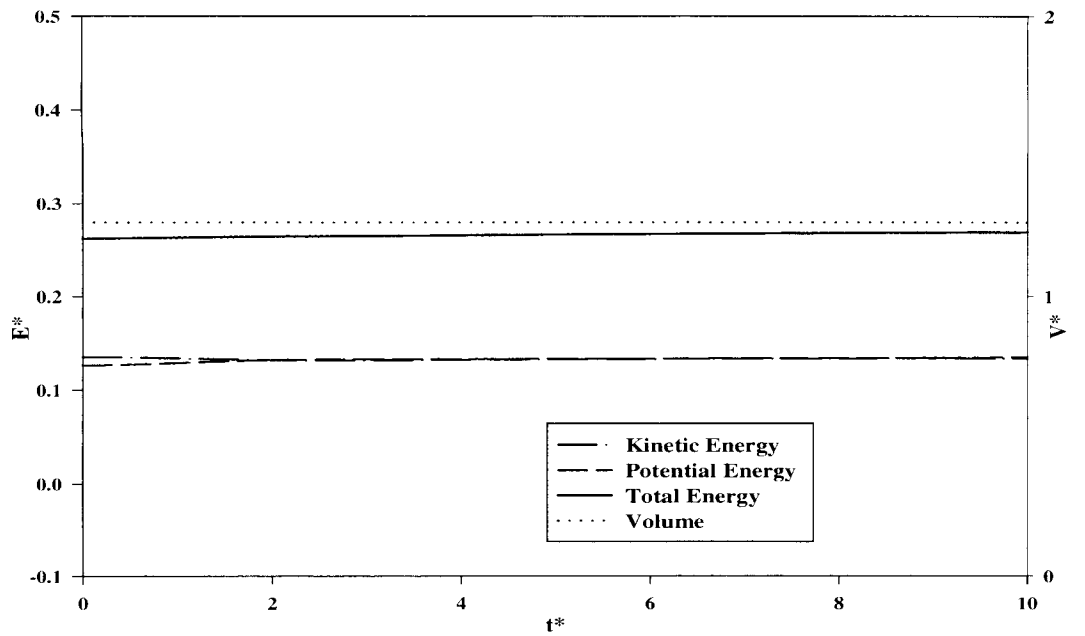

Figure 3.4: Numerical simulation of propagation of a solitary wave with $H/h_0 = 0.30$ over constant water depth. Evolution of the potential energy, kinetic energy, and volume as a function of normalized time

We can see that the numerical results agree well with the theory even around the sharp discontinuity (bore). The numerical scheme can reconstruct the jump in 2 $\sim$ 3 cells, and neither obvious numerical dissipation nor oscillation can be observed in the solution. This demonstrates that the WENO scheme can indeed capture a shock (bore) without spurious oscillations while maintaining high order of accuracy at smooth regions without shock.

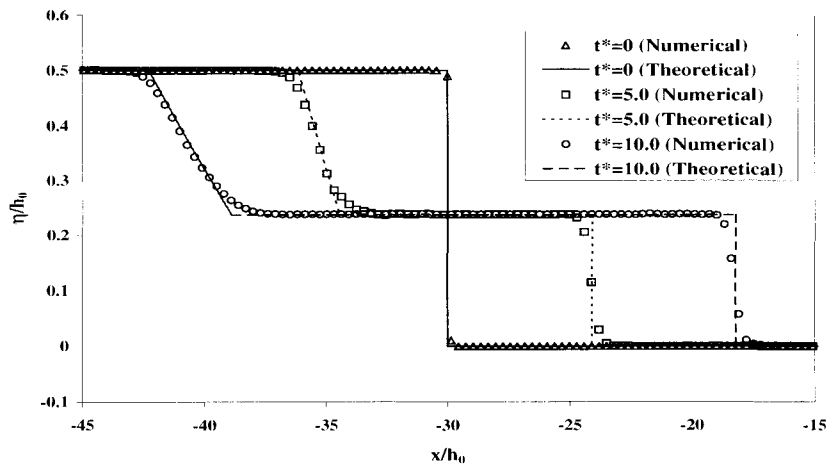

Figure 3.5: Numerical simulation of dam-break flow with the ratio between upstream water depth and downstream water depth: $h_1/h_2 = 1.5$

Chapter 4 Experimental Apparatus and Procedures

4.1 Wave Tanks and Wave Generation System

4.1.1 Wave Tanks

Three wave tanks were used to investigate solitary wave run-up. To generate a breaking wave for a relatively small incident wave height ($0.03 < H/h_0 < 0.4$), the slope of the beach should be quite gentle (usually 1:15 or smaller). Of course, a breaking wave can be generated on a steep slope if the incident wave height is large enough. Two wave tanks were used for breaking solitary wave studies: (i) a 31.73 m long wave tank located at the W. M. Keck Hydraulics Laboratory of the California Institute of Technology (denoted as Caltech West Tank, CWT), (ii) the 45.7 m long wave tank located at the Coastal Engineering Research Center, Waterways Experimental Station, USACE (denoted as CERC). For non-breaking solitary wave run-up on a steep slope, the length of the wave tank is not critical and a shorter wave tank (15.25 m long) located at the W. M. Keck Hydraulics Laboratory of Caltech was used (denoted as Caltech Student Tank, CST).

The Caltech West Tank (CWT) is 31.73 m long, 39.37 cm wide, and 60.96 cm deep consisting of 9 identical sections. It has been described by Hammack (1972), Goring (1979), and Synolakis (1986). A schematic drawing of the wave tank is shown in Figure 4.1 and a typical section is shown in Figure 4.2; the dimensions are in

English units. The wave tank was constructed with glass sidewalls throughout and a painted structural steel bottom. The glass wall of each section is 1.52 m long, 63.50 cm high and 1.27 cm thick. The bottom is leveled carefully with the deviation from the horizontal surface less than ±2.5 mm. The joints along the edges of the glass and the bottom were sealed with silicone caulking to eliminate leakage. Stainless steel rails 3.81 cm in diameter are mounted along the top edge of the wave tank and are leveled to within ±0.3 mm. Movable instrument carriages are designed for these rails. A steel scale is mounted along the top edge of the tank to provide an accurate measure of distance. An aluminum ramp was installed at one end of the flume joined to the constant depth region with the toe of the slope 17.30 m from the wave generator. The beach was 14.15 m long constructed of 5 panels of 0.64 cm thick anodized aluminum plate. A frame was constructed of aluminum angles (2.5 in x 2.5 in) to support the beach, with the material anodized before assembling. Each plate was fixed to the aluminum frame by countersunk screws, and the gap above the heads of the screws was filled with wax to guarantee the smoothness of the slope surface. The edges of the plates were machined with a groove on one plate and a matching protrusion on the other resulting in a "tongue and groove" joint. This provided a smooth surface across the joints and a rigid plane beach face to be mounted to the frame; where there was a small gap between plates, wax was used. The frame consisted of five modules, each 2.83 m long. Each module was supported on four leveling legs with screws whose length can be adjusted according to the beach slope. (The toe section only had two adjustable legs.) A detail of a leveling screw is shown in Figure 4.3. The aluminum frame was installed in the tank by first placing one frame module on the tank bottom without the beach plate. Then the slope of the frame module was adjusted to the desired angle by changing the four leveling screws at both ends. This process was repeated until all the frame modules were set in place and adjusted to the same slope. This method allowed each frame module to be leveled independently

without adjusting the adjacent module. The leveling screws were locked in place. The aluminum plates were attached to the frame and sealed in place with silicone. For the breaking solitary run-up experiments the beach was set at the slope of 1 vertical to 15 horizontal with a deviation from a plane surface of less than ± 1 mm. This slope was chosen so that a range of offshore wave heights could be used with the wave breaking either on run-up or run-down. (The ramp is also shown in Figure 4.2.) A photograph of the wave tank and beach is presented in Figure 4.4. To balance the hydrostatic pressure acting on the sloping plate, the wave tank section behind the plate was filled with water so that the still water level was the same as that in the test section.

The maximum run-up of breaking solitary waves for water depths $h_0 \geq 30.48$ cm were measured in the CERC wave tank. The CERC wave tank is 45.7 m long, 0.9 m wide and 0.9 m deep. A sketch is presented in Figure 4.5 showing the wave tank and the setup of the experiments. The beach used in the CERC tank was constructed of painted plywood and the slope was set at 1:15. Thus, the experimental data from this tank could be compared to that from Caltech West Tank (CWT). The plywood beach was sealed to the tank walls and the tank bottom with silicone.

Non-breaking solitary wave run-up experiments were conducted in the relatively short wave tank at Caltech (CST). The wave tank is 15.25 m long, 39.6 cm wide, and 61 cm deep and consists of 5 identical sections that are each the same as those in the CWT. The plane beach used was 2.83 m long and was composed of one beach module used in the CWT. A small wedge made of lucite was machined and installed at the toe of the slope to eliminate the gap between the wave tank bottom and the beach. The beach was installed with the toe of the slope 12.35 m from the wave generator and the slope of the beach was adjustable also; for these experiments it was set at 1:2.08 with a deviation from a plane surface of less than ± 1 mm. This slope was chosen so that a reasonably large offshore wave height could be used without

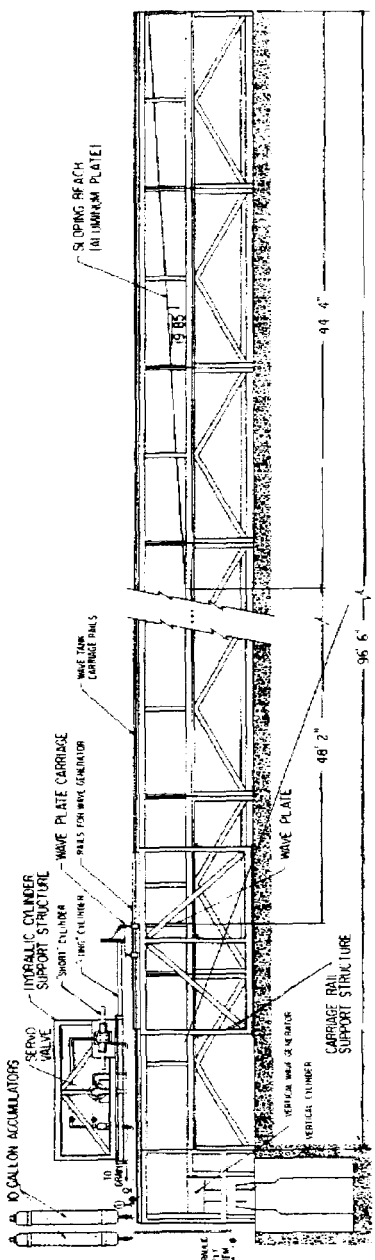

Figure 4.1: Schematic sketch of the Caltech west tank (CWT, after Synolakis (1986))

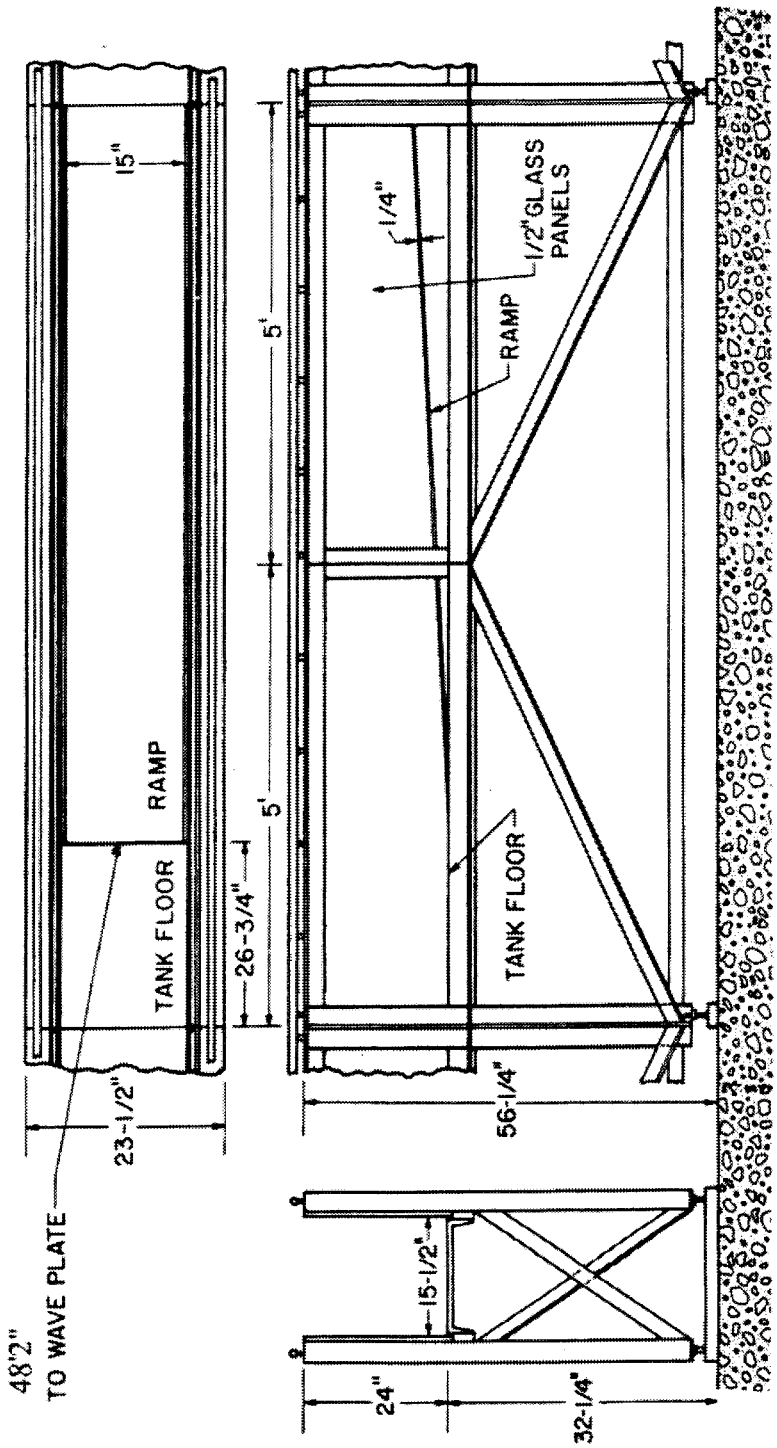

Figure 4.2: Schematic sketch of one section of the Caltech west tank (CWT, after Synolakis (1986))

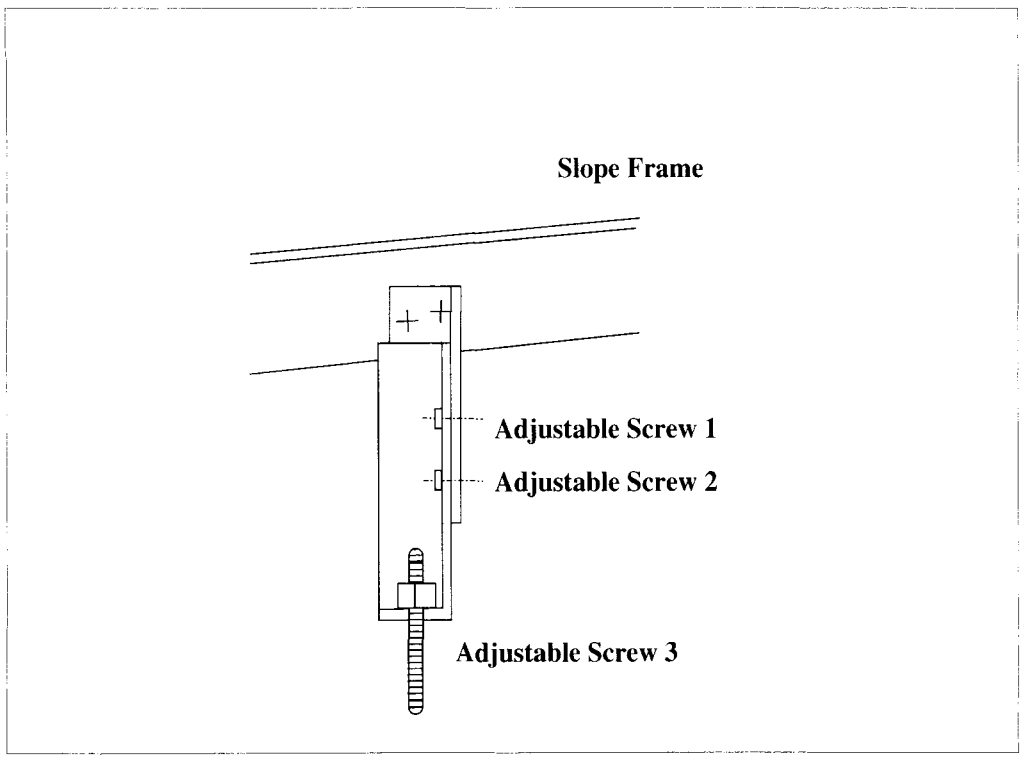

Figure 4.3: Schematic sketch of the adjustable legs used to support the beach frame of CWT

the wave breaking either on run-up or run-down. A photograph of the non-breaking solitary wave run-up experimental setup is shown in Figure 4.6.

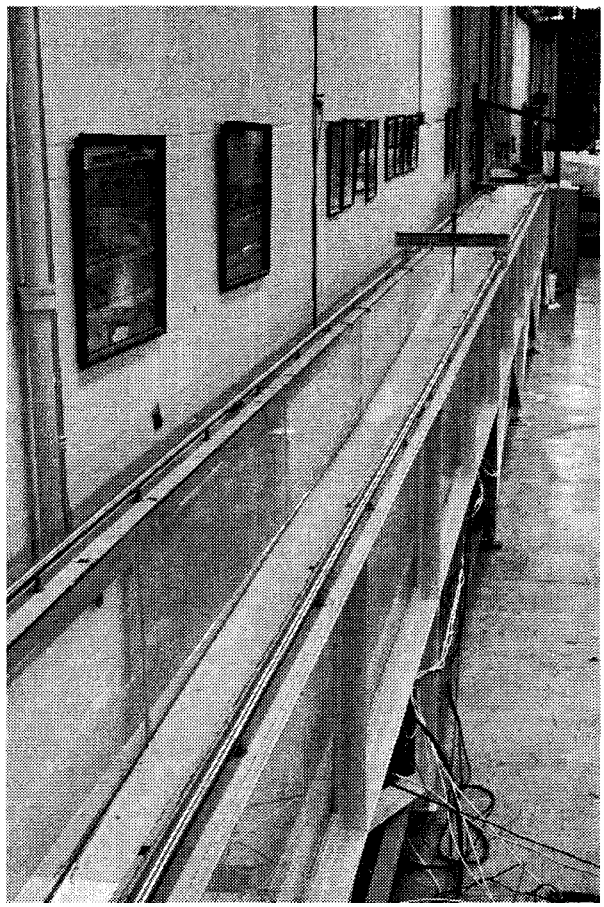

Figure 4.4: A photograph of the ramp and the Caltech west tank (CWT)

4.1.2 Wave Generation System

4.1.2.1 Hydraulic System

The wave generation systems used for the two Caltech wave tanks are similar and were described by Goring (1979), Synolakis (1986), and Ramsden (1993). It includes the hydraulic supply system, the servo-valve flow controller, the trajectory generation system, and the bulkhead wave generator. A systematic sketch of the generation system is shown in Figure 4.7 after Ramsden (1993). A photograph of the

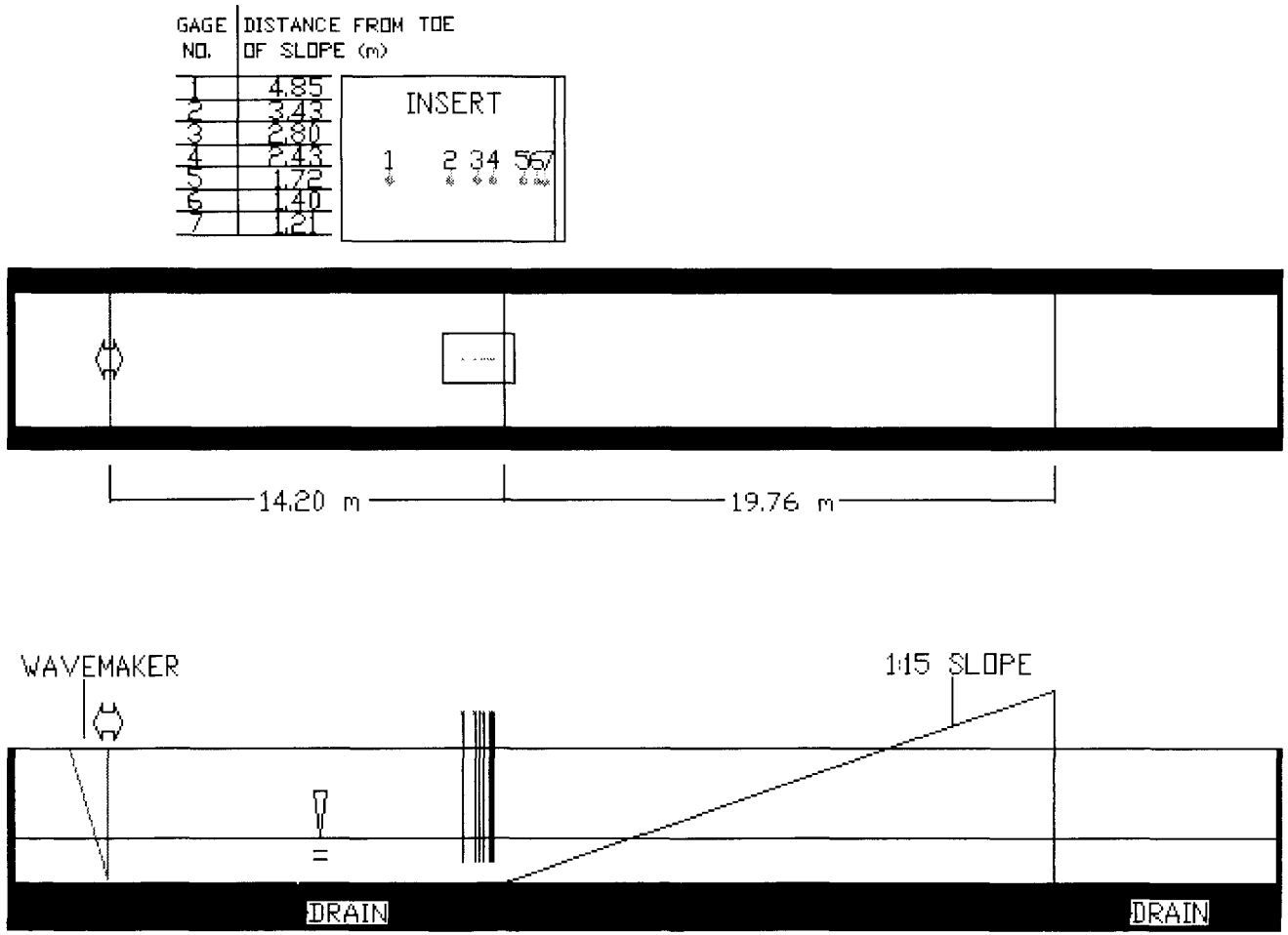

Figure 4.5: Schematic sketch of the CERC wave tank (CERC)

Figure 4.6: A photograph of the ramp and the Caltech student tank (CST)

wave generator is also shown in Figure 4.8. The wave generating carriage traveled on rails supported by a frame fixed to the floor isolated from the wave tank. Thus, any vibration caused by the wave generation would not affect the wave tank. The rails are Pacific-Bearings hardened steel rods of 3.175 cm diameter, model No. SA-20-120. Rubber windshield wiper blades are attached around the perimeter of the vertical bulkhead that composes the generator to act as a seal to the wave tank sidewalls and bottom while the plate is moving.

The hydraulic power supply system used to drive the wave generator consists of a Denison constant flow pump rated at 0.011 m^3/min (2.9 GPM), which supplies the hydraulic system with oil at an operating pressure of 20.68 MPa (3000 psi) from an oil reservoir with 0.152 m^3 (40 Gal) capacity. It is powered by a 5.6 kW, 1800 rpm motor. The temperature of the oil is controlled by a water-cool heat exchanger set at

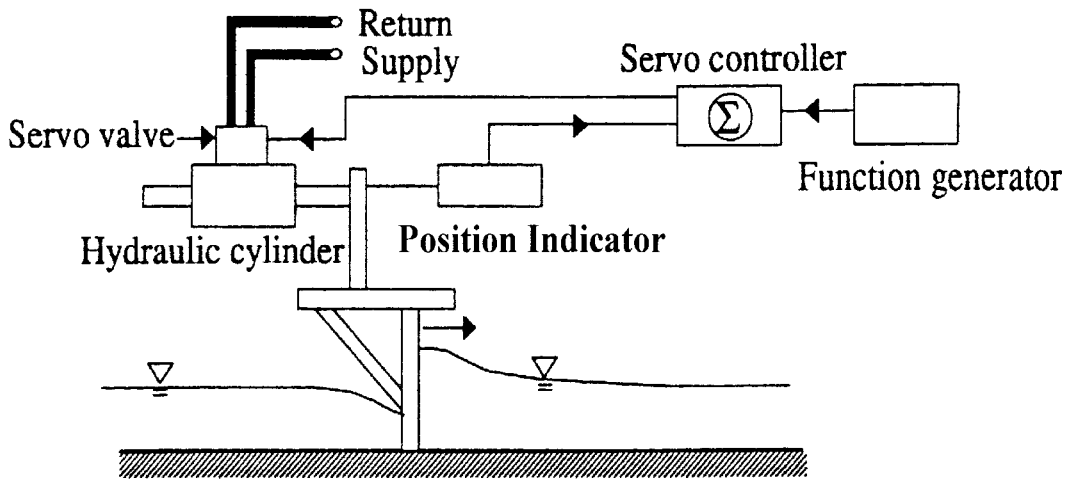

Figure 4.7: Schematic sketch of wave generation system (after Ramsden (1993))

23.9°C. An unloading valve located downstream of the oil pump directs the oil flow to the servo-valve when the downstream pressure is below the operating pressure. Thus, a constant pressure supply of oil is always available for the hydraulic cylinder shown in Figure 4.8. Two oil accumulators are installed and can be seen in Figure 4.8. These accumulators supply hydraulic fluid when the available flow rate in the hydraulic power supply is exceeded for the desired plate trajectory.

Two hydraulic cylinders were used in the generation system for the CWT. One cylinder is a Miller DH77B cylinder with a 6.35 cm bore and a 3.49 cm rod, and allows strokes up to 2.44 m. This cylinder is generally used when generating solitary waves. The other cylinder is a Miller DER-77 model with a 12.7 cm bore and 4.45 cm rod, and permits a stroke of 40.6 cm. This is especially useful for generating long period progressive waves. Either cylinder can be connected to the wave carriage. A servo-valve (Moog, model 72-103) controls the flow of the hydraulic fluid to the hydraulic cylinder depending on the current provided to it by the servo-controller (

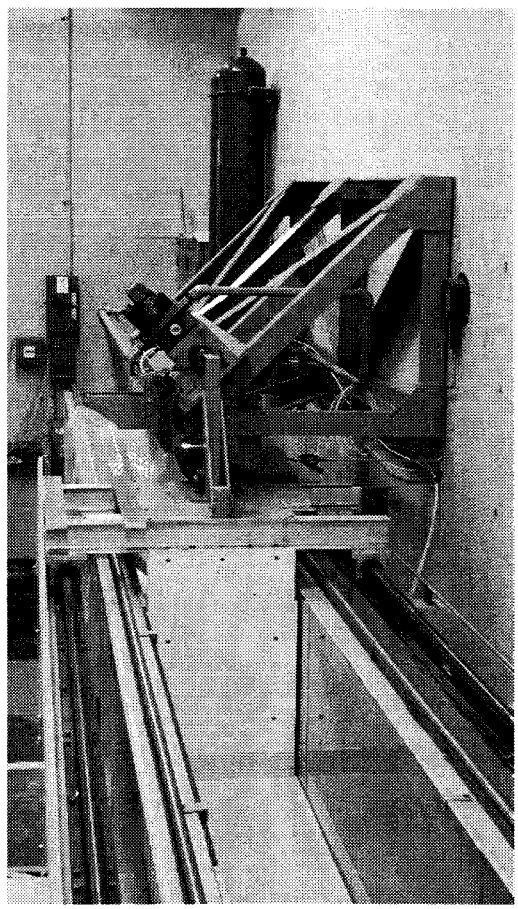

Figure 4.8: A photograph of the wave generator (CWT)

Moog, model 82-151); it is rated at 0.227 m^3/min (60 GPM) at 40 mA current.

The servo-valve is actuated by the servo-controller, which compares the current position of the wave paddle to the desired position prescribed by the wave generation trajectory. In the ideal situation without friction and the response of the mechanical system, the wave paddle velocity is proportional to the oil flow rate through the valve, which is itself proportional to the voltage signal from the trajectory generator. Thus, ideally only a voltage proportional to the desired piston trajectory is required for the wave generation. However in the actual situation, mechanical response and

the friction between the wave paddle and tank often distorts the paddle movement compared to the desired trajectory, i.e., the wave generated by the paddle will not be the shape desired. To correct this, feedback must be provided in the generation system, and the servo-controller does this. If the paddle position is the same as that desired, the output from the servo-controller is zero. Otherwise, a signal proportional to the position difference will be sent to the servo-valve to control the oil flow rate, and the paddle velocity is changed accordingly. This process continues until the desired position is achieved. The controller was modified by the addition of a resistor to allow fine tuning of the system damping and of a Dither oscillator to provide a 600Hz excitation to the valve. This continuous excitation reduces the force required to overcome static friction and enables smoother movements from an at-rest position. The amplitude and the frequency of this excitation does not produce any detectable free surface motions.

Two different transducers were used to measure the paddle position and to provide a feedback voltage to control the plate motion. When the long cylinder was used to drive the wave paddle, a ten-turn potentiometer riding on a precision rack was used in a rack and pinion arrangement. When the short cylinder is used, a Linear Variable Difference Transformer (LVDT) was used. Details of both transducers can be found in Goring (1979).

Wave generation systems of the CERC wave tank and the CST are similar, except the cylinder used in the CST is a smaller diameter compared to the CWT, with a 3.76 cm bore, a 2.57 cm rod, and allowing strokes up to 50 cm.

4.1.2.2 Trajectory Generation

The desired trajectory of the wave generator was supplied to the servo-controller as a time series of discrete voltage levels. The trajectories were generated with a personal computer using the method described by Goring (1979). The signal then was transferred from the computer to the servo-controller by means of a D/A converter with buffer storage (manufactured by Shapiro Scientific Instruments (SSI), Corona del Mar, CA). An amplifier that was also designed by SSI was used to adjust the gain of the generated signal so that a large range of the motions could be realized. The initial position of the wave paddle can be also adjusted by adding or subtracting an offset voltage from the signal sent to the servo-valve. The relation of the gain setting to the desired stroke of the wave paddle was determined and the resulting calibration curve was used in the experiments. A calibration curve for the CWT wave generation system is shown in Figure 4.9. A sample trajectory output from the personal computer for the generation of solitary wave is presented in Figure 4.10.

4.2 Water Surface Elevation Measurements

The water surface time-histories were measured using wave gages. Two types of wave gages were used in this study: (i) a resistance-type wave gage and (ii) a capacitance wave gage. The next discussion describes the principles and the operations of these gages.

4.2.1 Resistance Wave Gage

A typical schematic sketch of a resistance wave gage is shown in Figure 4.11. It consists of a pair of stainless steel wires of diameter 0.254 mm spaced 4.06 mm apart.

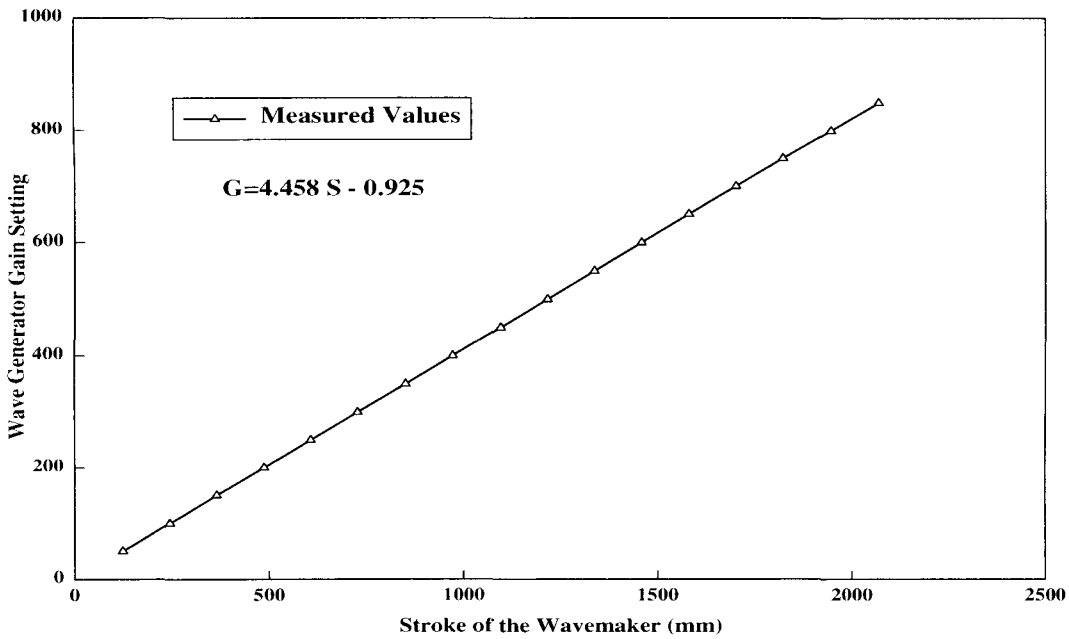

Figure 4.9: Calibration curve of the wave generator gain setting to stroke of the wavemaker

The wires are insulated from each other and are stretched taut between the open ends of a thin rod bent in a $\pi-$shape. When immersed in a conducting fluid, the gage acts as a variable resistor in the Wheatstone bridge circuit shown in Figure 4.11. The resistance between the wires varies with the depth of immersion in water. Initially the bridge circuit is balanced with the gage immersed at the still water level. As the water level changes, the voltage imbalance caused by the changed resistance of the gage is monitored and amplified by a preamplifier. The output from the preamplifier then was converted to digital signal and recorded by the data acquisition system.

The resistance wave gage used in the experiments was calibrated by changing its vertical position relative to the water using a Vernier scale accurate to 0.1 mm. A

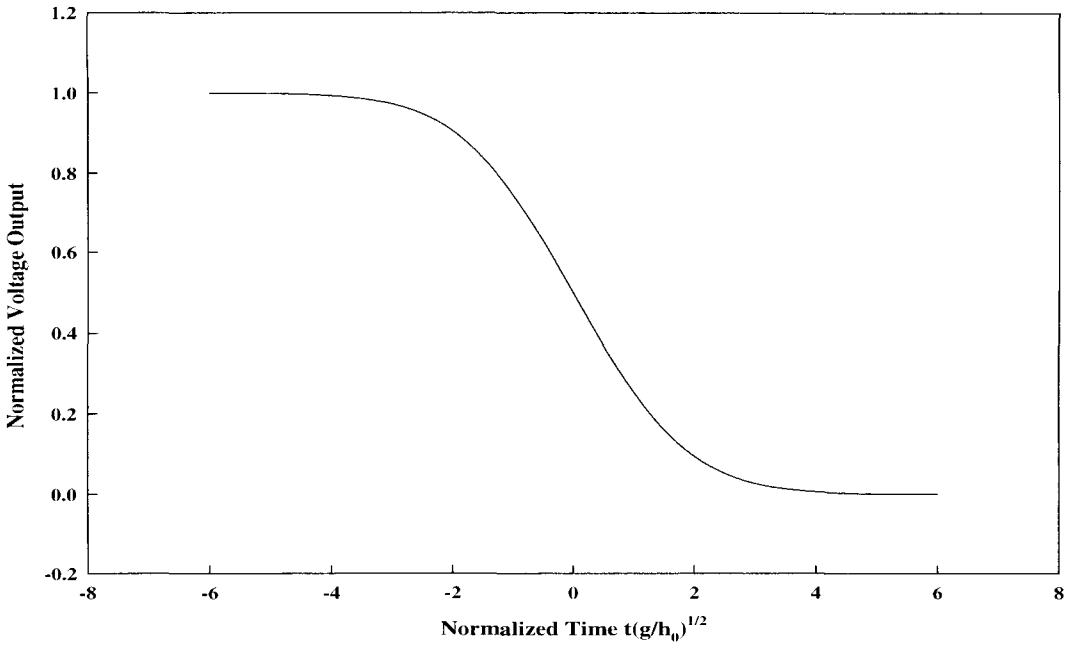

Figure 4.10: The wave generator trajectory signal for a solitary wave

typical calibration is shown in Figure 4.12. The range of the calibration covers the maximum wave height of the incident solitary wave and also half the depth of the water. The depth of the immersion of the wave gage was changed in increments of 0.5 cm while recording the voltage output of the electronics. A second-order polynomial was fitted to these data with the coefficients determined by a least squared regression method. The polynomial equation obtained was then used to determine the wave surface elevation relative to the initial water surface elevation in experiments. Figure 4.12 also shows the calibration one hour after the first calibration. The good agreement between the two calibration curves indicates that the gage and its electronics are stable for at least this period of time. The response of resistance wave gages has been studied over a wide range of frequencies and amplitudes in the past by Wiegel

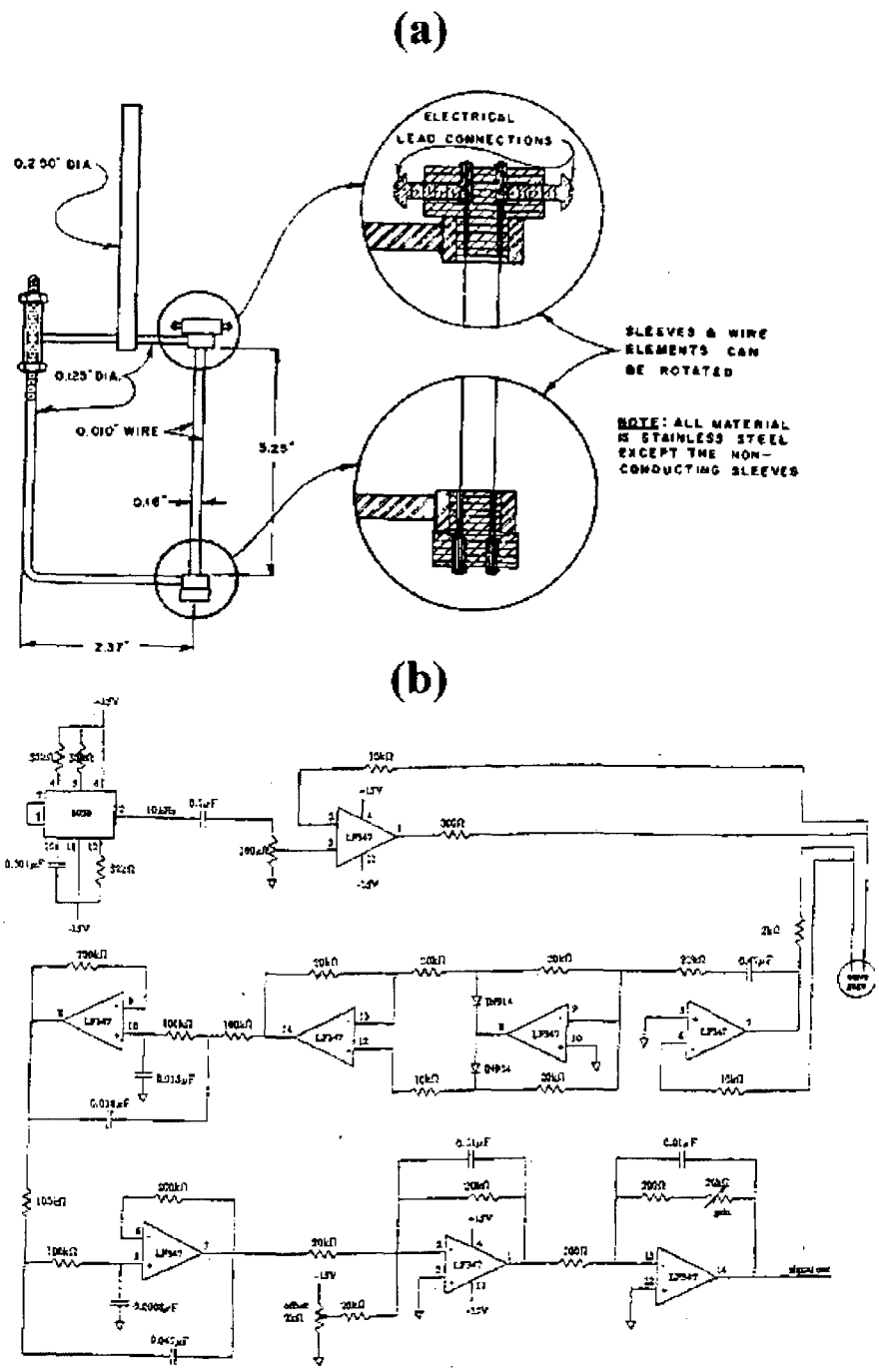

Figure 4.11: Schematic sketch of the resistance wave gage and its electronic circuit. (after Raichlen (1965) and Waniewski (1999))

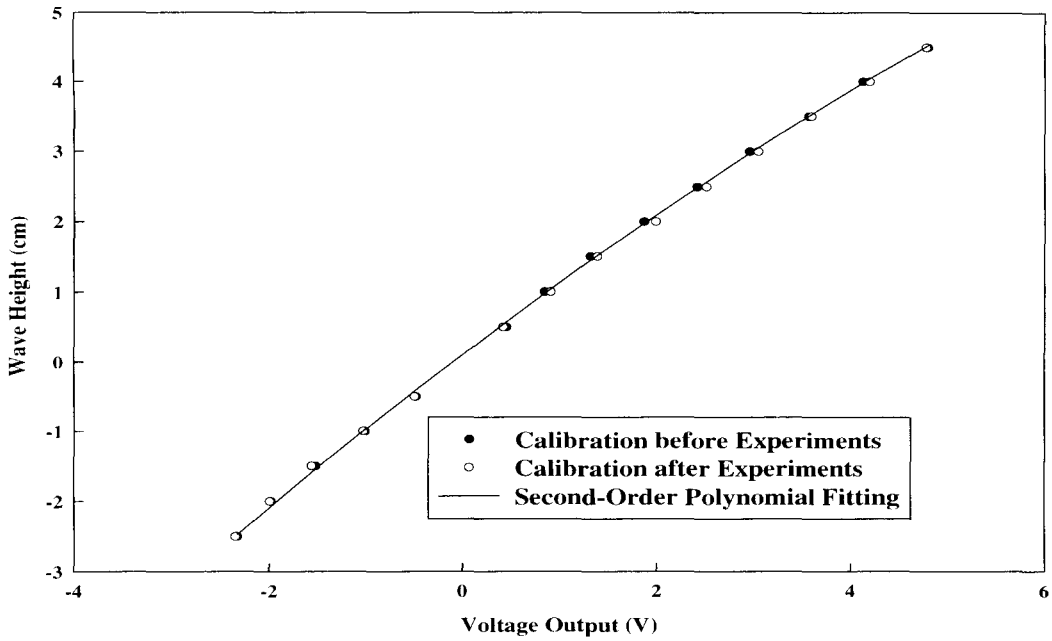

Figure 4.12: Calibration curve of the resistance wave gage

(1955) and Dean and Ursell (1959) and discussed by Ramsden (1993). It was found that the errors in amplitude were within 5% of the range for small-scale laboratory water waves. (In Figure 5.2 of Chapter 5 a comparison of the wave amplitude obtained from resistance wave gages and that from a high-speed video recording will be presented. This comparison showed that the resistance wave gage appears to have adequate dynamic response to resolve the time varying water surface of the solitary wave used in this investigation.) The error of varying the position of the wave gage and the error caused by the approach of the gage to the tank bottom is also discussed by Ramsden (1993). These errors were not found to be significant.

4.2.2 Capacitance Wave Gage

The resistance wave gage described above cannot be used to measure the wave amplitude for locations close to the initial shoreline and the locations above the shoreline on the slope. When the locations are close to the shoreline the local water depth decreases and the calibration is not possible. Also, the gages cannot be calibrated in deeper water and then moved back, since strong boundary effects exist when the gages are too close to the surface of the slope. For such locations, a capacitance wave gage consisting of a single wave probe was used in the experimental investigation combined with a special calibration procedure that will be discussed presently.

A photograph of the capacitance wave gage used is shown in Figure 4.13 and discussed by Synolakis (1987). It consists of a wave probe with the associated electronics directly connected to the gage. The probe was made of a steel rod of 0.76 mm diameter and was fit into a glass capillary tube with a 1.58 mm outside diameter. The electronic circuit of the gage can be found in Synolakis (1986). An external oscillator was used to drive a field effect transistor (FET), which provides current to the wave probe. The current passed through the probe and then was converted to a voltage signal by a current to voltage converter. During the calibration, the wave gage was moved along the slope by changing its position and height, but the distance between the tip of the probe and the surface of the slope was kept constant, thus, the recorded voltage output from the electronics was changed also according to the immersion of the probe in the water. This voltage signal was then fitted by essentially the same method used to calibrate the resistance wave gage. Since the distance of the probe to the surface of the slope was always maintained the same, the boundary effects were eliminated by the calibration. The calibration process was performed in a location with relatively deep water and then moved back to the actual measurement location. A typical calibration curve for the capacitance wave gage is presented in Figure 4.14.

Synolakis (1986) compared the measurement of wave amplitude on a dry bed taken by the capacitance wave gage to that of a high-speed movie camera operated at 63.25 frames per second. Good agreement was found during run-up, but there were small differences observed during run-down. Synolakis (1986) attributed the difference to the difficulty of identifying the free-surface location in the movie frames because the windows of the tank were wetted during the run-up. Differences were also found during the present study. However, there is an additional probability that may contribute to this error. When using a capacitance wave gage similar to the one in Figure 4.14 to measure the water amplitude on a dry bed, the flowing water runs up on the wave probe. This can cause the wave gage to report a higher amplitude than the actual value. This error may become important when the water velocity is large and the water level is small, as in the run-down process.

4.3 Run-Up Gage

A unique gage was developed in the present investigation to measure the time-history of the run-up of a solitary wave, unbroken or broken, on a plane sloping surface. A schematic sketch of the run-up gage is presented in Figure 4.15. The run-up gage consists primarily of a laser and a photodiode camera (LC300A, manufactured by EG&G Reticon). The camera is identical to an ordinary camera in terms of the optics with the exception that the photographic film is replaced by a photodiode array capable of discriminating 1024 parts in an array length of 26.01 mm. Measurements are obtained from the camera by determining the position of a light spot on the array, which then defines the voltage output of the photodiode array and associated electronics. A small adjustable mirror was located at the top of the sloping beach with the light emitted from the laser directed at this mirror. The reflected beam was

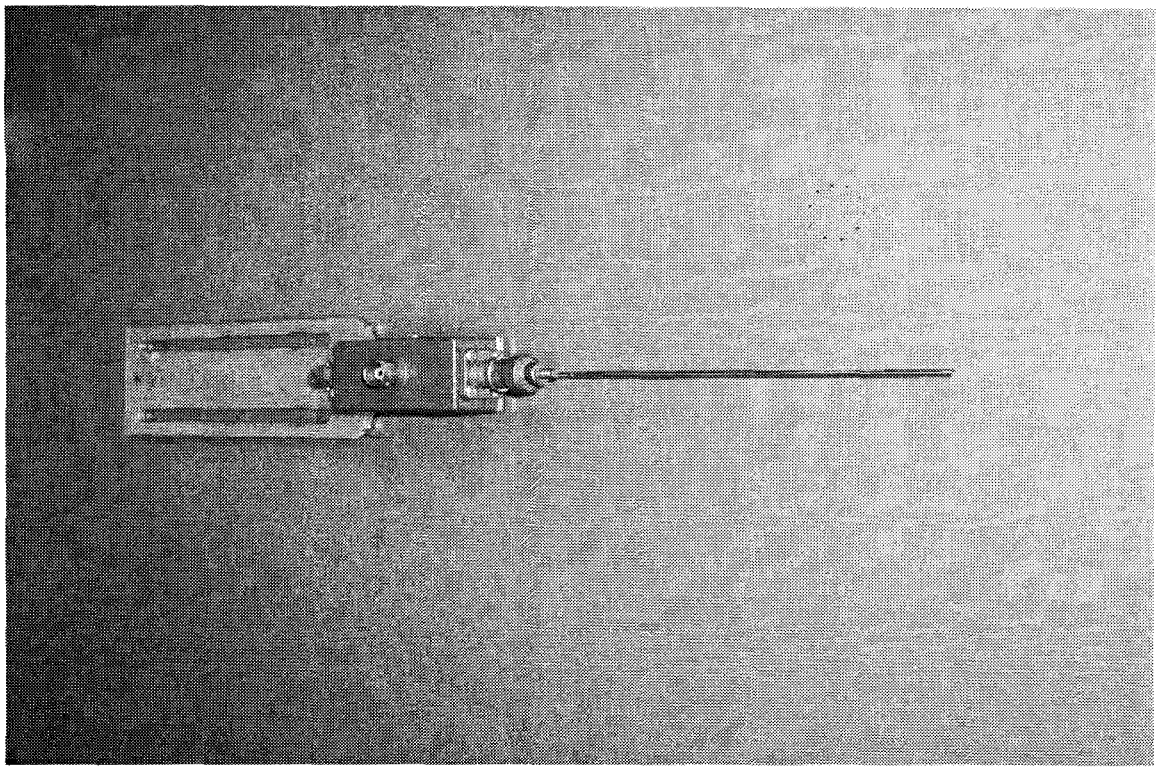

Figure 4.13: A photograph of the capacitance wave gage

adjusted such that it was directed down the slope, parallel to it, and somewhat less than 0.5 mm above the surface. As the tip of the run-up tongue progressed up the slope, the laser was reflected from its tip and focused on the photodiode array of the Reticon camera. Based on the length of the slope imaged by the camera (about 60 cm), the precision of the position of the tip of the run-up tongue was about ± 0.6 mm.

The electrical output signal from the camera was a composite video signal, which included a timing pulse and an analog signal that represented the gray scales of the line measured along the slope. Because the intensity of the laser spot on the slope was much larger than the ambient light, a pulse-like signal, which showed the location of the laser spot, can be found in the analog signal from the camera, as illustrated in Figure 4.16. After passing through a comparator circuit and signal conditioning

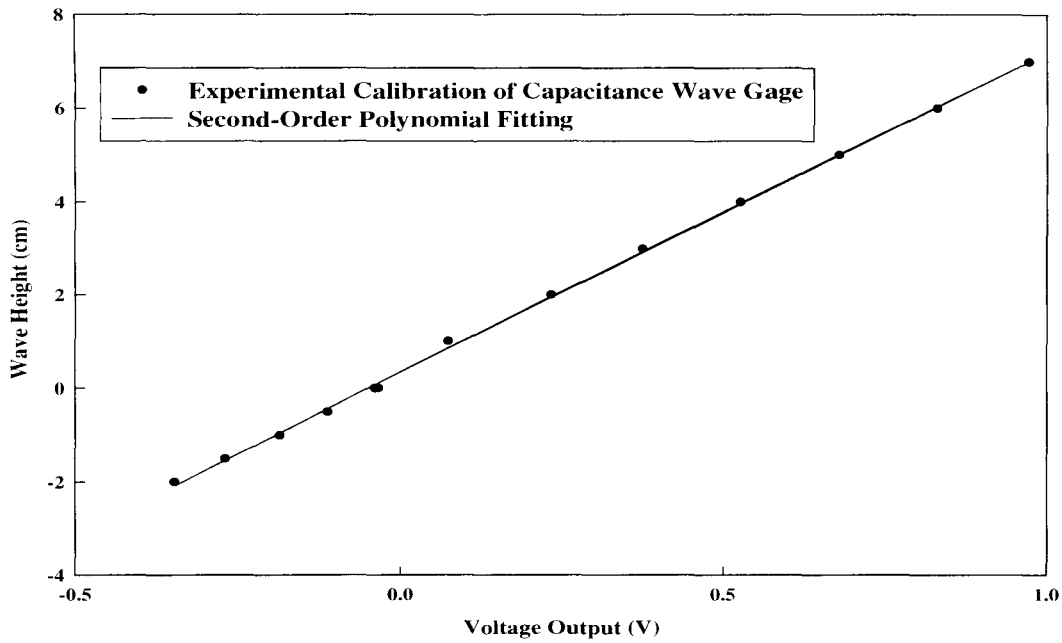

Figure 4.14: Calibration curve of the capacitance wave gage

circuit, the analog signal was converted into a pulse train, where the duty cycle (defined as the ratio of the time the pulse equals unity to the period of the signal) was set by the laser spot. This pulse train was then integrated to give an analog voltage output whose amplitude is directly proportional to the time-wise length of the duty cycle. The analog output was digitized to determine the run-up. The run-up gage was calibrated by reflecting the laser into the camera at known positions along the slope. A typical calibration curve is presented in Figure 4.17. There are some limitations to the use of this instrument during the run-down process, since once the beach is wet it is difficult to define the leading edge of the run-down by optical reflection. The comparison of the run-up tongue measurement by this particular run-up gage and high-speed video is presented and discussed in Chapter 5. It has been

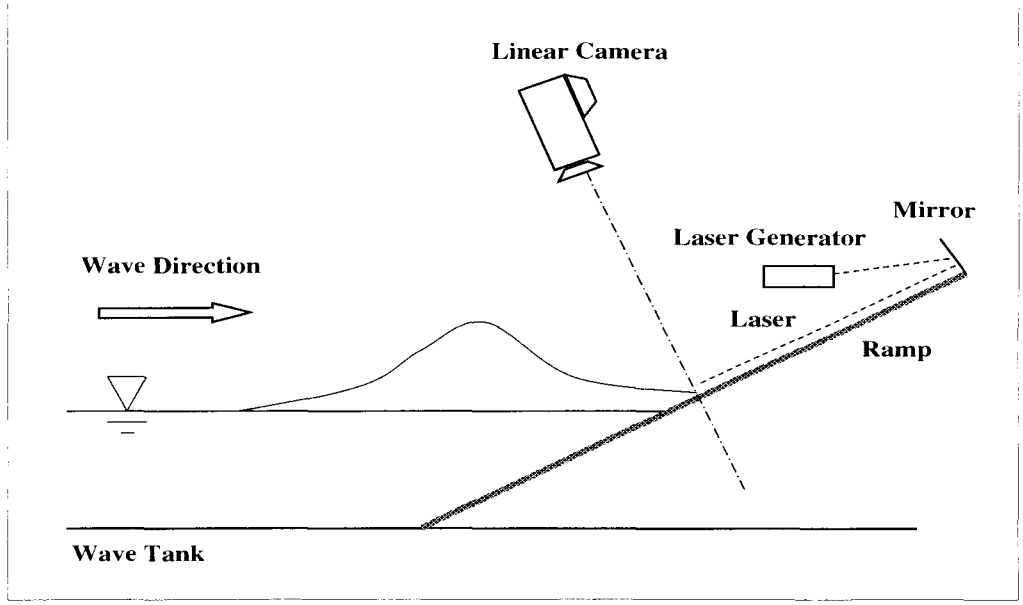

Figure 4.15: Sketch of the run-up gage

found that this laser run-up gage appears to have promise for certain types of wave measurements.

4.4 Water Particle Velocity Measurement

The water particle velocity was measured using a Laser Doppler Velocimeter (LDV) manufactured by TSI (signal processor model IFA 550 with model 9201 Colorburst multicolor beam separator). The frequency range of the signal processor was 1 kHz to 15 MHz, with a time resolution of the measurement 2 ns. A frequency shift of 200 kHz between the reference beam and the scattered beam was set for the system with a filter with the range between 100 kHz and 300 kHz. These settings

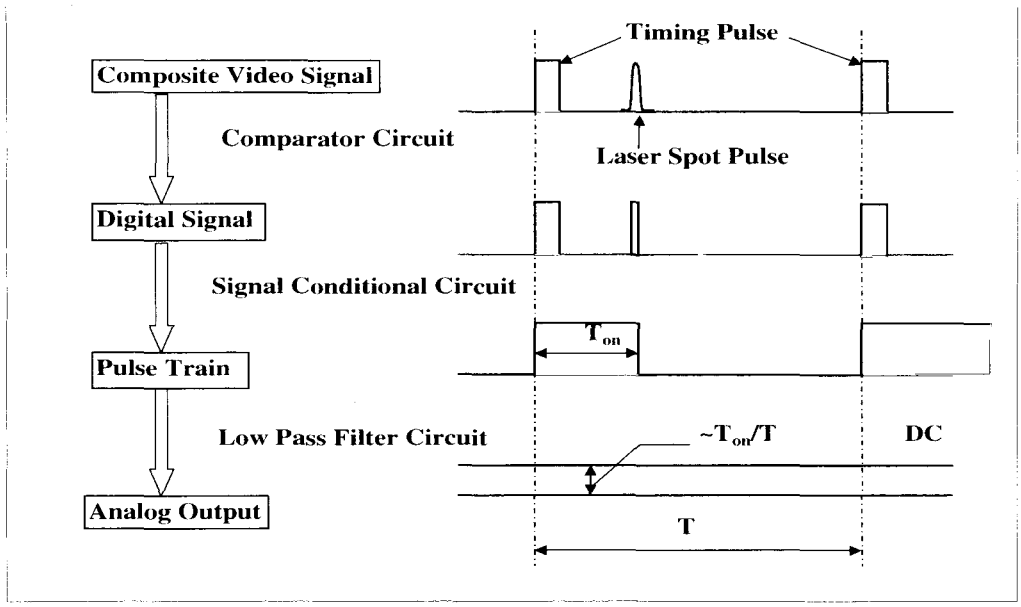

Figure 4.16: Sketch of the working principle of the run-up gage circuit

were sufficient to measure the particle velocities of the solitary waves before and close to breaking. Once the wave broke, air bubbles entrained in the breaking region obscured the laser beam and velocity data could not be obtained. Two channels of signal processors were available; thus, two velocity components, i.e., the horizontal velocity and the vertical velocity can be measured. The data acquisition mode of the LDV system was set to random, which meant that the horizontal velocity signal and vertical velocity signal could be independently acquired during the experiments. The signals from the processors were transmitted to a microcomputer in the form of 16-bit parallel digital data. The microcomputer, which is IBM-AT compatible, is equipped with "flow information display (FIND)" software by TSI. Both statistical and time-history velocity data can be obtained directly using this software. A schematic sketch

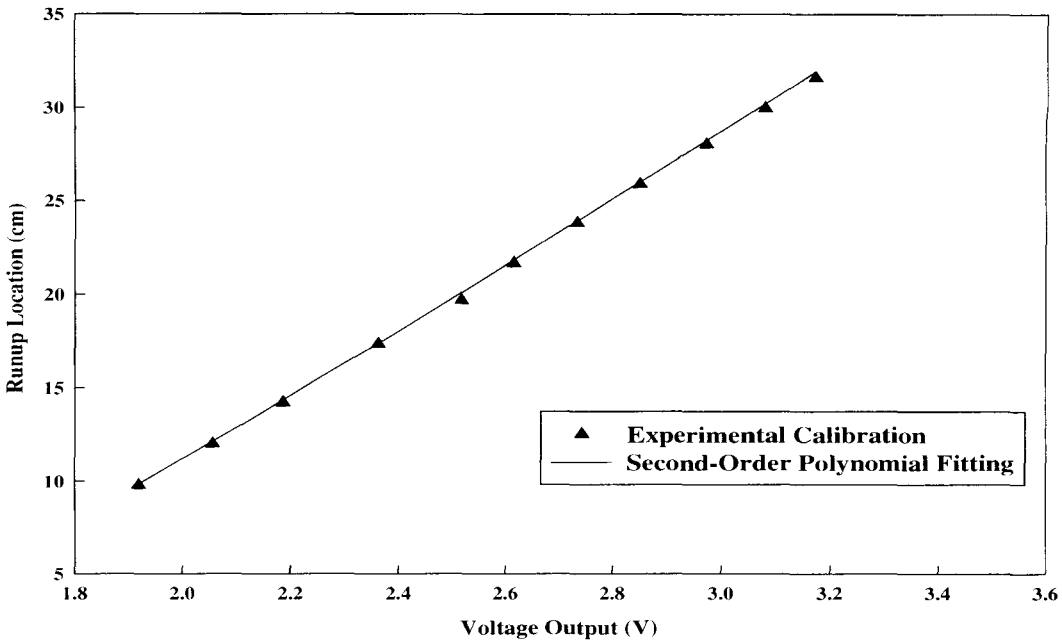

Figure 4.17: Calibration curve of the run-up gage

of the LDV system is shown in Figure 4.18 from the TSI LDV system manual.

The transmitting probe, which both transmits the laser beam and receives the backscattered signal, was supported on a special platform mounted atop a tripod. The platform could be moved in two horizontal directions by means of twin screws and raised and lowered using an adjustment on the tripod. The horizontal coordinates of the laser beam could be determined accurately within 0.1 mm by a scale attached to the platform. The vertical position of the laser beam was determined by a point gage on the wave tank. The laser probe could be rotated to align the beams with the slope to measure the wave particle velocity parallel to the slope.

Water particle velocities were obtained at several locations ranging from the toe of the slope to locations near the initial shoreline. The scatter beams from the LDV

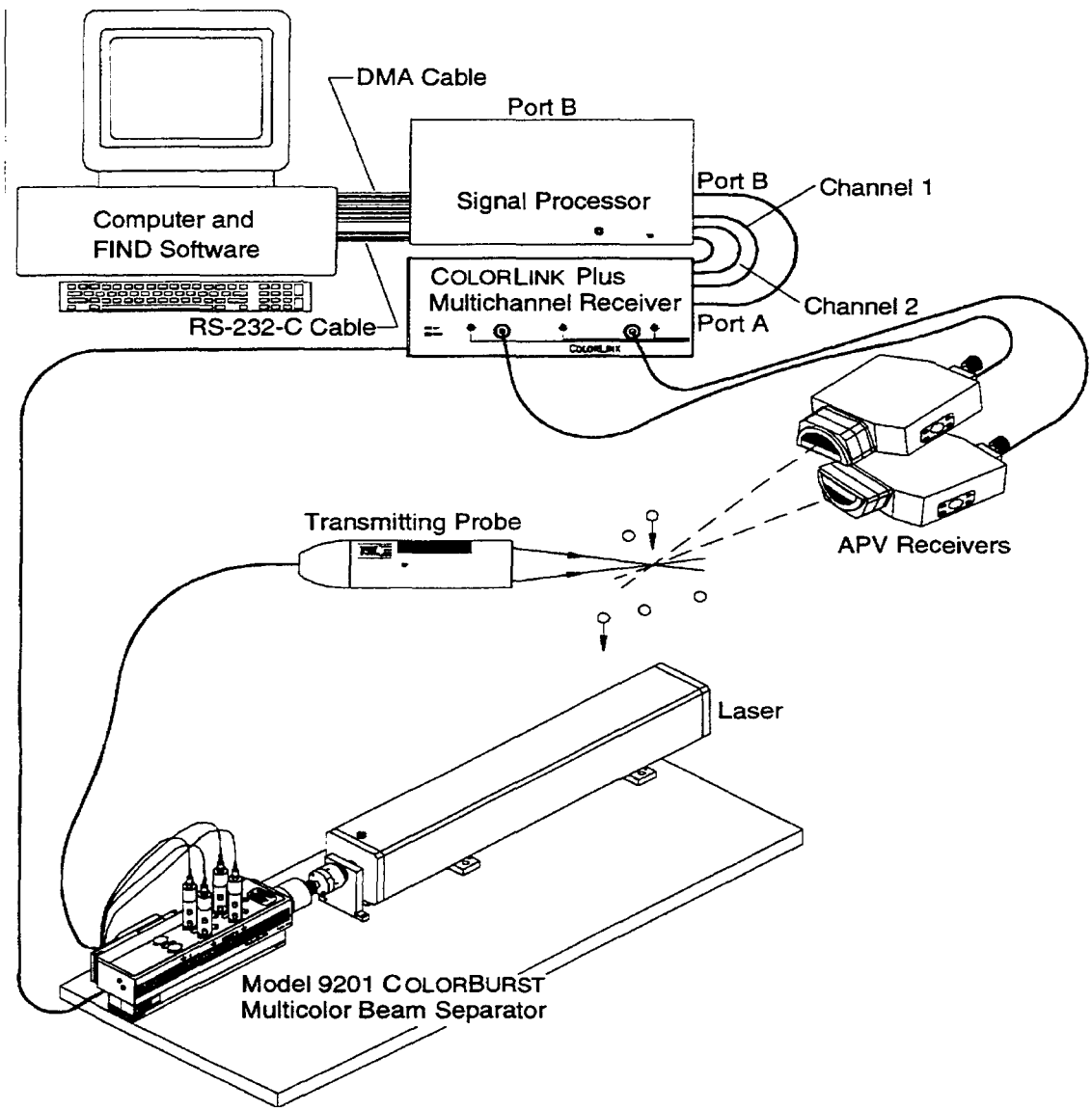

Figure 4.18: Schematic sketch of the LDV system

system were focused at a position 20 cm from the glass wall of the wave tank (roughly along the centerline of the wave tank) to prevent sidewall effects. A wave gage (capacitance wave gage or resistance wave gage, depending on the local water depth of the measurement point) was placed in the wave tank above the laser beams to simultaneously measure the elevation of the water surface. If the local water depth was not deep enough to permit both the wave gage and the laser beams being at the same position, the laser beams were positioned a very short distance behind the wave gage. The distance was usually less than 3 mm so that, considering the horizontal length scales of the waves, the measurement could be regarded as having been performed at a single location.

4.5 High-Speed Video Equipment

The wave breaking process, run-up, and splash-up were recorded using two high-speed video cameras. Both are model HR-500 Motionscope high-speed video cameras manufactured by Redlake Camera Corporation. The camera can record and store a sequence of video images of an event at frame rates of 60 to 500 frames per second, with a maximum shutter speed of 1/10,000 per second. The resolution of the recording is 480 x 420 pixels for a recording speed of 250 frames per second and 240 x 210 pixels for a recording speed of 500 frames per second. The camera consists of a CCD camera head, a display monitor, and a control panel. A photograph of the camera and display monitor are shown in Figure 4.19. A memory buffer is integrated into the camera system to store the images captured by the CCD camera. The number of frames that can be stored in the buffer is determined by the recording speed. For example, for 500 frames per second speed, 2,048 frames (4.1 seconds of data) can be stored, while at 250 frames per second, since the recording resolution is higher, only 512 frames

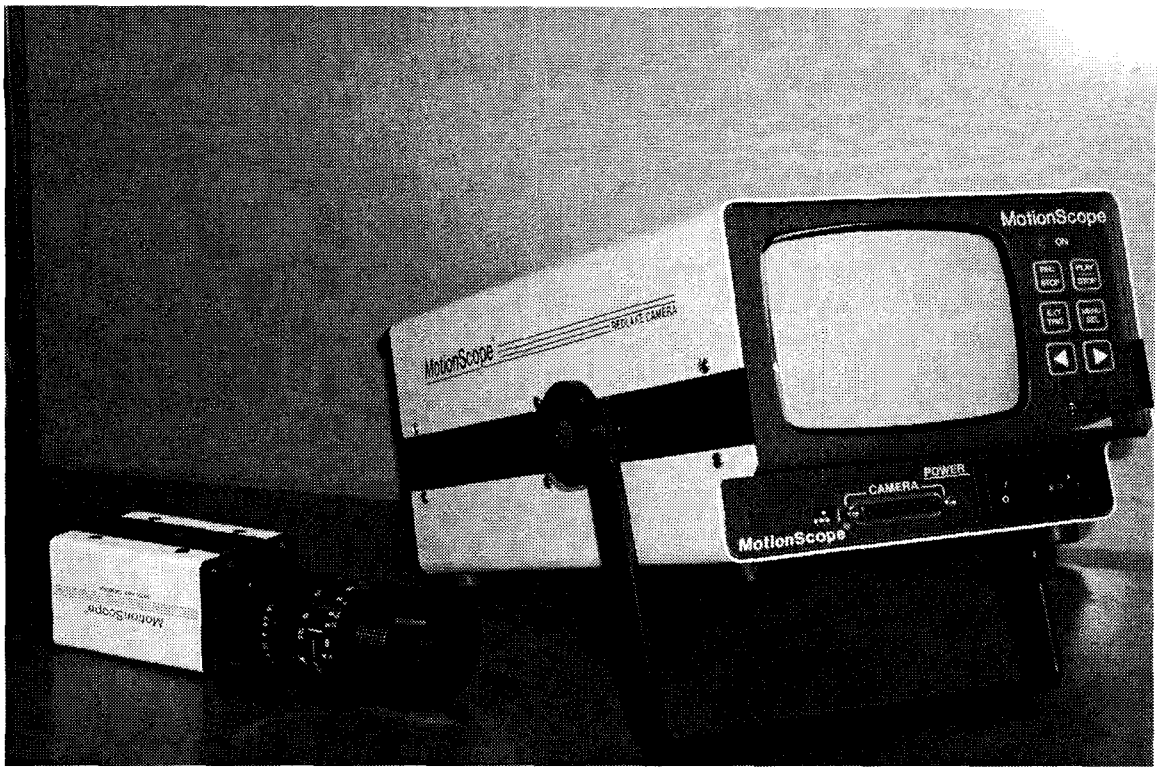

Figure 4.19: A photograph of the high-speed video camera and display monitor

(2.0 seconds of data) can be stored. A standard RS-170 NTSC and PAL video out (Video and S-Video) port are available so that the images can be recorded on video tape to be analyzed later. A typical image obtained with the high-speed video camera is shown in Figure 4.20. The frame number and the time of the frame in milliseconds are also displayed with the image. Other information related to the recording, such as the recording speed, the trigger mode of the camera, and the shutter speed are displayed and can be seen in Figure 4.20.

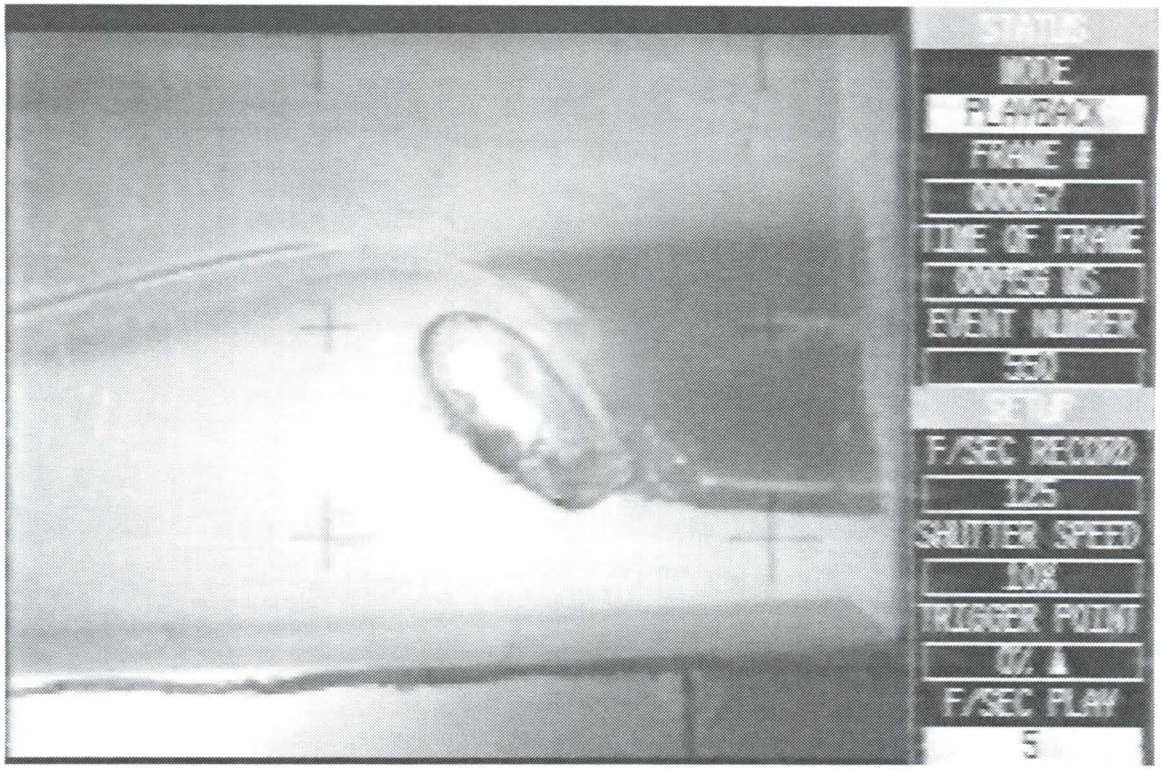

Figure 4.20: A typical image from the high-speed video recording

4.5.1 Sideview Recording

The wave propagation and breaking process were recorded with the high-speed camera positioned perpendicular to the glass walls of the wave tank. A sketch of the arrangement of the equipment is presented in Figure 4.21. A special carriage to support the camera and lights that can be moved on the tank rails was constructed. The carriage consisted of a steel frame resting on a movable carriage with a triangle-shaped leg, which was about 2 m long, oriented perpendicular to the tank centerline and extending from the side of the wave tank. The extended leg was detachable and was bolted to the steel frame. At the end of the leg two vertical steel bars and a horizontal steel bar were clamped. The camera head and the lights used for the

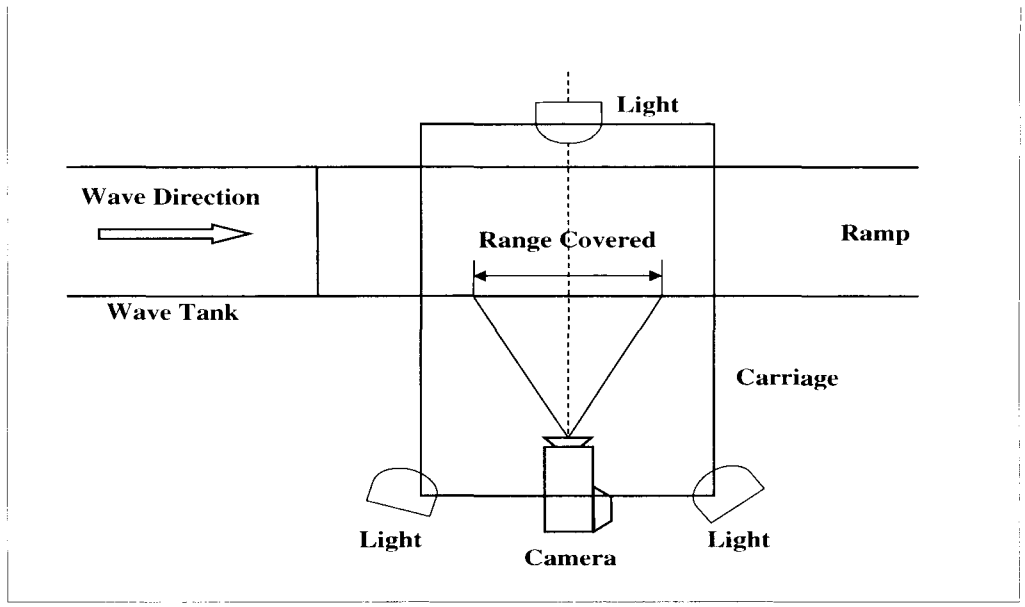

Figure 4.21: Sketch of the experimental arrangement for sideview recording

recording were attached to these bars. A vertical bar was connected to the carriage on the far side of the wave tank to carry lights (see Figure 4.21). The camera was located approximately 1.5 m from the wave tank sidewall, resulting in a record area about 50 cm x 60 cm. During the experiments, the carriage was normally moved at the speed of the incident waves. This maximized the area and the time that could be covered during one experiment.

The recording area was illuminated with three 500 Watt Lowel ViP lights; two lights were placed near the high-speed camera, one on each side of the camera. The other light was placed on the opposite side of the wave tank. A translucent panel was placed on the far side of the wave tank to provide a uniformly illuminated background and to prevent direct light on the camera.

Fiducial marks on the glass sidewall of the water tank were used to assist in defining the video images. Each mark was made of black tape and stuck to the outside glass wall of the wave tank. For the non-breaking solitary wave run-up study, a grid with lines spaced 5 cm apart was attached to the glasswall for the full test section. Since the region of wave breaking is relatively large, only cross-shaped marks 20 cm apart were attached to the glass. Both the grid and the simple marks were used to define the wave and to correct any image distortion due to the position of the camera relative to the tank (see section 4.5.3).

4.5.2 Overhead Recording

The wave run-up on the sloping beach and the splash-up on the vertical wall were also recorded using a stationary high-speed video camera. The camera was mounted on a swivel bracket attached to the inner frame of the carriage discussed in earlier section. A sketch of the camera arrangement is shown in Figure 4.22. Using the swivel bracket the position and angle of the camera were adjusted such that a viewing area of 60 cm x 60 cm centered on the centerline of the wave tank could be recorded. A 500 Watt Lowel ViP light was also mounted on the carriage to provide illumination. The angle of the light was adjusted to minimize reflections. A photograph of the high-speed camera in the overhead position is shown in Figure 4.23. A scale was attached to the vertical wall or the slope to provide reference for measurements. The space between lines on the scale was 5 cm for the run-up study and 2 cm for the vertical wall splash-up experiments. This arrangement provided sufficient spatial precision for the experiments.

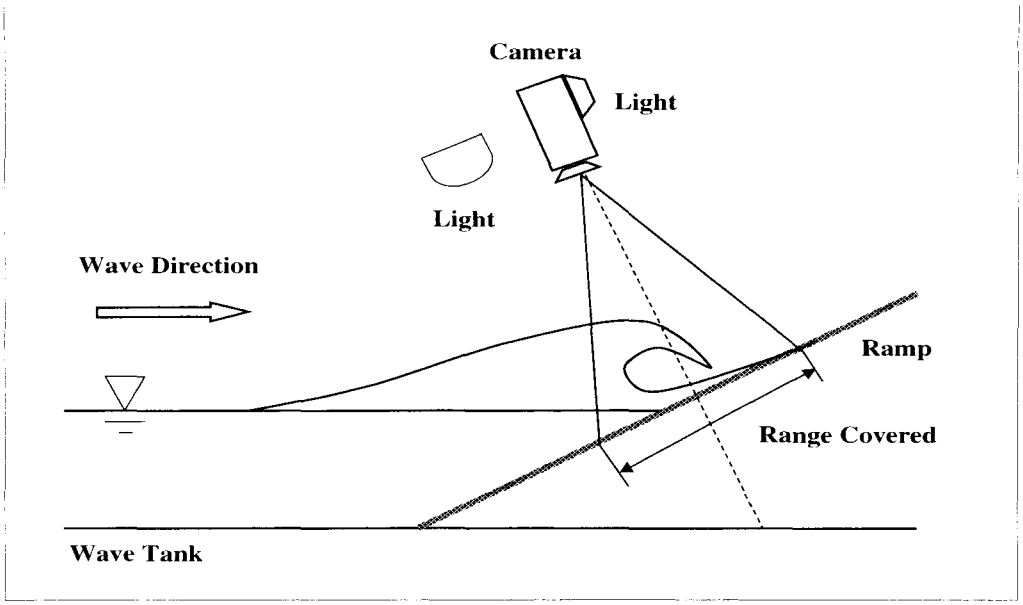

Figure 4.22: Sketch of the experimental arrangement for overhead recording

4.5.3 Image Processing

The images recorded on videotape were digitized using a PCI image board installed on an IBM-AT compatible personal computer. The image board (model PIXCI-SV4) was manufactured by EPIX Corporation, and it can capture/convert images at a speed of 30 frames per second. The color information in the video image was digitized into gray level intensities ranging from 0 to 255 (8 bits) for each pixel. The maximum resolution of each image is 754 x 480 pixels for NTSC format video and 922 x 580 for PAL format video signal. Software developed by EPIX performed the image capturing and analysis.

It was found that the images obtained using the high-speed video were often

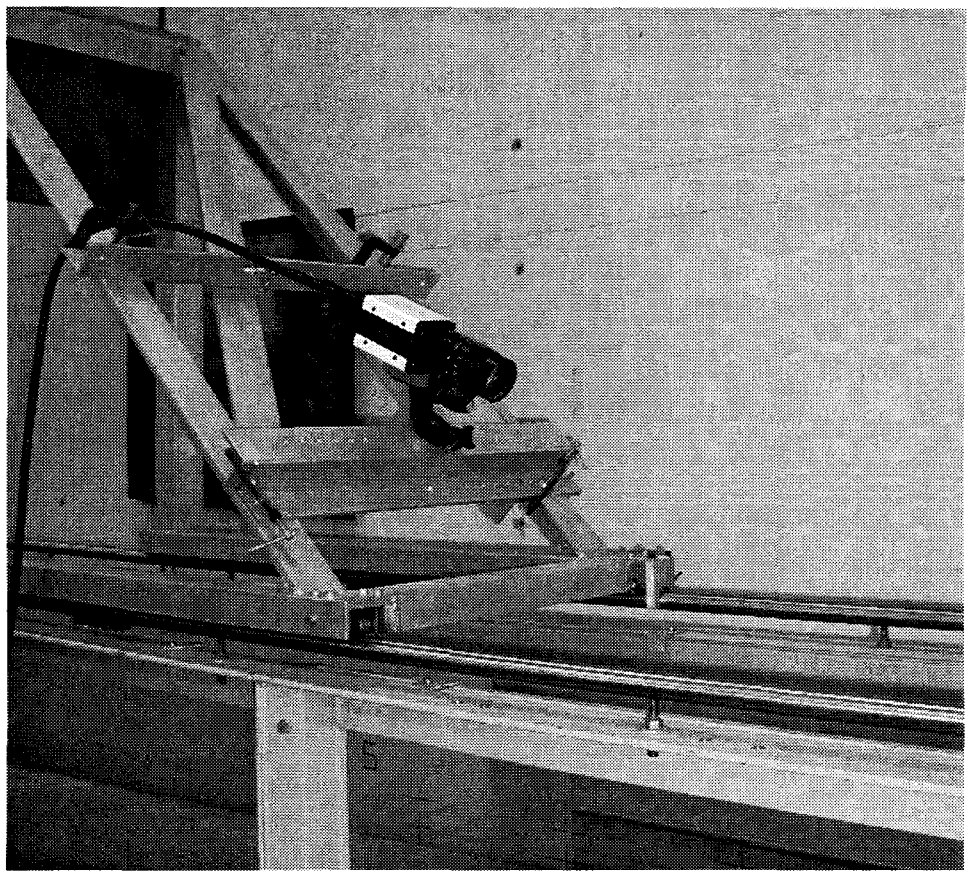

Figure 4.23: A photograph of the high-speed video camera in the overhead position and the carriage used

distorted due to the combination of the viewpoint of the camera and its optics. The distortion is quite pronounced if the axis of the camera is not perpendicular to the wave tank sidewalls or if the observation area is too large. To accurately determine the wave shape and locations of the run-up/splash-up, this distortion has to be eliminated either by carefully positioning the camera or by image processing. Due to the difficulty of accurately positioning the camera and of the requirement to maximize the area covered, image processing was used to minimize distortion.

Considering correcting the optical distortion, a recorded frame can be viewed as

a linear transformation from the physical coordinate system on the glass walls of the wave tank to the new coordinate system on the image, i.e., the recording plane of the camera. The distortion that comes from both perspective and the optical elements of the camera can be corrected using standard 2-D projective geometry theory. Thus, if the homogeneous coordinates were used to represent a point, the transformation can be expressed as :

$$\begin{pmatrix} x \\ y \\ w \end{pmatrix} = M \begin{pmatrix} s \\ t \\ 1 \end{pmatrix} \tag{4.1}$$

where M is the linear mapping function, $(x, y, w)^T$ represents a point in physical coordinates, and $(s, t, 1)^T$ represents the corresponding point in image coordinates. The quantity w is a normalization scale, where $w = 0$ refers to a point at infinity; the value of (x, y) shows direction. In another word, $(x/w, y/w)$ is the location of the point in x-y coordinates.

The transformation function M can be obtained by considering the mapping of a rectangle from the physical coordinates to the image coordinate as shown in Figure 4.24. The infinity point in horizontal direction $((1, 0, 0)^T$ in homogeneous representation of the physical coordinate) was mapped into point $\vec{h_s}$, the point of infinity in vertical direction $((0, 1, 0)^T)$ was mapped into point $\vec{h_t}$ and the center of the rectangle $((0, 0, 1)^T)$ was mapped to point $\vec{h_c}$. These three points were sufficient to determine the transformation M:

$$(\vec{h_s}, \vec{h_t}, \vec{h_c}) = M^{-1} \begin{pmatrix} 1 & 0 & 0 \\ 0 & 1 & 0 \\ 0 & 0 & 1 \end{pmatrix} \tag{4.2}$$

where $\vec{h_s}$, $\vec{h_c}$, $\vec{h_t}$ were obtained from the coordinates of the four corner points of the

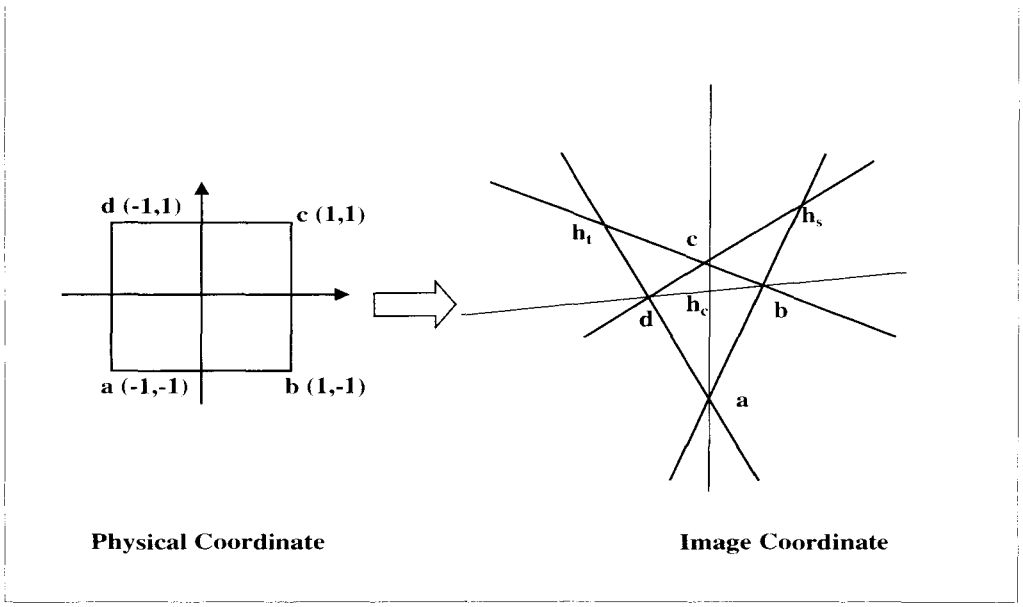

Figure 4.24: The illustration of the mapping transformation used in the image processing

rectangle in the image as:

$$\vec{h_s} = (\vec{a} \times \vec{b}) \times (\vec{d} \times \vec{c}) \tag{4.3}$$

$$\vec{h_t} = (\vec{b} \times \vec{c}) \times (\vec{a} \times \vec{d}) \tag{4.4}$$

$$\vec{h_c} = (\vec{a} \times \vec{c}) \times (\vec{d} \times \vec{b}) \tag{4.5}$$

where $\vec{a}$, $\vec{b}$, $\vec{c}$, $\vec{d}$ are the vector representation of the homogeneous coordinates for the four corner points of the rectangle, as shown in Figure 4.24.

Thus, once the location of the wave in the image was obtained, the corresponding physical location could be calculated from Eq. 4.1. During experiments, the observa-

tion area to be recorded was divided into several rectangles with the fiducial marks described above and the physical locations of the rectangle corner points were measured in advance. All the points inside a rectangle in the image were calibrated by the coordinates of the corners, the distortion caused by the optics of the camera was then eliminated.

4.6 Vertical Wall

A vertical wall extending the entire width of the wave tank was used in the solitary wave splash-up experiments. It was 90 cm high and 60 cm wide, and was constructed of 1.40 cm thick lucite. The perimeter of the wall was sealed by rubber windshield wiper blades to prevent water leakage from the gap between the wall and wave tank. The surface of the vertical wall was carefully painted with several layers of paint so that the surface was smooth. A scale consisting of black lines 2 cm apart was painted on the surface. The vertical wall was mounted on an instrument carriage so that its position on the slope could be changed between experiments. Lead weights placed on the slope behind the vertical wall increased the rigidity of the wall.

4.7 Data Acquisition System

The voltage signal from the wave gages and the run-up gage were acquired by a Macintosh personal computer with a MacADIOS-8ain analog-to-digital board controlled with Superscope II software developed by GW Instruments. The accuracy of the A/D conversion was $\pm 5mV$ over 20 V range. The maximum sampling rate of the A/D board was 1 MHz. During the experiments, the trials were recorded with a

sampling rate of 200 Hz, and the calibrations were recorded with the sampling rate of 100 Hz.

4.8 Experimental Procedures

4.8.1 Measurements of the Run-Up of Solitary Waves on Slopes

A schematic of the solitary wave run-up experiments was presented in Figure 3.1. The origin of the coordinate system was chosen at the initial shoreline position of the water on the slope, with the positive x axis directed offshore towards the wave generator and y axis directed upward from the still water level. The water level in the wave tank was measured by a point gage located at the toe of the slope, which had an accuracy of ± 0.1 mm. The measurement was also performed after a series of experiments; if necessary more water was added to the tank to keep the water depth constant. Three computers were used during the experiments for wave generation and data acquisition. The first computer was used to generate the solitary wave trajectory, the second computer was used to process the data from the wave gages and the high-speed video camera, and the third computer was used to control the LDV system.

The initial incident wave height H/h_0 was determined using a resistance wave gage described above. It was located at half of a characteristic length, $L/2$, of the incident solitary wave from the toe of the slope, where L was defined in Eq. 3.25. The wave gage was calibrated before and after the experiment. When the desired solitary wave was generated by the wave generation system with the first computer, the data acquisition system was also started in the second computer. An electronic signal

was sent to the two high-speed video cameras and the third computer to trigger the video recording and to start the LDV system data collection. A time delay ranging from several milliseconds to tens of seconds could be set to control the high-speed video camera depending on the camera locations; the exact value of this time delay was determined by one or two test runs before the experiments. Therefore, once the wave generator was started, all the data acquisition and video recording were automatically controlled through electronic trigger signals, which were all properly referenced to each other in time.

The time-histories of the run-up of the solitary waves on the slopes were measured by two methods: (i) the run-up gage introduced in the previous section. It was calibrated before each experiment. This gage was used for non-breaking solitary wave run-up. (ii) High-speed video recording. The run-up gage was not applicable for breaking solitary wave run-up on a gentle slope since the light spot generated by the laser reflection on the breaking wave front was too weak to be captured by the linear camera. For this case, the high-speed camera was used to record the wave front time-histories. The time-histories of the run-down process could not be recorded by the high-speed video camera because the surface of the slope was already wetted by the run-up wave; therefore, the run-down stream cannot be recognized in the images. Thus, only the run-up portion of the time-histories was available for breaking solitary wave run-up.

The maximum run-up of the solitary wave on the slope was also measured by two methods: (i) high-speed video recording and (ii) visual observations plus the point gage. The high-speed video recording can give the most accurate measurement, but several trial runs have to be conducted before the actual measurement to determine the recording region that covers the maximum run-up position. The visual observation method is relatively simple. The run-up water will leave a clear intersection line

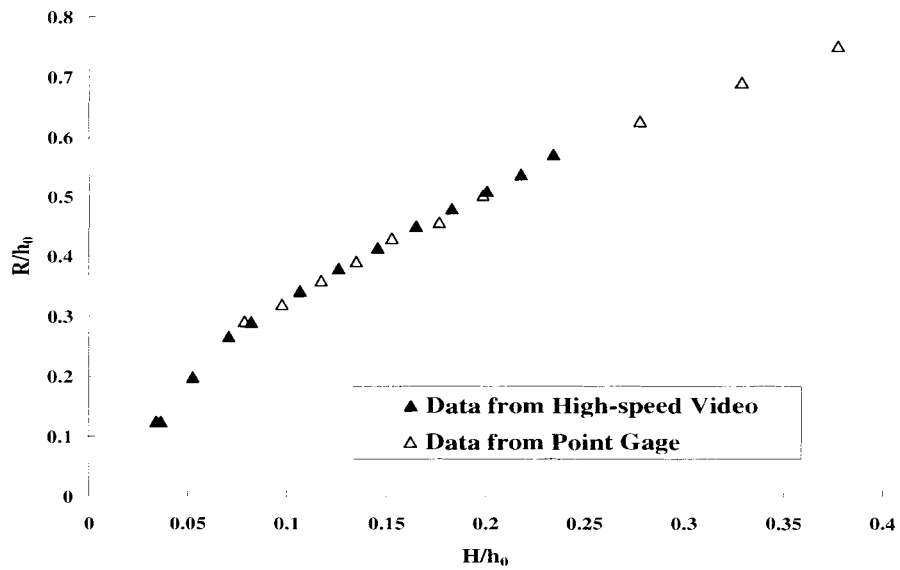

Figure 4.25: The comparison of maximum run-up obtained from the high-speed video and visual observations

between the wet surface and the dry bed. During the experiment, the position of the intersection line was marked either by the placement of a small weighted marker made of steel or by marking the slope surface directly. Then the height of the mark with respect to the initial shoreline line was measured by a point gage. This height was regarded as the maximum run-up of the incident solitary wave. The accuracy of the point gage used for the purpose was within ± 0.1 mm. Figure 4.25 shows the experimental data for solitary wave maximum run-up from both these methods, it can be seen that the data from visual observation method agreed with the high-speed video very well, thus, most of the maximum run-up data was measured by the visual method.

4.8.2 Measurements of the Splash-Up of Solitary Waves on Vertical Walls

A sketch showing the arrangement for the measurement of splash-up of solitary waves on a vertical wall is shown in Figure 4.26. The experimental setup was the same as that of the run-up experiments on a slope except a vertical wall was mounted on the slope. The vertical wall position on the slope could be changed to investigate the effects of different breaking conditions on the splash-up. The splash-up was recorded using high-speed video. If the wave contacted the vertical wall before breaking or after breaking, the splash-up on the vertical wall was relatively small and consisted of a run-up "water sheet", and the whole process could be recorded by the camera. However, when the wave broke near the position of the vertical wall the splash-up was quite high and broke up with the drops and spray. Some fluid was even ejected about 1 m $\sim$ 2 m above the wall and nearly reached the ceiling of the laboratory. For this case, the maximum height of the splash-up was estimated. A second high-speed video camera was placed on one side of the wave tank to record the shape of wave breaking from a sideview. These two high-speed video cameras were referenced to each other in time so that both the wave shape and the splash-up on the vertical wall could be obtained simultaneously.

4.8.3 Other Experimental Procedures

Approximately 15 $\sim$ 20 minutes was allowed between two consecutive runs in the experiments to ensure that the wave generated in the second run was not contaminated by the previous waves and the experiments were reproducible. During this period of time, the wave amplitude and the wave particle velocity in the wave tank were measured several times, the second run began only when no detectable variation

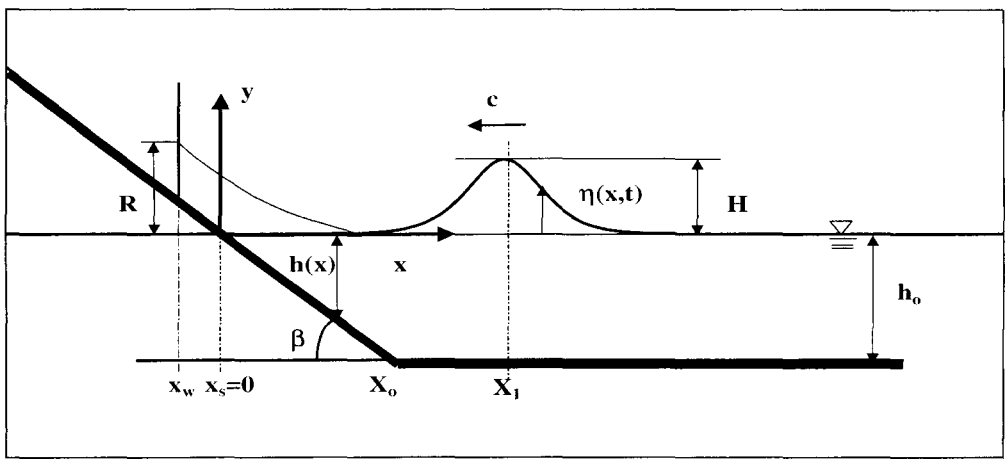

Figure 4.26: Schematic sketch of the experimental arrangement for a solitary wave splash-up on vertical walls

in the amplitude and velocity could be found in the measurement.

The water was chemically treated to reduce algae growth, and after changing the tank water it was allowed to stand for at least 24 hours to purge the tank of small suspended air bubbles. Usually after the experiments, which lasted one or two days, all the water in the tank was replaced.

Chapter 5 Presentation and Discussion of Results

The results presented in this chapter are based on the experimental measurements and numerical simulations for three cases of solitary wave run-up: (i) the non-breaking solitary wave run-up on relatively steep slopes, (ii) breaking solitary wave run-up on gentle slopes, and (iii) breaking solitary wave splash-up on vertical walls. In each case the characteristics of the interaction between the wave and the slope/wall during the run-up and splash-up process such as wave shape, time-history, and wave velocity were measured experimentally and compared with the results from theoretical analyses for non-breaking solitary wave run-up and numerical results from the WENO scheme for breaking waves presented in Chapter 3. The experimental conditions of the slopes and initial incident solitary waves for the run-up process are given in table 5.1. The measurement of maximum run-up has also been conducted over a wide range of water depths and wave heights for the three slopes: 1:2.08, 1:15, and 1:19.85. The parameters of these measurements are shown in table 5.2.

The water depth in the constant depth region seaward of the toe of the slope, h_0,

Type of Run-up	slope	H/h_0	$h_0(cm)$	L/h_0
Non-breaking	1:2.08	0.163	21.51	6.23
Breaking	1:15	0.30	30.48	4.59
Breaking	1:19.85	0.30	30.48	4.59

Table 5.1: Wave parameters for run-up process of solitary waves

Type of Run-up	Wave Tank	Slope	$h_0(cm)$		H/h_0	
			h_{0min}	h_{0max}	H_{min}	H_{max}
Non-breaking	CST	1:2.08	16.30	21.51	0.02	0.35
Breaking	CWT	1:15	7.00	30.48	0.05	0.45
Breaking	CERC	1:15	30.48	76.20	0.04	0.20
Breaking	CWT	1:19.85	30.48	30.48	0.04	0.40

Table 5.2: Wave parameters for maximum run-up of solitary waves

is chosen to normalize all the length parameters such as wave height H, horizontal coordinate x and vertical position y in the following discussion. The purpose of this arrangement is to permit the reader to quickly envision the relative wave conditions and scales, so the results can ultimately be used with field conditions. In this frame of reference $x^* = x/h_0 = 0$ is the initial shoreline and $x^* = 1/s$ is the toe of the slope, where the tangent of the slope angle, i.e., $tan\beta = s$. In this discussion, the time, t, is normalized by the time scale parameter $1/\sqrt{g/h_0}$ and the time coordinate is plotted from left to right; this gives a visual presentation which is the same as that of the definition sketch, Figure 3.1.

The detailed list of experimental runs and results is presented in Appendix. For purpose of clarity, the definition sketch of the solitary run-up presented in Chapter 3 is repeated in Figure 5.1.

5.1 Solitary Wave Characteristics

Solitary waves were used throughout this study as a model of a tsunami in nature. The wave generation method proposed by Goring (1979) has been used and is described in Chapter 4. The algorithm can be used to generate a solitary wave with high accuracy in the laboratory.

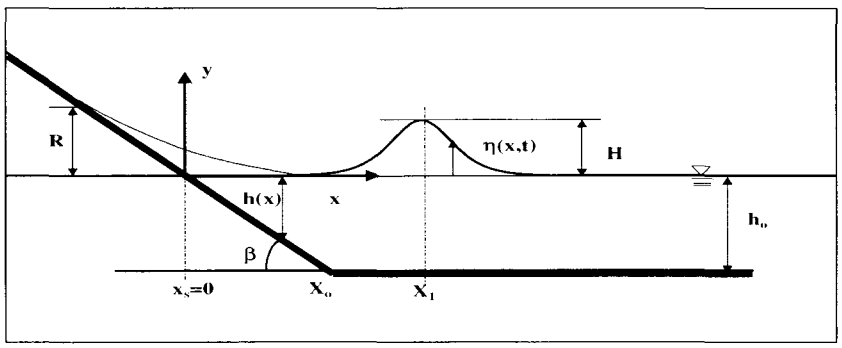

Figure 5.1: Definition sketch of the solitary wave run-up

To test the accuracy of the solitary wave generated in experiments, the wave profile and the wave velocity measured in the laboratory are compared with the corresponding theoretical data from third-order solitary wave theory.

The wave profile is presented in Figure 5.2 for a solitary wave with a relative wave height in the constant depth portion of the wave tank of $H/h_0 = 0.276$. The theoretical solitary wave profile obtained from a third-order theory is also included in Figure 5.2. The wave was measured in the constant depth region seaward of the toe of the slope with $h_0 = 30.48$ cm. The incident wave height $H/h_0 = 0.276$ is measured at the location $x/h_0 = 24.64$, i.e. far from the toe of the slope. The ratio of the distance from the measurement point to the wave generator paddle to h_0 is 32.81. Two techniques were used in these measurements: (i) a resistance wave gage, and (ii) high-speed videos. There is good agreement between these two experimental methods and with the theory indicating both that the video method of obtaining the profile is quite reliable and that the non-linear wave generation technique used produces a well formed solitary wave in the constant depth region of the tank. Small oscillatory waves were found in the region for $t^* > 5$, i.e. the tail of the wave, which are due to the first-

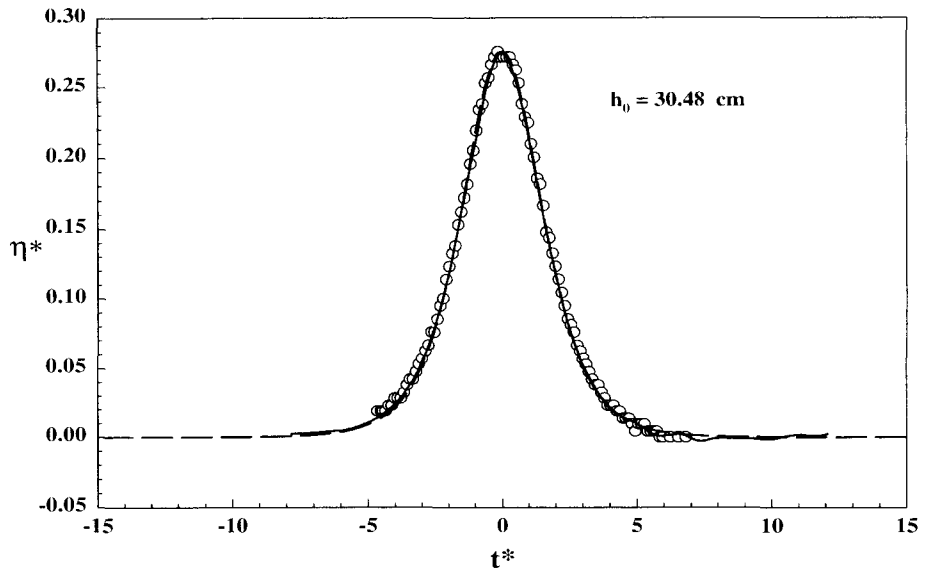

Figure 5.2: Comparison of high-speed video and wave gage output to the third-order theory for solitary wave profile with H/h_0=0.276. The dashed line is the third-order theory, the solid line is the experimental data obtained from the wave gage, and the circles are the experimental data obtained from the high-speed video

order wave generation method. The wavemaker generates the wave according to the first-order theory, which is not an exact solitary wave form. Therefore, as the wave propagates along the wave tank, dispersive effects and non-linear effects transform the wave into a soliton followed by a small oscillatory tail. The generated solitary wave height is generally smaller than that specified in the procedure used in the wave generation; as mentioned earlier, this is both because the generation procedure is accurate to first-order and due to viscous effects on the free surface and the bottom of the wave tank.

The normalized horizontal velocities and vertical velocities $u^* = u/\sqrt{gh_0}$ and $v^* = v/\sqrt{gh_0}$ of solitary waves were measured in the constant depth region of wave tank using a LDV, and the results are presented in Figure 5.3 and Figure 5.4. The

measurements were conducted in the relatively deep wave tank at the Coastal Engineering Research Center, USACE. (This wave tank denoted as CERC was described in Chapter 4.) A water depth $h_0 = 60.96$ cm was used with an incident wave height $H/h_0 = 0.20$. The velocities at three depths were measured: $y/h_0 = -0.016$, which is close to the still water level; $y/h_0 = -0.328$; and $y/h_0 = 0.148$. These velocities are compared with the third-order theoretical velocity at the still water level $y/h_0 = 0.0$. It is seen that the measured horizontal and vertical velocities in the region above the still water level are shown only for a small time when the four laser beams used in the LDV were in the water; when the beams were out of the water, no data could be obtained. All measured velocities agreed well with each other except near the maxima (around $t^* = 0$) where the maximum velocity decreases with depth, as would be expected. Away from the maxima, the difference between these measurements is small. The vertical velocities shown in Figure 5.4 were relative small compared to the horizontal velocities especially as the bottom is approached. This demonstrated that the assumption of a small (or negligible) vertical velocity made in shallow water wave theory is reasonable. Since all of these measurements were obtained from several different experiments, the reproducibility of the solitary wave generated also was confirmed.

5.2 Non-Breaking Solitary Wave Run-up

5.2.1 Wave Amplitude and Velocity Time-Histories

A solitary wave with a relative wave height $H/h_0 = 0.163$ was used in the run-up experiments with a water depth of 21.51 cm and a beach slope of 1:2.08. The water surface time-histories using the WENO numerical scheme, the non-linear theory and

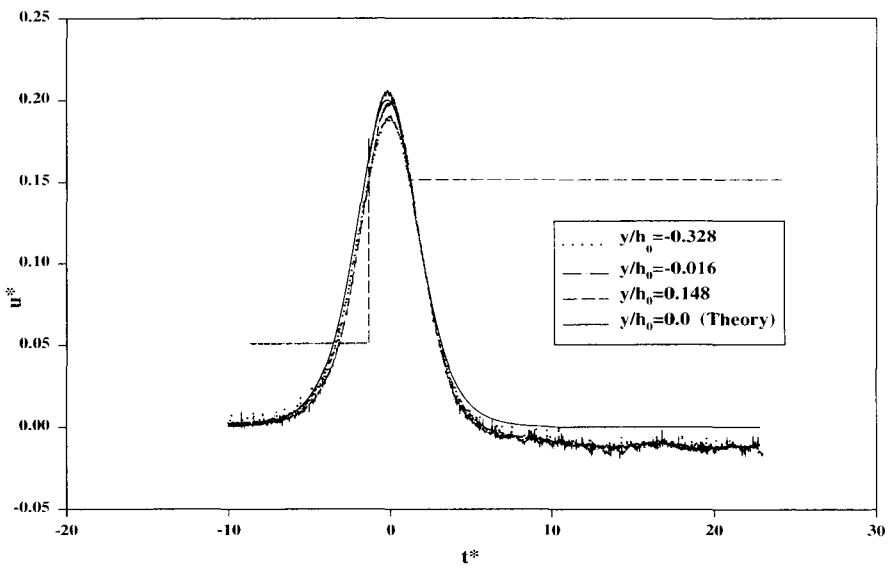

Figure 5.3: Comparison of LDV measurement of horizontal velocity in CERC tank to the third-order theory for solitary wave with H/h_0=0.20. The solid line is the third-order theory at $y/h_0 = 0.0$, the dotted line is the LDV data obtained at $y/h_0 = -0.328$, the dash-dotted line is the LDV data obtained at $y/h_0 = -0.016$, and the dashed line is the LDV data obtained at location $y/h_0 = 0.148$

the approximate non-linear theory presented by Synolakis (1986) are compared to experimental results at nine locations in Figures 5.5 for this plane beach. (It is noted that x* = 0 refers to location of the original shoreline; positive values are offshore and negative values are onshore of that position. Therefore, $x^* = 2.08$ is located at the toe of the slope for this beach.)

When calculating the wave amplitude, and horizontal velocities using Eqs. 3.45 to 3.49, the actual location (x, t) in the physical plane has to be calculated from the transformed plane (σ, λ), since all the equations are explicit in terms of σ and λ. These calculation can be performed iteratively using Newton's method and the actual location x, t can be obtained by the method described below: (All the calculation

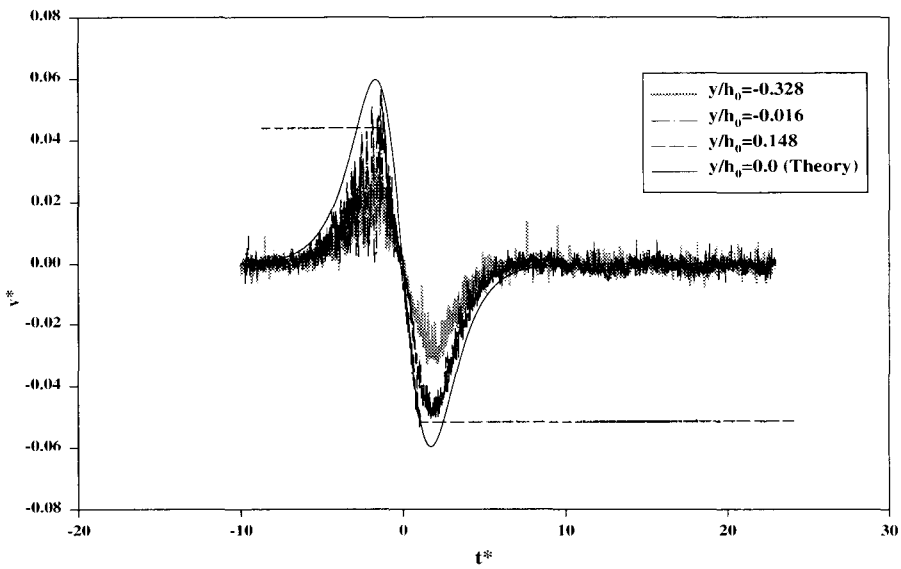

Figure 5.4: Comparison of LDV measurement of vertical velocity in CERC tank to the third-order theory for solitary wave with $H/h_0 = 0.20$. The solid line is the third-order theory at $y/h_0 = 0.0$, the gray dotted line is the LDV data obtained at $y/h_0 = -0.328$, the black dash-dotted line is the LDV data obtained at $y/h_0 = -0.016$, and the dashed line is the LDV data obtained at location $y/h_0 = 0.148$

was performed using Mathematica.) The relations between (σ, λ) and (x, t) are the transformation equations, i.e., Eqs. 3.48 and 3.49. If we differentiate Eq. 3.48 in terms of σ and Eq. 3.49 in terms of λ, the following equations are obtained:

$$\frac{dx}{d\sigma} = cot\beta\left(\frac{\sigma}{8} - \frac{\Psi_{\lambda\sigma}}{4} + \frac{u(\Psi_{\sigma\sigma} - u)}{\sigma}\right) \tag{5.1}$$

$$\frac{dt}{d\lambda} = cot\beta\left(\frac{\Psi_{\lambda\sigma}}{\sigma} - \frac{1}{2}\right) \tag{5.2}$$

To seek the wave characteristics at a particular location (x, t), the above equations

can be written in difference form yielding the following expressions:

$$\sigma_{i+1} = \sigma_i - \frac{x(\sigma_i, \lambda_i) - x^*}{cot\beta(\frac{\sigma}{8} - \frac{\Psi_{\lambda\sigma}}{4} + \frac{u(\Psi_{\sigma\sigma} - u)}{\sigma})} \tag{5.3}$$

$$\lambda_{i+1} = \lambda_i - \frac{t(\sigma_i, \lambda_i) - t^*}{cot\beta(\frac{\Psi_{\lambda\sigma}}{\sigma} - \frac{1}{2})} \tag{5.4}$$

where (x^*, t^*) is the specific location of the wave in space and time and i is the iteration index. The calculation process begins by choosing an initial value of σ_1 and λ_1, and substituting them into Eqs. 3.45 to 3.49 to get $x(\sigma_1, \lambda_1)$, $t(\sigma_1, \lambda_1)$, u and $\Psi_{\lambda\sigma}$, $\Psi_{\sigma\sigma}$. If $|x(\sigma_1, \lambda_1) - x^*|$ is less than some prescribed small quantity, the process stops. Otherwise new values of σ_i and λ_i are calculated from Eqs. 5.3, 5.4, and the process continues until the required accuracy is achieved. This iteration converges very fast in the calculations; usually in less than 10 steps the desired accuracy can be achieved.

As seen in Figure 5.5, for the locations that are near the toe of the slope, the non-linear theory agrees quite well with the experiments especially for the portion of the water surface-time history which corresponds to the incident wave. The differences between the theory of Synolakis (1986), the present theory and the experiments in this region are relatively small; this feature will be discussed later. As locations close to the initial shoreline position, i.e., $x^* = 0$, are approached the solitary wave increases in height and deforms. Non-linear effects cannot be neglected in that region; the present non-linear theory appears to properly handle the non-linear effects. Shoreward of the initial shoreline, since there is no water at those elevations until the run-up tongue reaches that location, both the experimental and theoretical results are available only for an abbreviated interval of time. Out of this interval, the measurement was zero since no singnal was detected by the probe. The present non-linear theory agrees well with the experimental data for these locations.

The numerical results for wave time-histories from the WENO scheme described

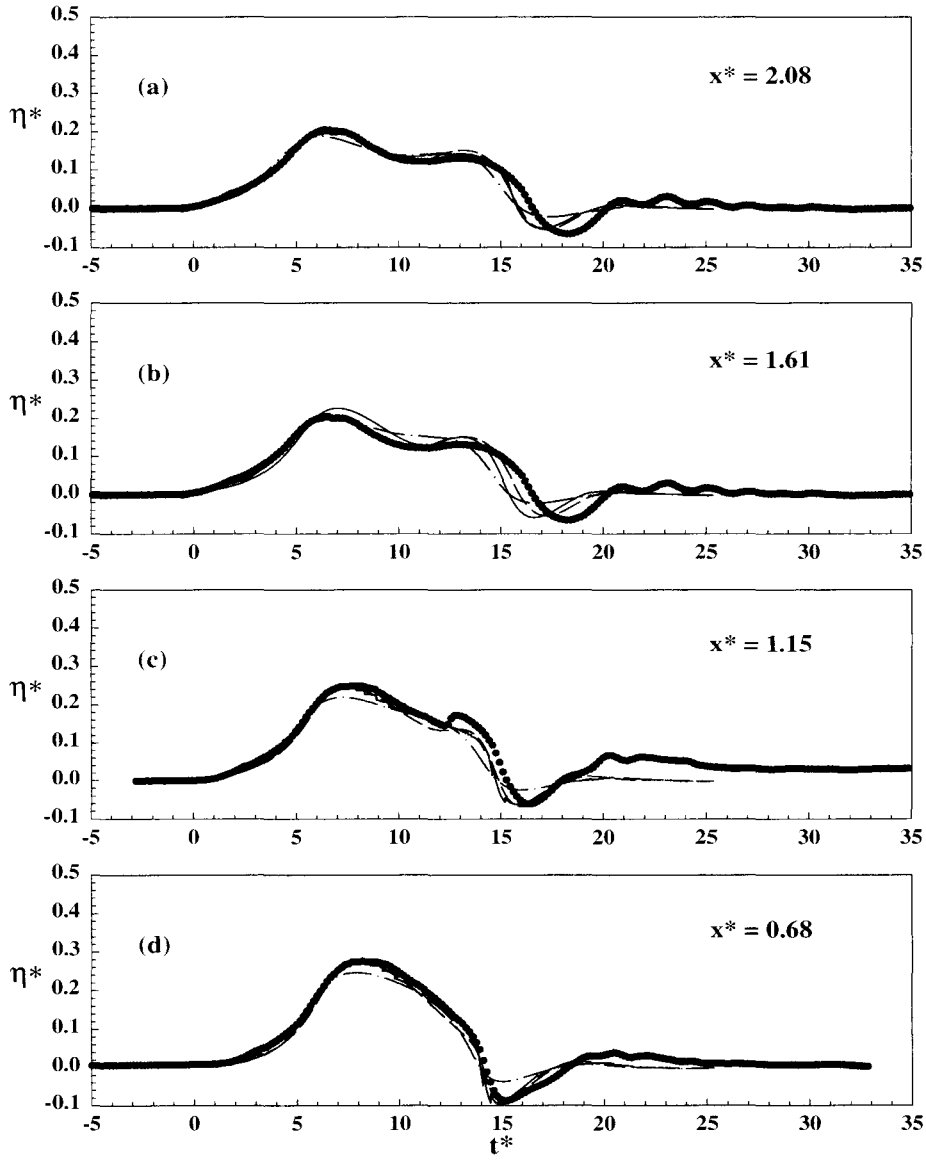

Figure 5.5: (a)-(d) Run-up of solitary wave with $H/h_0 = 0.163$ on 1:2.08 slope. Normalized wave amplitudes are shown as a function of normalized time at different locations. The solid line is the numerical simulation, the dashed line is the non-linear theory, the dash-dotted line is the approximate non-linear theory of Synolakis (1986), and the circles are the experimental data.

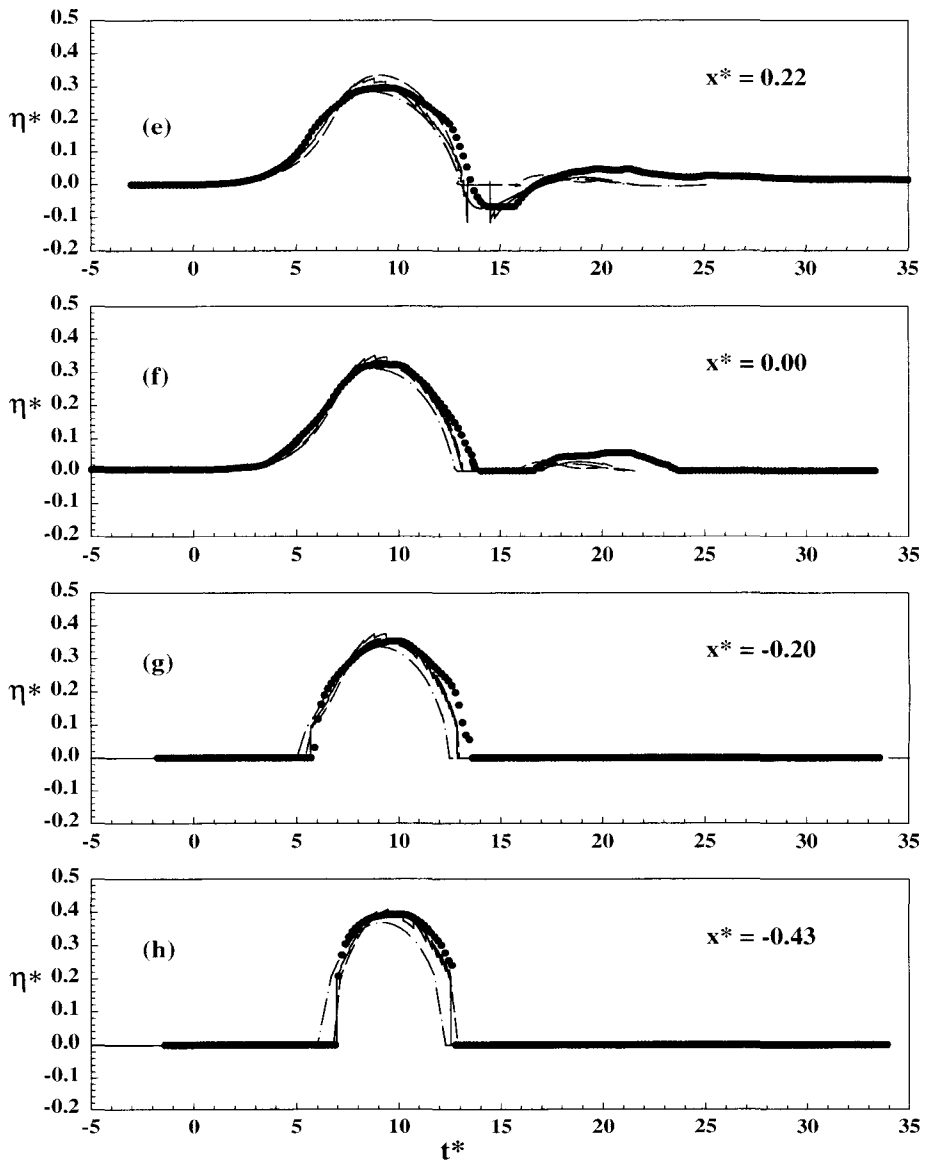

Figure 5.5: (e)-(h) (continued) Run-up of solitary wave with $H/h_0 = 0.163$ on 1:2.08 slope. Normalized wave amplitudes are shown as a function of normalized time at different locations.

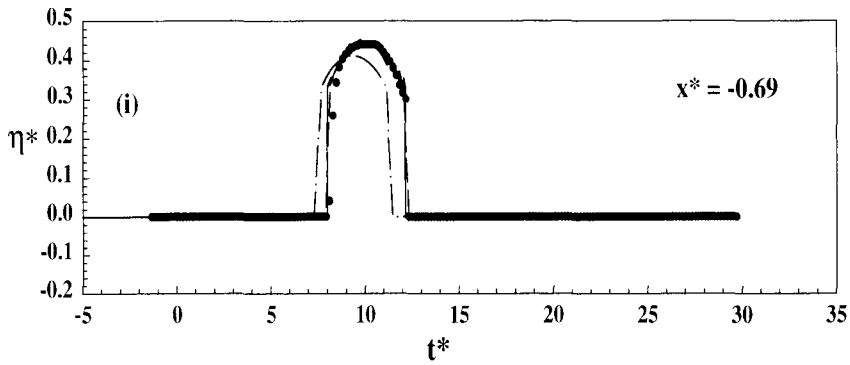

Figure 5.5: (i) (continued) Run-up of solitary wave with $H/h_0 = 0.163$ on 1:2.08 slope. Normalized wave amplitudes are shown as a function of normalized time at different locations.

in Chapter 3 are also presented in Figure 5.5 as solid lines. In general the numerical results agree well with both the non-linear theory and experimental data. This is no surprise since both the numerical scheme and non-linear theory solve the same NLSW equations. When comparing the numerical results with the experimental data for a specific location, the numerical solutions from the computational grid which is the closest to the actual x coordinate are chosen for comparison. Since the actual x-coordinate of the calculation grid changes during the computing because of the mapping technique used in the numerical scheme, the grid closest to the actual location will vary in the calculation. This causes small variations in the data for the wave shape. There is also a small time-lag between the numerical data and the experimental data for the reflected wave and the cause for that needs further investigation.

The normalized horizontal and vertical velocities $u^* = u/(gh_0)^{1/2}$ and $v^* =$

$v/(gh_0)^{1/2}$ in these experiments were measured in the region near the original shoreline and offshore at normalized depths which vary with the measurement location; in general, the measurements were at mid-depth. These experimental results are presented in Figures 5.6 and are compared to the non-linear theory developed in this study, the numerical simulation from the WENO scheme, and to the approximate non-linear theory of Synolakis (1986). Note that there are no predicted vertical velocities, since the shallow water theory assumes the vertical velocities are negligible. The experimental measurements for all locations, even those close to the initial shoreline, show the vertical velocity is less than 20% of the horizontal velocity. The present non-linear theory appears to predict the horizontal velocity reasonably well with some deviation near the maxima for the run-up on a 1:2.08 slope. The numerical results agree with both the experiments and the non-linear theory very well at most of the locations except at the location $x^* = 0.22$, where the numerical simulation predicts a shock like discontinuity in the run-down process and thus a much higher peak velocity than the non-linear theory.

5.2.2 Free Surface Profiles

Water surface profiles on the 1:2.08 slope are presented in Figures 5.7 at the indicated non-dimensional times. The non-linear theory, the numerical simulation and the approximate non-linear theory of Synolakis (1986) are compared to the experimental results. In the initial run-up stages the difference between the two theories, the numerical results and the experimental data is small. As the run-up proceeds, the non-linear theory obtained in the present study appears to agree better with the experimental results than the approximate non-linear theory. This would be expected, since the non-linear effects become more important as the run-up process proceeds, especially during run-down, see Figure 5.7 (f) and 5.7 (g) for $t^* = 11.2$ and $t^* = 12.2$,

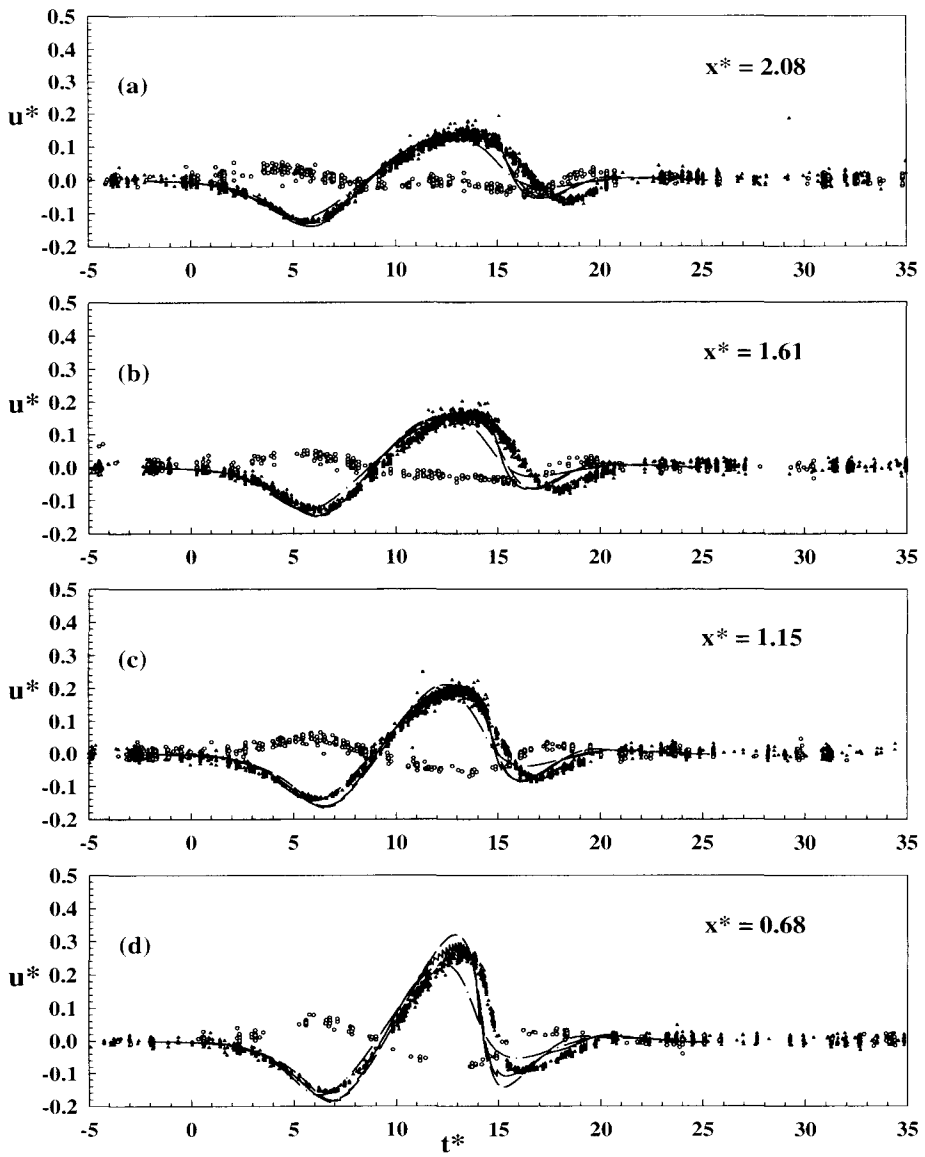

Figure 5.6: (a)-(d) Run-up of solitary wave with $H/h_0 = 0.163$ on 1:2.08 slope. Normalized wave velocities are shown as a function of normalized time at different locations. The solid line is the numerical simulation, the dashed line is the non-linear theory, the dash-dotted line is the approximate non-linear theory of Synolakis (1986), the triangles are the experimental horizontal velocities, and the circles are the experimental vertical velocities.

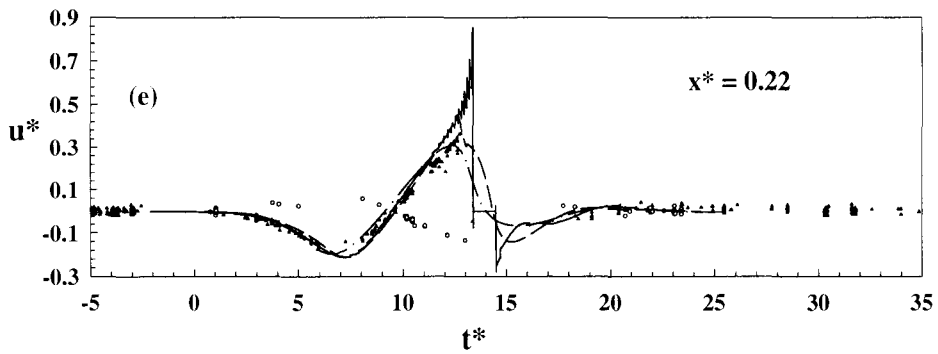

Figure 5.6: (e) (continued) Run-up of solitary wave with $H/h_0 = 0.163$ on 1:2.08 slope. Normalized wave velocities are shown as a function of normalized time at different locations.

respectively. For this slope, breaking did not occur during run-down. For all times it is apparent that both theories agree reasonably well with the experimental data as the distance offshore from the initial shoreline increases. This supports the assumption that the effects of non-linearities are small and can be neglected near and offshore of the toe of the slope. In the region near the run-up maxima (Figure 5.7 (e), $t^* = 10.2$) the present theory tends to overestimate the amplitude of the run-up tongue compared to the experiment. This may be due to the effect of friction and / or the use of the meniscus to define the wave amplitude in the experiments.

Experimental data are presented in Figure 5.8 from Synolakis (1986) for the variation in water surface amplitude with distance on a plane beach inclined at a slope of 1:19.85 along with the numerical results and the non-linear theory from this study and the approximate non-linear theory from Synolakis (1986) for four non-dimensional times. Since the slope was relatively gentle in those experiments, it was necessary to

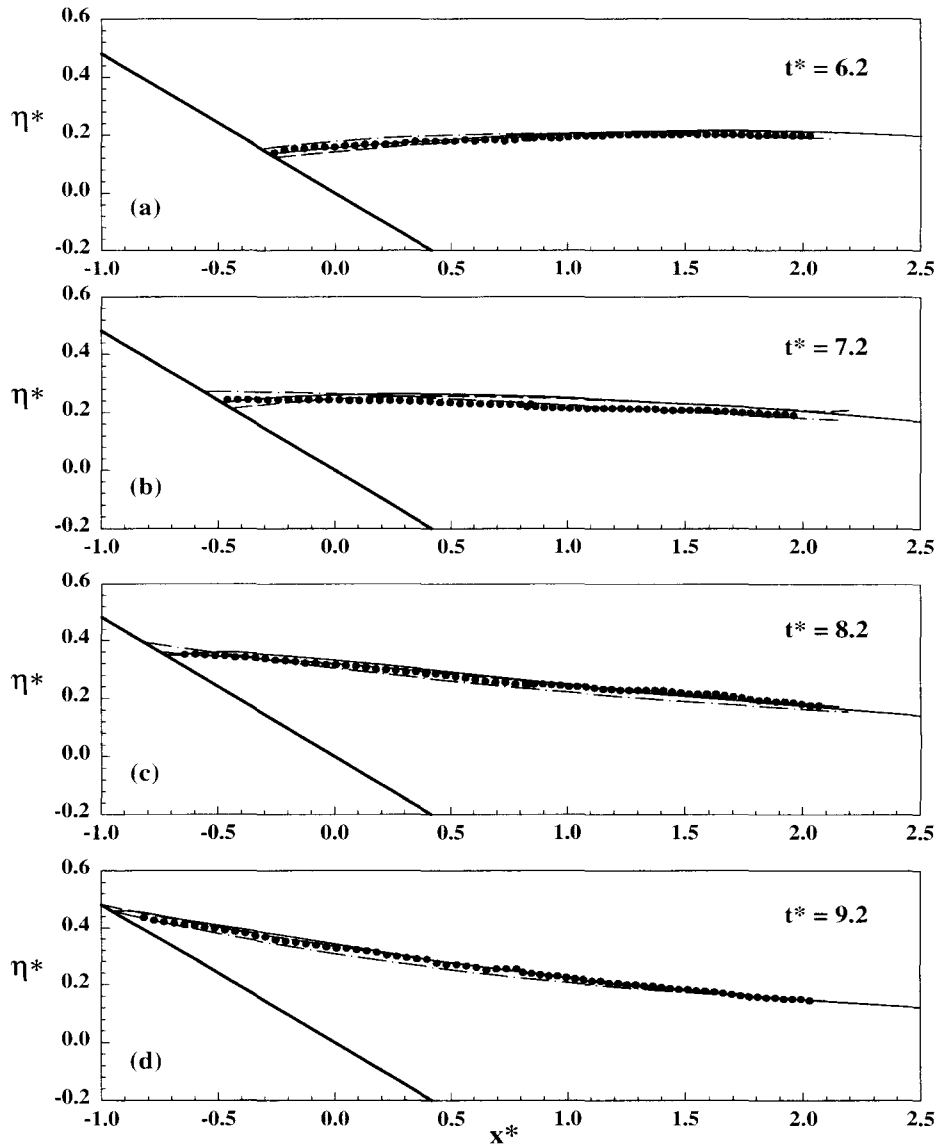

Figure 5.7: (a)-(d) Run-up of solitary wave with $H/h_0 = 0.163$ on 1:2.08 slope. Normalized surface profiles are shown as a function of normalized distance at different times. The solid line is the numerical simulation, the dashed line is the non-linear theory, the dash-dotted line is the approximate non-linear theory of Synolakis (1986), and the circles are the experimental data.

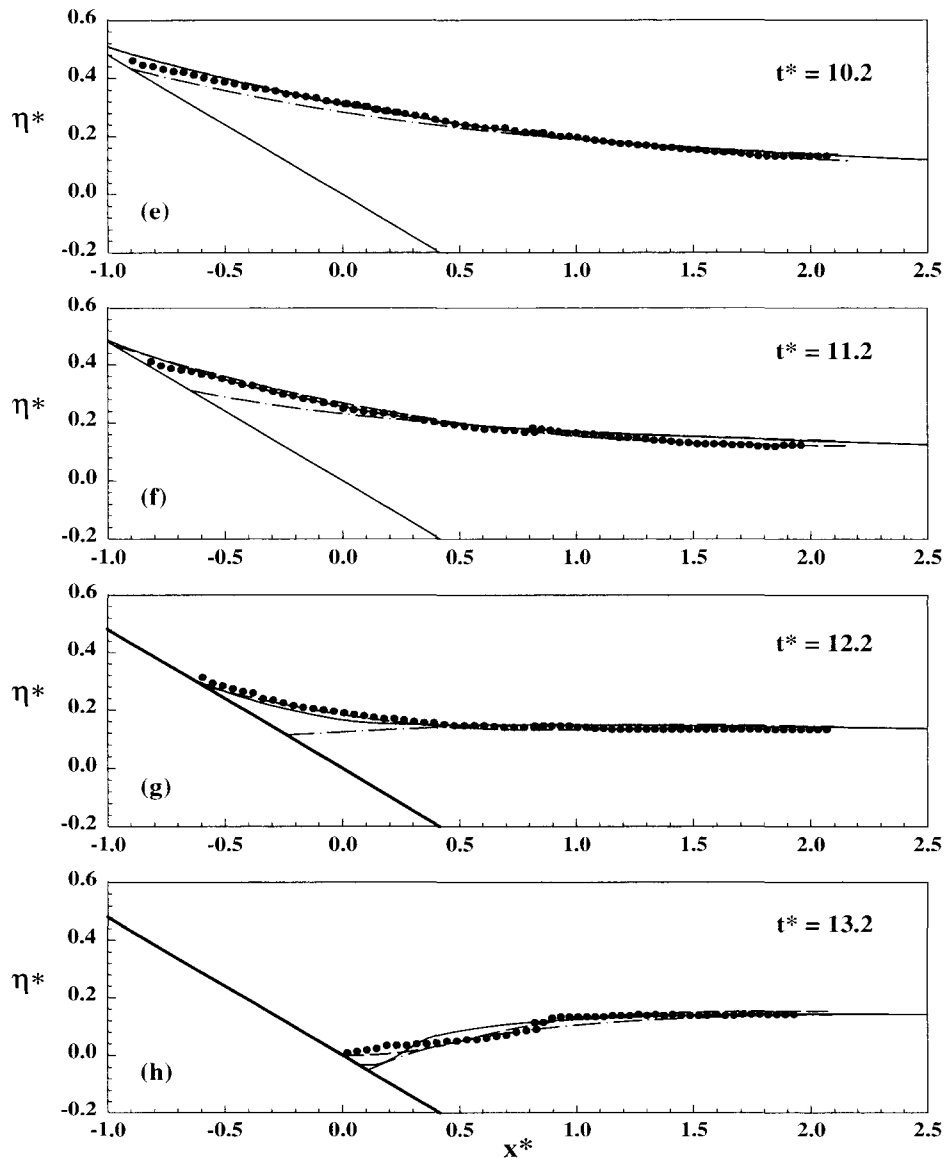

Figure 5.7: (e)-(h) (continued) Run-up of solitary wave with $H/h_0 = 0.163$ on 1:2.08 slope. Normalized surface profiles are shown as a function of normalized distance at different times.

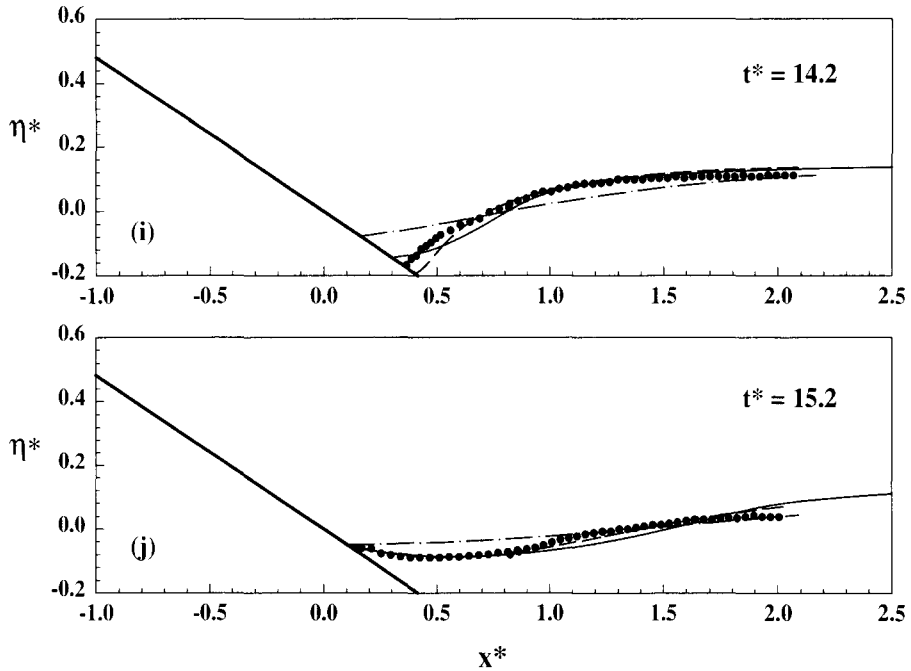

Figure 5.7: (i)-(j) (continued) Run-up of solitary wave with $H/h_0 = 0.163$ on 1:2.08 slope. Normalized surface profiles are shown as a function of normalized distance at different times.

use a much smaller wave than was used in the present study to prevent wave breaking during run-up, i.e., $H/h_0 = 0.0185$. For the cases shown, both theories agree well with the experimental data. The difference between the two theories and the numerical results is almost undetectable, since for such small relative wave height the non-linear effects are relatively unimportant compared to those for the larger wave whose results were shown in Figure 5.7 .

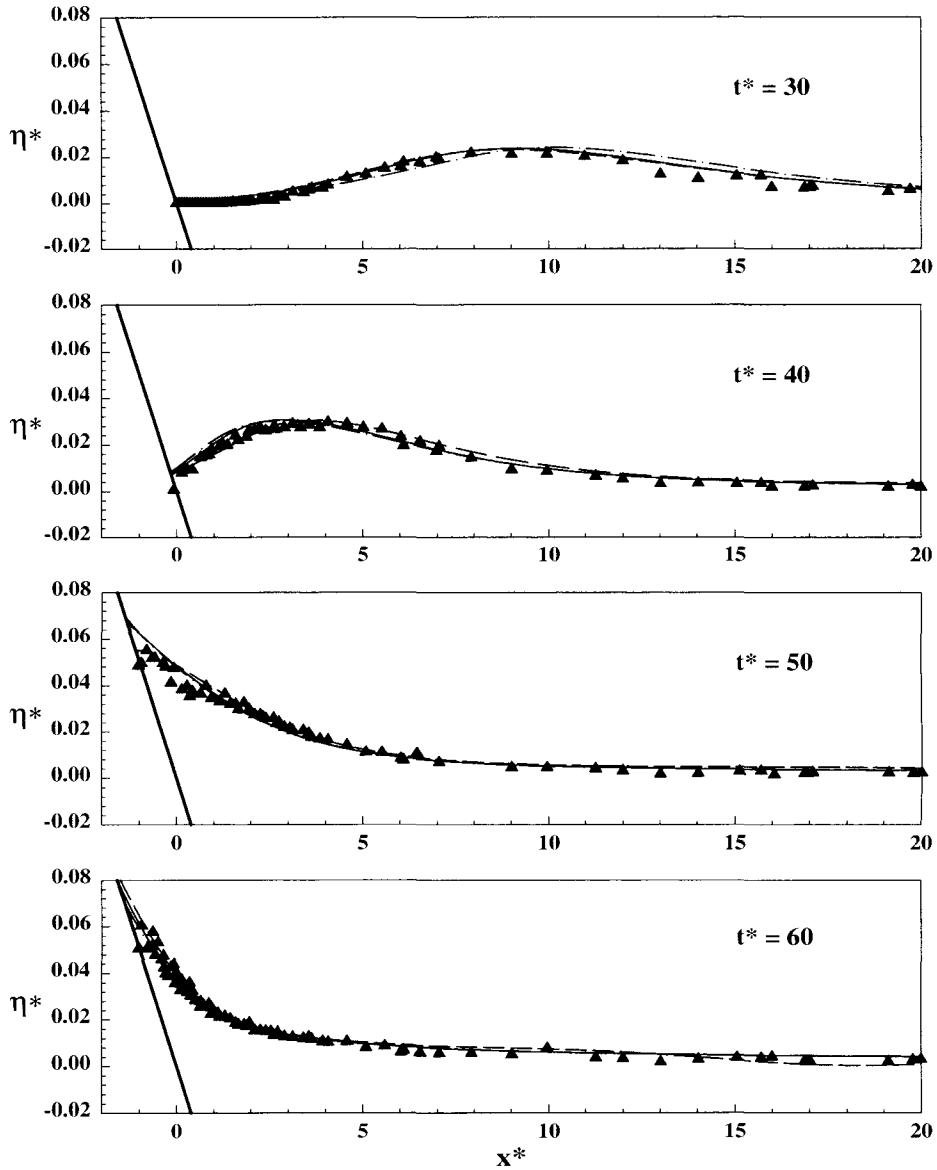

Figure 5.8: (a)-(d) Run-up of solitary wave with $H/h_0 = 0.0185$ on 1:19.85 slope. Normalized surface profiles are shown as a function of normalized distance at different times. The solid line is the numerical simulation, the dashed line is the non-linear theory, the dash-dotted line is the approximate non-linear theory of Synolakis (1986), and the triangles are the experimental data from Synolakis (1986).

5.2.3 Shoreline Movement and Maximum Run-Up

The normalized run-up is shown as a function of normalized time in Figure 5.9 for run-up on a 1:2.08 slope. Experimental data are presented from two methods: the laser run-up gage discussed earlier and high-speed video results. During the run-up process ($t^* < 10$), both experimental methods are in excellent agreement. During the run-down process ($t^* > 10$), the wave retreats so quickly that the reflected laser spot is too weak to be captured by the photodiode camera. Therefore, only the high-speed video recording data are shown. Both the theory from the present study and the approximate non-linear theory predict the run-up stage very well for $t^* < 8$. The non-linear theory agrees better with the data in the region of the maximum run-up than the approximate non-linear theory. The approximate non-linear theory underestimated the run-down trough, as was seen in Figure 5.7. It can be found that the maximum run-up obtained from the direct numerical calculations of Eq. 3.23 and Eq. 3.51 were larger than that predicted by the approximate formula, i.e., Eq. 3.26 and Eq. 3.52, respectively. For example, the difference of the maximum run-up between the present non-linear theory and the approximate non-linear theory proposed by Synolakis (1986) is about 11%, but that predicted by the approximate formula, i.e., is only 5%. This suggests that direct numerical calculation is necessary if accurate run-up is desired. The numerical results agree with the experimental data very well especially around the maximum run-up position, which shows that the current numerical scheme can model the movement of the shoreline with high accuracy. The good agreement also shows that the computation domain mapping technique used in the numerical method is very stable and efficient in calculating the shoreline position.

The variation of the maximum run-up with relative wave height, H/h_0, is presented in Figure 5.10 for the slope of 1:2.08. Experimental results and the results of

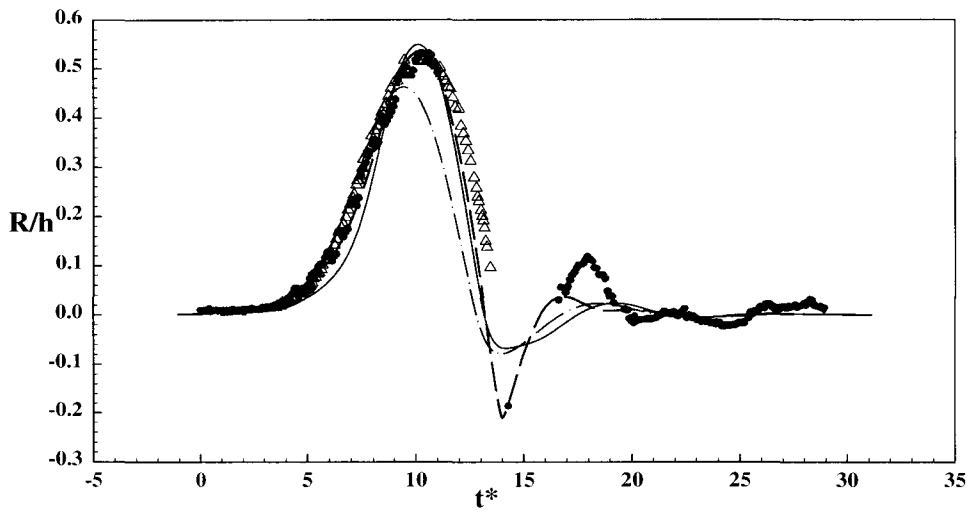

Figure 5.9: Run-up of solitary wave with $H/h_0 = 0.163$ on 1:2.08 slope. Normalized shoreline position is shown as a function of normalized time. The solid line is the numerical simulation, the dashed line is the non-linear theory, the dash-dotted line is the approximate non-linear theory of Synolakis (1986), the circles are the experimental data from the run-up gage, the triangles are the high-speed video recording.

the present theory, Eq. 3.52, and the results of the approximate non-linear theory, Eq. 3.23, are shown for comparison. The non-linear theory from the present study agrees quite well with the experimental data for the full range of the wave heights investigated. It is noted that the differences between the results of the present theory and those of Synolakis (1986) are small. This is to be expected, as can be seen in Figure 5.11, where the ratio of the correction term of present non-linear theory to the approximate non-linear theory of Synolakis (1986), R_{cr}/R_s, is plotted as a function of the relative wave height, H/h_0, for constant values of slope from Eq. 3.55. Figure

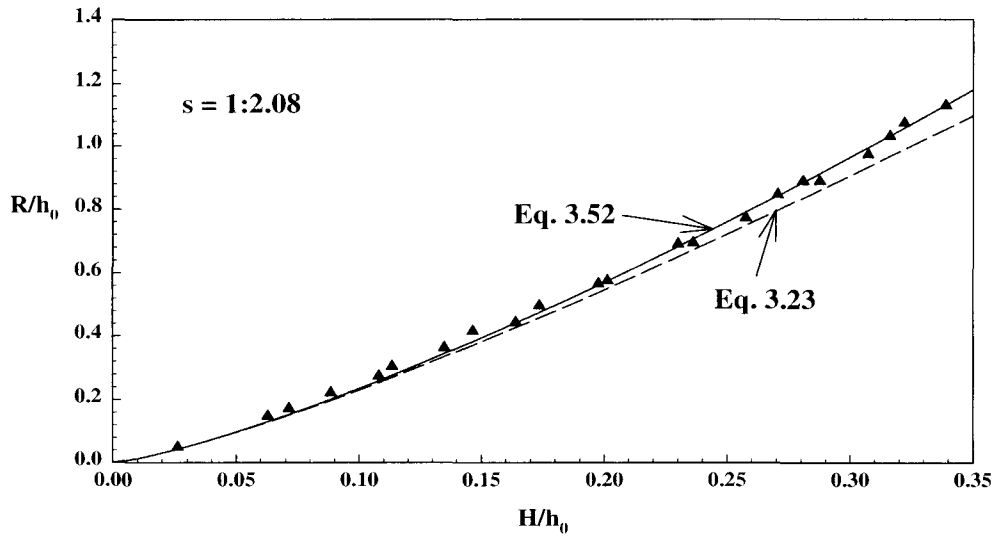

Figure 5.10: Normalized maximum run-up as function of incident wave height H/h_0 for a slope of 1:2.08. The solid line is the non-linear theory, the dash-dotted line is the approximate non-linear theory of Synolakis (1986), the triangles are experimental data at $h_0 = 21.51cm$.

5.11 shows that wave breaking limits the relative wave height of non-breaking waves for which either of the two theories can be applied. The limit of relative wave height for wave breaking on run-up is defined here as:

$$H/h_0 = 0.8183(cot\beta)^{-10/9} \tag{5.5}$$

from the theoretical analysis of Synolakis (1986) by considering the Jacobian of the Carrier and Greenspan (1958) transformation. Combining this expression with Eq. 3.55 gives the "breaking limit" curve presented in Figure 5.11. At wave breaking

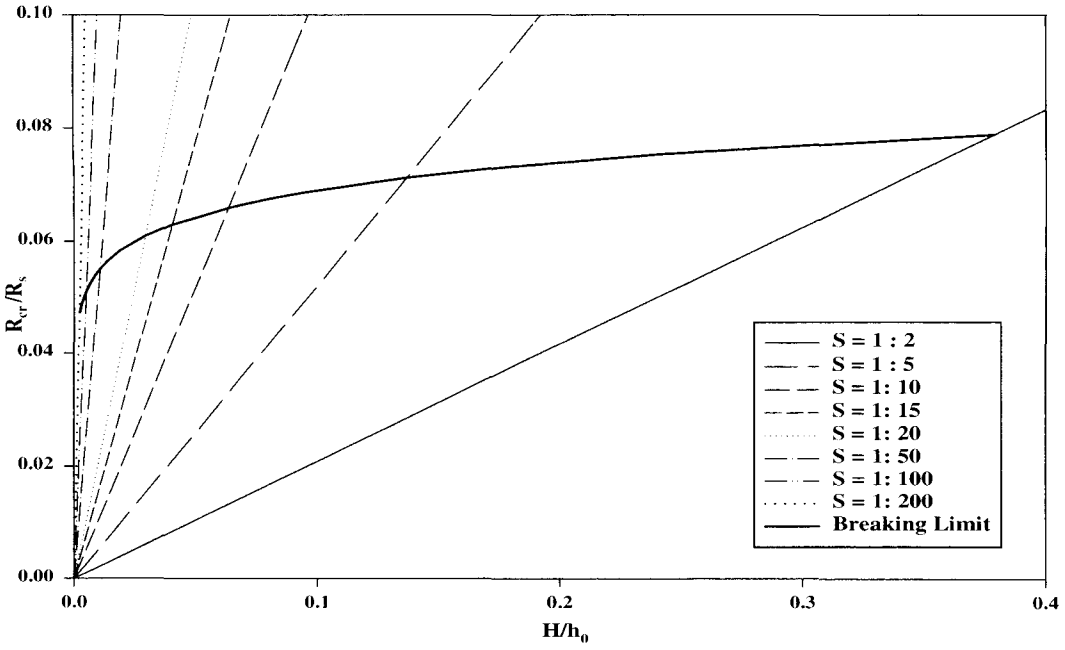

Figure 5.11: The variation of the ratio of R_{cr} to R_s as a function of the relative incident wave height and beach slope. The limit due to wave breaking suggested by Synolakis (1986) is shown also.

the non-linear correction term varies from only about 5% to 8% for slopes from 1:200 to 1:2, respectively. However, as mentioned earlier, the approximate formulas underestimate the maximum run-up; therefore, the correction by the present non-linear theory is somewhat larger than that predicted by Figure 5.11. The magnitude of the correction term is also determined by the breaking limit used. If a weaker breaking limit is adopted, larger correction can be expected. The approach presented here sheds light on the influence of both slope and relative wave height on the highly non-linear run-up process. Nevertheless, for practical engineering problems the approach of Synolakis (1986) appears to be sufficient to predict the maximum run-up of non-breaking solitary waves.

5.2.4 Energy Transformation in the Run-Up Process

One goal of the present research is to investigate the energy transformation and energy dissipation during the solitary wave run-up process, especially for breaking solitary waves in order to predict the maximum run-up from the energy considerations alone. In this section, the energy transformation associated with non-breaking wave run-up will be discussed. For the non-breaking solitary wave run-up, since the wave shape and velocities are continuous for the run-up and run-down process, the total energy of the wave should be conserved. Any energy loss due to the viscous effects on the free surface and wave tank bottom which are generally small will be neglected here. This will be verified and discussed later in the discussion of energy consideration associated with breaking waves.

The numerical scheme developed in Chapter 3 is based on the non-linear shallow water equations which is a depth-averaged model. This means the variation of the horizontal velocities in the vertical direction is zero over the water depth. Thus, the energy computation is greatly simplified. The kinetic energy, E_K, and potential energy, E_P, can be obtained from the following expressions:

$$E_K = \int_\Gamma \frac{1}{2}\rho(h+\eta)u^2 dx \tag{5.6}$$

$$= \Sigma_{i=1}^{i=N} \frac{\rho}{2}\left[\frac{(\eta_i + h_i) + (\eta_{i-1} + h_{i-1})}{2}\right] u_i^2 \delta x$$

$$E_P = \int_\Gamma \frac{1}{2}\rho g(h+\eta)^2 dx \tag{5.7}$$

$$= \Sigma_{i=1}^{i=N} \frac{\rho g}{2}\left[\frac{(\eta_i + h_i) + (\eta_{i-1} + h_{i-1})}{2}\right]^2 \delta x$$

where Γ is the length of the computation domain as in Chapter 3, δx is the grid size in x direction, and N is the total number of the grids. Adding the potential energy and kinetic energy together, the total energy of the wave can be obtained.

Performing this calculation during each time step of the numerical simulation, the energy transformation and the conservation of energy during the run-up and run-down process can be investigated. In the following discussion, the energy and volume were non-dimensionalized by the following parameters:

$$E^* = \frac{E}{\rho g h_0^3} \qquad V^* = \frac{V}{h_0^2} \tag{5.8}$$

(It is assumed that width section in the direction of the wave crest is unity thus, the non-dimensionalized parameters used above are one order less than that for a three-dimensional problem.)

The variation of the calculated energy of a solitary wave with normalized time is presented in Figure 5.12 for H/h_0=0.163 and a slope 1:2.08. The corresponding variation of energy for a solitary wave with a wave height H/h_0=0.025 on a slope 1:15 is presented in Figure 5.13. Both of these cases are for non-breaking solitary waves. As the waves move toward the slope, the wave shape deforms as the depth decreases; this has been described before. During the run-up process the kinetic energy decreases and transforms to potential energy. This can be seen clearly in Figures 5.12 and 5.13.

For the non-breaking wave run-up on 1:2.08 slope, as the wave reaches the maximum run-up position, the potential energy reaches a maximum and the kinetic energy goes to zero. This result will be used in the development of an energy balance model later in this chapter. After that, during the run-down process, the potential energy begins to transform to kinetic energy with the kinetic energy being equal to the potential energy for $t^* > 13$. During the whole process, both the total energy and total volume are constant which means the mass and the energy are conserved. (Small oscillations in volume are found numerically especially during the run-down process. In the calculations, linear accuracy methods were used to calculate the energy and

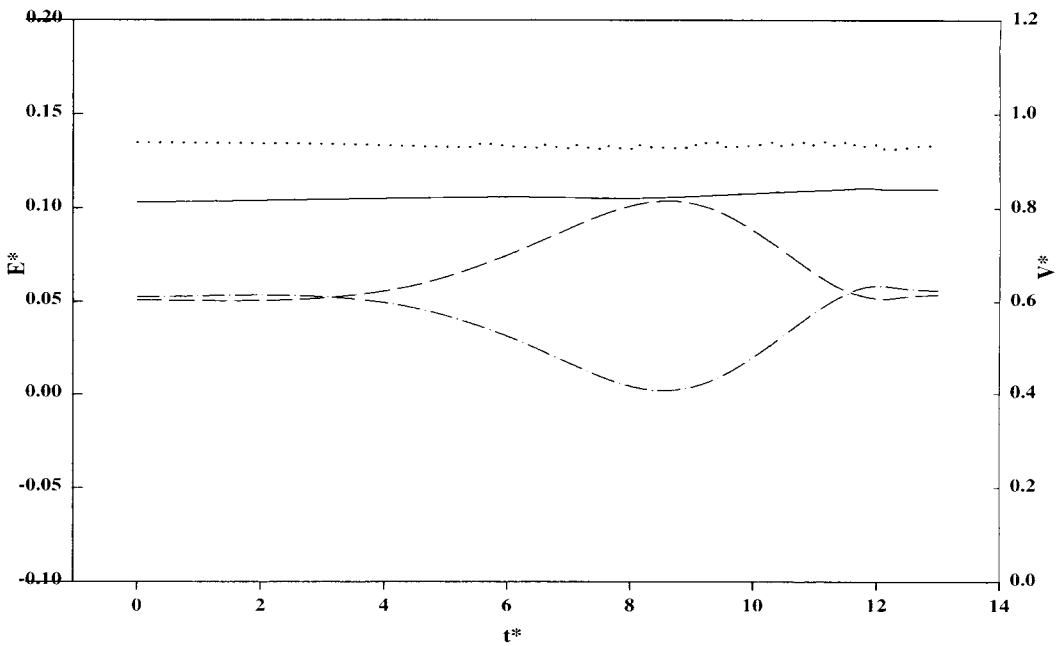

Figure 5.12: Calculated normalized energy of non-breaking solitary wave run-up with H/h_0=0.163 on 1:2.08 slope as a function of normalized time. The solid line is the total energy associated with the wave, the dashed line is the potential energy, the dash-dotted line is the kinetic energy, and the dotted line is the volume of the wave.

volume for efficiency of the computing. If higher-order methods had been used, this oscillation should be avoided.)

For the non-breaking wave run-up on 1:15 slope shown in Figure 5.13, a relatively large variation in volume calculation was found, and the computed kinetic energy at the maximum run-up, i.e., $t^* \approx 40$, was at a small positive value and not equal to zero, which suggested either a small reflective wave may exist in the computing domain, or the wave still has a small water particle velocity. Nevertheless, considering the balance between kinetic energy and potential energy at the time of maximum run-up, neglecting the kinetic energy at that time seems reasonable.

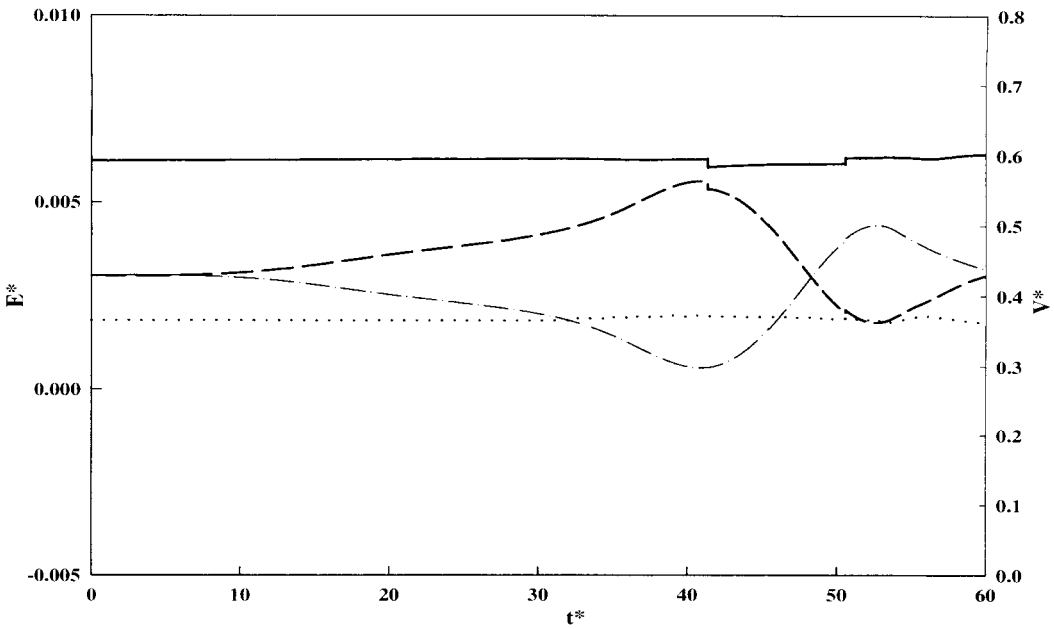

Figure 5.13: Calculated normalized energy of non-breaking solitary wave run-up with H/h_0=0.025 on 1:15 slope as a function of normalized time. The solid line is the total energy associated with the wave, the dashed line is the potential energy, the dash-dotted line is the kinetic energy, and the dotted line is the volume of the wave.

5.3 Breaking Solitary Wave Run-Up

This section describes results for the run-up of breaking solitary waves on plane beaches. For the two gentle slopes used in this study, 1:15 and 1:19.85, the incident solitary wave breaks even for a very small wave height, i.e., $H/h_0 \approx 0.04$. Experimental results for the wave breaking characteristics such as: wave shape, shoaling, wave celerity and, for the plunging breaker, the shape of the jet produced are presented and compared with numerical results. The experiments show that the wave breaking process is such a complicated process that even sophisticated numerical models

cannot model its details. On the contrary, if only the run-up process and maximum run-up are of interest, the wave produced after breaking can be simplified as a propagating bore which is analogous to the shock wave in gas dynamics as described in Chapter 3. The numerical results from the non-linear shallow water wave theory and the WENO scheme will be presented and compared to the experimental results in this section.

5.3.1 Wave Breaking Characteristics

5.3.1.1 Wave Shape

Several types of breaking waves have been reported by other researchers: spilling, surging, collapsing, and plunging breaking. For the slopes used in this study, most of the waves break as plunging breakers. A photograph of a breaking solitary wave for an incident relative wave height of $H/h_0 = 0.30$ is shown in Figure 5.14. This picture clearly shows the shape of the wave after the breaking point (the breaking point is defined here as when the front face of the wave crest becomes vertical.) The tip of the jet formed by the post-breaking wave has touched the front face of the wave already in Figure 5.14.

Figure 5.15 and Figure 5.16 show the evolution of the solitary wave during the breaking process for incident wave heights of $H/h_0 = 0.30$ and $H/h_0 = 0.45$, respectively. Both experimental results and numerical results are shown; the latter are from Grilli et al. (1997) and will be discussed presently. A portion of this section is taken from the discussion by Li and Raichlen (1998) of the paper by Grilli et al. (1997). The experimental results were obtained from high-speed video recordings. The high-speed video camera used (described in Chapter 4) operated at 250 frames per second; this provided the required spatial and time accuracy needed. Due to the limited

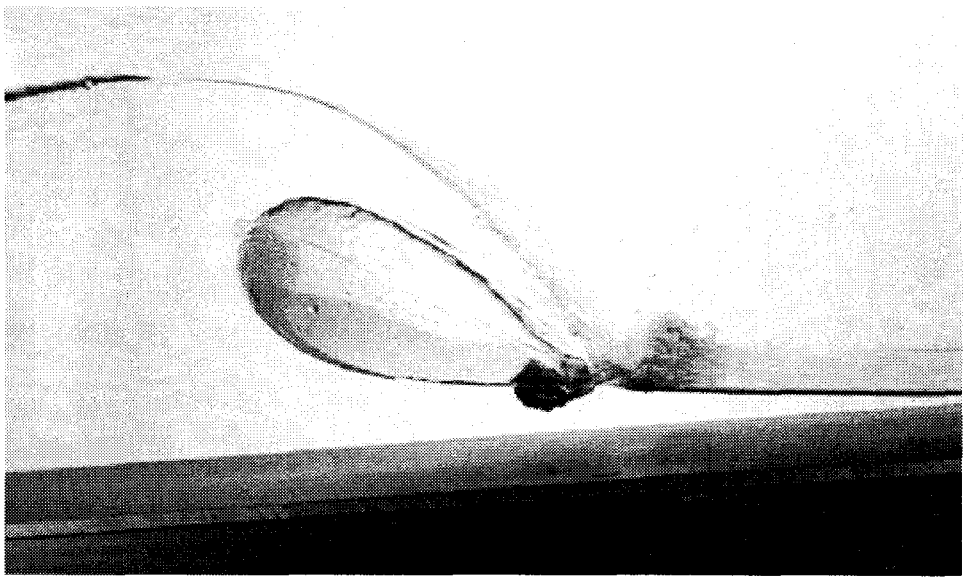

Figure 5.14: Photograph of a typical plunging breaking wave with beginning splash-up

data storage of the high-speed video camera and hence the recording time available, i.e., 2.1 seconds, it was necessary to repeat each wave several times with the camera moved to cover the complete wave breaking process. Since the wave generation system is very reproducible, i.e., the amplitudes of the waves generated during consecutive runs differ by only about 1% , this procedure is acceptable. The images from the high-speed video were calibrated to minimize distortion and error associated with the optical measurement method and the wave shape was obtained from the images using standard image processing method. The development of the plunging breaking wave is shown clearly in these figures. As the solitary wave propagates on the slope, the shape appears quite asymmetric and the front face of the wave steepens reaching a vertical slope which marks the beginning of the breaking process. From this point, a water jet is formed at the crest of the plunging wave, and this jet is projected forward until it impinges upon the leading portion of the wave, the still water region ahead, or the "dry" slope depending on the initial wave height of the incident solitary wave and

the slope investigated. These define where the wave breaks relative to the original shoreline. The shape and trajectory of the jet after breaking have implications with regard to the ingestion of air and production of turbulence in the breaking process; these free surface characteristics were measured carefully in the experiments.

The numerical results from Grilli et al. (1997) using a two-dimensional fully non-linear potential flow wave model (FNPM) are also shown in Figure 5.15 and Figure 5.16 to compare with the experimental results. The numerical model was solved by the Boundary Element Method (BEM) and the calculation was carried up to the point where the jet touches the water ahead. After that point since a singularity forms at the jet contact point the computing has to be terminated. The normalized time for each case is shown in the figure also where $t^* = t\sqrt{g/h_0}$. To compare with the numerical results of Grilli et al. (1997), the origin of time is chosen when the crest of the wave is at the toe of the slope. (This is different from that used in the earlier discussion where the time origin was set as the time wave crest was located one-half of the characteristics length of solitary wave ($L/2$) from the toe of the slope.) Also, Grilli et al. (1997) chose the toe of the slope as the origin of the x coordinate, and positive x was directed shoreward. In the following, this coordinate system is adopted to present the experimental results from the present study in order to compare directly to the numerical results of Grilli et al. (1997). In both Figure 5.15 and Figure 5.16 it is seen that the experimental wave profiles after breaking tend to lag that predicted by the numerical model for the same non-dimensional times, t^*. This may due to the influence of bottom and sidewall friction in the experiments, which are neglected in the inviscid non-linear theory.

In Figure 5.17 and 5.18 the shapes of the jet for the times when the tip of the jet nearly touch the front face of the wave are shown in detail for $H/h_0 = 0.30$ and $H/h_0 = 0.45$, respectively. It can be seen that the jet from the experiments is different

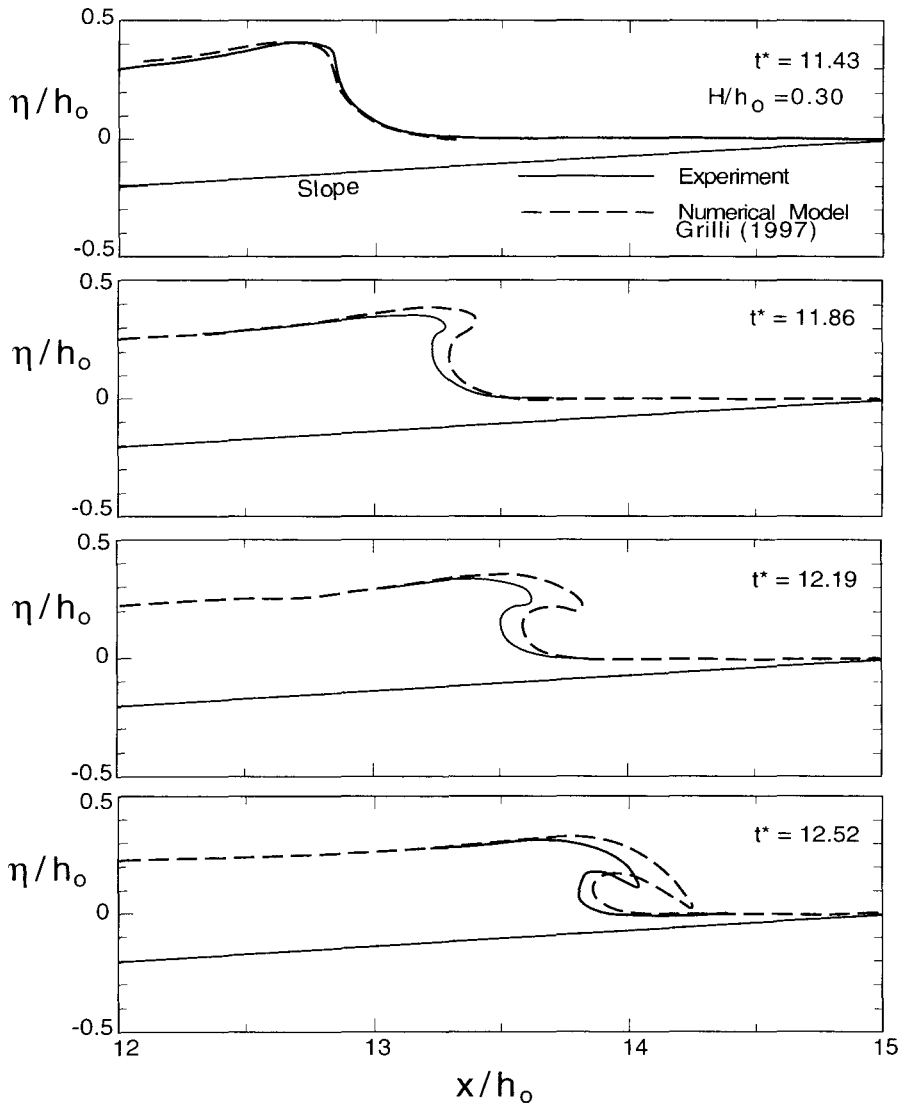

Figure 5.15: Comparison of breaking and post-breaking wave shape obtained from high-speed video and from numerical results of Grilli et al. (1997) for $H/h_0 = 0.30$. The solid line is the experimental results and the dashed line is the numerical results.

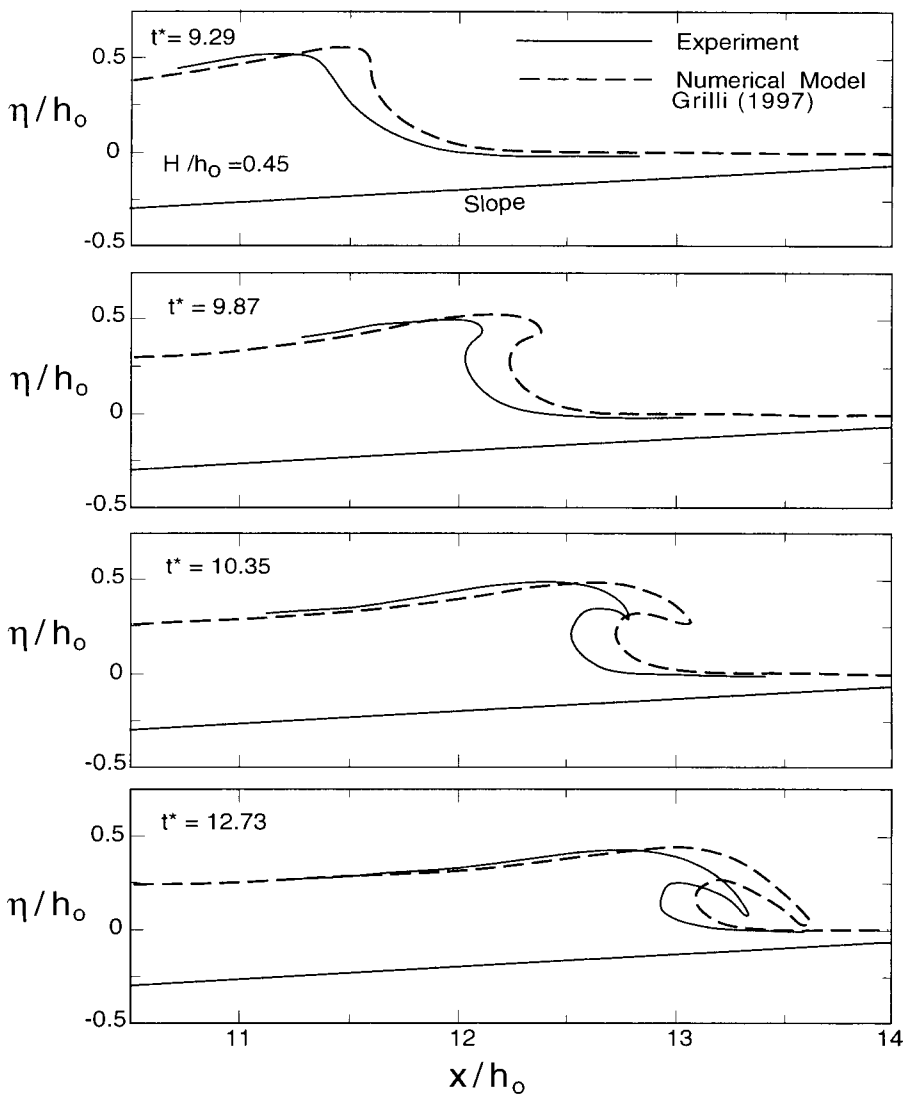

Figure 5.16: Comparison of breaking and post-breaking wave shape obtained from high-speed video and from numerical results of Grilli et al. (1997) for $H/h_0 = 0.45$. The solid line is the experimental results and the dashed line is the numerical results.

from that in numerical results near the location of jet impact. The experimentally defined jet is considerably thinner than its numerical counterpart. In Figure 5.19 the jet shape obtained from experiments is presented for $H/h_0 = 0.45$ for a non-dimensional time chosen such that the location of the tip of the jet is approximately the same as that in numerical results. This corresponds to time shift of about $\delta t^* = 0.183$ and the time in the experiments is $t^* = 12.913$ instead of 12.73 used in the numerical results. When compared this way, the trajectories of the jet are similar but the jet thickness from the experiments is generally about one-half of that obtained from the numerical simulation. This difference shows that even after solving a fully non-linear numerical model it is difficult to define the location and details of the free surface.

The variation of the ratio of the local wave height to the incident wave height at the constant depth portion of the wave tank, H'/H, is plotted in Figure 5.20 as a function of the ratio of the depth in the constant portion of the tank to the local depth, h_0/h, for both the experiments and the numerical results of Grilli et al. (1997). The region investigated in the experiments is from the shoaling region just before breaking to a relative distance $x/h_0 = 13.83$ for $H/h_0 = 0.3$, and to $x/h_0 = 13.89$ for $H_0/h_0 = 0.45$. As before, the experimental results were obtained from a frame-by-frame analysis of the high-speed video. Since the crest of the wave is often somewhat flat after wave breaking, a relatively large error may exist in defining the position of the crest. Nevertheless, in both cases the agreement between the experiments and the numerical theory for the shoaling, maximum wave height at breaking, and the general collapse of the wave is very good. These good agreements demonstrate that although the details of wave breaking are not possible to model, the global parameters such as wave shoaling curve, and the wave profile outside of the breaking area can be obtained relatively accurately. This "macro agreement" past breaking will be revisited in the

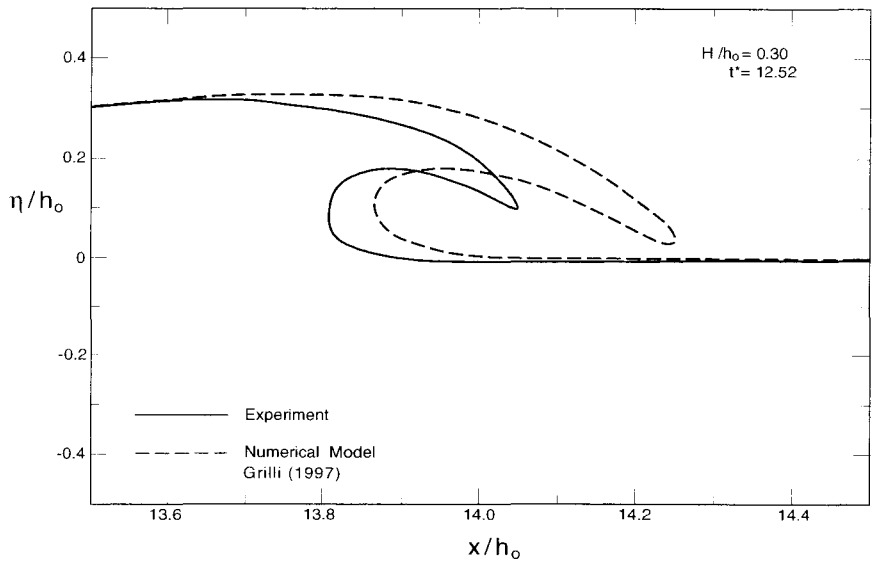

Figure 5.17: Detailed comparison of breaking jet obtained from high-speed video and numerical result at time of impact of jet in front of wave for $H/h_0 = 0.30$. The solid line is the experimental results, the dashed line is the numerical results from Grilli et al. (1997).

section that discusses the run-up of breaking and broken waves.

5.3.1.2 Geometry of the Jet

With plunging breaking waves, the water jet projecting ahead of the wave can cause turbulence, energy dissipation, and the entrainment of the air bubbles when it impacts the water surface. To gain more knowledge of the characteristics of the plunging jet, the geometry of the jet for one case was also measured in the experiments. The incident wave height of the solitary wave investigated was $H/h_0 = 0.30$,

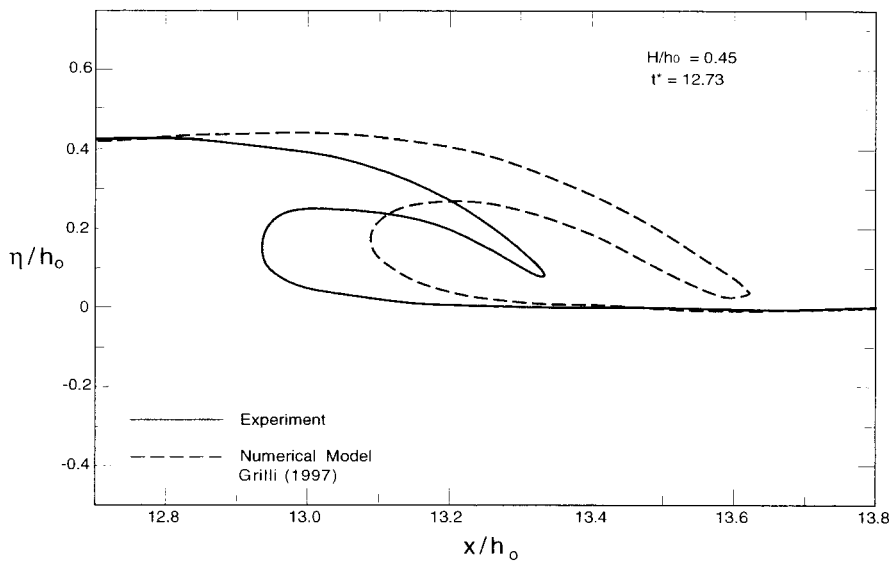

Figure 5.18: Detailed comparison of breaking jet obtained from high-speed video and numerical result at time of impact of jet in front of wave for $H/h_0 = 0.45$. The solid line is the experimental results, the dashed line is the numerical results from Grilli et al. (1997).

the bottom slope was 1:15. A schematic drawing of the jet of a plunging breaking wave is illustrated in Figure 5.21. Three parameters were used to define the jet: (i) The trajectory of the tip of the jet. This trajectory will define the motion and location of the jet and the impact point. The distance between the tip and the breaking point with respect to the constant water depth seaward of the slope, i.e, $((x_b - x_t)/h_0, y_t/h_0)$ was used to represent the trajectory. (ii) The length and thickness of the jet before impingement. The length of the jet L_1 was defined as the horizontal distance from the tip of the jet to the nearest location of the wave surface which was vertical, as shown in Figure 5.21. Two parameters were used to define the thickness of the jet;

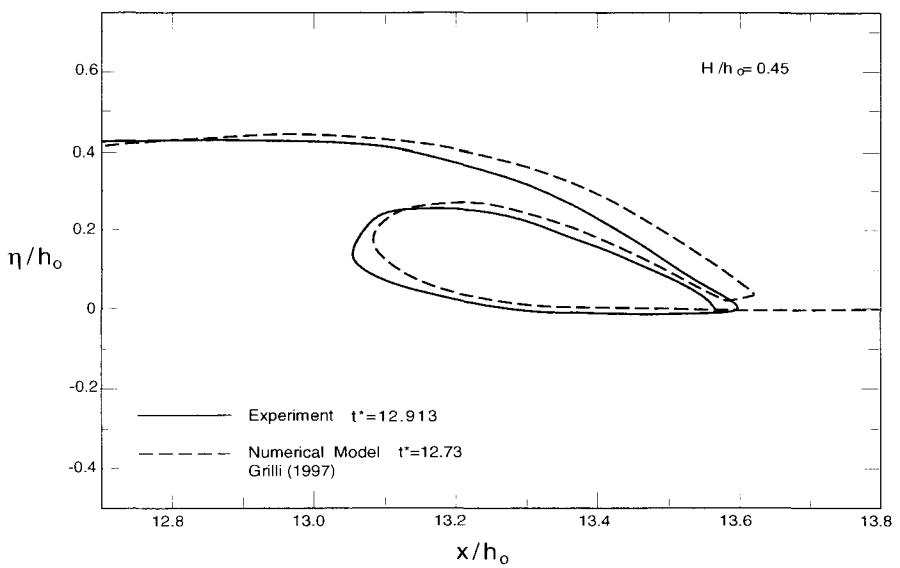

Figure 5.19: Detailed comparison of breaking jet from numerical result to experimental shape after shifting the latter by $\delta t^* = 0.183$ at time of impact of jet on front of wave for $H/h_0 = 0.30$. The solid line is the experimental results, the dashed line is the numerical results from Grilli et al. (1997).

one is the thickness of the jet at the wave vertical plane, i.e, L_2, the other is the thickness of the jet at half length of the jet, i.e, L_3. These two variables not only describe the thickness of the jet but they also show how the thickness changes at different locations. (iii) The horizontal impinging velocity of the jet. This can describe "the strength of the impingement", i.e., how strong the momentum exchange happens at the impingement point.

Figure 5.22 shows the trajectory of the tip of the impinging jet. In the Figure 5.22 a curve which is denoted as the "free-falling" curve as simply the trajectory of a free-falling jet is also shown. The initial horizontal velocity of the free-falling jet is

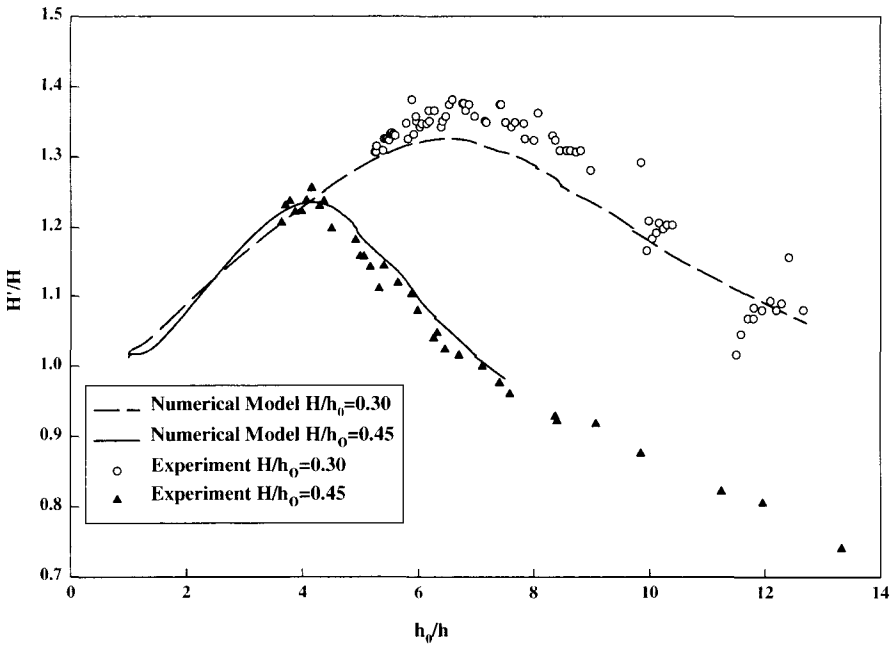

Figure 5.20: Comparison of variation relative wave height on slope H'/H to the relative water depth h_0/h from experiments and from numerical results. The circles are the experimental results for $H/h_0 = 0.45$, the triangles are the experimental results for $H/h_0 = 0.30$, the dashed line is the numerical results from Grilli et al. (1997) for $H/h_0 = 0.45$, the solid line is the numerical results from Grilli et al. (1997) for $H/h_0 = 0.30$.

chosen to be the wave celerity in the constant depth region seaward of the slope, and the initial jet tip position was chosen from the experiment. The assumption is made here that the water particle velocity at breaking is essentially equal to the wave speed just before the wave propagates up the slope. Thus, the trajectory can be described as:

$$y_{th} = -\frac{g}{2}[\frac{x_{th} - x_{t0}}{c_{th}}]^2 + y_{t0} \tag{5.9}$$

where (x_{th}, y_{th}) is the theoretical location of the tip according to free-falling assump-

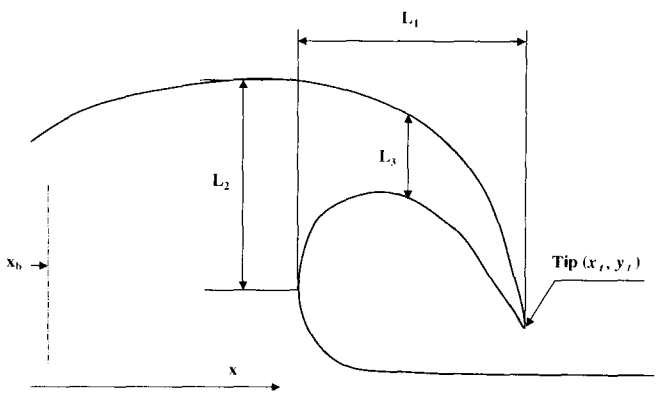

Figure 5.21: Definition sketch of the jet produced by the plunging breaking wave

tion, (x_{t0},y_{t0}) is the initial jet tip location from experiments, and $c_{th} = \sqrt{g(h_0 + H)}$ is the theoretical wave celerity in the constant depth region. The good agreement between the experimental results and the free-falling curve shows that once the water jet is propelled from the breaking wave, the trajectory is the same as that of a free-falling jet, until it impinges on the free surface. To verify this result, the horizontal velocity of the jet tip was also calculated from the high-speed video images, and is shown in Figure 5.23 as a function of the jet location with respect to the breaking point $(x_b - x_t)/h_0$. The horizontal velocity was computed by dividing the distance between the x coordinate of the tip in consecutive images by the time interval between frames. Because of the limits of the spatial and time accuracy of the high-speed video, the velocity data obtained this way have a relatively large variation, especially when the tip of the jet is close to the free surface. The shape of the tip makes the measurement of the tip location difficult. Large variation also exists at the initial stage of the jet because the jet dimension is very small and the error associated with obtaining the

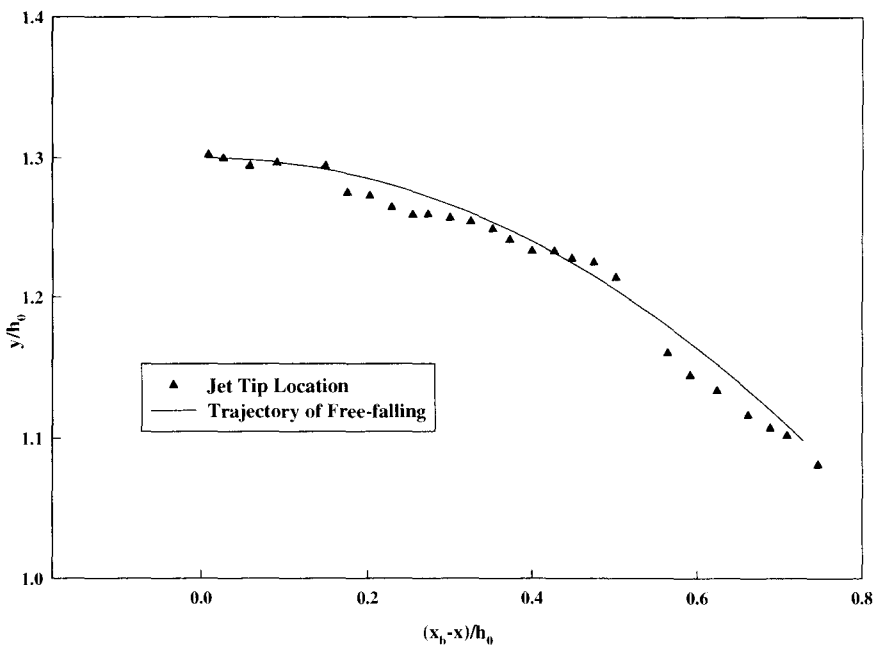

Figure 5.22: Trajectory of the tip of the jet produced by the plunging breaking wave. The triangles are the experimental results, the solid line is the fitted free-falling curve.

jet tip location from the video images is relatively large. Nevertheless, it seems that the horizontal velocity of the jet tip is almost constant over most of the jet trajectory. The theoretical wave celerity c_{th} described above is also shown in the Figure 5.23. The results suggest that the wave velocity at breaking is of the same order as the wave celerity in the constant depth region offshore. This has been pointed out by other researchers, for example, Skjelbreia (1987).

The water velocity V_m and the angle of impact of the jet trajectory, θ_m, at impingement can be derived from the free-falling jet trajectory. If we assume the maximum height of the wave at breaking is H_b measured from the free surface where impact will take place, the wave breaking velocity is $V_b \approx c_{th}$, the impingement velocity and

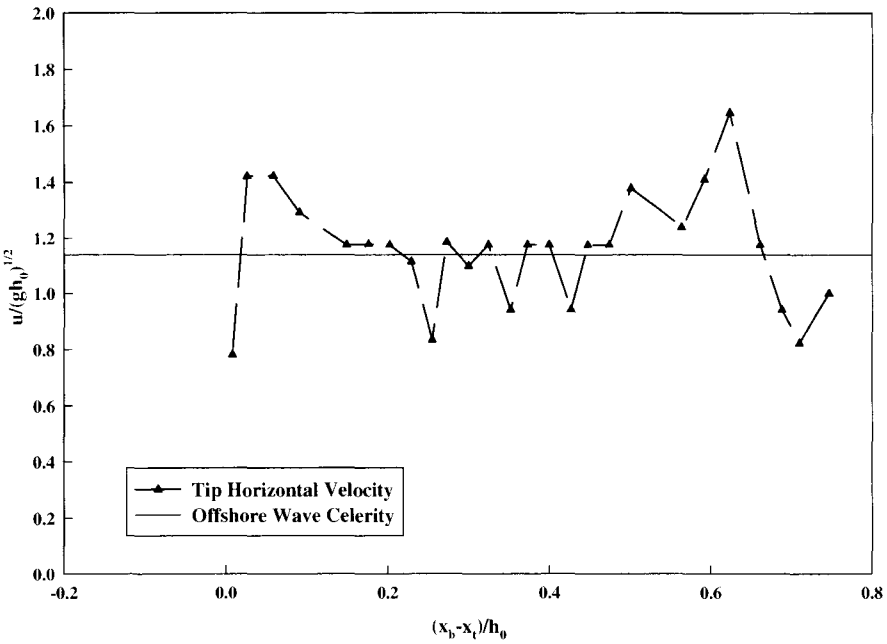

Figure 5.23: Horizontal velocity of the tip of the jet produced by the plunging breaking wave. The triangles with the dashed line are the experimental results, the solid line is the theoretical wave celerity of the incident solitary wave in the constant depth region.

angle is:

$$V_m = \sqrt{c_{th}^2 + 2gH_b} \tag{5.10}$$

$$\theta_m = \arctan[\frac{c_{th}}{\sqrt{2gH_b}}] \tag{5.11}$$

The length of the jet with respect to the distance between the location where the wave crest breaks, i.e., x_b, and the location of the tip, x_t, is shown in Figure 5.24. It was seen that the length of the jet increases linearly as the plunging breaking wave and the jet propagates on the slope. A linear curve from linear regression analysis is

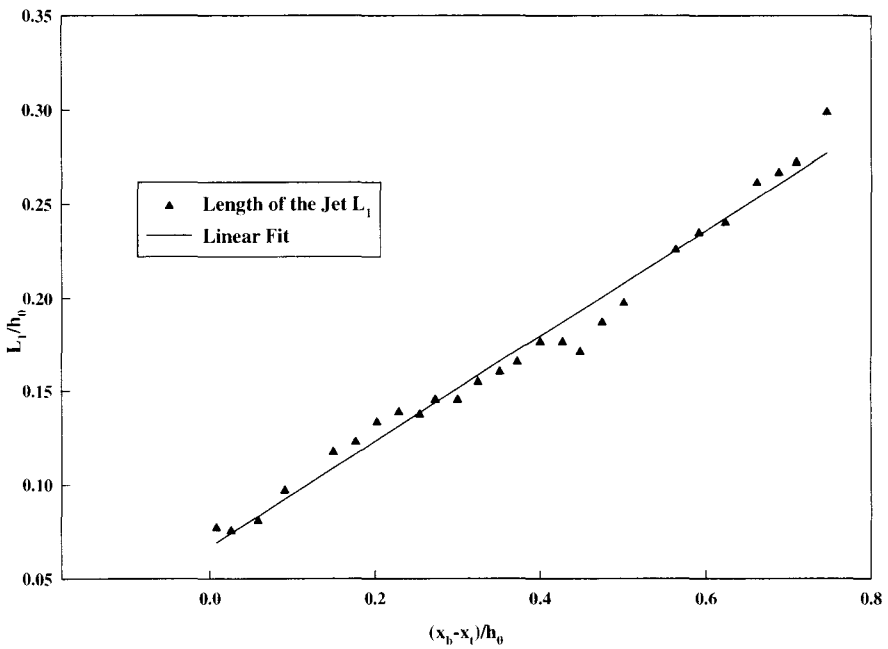

Figure 5.24: Horizontal length of the jet produced by the plunging breaking wave. The triangles are the experimental results, the solid line is the fitted curve from a linear regression analysis.

also presented in the figure as the form:

$$\frac{L_1}{h_0} = 0.282[\frac{x_b - x_t}{h_0}] - 0.067 \tag{5.12}$$

Since the velocity of the water jet tip is constant from above analysis, the wave celerity of the plunging breaking wave is less than the jet tip velocity at the order of incident wave height (0.282) from the linear regression analysis.

The thickness of the jet at the middle of the jet and the thickness of the jet at the location that the plunging wave surface becomes vertical are shown in Figure 5.25. It can be found from the experiments that both these measurement for the jet thickness

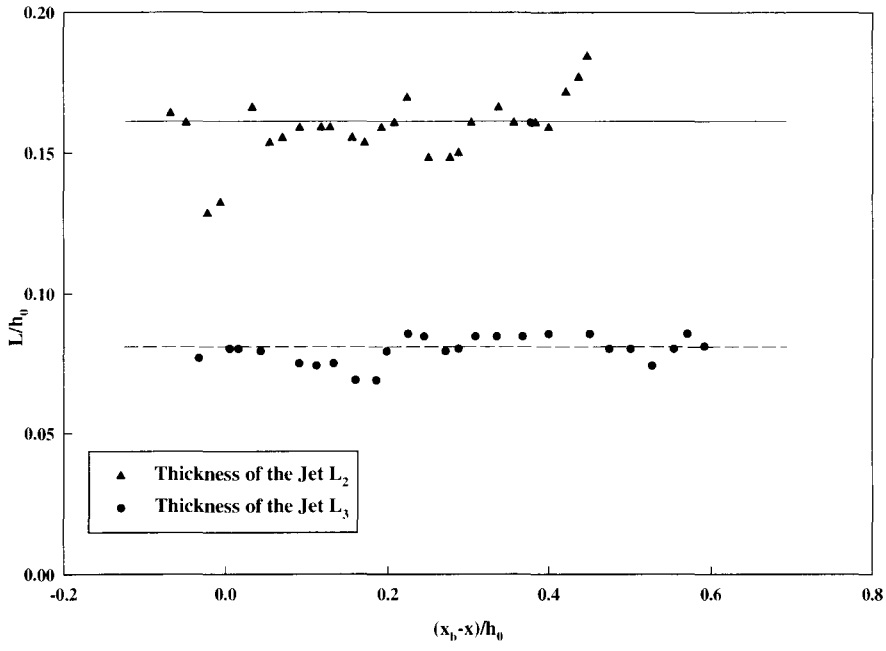

Figure 5.25: Thickness of the jet produced by the plunging breaking wave. The triangles are the experimental data for L_2, the circles are the experimental data for L_3. The solid line and dashed line are the fitting curves from linear regression analysis for L_2, L_3 respectively.

are almost constant. The thickness of the jet at the middle length, i.e, L_3, is about half of that at the base of the jet L_2.

The overall geometry of the impacting jet produced by the plunging breaking wave was measured accurately during the experiments. These geometric parameters which describe the jet associated with the plunging breaker can be used to model the jet impingement process perhaps leading to a better understanding of the air entrainment, and the energy dissipation associated with plunging breaking waves.

5.3.1.3 Splash-Up

As the plunging breaker propagates up the slope, the jet propelled from the wave may strike the dry bed of the slope or the water ahead of the wave depending on the incident wave height and the slope of the beach. Figure 1.1 showed the photographs of a case where the jet impinges on the water ahead of the wave. As the jet impinges on the free surface ahead of the wave, a reflected jet is propelled from the impact point and the splash-up process is initiated. The reflected jet appears not to be symmetric with the incident jet as shown in Figure 1.1-(e), but reflects at a angle greater than the incident angle perhaps due to the movement of the jet and plunging wave with respect to the slope. The surface of the reflected jet is not as smooth as the incident jet, and drops can be seen to separate from the splash-up jet. As the incident wave moves toward the shoreline, the shape of the splash-up (reflected) jet changes and curves back toward the incident wave, more and more water was dropped on the incident jet in the form of spray and drops as time progresses. Finally the incident jet breaks up and the whole reflection structure collapses into a turbulent mess with apparent vortex generation. This process can be seen clearly in Figure 1.1-(i),(j).

Shortly after the impingement of the incident jet on the free surface the originally smooth wave surface around the impact point becomes rough, as shown in (d) of Figure 1.1 which suggests that a short wave is generated reversely propagating with respect to the incident wave. The rough area caused by this reversed wave gets larger as the splash-up process continues, and the air entrained into the wave and jet can be seen as the form of the bubbles in the pictures.

The splash-up process described above can be used to explain the generation of the counter-rotating vortex proposed by Skjelbreia (1987). The stage of the reflection process is illustrated in Figure 5.26. In this illustration, the incident jet, reflected jet,

reverse flow under the impingement point, and the motion of the water separated from the splash-up jet are shown diagrammatically. The direction of the flow is represented by the arrows. Three possible vortices are illustrated here: (i) the clockwise vortex formed by the incident jet and the reversed flow under the jet, (ii) the clockwise vortex formed by the reflected jet from the impingement point and the reversed flow generated by the impact of reflected jet on the water, and (iii) the vortex formed by the flow of water separated from the splash-up which falls on the incident jet and the water flow beneath the impingement point. This vortex is counter-clockwise rotating as shown in the sketch and could only be formed if the jet penetrates a significant depth of water before splash-up, which can also be found in Figure 1.1 -(i) and (j) where the complete wave breaking and splash-up process is shown. Initially the amount of spray and drops separated from the splash-up is small and the water depth of impingement is small; thus, the vortex is very weak. When the wave is close to the initial shoreline position, most of the water in the splash-up jet will fall back toward the incident wave, and the strength of the counter-clockwise vortex increases. When the broken wave consisting of the incident jet, the reflected jet, and the plunging wave behind collapses, three "large" vortical structures are left in the flow and finally transform to smaller vortices and show evidence of energy dissipation. This discussion has been primarily qualitative, and the existence of these vortices must be verified by experiments directly using methods such as particle image velocimetry. Skjelbreia (1987) used velocity measurement by Laser Doppler Velocimetry (LDV) to infer the existence of counter-rotating vortices.

If the incident wave height of the attacking solitary wave is small, the wave breaks up the slope near the original shoreline. Thus, the point of impingement of the jet generated by the plunging breaking wave is located on the dry slope rather than on the water surface. In this case, a reflected jet cannot be produced, and the incident

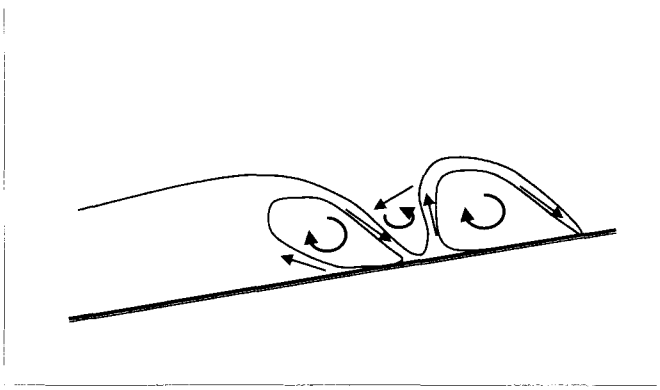

Figure 5.26: The illustration sketch of the vortices generated by the plunging breaking wave

jet and breaking wave behind the jet simply collapse after breaking. A photograph of this kind of plunging breaking is presented in Figure 5.27 (a). For comparison, the case of plunging breaking with splash-up is shown in Figure 5.27 (b).

The reason for the difference between wave breaking with and without splash-up is puzzling, but perhaps it can be explained by considering two simple cases of a moving water jet impinging: (i) on a dry inclined plate or (ii) on the surface of a quiescent pool with a small depth. Because the scale of the jet and its Reynolds number are relatively large, it is reasonable to neglect viscous effects and the effects of surface tension relative to the kinematics and dynamics of the problem. Considering first the case of a moving jet impacting a dry sloping surface, if assuming zero vorticity associated with the jet, one can use potential theory to describe the jet-plate interaction, e.g., see Milne-Thomson (1968). The impingement point, considered as the center of the jet, is a stagnation point that separates the flow running up the slope from that running down the slope. A jet that is reflected from the bottom and directed upward is not

generated and the run-up tongue is simply composed of the water associated with the portion of the jet running up along the slope.

When the plunging jet impacts the surface of a small depth of water, the jet interacts with the original still water surface before reaching the sloping bottom. This physical process is complicated and various vortical motions are generated such as those three types discussed earlier in the small region composed of the plunging jet, the water beneath the impingement point, and the base of the incoming breaking wave. Here only a tentative explanation is proposed to describe this complex process. When the translating jet impacts the water surface it will push a "wedge shape" portion of water that was originally still (zero water particle velocity) forward up the slope to form the run-up tongue. At the same time the momentum exchange between the jet and the water up-slope redirects the jet upward and away from the slope, i.e., prevents it from running along the slope as in the dry slope case. Since the breaking wave and the impinging jet advance shoreward with a relatively large speed (close to the celerity of the wave in the constant depth region), the down-slope force that acts on the jet as it impacts the quiescent region is relatively large and the water associated with it can be deflected upward relatively violently. Thus, the reflected jet and splash-up is produced. (A physical process that may be analogous to this splash-up is how the snow in the path of a snow-plow is deflected forward into the air by the moving plow.)

Considering the difference in the breaking process between the "dry slope" breaking and the case of breaking in a depth of water, the development of vortices would be very different. In the case of plunging breaking without splash-up as shown in Figure 5.27, since no reflected jet generated, one would not expect counter-rotating vortices to be found, but this must be verified by experiments. Also, the energy dissipation and the resulting run-up process must be different in these two cases because of the

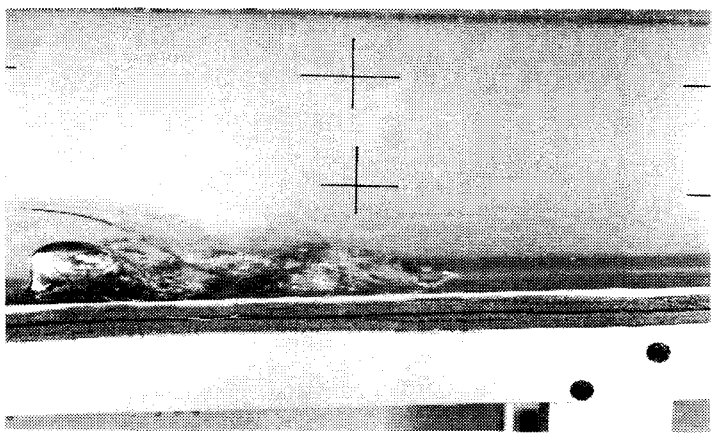

(a)

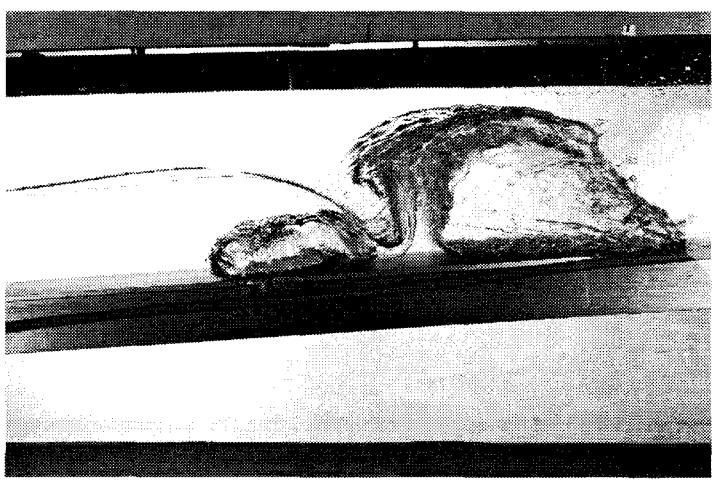

(b)

Figure 5.27: Photographs of two cases of the plunging breaking of solitary waves on 1:15 slope. (a). Plunging breaking without splash-up; $H/h_0 = 0.10$. (b). Plunging breaking with splash-up; $H/h_0 = 0.40$

difference between the impingement processes. This will be discussed later in this chapter when the numerical and experimental run-up results are presented.

5.3.2 Breaking Solitary Wave Run-Up – Comparison with Results from the WENO Scheme

In this section the numerical results from the WENO scheme described in Chapter 3 to treat breaking solitary wave run-up will be presented and compared to experimental results.

5.3.2.1 Wave Amplitude and Velocity Time-Histories

The water surface time-histories at eight different locations for an incident relative wave height $H/h_0 = 0.263$ breaking on a 1:19.85 slope are presented in Figure 5.28. Both the numerical results from the WENO scheme and the corresponding experimental results from the wave probe are shown. The eight locations shown cover the range from the toe of the slope to locations above the initial shoreline position. The scale of the ordinate of each part of the figure is the same so that the relative height of the wave at different locations can be compared easily. It can be seen that as the wave runs up the slope the wave height increases gradually and the front face of the wave steepens because of the non-linear effects. At breaking, the front face becomes vertical, and shoreward of this position the wave height decreases dramatically. The numerical scheme can model this wave shoaling and decaying process well, as the good agreement between the numerical results and experimental results demonstrate. It is noted that at locations close to the initial shoreline position (Figure 5.28 (e) and 5.28 (f)), the numerical scheme predicts a much steeper water surface time-history

than experiments. Since the breaking process is only represented as a sharp discontinuity in the numerical model, this difference is probably due to the over-simplified numerical modeling of the wave breaking process. Also, it has been noted before that in the experiments the existence of the plunging jet and air entrainment associated with the breaking wave can reduce the accuracy of the measurement from the wave probe; this error may also contribute to the disagreement between experimental and numerical results. Zhang (1996) showed by numerical simulation that dispersion effects may be important during the run-down process for non-breaking solitary wave run-up. This statement may also be true for breaking solitary waves, as shown in Figure 5.28 (b)-(d). It is seen that the numerical scheme is relatively poor in treating the run-down process. The numerical results show the existence of a bore propagating away from the slope, but only a somewhat undular reflected wave was recorded in the experiments. During the experiments, it can be found that a "hydraulic jump" is generated near the initial shoreline by the run-down water along the slope, which can be seen in Figure 5.28 (d). The "hydraulic jump" does not propagate and essentially generates the undular reflected wave at the end of the run-down process.

Figure 5.29 shows the water particle velocity time-histories during the run-up process for a relative incident wave height: $H/h_0 = 0.263$. These are the same conditions as shown for the wave amplitude time-histories in Figure 5.28. The velocities were normalized by $\sqrt{gh_0}$ as before. The measurement was at mid-depth. Because of the relatively low sampling rate of the LDV system used for the velocity measurements, velocity measurements for locations above the position of the initial shoreline are not available; only the locations from the toe of the slope to a location near the initial shoreline were sampled. For the location near the toe of the slope, the numerical result agrees well with the experiments. The velocity time history is similar to the original solitary wave shape, which shows the reflection from the slope before the

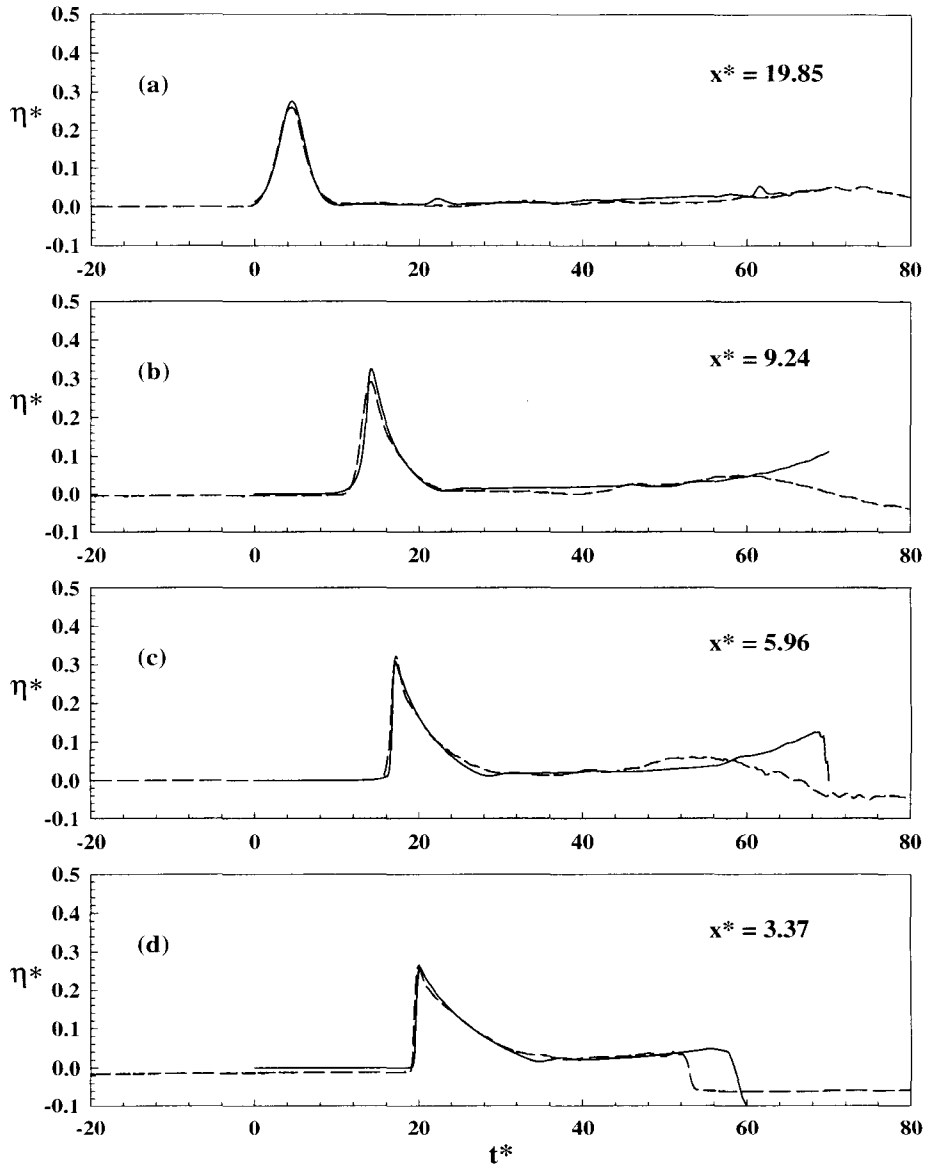

Figure 5.28: (a)-(d) Run-up of solitary wave with $H/h_0 = 0.263$ on 1:19.85 slope. Normalized wave amplitudes are shown as a function of normalized time at different locations. The solid line is the result of numerical simulation, the dashed line is the experimental data from the wave probe.

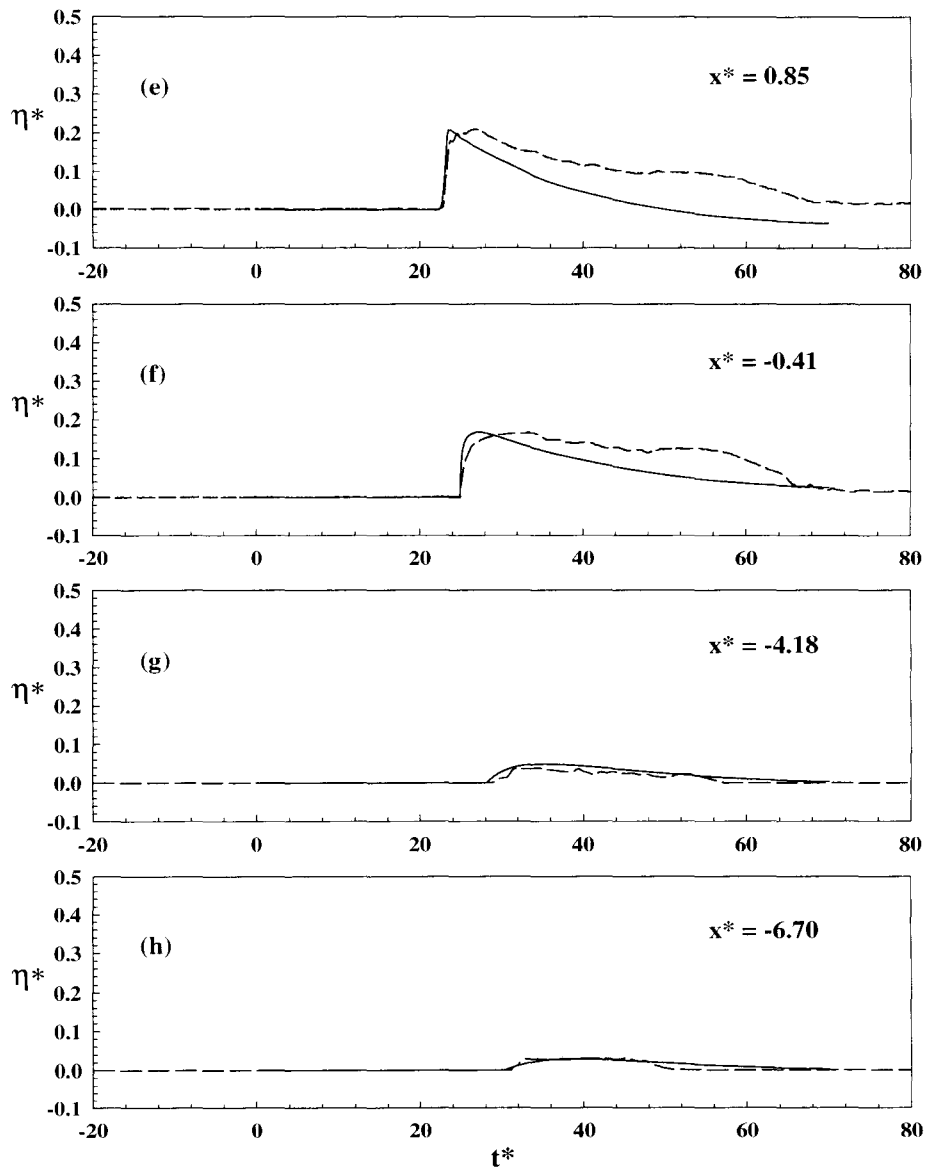

Figure 5.28: (e)-(h) (continued) Run-up of solitary wave with $H/h_0 = 0.263$ on 1:19.85 slope. Normalized wave amplitudes are shown as a function of normalized time at different locations.

run-down process must be small. (This has also been observed from water surface observations by Synolakis (1986).) In the following section this property of breaking solitary wave run-up will be used in developing an energy balance model to predict the maximum run-up.) The numerical simulation overestimates the maximum velocity near that point of wave breaking, as can be seen in Figure 5.29 (b). Just after the wave breaks, experimental data are not available in the breaking region due to the presence of bubbles generated by the plunging jet of the breaking wave. These bubbles obscure and scatter the laser beam of the LDV. Past the breaking point, the "triangular shape" of the variation with time of the breaking wave velocity is seen very clearly both in experimental and numerical results similar to the water surface variation shown in Figure 5.28 (c), (d) and (e). Overall, the numerical results agree well with the experimental except in the region close to breaking. It is obvious that the details of wave breaking are so complex that they cannot be simulated by this simplified shock model.

5.3.2.2 Free Surface Profiles

The water surface profiles, i.e., the water surface elevation variations with distance, for an incident wave height of $H/h_0 = 0.30$ are presented in Figure 5.30 for different non-dimensional times. Figure 5.30 covers the full run-up and run-down process. The numerical results from the WENO scheme presented in Chapter 3 are compared to the experimental data of Synolakis (1986). The experimental results were obtained from a combination of $10 \sim 12$ wave probes, and the variation of the free surface with distance at different times was constructed from the water surface time-histories at various locations. As the wave shoals, the front face becomes steeper compared to the rear face and the shape becomes asymmetrical, see Figure 5.30 (b) and (c). The numerical results clearly show this trend and are confirmed by the experimental

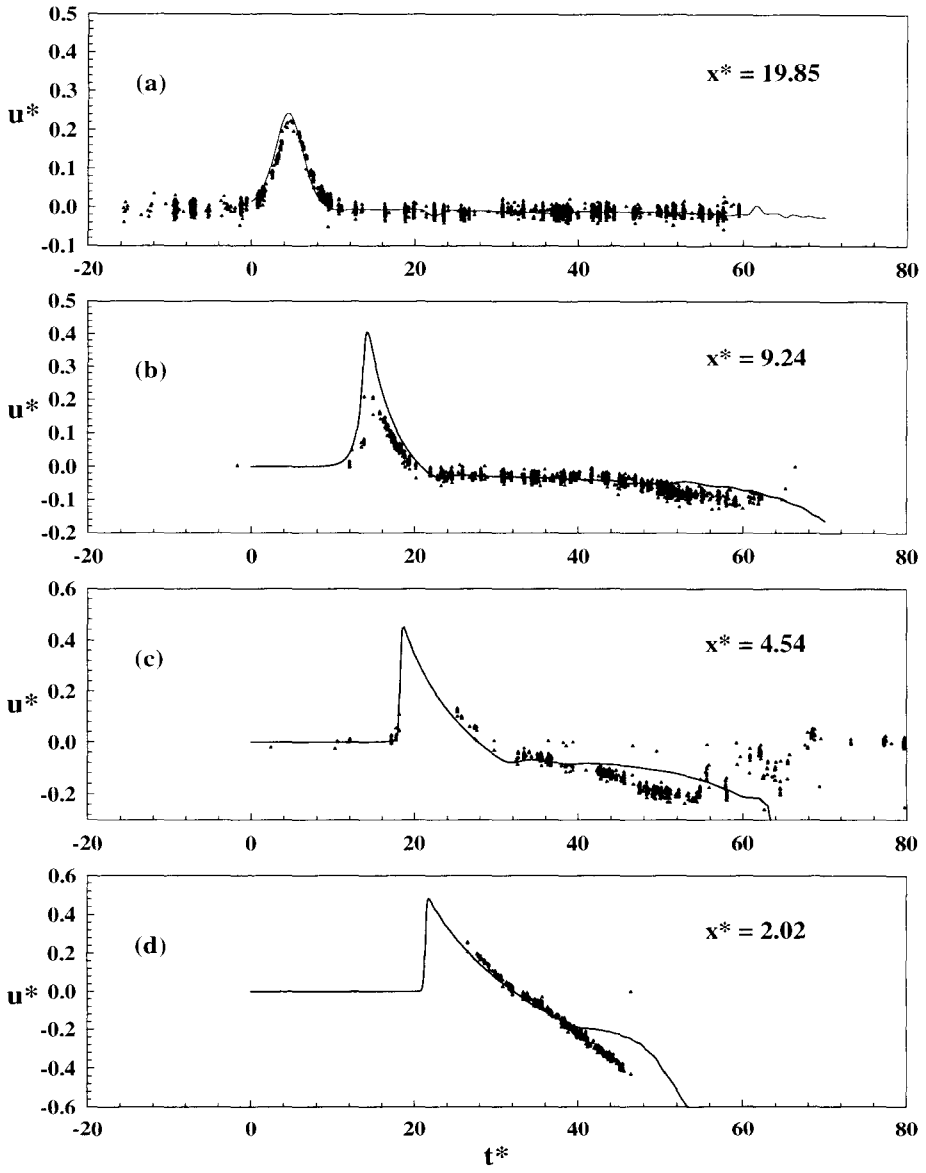

Figure 5.29: (a)-(d) Run-up of solitary wave with $H/h_0 = 0.263$ on 1:19.85 slope. Normalized wave velocities are shown as function of normalized time at different locations. The solid line is the result of numerical simulation, the triangles are the experimental data from LDV.

data. At $t^* = 10$ the numerical results overestimate the maximum height of the wave by about 10%. As time increases, the front face gets steeper and ultimately becomes vertical, this is defined as the breaking point in the numerical model. This occurs for $15 < t^* < 20$. The wave height reaches a maximum value at this time and decreases after the wave breaks. As described before, the wave probe cannot accurately measure the details of the breaking wave front because of the air entrained in the breaking wave. Nevertheless, the shock-like front face of the breaking wave is found in Figures 5.30 (b) and (c). There appears to be a shift in x/h_0 of the front face of the breaking wave between the numerical data and experimental data as seen in Figure 5.30 (c). Considering the violence of the wave breaking process and the simplicity of the numerical model, this shift may either be caused by the over-simplified model or the measurement error associated with the breaking wave or a combination of both.

As the breaking wave propagates up the slope, it collapses near the initial shoreline position and the wave height decreases dramatically. These processes described in section 5.3.1 were found in the experiments, i.e., the jet formation and the creation of the vortices and the splash-up. However away from the front tip of the wave, the shape changes slowly. The physical length of the wave collapse region is around the order of the initial water depth and is small compared to the characteristic length of the solitary wave. This implies that, including the shock structure into the long wave model, the long wave assumptions should still be valid even during the wave breaking process. The favorable agreement between the numerical results and the experimental results found in Figure 5.30 (d) and (e) provides additional support for the shock model. There are some differences between the numerical data and experimental data near the run-up tip shown in Figure 5.30 (g), (h). These discrepancies may be due to the assumption of the hydrostatic pressure distribution in the shallow water

equations as explained by Lin et al. (1999), or simply that the shock model cannot model the details of the complicated process of the jet and the splash-up. The tip effects get smaller and finally disappear as the wave swashes up the slope. The numerical results agree well with the experiments for this stage (Figure 5.30 (e) and (f)). The maximum run-up occurs about $t^* = 37$.

The wave run-down process begins after the wave reaches the maximum run-up. The water retreats as the trailing edge of the solitary wave still propagates toward the slope. This retreating stream interacts with the wave tail and creates a region of large free surface curvature near the initial shoreline position. This interaction develops a "hydraulic jump" near the initial shoreline as seen in Figure 5.30 (j). The hydraulic jump is modeled as a discontinuity (shock) in the numerical method also. The sharp angle of the water surface obtained in the numerical results shown in Figure 5.30 (k) and (l) is not realistic. In the laboratory the front collapses and foam can be found in this region. However, both the position of the jump and the height difference between upstream and downstream are predicted well by the numerical method.

It can be found that the thickness of the run-down stream predicted by the numerical method is smaller than the experimental results. The difference may be due to a systematic error associated with the capacitance wave gages used by Synolakis (1986). When using a wave gage to measure the height of a stream with a significant velocity, the depth measurement is larger than the actual value because the stream tends to run-up on the probe due to the velocity of the run-down stream, this has been discussed in Chapter 4.

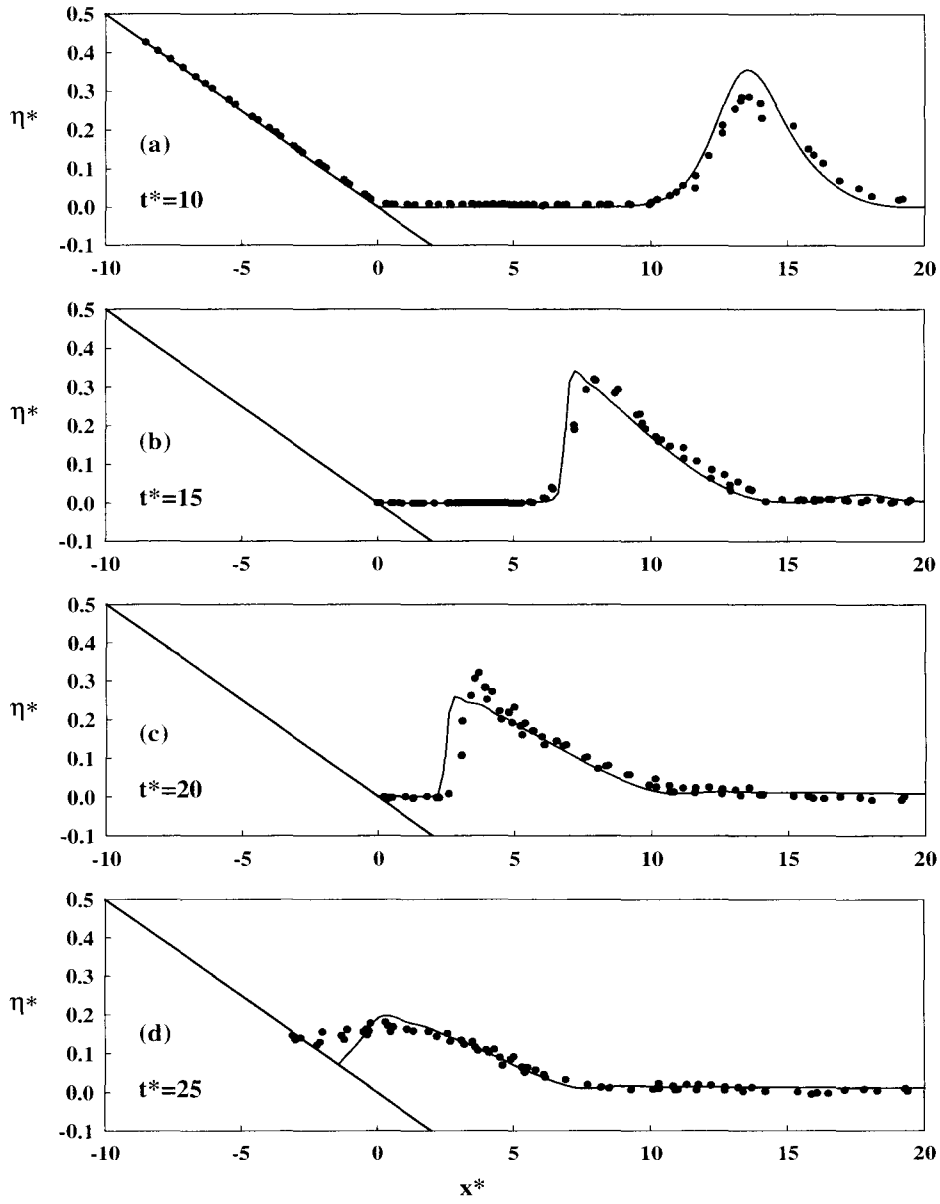

Figure 5.30: (a)-(d) Run-up of solitary wave with $H/h_0 = 0.3$ on 1:19.85 slope. Normalized wave surface profiles are shown as a function of normalized distance from the initial shoreline at different times. The solid line is the result of numerical simulation, the black circles are the experimental data from Synolakis (1986).

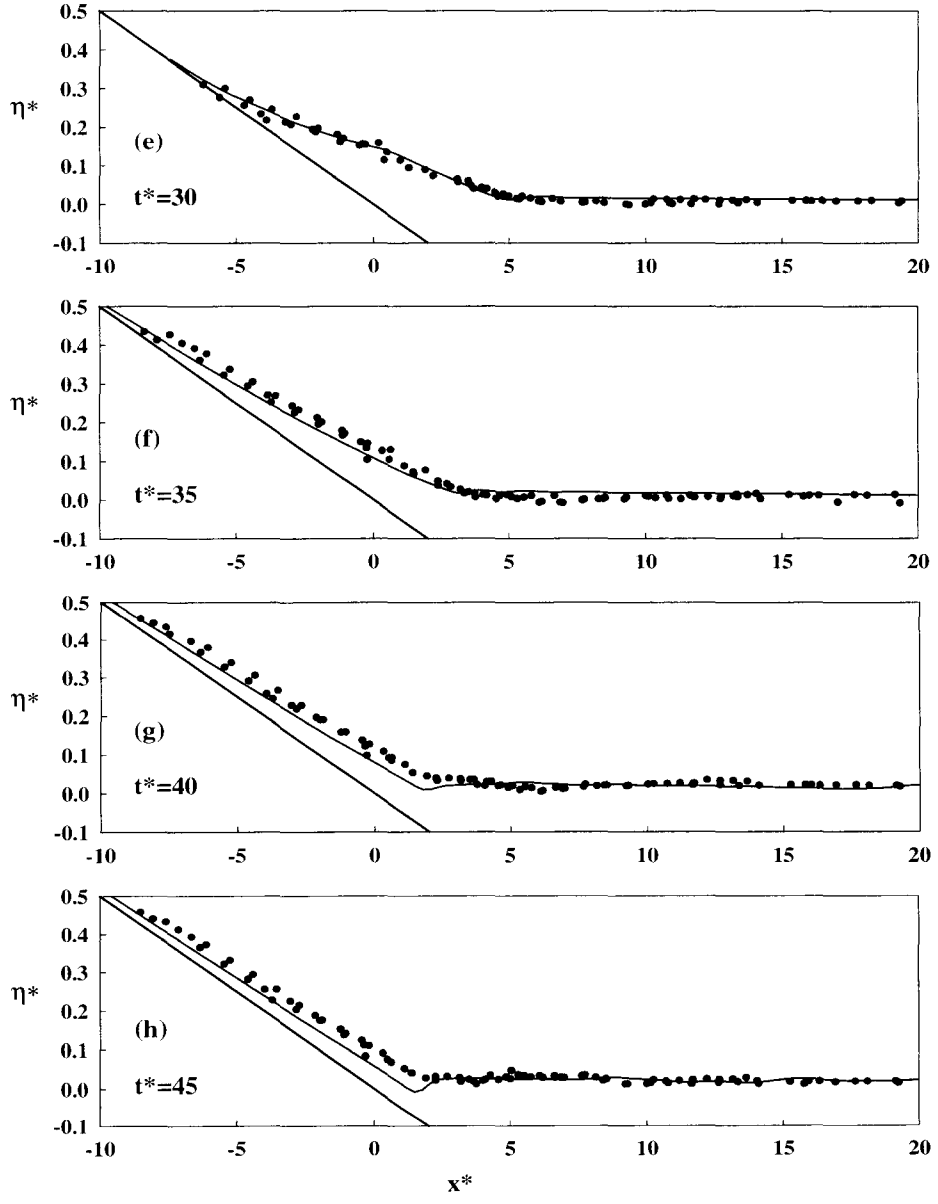

Figure 5.30: (e)-(h) (continued) Run-up of solitary wave with $H/h_0 = 0.3$ on 1:19.85 slope. Normalized wave surface profiles are shown as a function of normalized distance from the initial shoreline at different times.

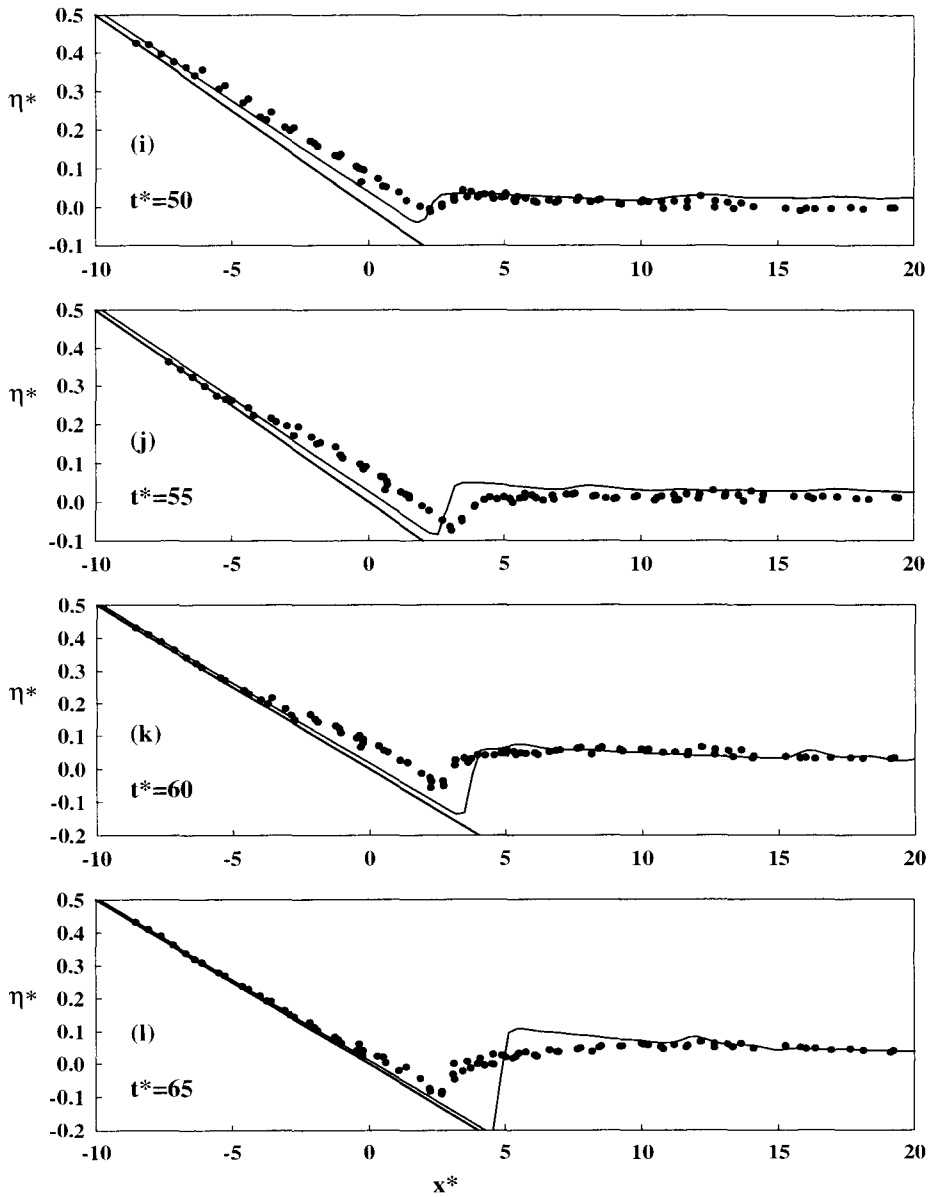

Figure 5.30: (i)-(l) (continued) Run-up of solitary wave with $H/h_0 = 0.3$ on 1:19.85 slope. Normalized wave surface profiles are shown as a function of normalized distance from the initial shoreline at different times.

5.3.2.3 Shoreline Movement and Maximum Run-Up

The normalized run-up is shown as a function of normalized time in Figure 5.31 for a solitary wave with $H/h_0 = 0.30$ on a 1:19.85 slope with the numerical results compared to the experimental results. The experimental data were obtained using the high-speed video camera. As the wave propagates up the slope, the contact line found between the tip of the run-up tongue and the dry slope is used to locate the actual shoreline at different times with the help of a scale attached to the surface of the slope. Because of the limited distance the high-speed video can cover on the slope, the experiment was repeated three times with the high-speed video camera moved to a new location each time. In this way the run-up time-history was recorded up to the maximum run-up. The results from different runs were assembled to give the whole picture of the run-up process. During the run-down process, since the slope was already wet, the contact line was indistinct and almost undetectable in the video recording. Thus, only the run-up phase of the shoreline position is presented. Good agreement was found between the numerical results and experiments which shows that the WENO numerical scheme can simulate the run-up and the shoreline position with relatively high accuracy.

The normalized maximum run-up, R/h_0, is shown as a function of incident wave height H/h_0 in Figure 5.32, 5.33 and 5.34 for three slopes: 1:5.67, 1:15, and 1:19.85 respectively. The experimental data for the 1:5.67 slope are from Hall and Watts (1953), where the solitary wave was generated by the simple impulsive motion of a vertical bulkhead. The experimental data for the 1:19.85 slope came from Synolakis (1986) for initial water depths ranging from 6.25 cm to 38.32 cm. The data for 1:15 slope were measured by the author for the different water depths shown. The wave generation system is the same for Synolakis's (1986) data and author's. Note that the data for 1:15 slope presented are from two wave tanks: the CWT and the CERC

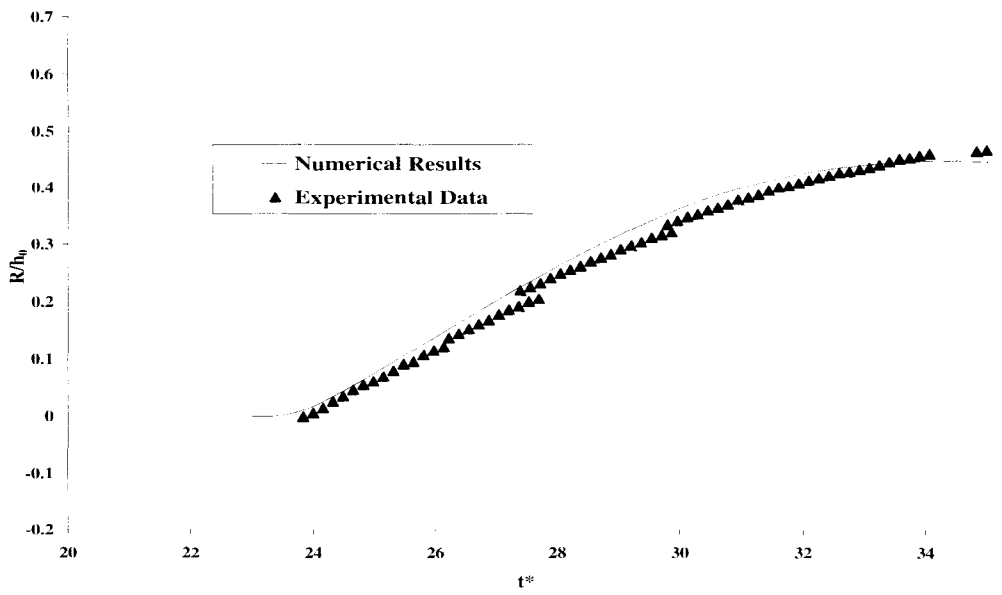

Figure 5.31: Run-up of solitary wave with $H/h_0 = 0.30$ on 1:19.85 slope. The normalized shoreline position is shown as a function of normalized time. The solid line is the numerical results, the circles are experimental data from high-speed video.

tank. These figures show clearly that the maximum run-up is predicted well by the WENO scheme combined with the non-linear shallow wave equations.

It was found in section 5.3.1 that the wave breaking process was quite different with and without splash-up. In figures 5.32 to 5.34 although the maximum run-up increases smoothly and there is no sudden increase or decrease between the plunging breaking without splash-up and plunging breaking with splash-up. However, the change of the maximum run-up with respect to the incident wave height differs significantly for the two case of breaking, i.e., with and without splash-up. This is shown in Figure 5.35 where the incremental change in the maximum run-up with wave height of a solitary wave on a 1:15 slope, $\delta R/\delta H$, is shown as a function of relative wave height, H/h_0.

Only the numerical results using the WENO scheme are shown. From experiments, the maximum wave height H/h_0 of the solitary wave which breaks without splash-up is 0.14 for 1:15 slope, this splash-up limit line is shown in Figure 5.35 as well as the breaking limit line proposed by Synolakis (1986), i.e., Eq. 5.5. Two lines were fitted to the data in the two regions separated by the splash-up limit line. It can be seen clearly that the slope of the incremental change is different in these two regions, i.e., the curvature of the curve R/h_0 vs H/h_0 is different. This suggests that the splash-up and plunging incident jet may affect the global variables of the wave run-up process such as maximum run-up, and as we have discussed, perhaps due to the different processes of air entrainment, vortex generation, and decay.

The normalized maximum run-up, R/h_0, is shown as a function of the cotangent of the angle of the slope investigated, $\cot\beta$, in Figure 5.36. Both the data for non-breaking and breaking solitary wave run-up are presented and separated by a line which represents the wave breaking limit (Eq. 5.5). The maximum run-up for non-breaking solitary wave was calculated from the non-linear theory in Chapter 3 (Eq. 3.52), and that for breaking solitary wave was obtained from the WENO numerical model. It can be seen in Figure 5.36 that the variation of the maximum run-up with the angle of the slope relative to horizontal is different for non-breaking solitary waves and breaking solitary waves. In the non-breaking region, the maximum run-up increases as the angle of the slope decreases, while for breaking waves the maximum run-up decreases as the slope becomes gentler. This is caused by two different effects. For non-breaking waves the energy dissipation relative to the incident wave energy is small and the run-up is controlled by gravity. For example, consider the same relative incident wave incident upon two different slopes. The forces that cause the run-up on the slope, neglecting bottom friction, are opposed by the component of weight of the run-up tongue acting parallel to and down the slope. Thus, as the slope angle

decreases, assuming the same volume in the run-up tongue for the same incident wave height and the two different slopes, the component of force opposing motion up the slope decreases allowing increasing run-up. In the case of breaking waves, this variation of the weight component with change in slope still occurs, but now the energy dissipation associated with wave breaking becomes a significant fraction of the incident wave energy and tends to control run-up. This can be seen in the following argument. As the angle of the slope decreases for a given offshore wave height, the wave will break further offshore. If one uses the bore model to describe the energy dissipated by breaking, as the angle of the slope decreases the bore will propagate a larger distance along the slope leading to increasing energy dissipation with decreasing slope angle. If one accepts this model, it appears from the experiments that for the breaking wave case, energy dissipation rather than gravity forces (weight component) may be in control. Therefore, the converse is true for breaking waves compared to non-breaking waves and as the angle of the slope decreases the run-up also decreases. This will be discussed later when we treat the run-up model constructed from energy conservation principles.

5.3.2.4 Energy Dissipation

One important effect of the wave breaking process is energy dissipation. The relatively good agreement between the numerical results and the experimental results for wave shape, water surface time-histories, and the maximum run-up suggests that the shock simplification used in the numerical model can represent some effects of wave breaking at least with regard to the global properties of the wave. Thus, taking a bore, i.e., a moving hydraulic jump, as a model of the broken wave, we will estimate the energy dissipation associated with wave breaking. It is realized that the wave breaking and splash-up processes as shown in Figure 5.27 are extremely complicated.

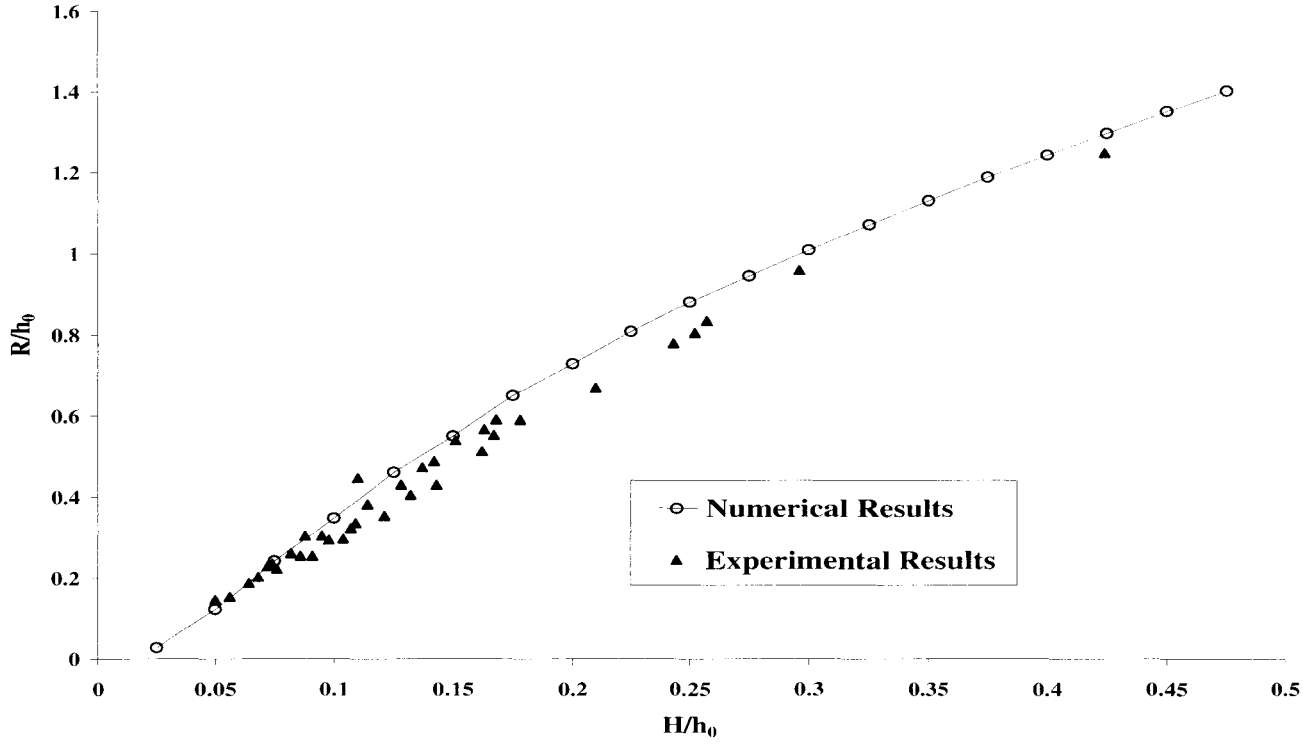

Figure 5.32: Maximum run-up of solitary wave on 1:5.67 slope. The normalized maximum run-up is shown as a function of incident wave height. The solid line with the hollow circles are the numerical results, the triangles are experimental data.

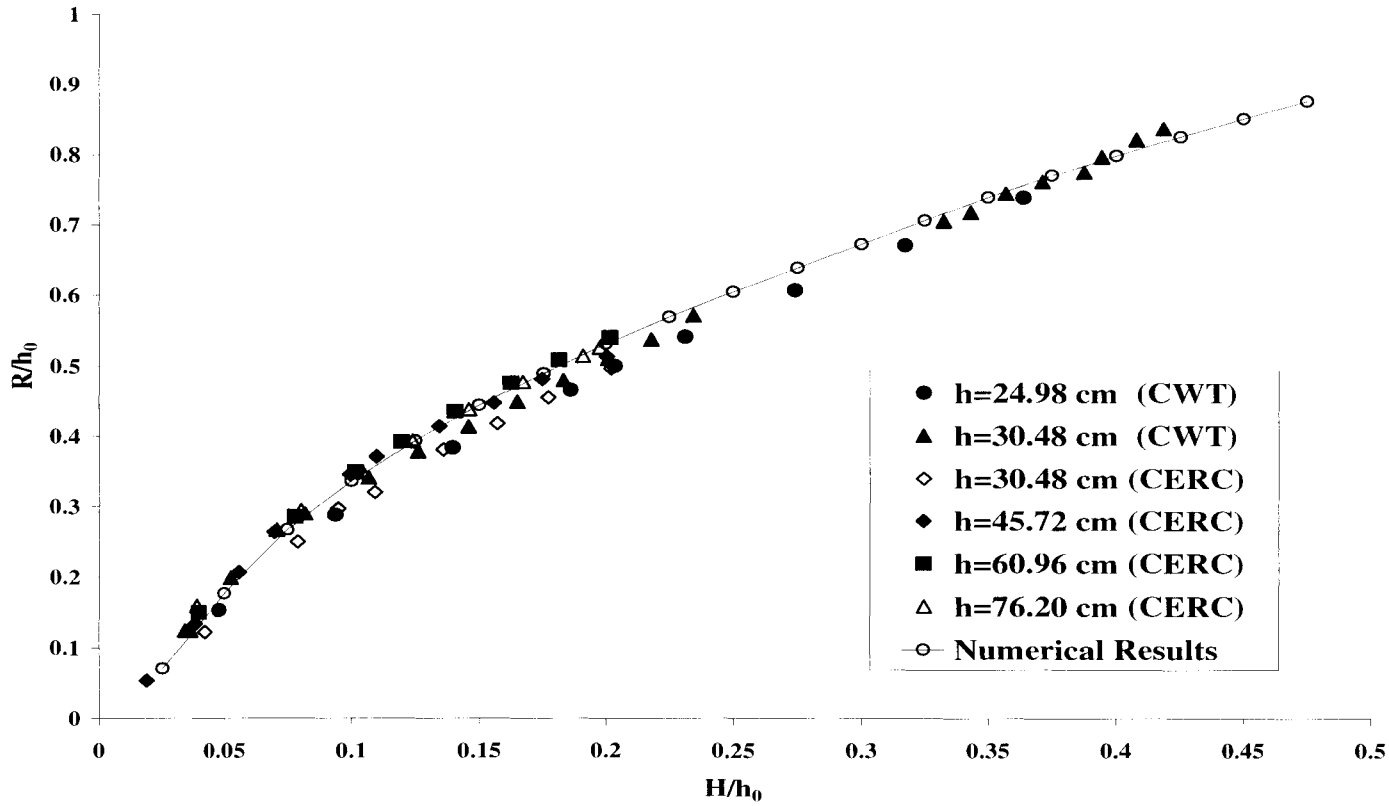

Figure 5.33: Maximum run-up of solitary wave on 1:15 slope. The normalized maximum run-up is shown as a function of incident wave height. The solid line with the hollow circles are the numerical results, the symbols are experimental data.

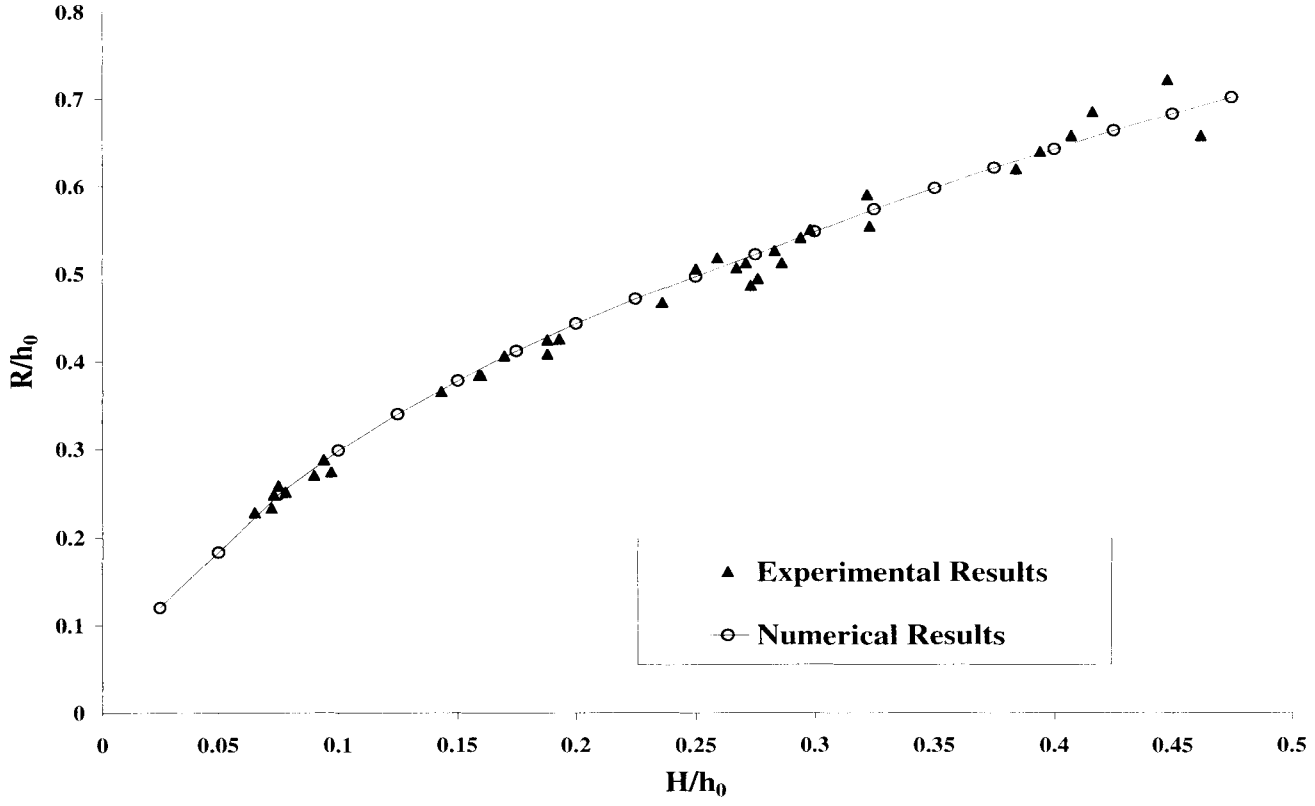

Figure 5.34: Maximum run-up of solitary wave on 1:19.85 slope. The normalized maximum run-up is shown as a function of incident wave height. The solid line with the hollow circles are the numerical results, the triangles are experimental data.

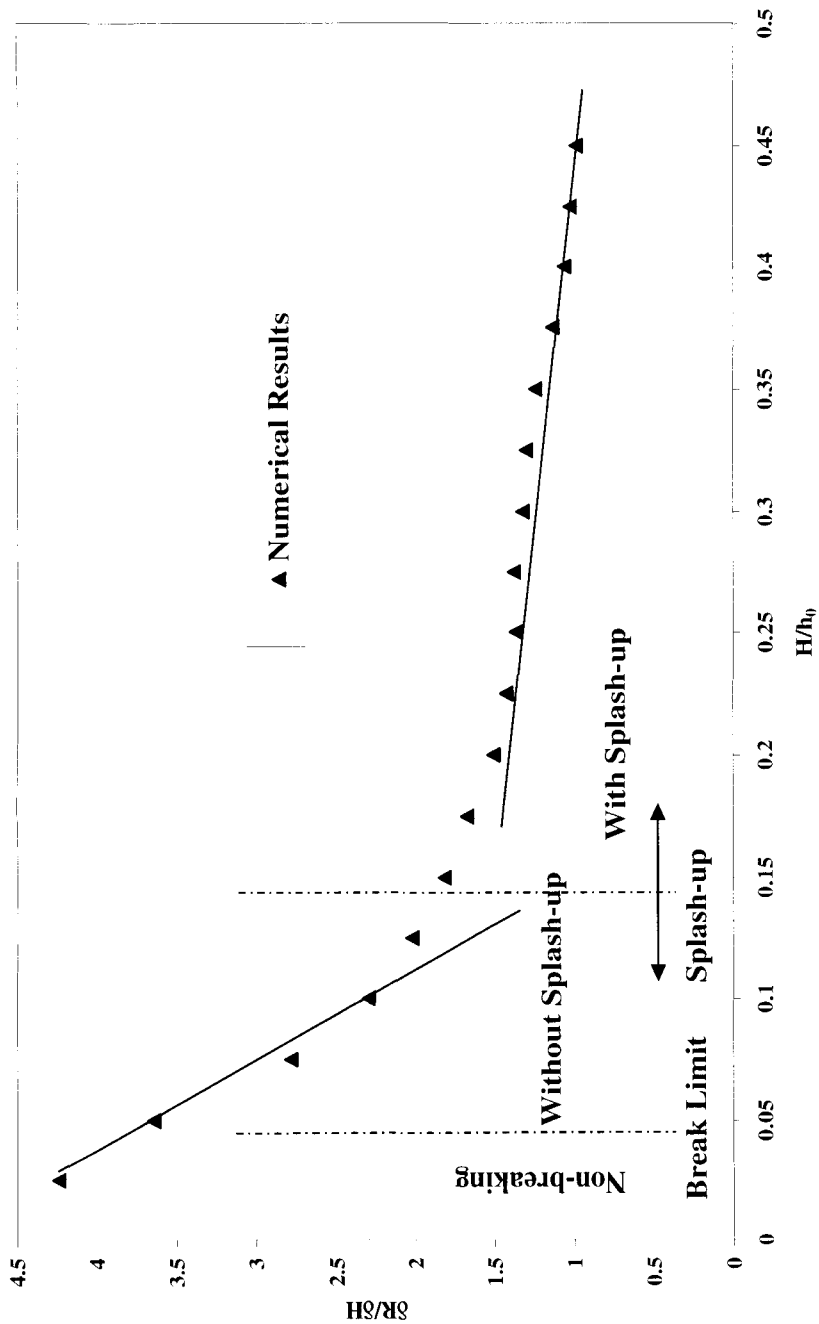

Figure 5.35: Incremental change in the maximum run-up with wave height, $\delta R/\delta H$, of a solitary wave on a 1:15 slope as a function of incident wave height

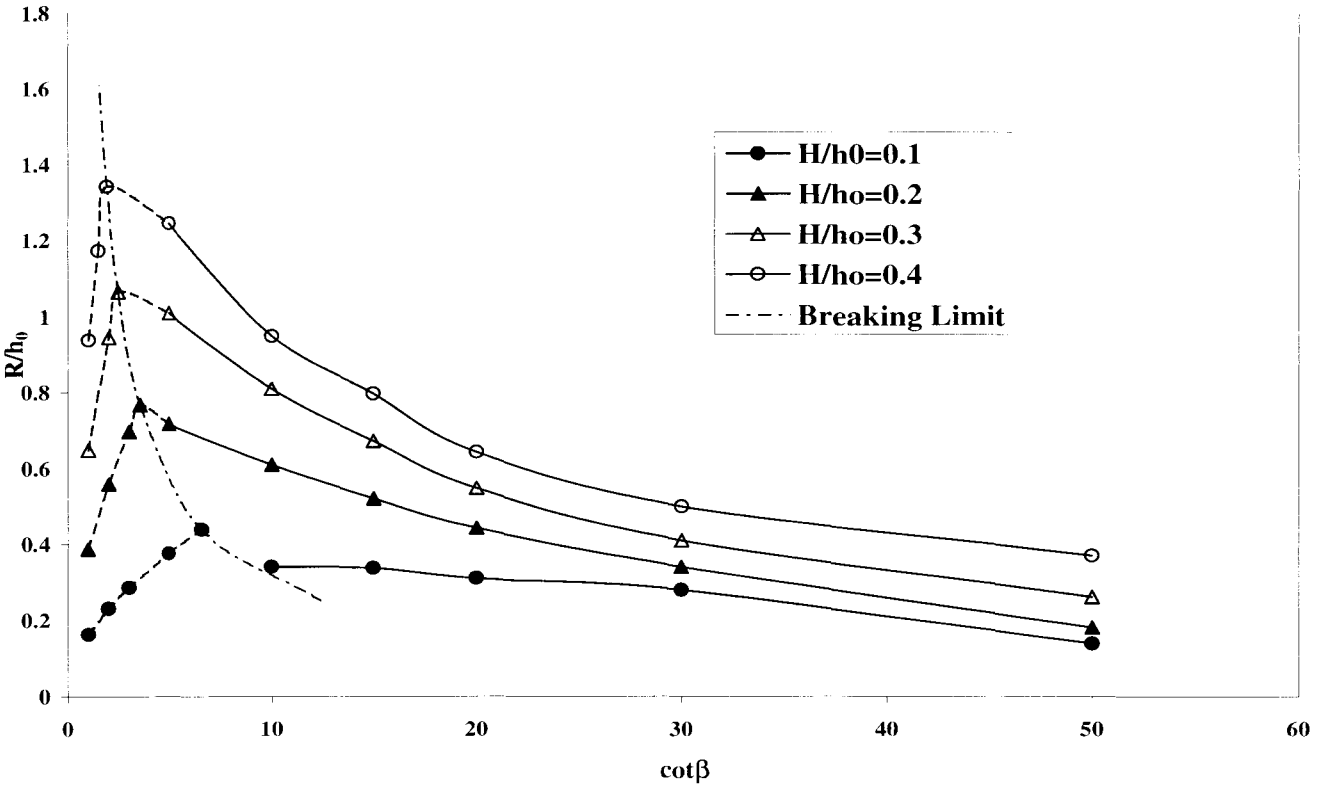

Figure 5.36: Maximum run-up of solitary wave as a function of slope angle for non-breaking and breaking waves for several incident relative wave height.

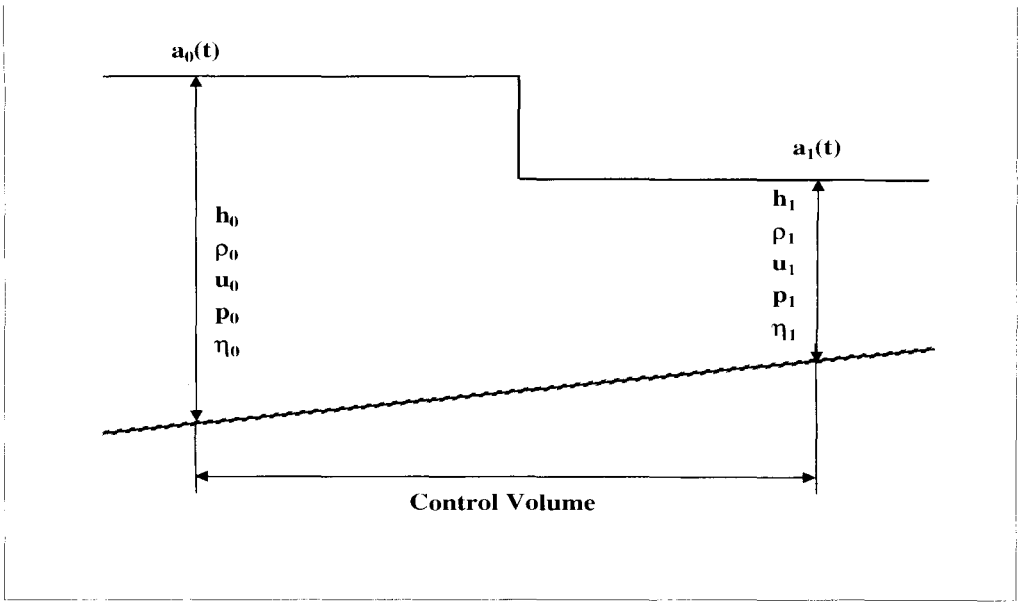

Figure 5.37: Schematic sketch for the discription of energy dissipation across a propagating bore

Therefore, this approach to determine the energy dissipation associated with breaking in terms of dissipation related to a bore is indeed a simplification of the process.

The mass conservation and momentum conservation equations for a bore are the same as the non-linear shallow water equations written in conservative form, i.e., Eqs. 3.58 and 3.59, except there is a discontinuity (a bore) in the domain to be considered. The rate of energy dissipation associated with a bore has been analyzed by Stoker (1957); for completeness his solution is presented herein. Considering a section enclosed by $a_0(t) \leq x(t) \leq a_1(t)$ such that the region is composed of a fixed mass, Stoker (1957) sought to analyze the energy dissipation across the bore (see Figure 5.37). The integrated forms of the shallow water equations (Eqs. 3.58 and

3.59) for the domain sketched in Figure 5.37 are as follows:

$$\frac{d}{dt}\int_{a_0(t)}^{a_1(t)} \rho(\eta + h)dx = 0 \tag{5.13}$$

$$\begin{aligned}\frac{d}{dt}\int_{a_0(t)}^{a_1(t)} \rho(\eta + h)udx &= \int_{-h_0}^{\eta_0} p_0 dy - \int_{-h_1}^{\eta_1} p_1 dy \\ &= \frac{1}{2}g\rho(\eta_0 + h_0)^2 - \frac{1}{2}g\rho(\eta_1 + h_1)^2 \end{aligned} \tag{5.14}$$

where $a_0(t)$, $a_1(t)$ are the vertical planes upstream and downstream of the water column that contains the bore, η_i, p_i, h_i are the wave amplitude, pressure and water depth at the vertical planes, respectively. In the Eq. 5.14, the shallow water assumption of a hydrostatic pressure distribution, $p = g\rho(\eta - y)$, has been used to derive the equation.

For continuous flow without a bore, i.e., a propagating wave without rapid changing shape, the energy equation can be derived directly from considerations of mass and momentum conservation. Thus, energy is conserved for the non-breaking solitary wave run-up, as shown before. However, the law of the conservation of energy does not hold across a bore. Theoretically fluid particles may gain or lose energy crossing the discontinuity. Since there is no energy source in the bore, the water particles cannot gain energy when crossing the bore, and energy must be lost. This inequality will be enforced in the following discussion to get a unique physically possible solution for the problem. For the same water column considered above, the integral form of energy equation is:

$$\begin{aligned}\frac{dE}{dt} &= \frac{d}{dt}\{\int_{a_0(t)}^{a_1(t)} [\rho(\eta + h)\frac{u^2}{2} + \frac{\rho g}{2}(\eta + h)^2]dx\} \\ &+ \int_{-h_1}^{\eta_1} p_1 u_1 dy - \int_{-h_0}^{\eta_0} p_0 u_0 dy \end{aligned} \tag{5.15}$$

where the first term in the equation on the right-hand side is the total energy change within the water column including kinetic energy and potential energy, the second term and third term respectively are the work done by the environment upon the water column at the vertical plane $a_1(t)$, $a_0(t)$.

For the limiting case where the length of the control volume, i.e., $a_0(t) - a_1(t)$, tends to zero, the following relations between the physical variables across the bore can be obtained from Eqs. 5.13 and 5.14:

$$\rho(\eta_1 + h_1)v_1 - \rho(\eta_0 + h_0)v_0 = 0 \tag{5.16}$$

$$\rho(\eta_1 + h_1)u_1v_1 - \rho(\eta_0 + h_0)u_0v_0 = \frac{1}{2}g\rho(\eta_0 + h_0)^2 - \frac{1}{2}g\rho(\eta_1 + h_1)^2 \tag{5.17}$$

where

$$v_0 = u_0 - \dot{\xi} \tag{5.18}$$

$$v_1 = u_1 - \dot{\xi} \tag{5.19}$$

are the relative upstream and downstream velocities with respect to the bore propagation speed $\dot{\xi}$ and:

$$\dot{\xi} = \frac{da_0(t)}{dt} = \frac{da_1(t)}{dt} \tag{5.20}$$

Using these relations and assuming a hydrostatic pressure distribution. Eq. 5.15 becomes:

$$\frac{dE}{dt} = \frac{1}{2}\bar{\rho}_1 u_1^2 v_1 - \frac{1}{2}\bar{\rho}_0 u_0^2 v_0 + \bar{p}_1 v_1 - \bar{p}_0 v_0 + \bar{p}_1 u_1 - \bar{p}_0 u_0 \tag{5.21}$$

where the quantities $\bar{\rho}_i$ and $\bar{p}_i$ are analogous to density and pressure in gas dynamics and are defined as:

$$\bar{\rho}_i = \rho(\eta_i + h_i) \tag{5.22}$$

$$\bar{p}_i = \frac{\rho g}{2}(\eta_i + h_i)^2 = \frac{g}{2\rho}\bar{\rho}_i^2 \tag{5.23}$$

Eliminating the variables v_i and replacing $\bar{p}_i$ with $\bar{\rho}_i$ the energy dissipation rate in Eq. 5.21 can be expressed in the simple form:

$$\frac{dE}{dt} = \frac{mg}{\rho}\frac{(\bar{\rho}_0 - \bar{\rho}_1)^3}{4\bar{\rho}_0\bar{\rho}_1} \tag{5.24}$$

where m is the mass flux across the bore:

$$m = \bar{\rho}_1 v_1 = \bar{\rho}_0 v_0 \tag{5.25}$$

It can be seen that energy is not conserved unless $\bar{\rho}_0 = \bar{\rho}_1$, i.e., the flow is continuous. If a bore exists in the flow domain, energy must be dissipated by the turbulence produced at the front of the bore. As stated before, wave breaking during run-up is assumed to be modeled as a propagating bore. Thus the rate of energy loss in the breaking wave run-up, i.e., dE/dt, can be obtained from Eq. 5.24.

The energy dissipation equation, Eq. 5.24, can be simplified further by solving for the bore propagation speed $\dot{\xi}$. Since the laws of mechanics are invariant with respect to axes moving at constant velocities, one of the three velocities in the problem u_0, u_1, or $\dot{\xi}$ can always be assumed to be zero without loss of generality. For example, if the upstream velocity $u_0 = 0$, from Eqs. 5.16, 5.17 the speed of the bore propagation can be written as :

$$\dot{\xi}^2 = \frac{g\bar{\rho}_1}{2\rho}(1 + \frac{\bar{\rho}_1}{\bar{\rho}_0}) \tag{5.26}$$

Substituting Eq. 5.26 into Eq. 5.24, the energy dissipation rate across a bore can be expressed as the function of the water depths across the bore:

$$D = \frac{dE}{dt} = \frac{1}{4}\rho g(d_0 - d_1)^3[\frac{g(d_0 + d_1)}{2d_0 d_1}]^{1/2} \tag{5.27}$$

where $d_i = h_i + \eta_i$ is the total water depth.

If the energy dissipation rate D in Eq. 5.27 is integrated over time from the start of the breaking process to the time of bore collapses T_c. (The time T_c is defined as the end of the wave breaking for the run-up process.) The total energy dissipated can be obtained as:

$$E_B = \int_0^{T_c} D dt = \int_0^{T_c} \frac{1}{4}\rho g(d_0 - d_1)^3[\frac{g(d_0 + d_1)}{2d_0 d_1}]^{1/2} dt \tag{5.28}$$

The WENO scheme presented in Chapter 3 solves the mass and momentum conservation equations across the shock; the energy conservation equation is automatically solved according to the above analysis. The total energy in the domain is calculated directly by integrating the potential energy and kinetic energy over the computing domain, i.e., Equations 5.6, 5.7. By comparing the value of the total energy at the time of the maximum run-up to the initial energy associated with the incident solitary wave, an estimation of the total energy dissipated by wave breaking can be obtained.

Figure 5.38 is the result of the calculated energy of a solitary wave with wave height H/h_0=0.30 which runs up a 1:15 slope. The energy and volume were normalized as in Eq. 5.8. It can be seen that as the wave propagates up the slope, the normalized kinetic energy decreases and potential energy increases since some kinetic energy is transformed into potential energy. A slight increase in total energy was found during the initial stage of the calculation and needs further investigation. Nevertheless, the total energy is still approximately conserved before wave breaking since no bore exists in the domain. When $t^* \approx 8$ the wave breaking process begins, both kinetic energy and potential energy decrease, but the rate of decrease is slightly different

from the computational results. This energy dissipation process stops when the wave reaches the initial shoreline position, which begins the run-up process at $t^* \approx 18$. The total energy is again conserved as the kinetic energy decreases and potential energy increases. The wave reaches the maximum run-up position around $t^* = 30$, where the potential energy reaches maximum value also. The kinetic energy at this position is very small, as seen in Figure 5.38. This small amount of energy may be associated with the mild reflected wave from the slope or the small and negligible water particle velocity assciated with the run-up tongue and will be discussed later. Past this point, the potential energy decreases and the kinetic energy increases as the water begins to run down the slope. The total volume associated with the wave is also presented in Figure 5.38 and it is found that the volume is constant for the run-up and run-down process, which shows the mass is conserved in the computing although slight variation is seen which is probably due to computational errors.

The total energy dissipation for the breaking solitary wave run-up can be obtained by comparing the total energy at the maximum run-up position, i.e., $t^* = 30$ in Figure 5.38, to the total energy in the incident wave, which can be calculated theoretically. Figure 5.39 shows the dissipated energy calculated this way as a function of incident wave height, H/h_0, for given slopes. Figure 5.40 shows the ratio of the dissipated energy due to breaking, E_B, to the energy associated with the incident wave, E_I, as function of incident wave height, H/h_0, for given slope. Five slopes ranging from 1:5.67 to 1:50 were investigated. It can be seen that as the incident wave height increases, the portion of the incident energy which is dissipated increases. For the 1:5.67 slope, wave breaking first occurs when $H/h_0 = 0.137$ according to the breaking criterion proposed by Synolakis (1986), the numerical results confirm this in that the energy dissipation is almost zero for $H/h_0 \leq 0.15$. The energy dissipation on more gentle slopes is larger than that on the steep slope for the same incident wave height.

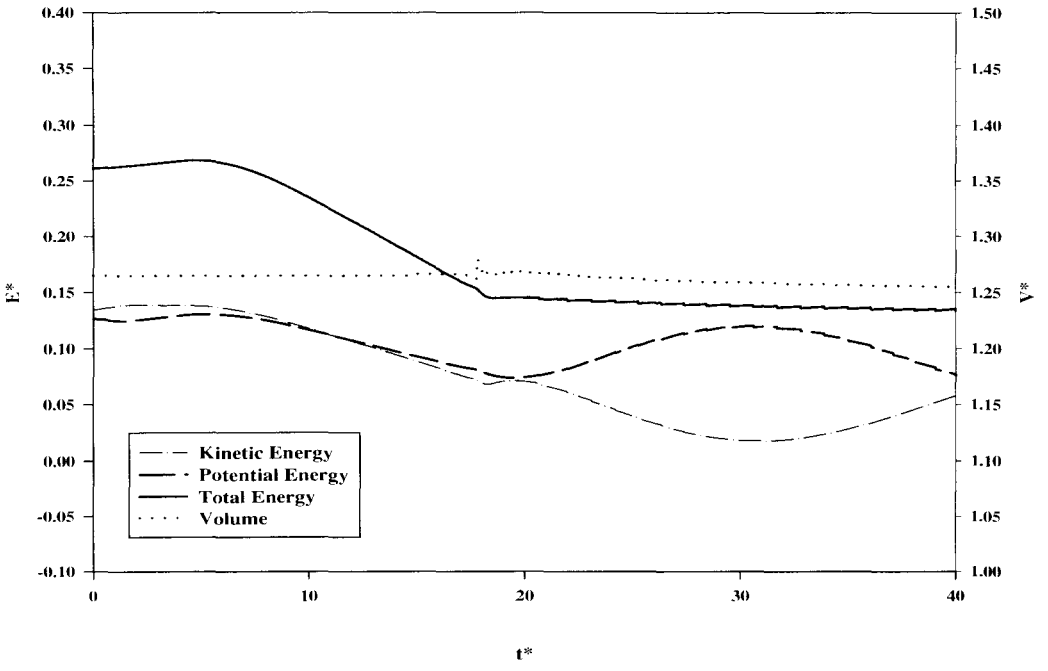

Figure 5.38: Calculated normalized energy of breaking solitary run-up with H/h_0=0.30 on 1:15 slope as a function of normalized time. The solid line is the total energy associated with the wave, the dashed line is the potential energy, the dash-dotted line is the kinetic energy, and the dotted line is the volume of the wave.

For example, almost 40% of the incident energy will be dissipated on a 1:15 slope for incident solitary wave with $H/h_0 = 0.30$, but only 5% on 1:5.67 slope. The energy dissipation predicted by the numerical model for 1:50 slope is larger than one would expect, i.e., almost 70% of the incident energy will be dissipated in the process even for a relative small incident wave height such as $H/h_0 = 0.2$; these results may need further investigation in the future research.

The calculated energy dissipation of solitary waves breaking on a slope obtained from Figure 5.39 was used to find an empirical formula to model this dissipation. The following equation obtained from linear regression analysis represents this relation of

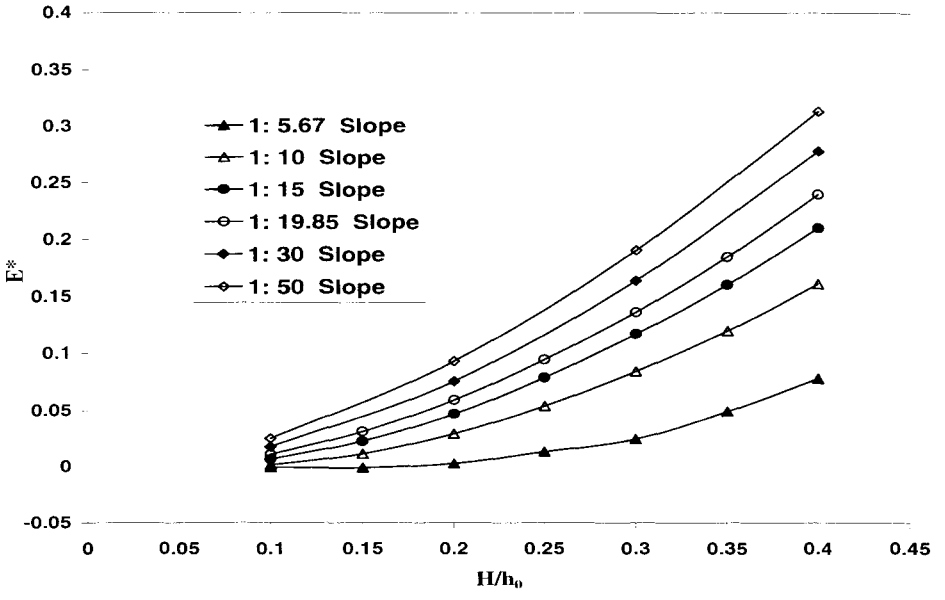

Figure 5.39: Energy dissipation for breaking solitary run-up as a function of relative incident wave height. Numerical results.

energy dissipated by breaking to the incident wave height and slope reasonably well:

$$\frac{E_B}{\rho g h_0^3} = 0.7(cot\beta)^{\frac{2}{5}}(\frac{H}{h_0})^{\frac{5}{2}} \tag{5.29}$$

Figure 5.41 shows the comparison of this empirical formula with the numerical results which were used to obtain Eq. 5.29. The abscissa is the numerical results and the ordinate is the prediction from the empirical formula with a line of identity shown. From the figure, the empirical formula appears to fit the data reasonably well; the relatively larger error appears to be for the 1:5.67 slope.

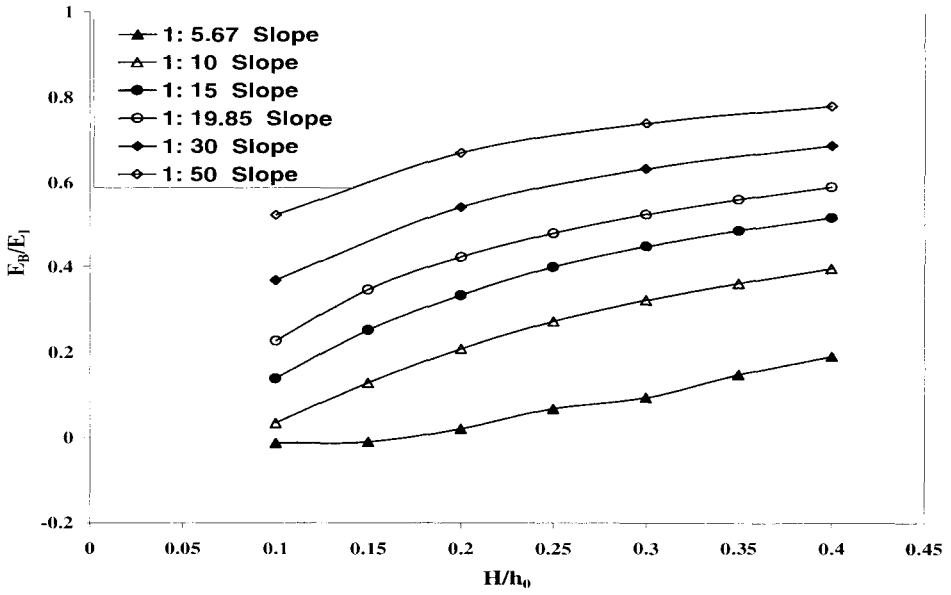

Figure 5.40: Ratio of dissipated energy to the incident wave energy for breaking solitary wave run-up as a function of relative incident wave height. Numerical results.

The relatively good agreement between the numerical results of the WENO scheme and the experimental results should be investigated further, since the bore structure used to model the wave breaking process in the numerical model considerably simplifies the physical process it represents. One possible reason for the good agreement when using this simplified model may be due to the relatively large length scales of both the incident wave and the run-up process compared to the length scale of the wave breaking region. In other words, although the wave breaking process is complex and difficult to be fully understood, the region that it affects is actually small (at the order of water depth). Thus, from this "macroscopic view", the wave breaking can

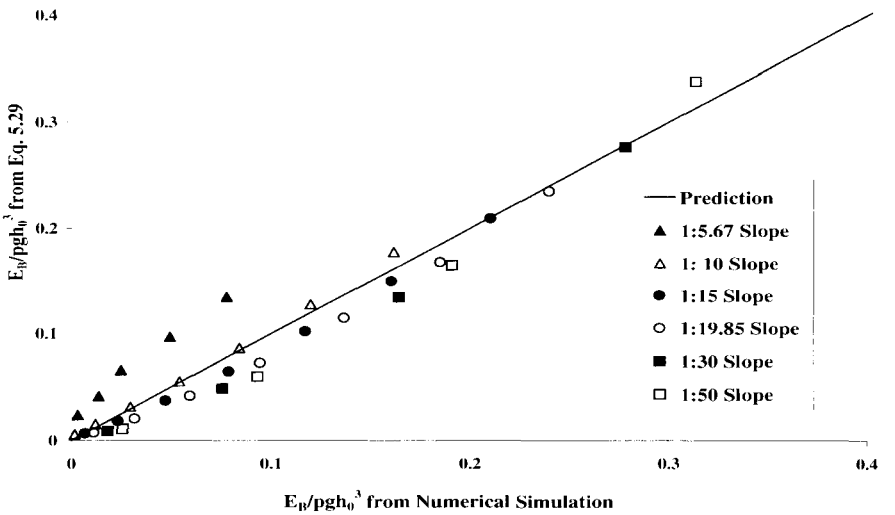

Figure 5.41: The energy dissipation of breaking solitary wave run-up: Comparison between numerical results and the empirical formula Eq. 5.41.

be regarded as a sharp discontinuity or an energy sink. In addition, the equations defining the numerical model correctly represent mass and momentum conservation across the breaking wave. If the mass and momentum exchange across the discontinuity are treated correctly, then, like the hydraulic jump or the dam-break problem, one should be able to obtain the global parameters of the characteristics of the wave run-up process such as the maximum run-up and the wave amplitude time-histories with reasonable confidence.

5.3.3 Breaking Solitary Wave Run-Up – An Exploration of Energy Conservation

In this section the results of an exploratory study of the energy conservation associated with the maximum run-up of breaking solitary waves will be presented. The thoughts which are developed here are base on what we will refer to as "the energy balance model".

In the previous sections we have proposed a theoretical solution for non-breaking solitary waves run-up on linearly varying slope and a numerical method to calculate the run-up of breaking solitary waves. These methods are complicated to use for prediction purposes. They either require a relatively long computation time or neglect some effects which may be potentially important according to the local bathymetry of the coast or special properties of the attacking tsunami. To overcome some of these problems, an energy balance model has been developed based simply on energy conservation considerations during the run-up process. Thus, it doesn't neglect such effects as non-linearities, dispersive effects, etc. The maximum run-up predicted is confirmed to some extent by experimental results.

In the following discussion the incident wave energy involved in the run-up process is specified and a general energy balance equation is presented. This equation assumes that the wave shape at the maximum run-up position is self-similar and the potential energy at this position is a function of the maximum run-up and the volume of the incident solitary wave. (These assumptions were confirmed by experiments as well as by the numerical model developed in the last section.) The empirical expression for energy dissipation during wave breaking developed in last section will be used to account for the energy loss. Based on this energy conservation model and the energy dissipation model based on a bore representation of wave breaking, a maximum run-

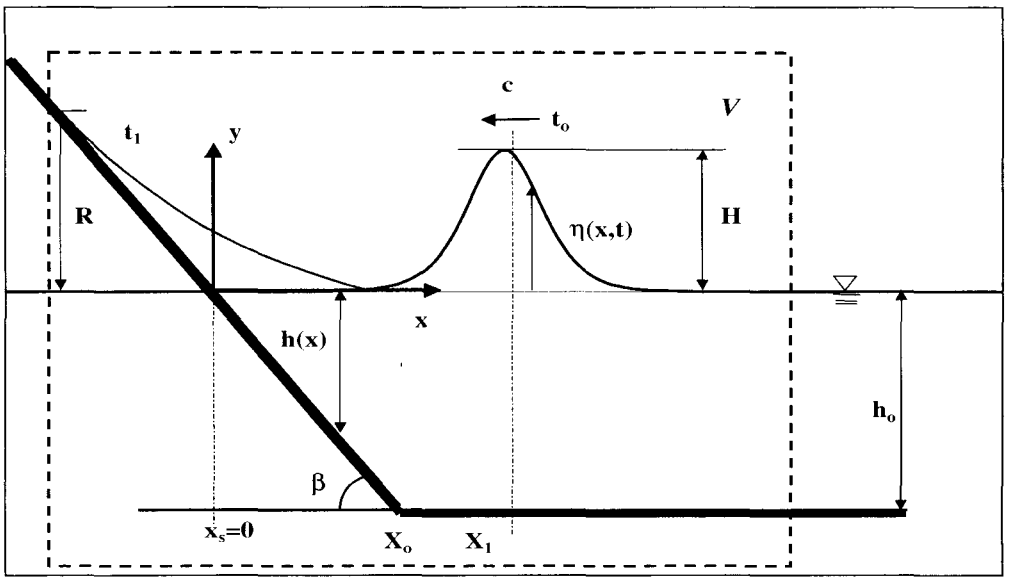

Figure 5.42: Definition sketch of the energy balance model for breaking solitary wave run-up

up prediction is presented.

5.3.3.1 Energy Conservation Considerations

Figure 5.42 shows the sketch of the problem investigated. Once the solitary wave is produced either by the wave generator in experimental conditions or by earthquake, landslide, etc, in nature, the wave with wave height H propagates towards the beach with inclination angle β, runs up on the beach to a maximum run-up R, and then the run-up tongue retreats and produces the major reflected wave propagating offshore. (There is also a minor reflected wave which occurs during the run-up process due to wave-slope interaction.)

Consider the control volume, V, shown in Figure 5.42. The control volume is selected in such a way that all the wave motion has been included in the control volume V. The wave motion and velocity at the seaward boundary of V is so small that both the mass and momentum influx at that boundary can be neglected although theoretically the wave length of the solitary wave extends to infinity. The left boundary of V includes the initial shoreline and the maximum run-up position on the slope. Therefore, all the run-up and run-down process is confined to the chosen control volume. This guarantees that there is no mass and momentum flux out of the control volume V.

The energy inside the control volume is analyzed next. As mentioned above, there is no mass or momentum flux at either the left or the right boundary; therefore, the work done by the environment at the left and right boundaries of the system defined in the control volume is zero. The energy transformation from the initial time t_0 to the time t_1 is investigated. The initial time t_0 is defined as the time that the solitary wave has the crest at position X_1. (X_1 is half of the characteristics length of the solitary wave ($L/2$) offshore of the toe of the slope, and L is defined in Eq. 3.25.) The final time t_1 is chosen as the moment that the run-up tongue reaches its maximum position on the slope. All the energy terms involved in the run-up process and the energy conservation equation are shown in Figure 5.43 and discussed below. The relative magnitude of each energy term is represented approximately by the width of the arrow in Figure 5.43.

Initially all the energy inside the control volume V is contained in the incident solitary wave, i.e., both the kinetic energy and potential energy. This is denoted as E_I. One form of the theoretical solitary wave shape and velocity up to the first-order

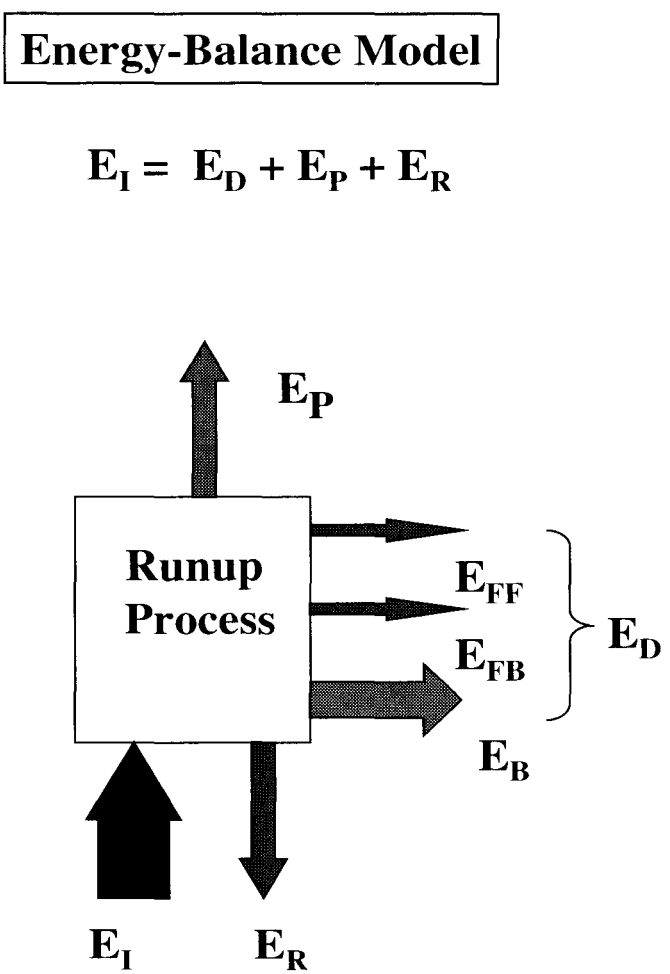

Figure 5.43: Illustration sketch of the energy balance model

accuracy are presented before and are repeated here for completeness:

$$\eta(x,t) = H sech^2(\sqrt{\frac{4H}{3h_0^3}}(x-ct)) \tag{5.30}$$

$$u(x,t) = \frac{c\eta}{1+\eta} \tag{5.31}$$

$$c = \sqrt{g(h_0+H)} \tag{5.32}$$

By integrating these and related expressions from $-\infty$ to ∞ the total volume, kinetic energy and potential energy of a solitary wave with wave height H are obtained:

$$V = \int_{-\infty}^{\infty} \rho\eta dx \tag{5.33}$$
$$= \rho[\frac{16}{3}h_0^3 H]^{\frac{1}{2}}$$

$$E_K = \int_{-\infty}^{\infty} \rho(\eta+h_0)\frac{u^2}{2}dx \tag{5.34}$$
$$= \frac{4\rho g}{3\sqrt{3}}H^{\frac{3}{2}}h_0^{3/2} + \frac{4\rho g}{15\sqrt{3}}H^{\frac{5}{2}}h_0^{\frac{1}{2}}$$

$$E_P = \int_{-\infty}^{\infty} \frac{\rho g}{2}(\eta+h_0)^2 dx \tag{5.35}$$
$$= \frac{4\rho g}{3\sqrt{3}}H^{\frac{3}{2}}h_0^{\frac{3}{2}}$$

Where kinetic energy and potential energy with respect to the incident solitary wave height are shown in Figure 5.44. It can be found that the kinetic energy is almost equal to the potential energy if the incident wave height is not too large. To simplify the discussion the following equation for the kinetic and potential energies is used:

$$E_K \approx E_P = \frac{4\rho g}{3\sqrt{3}}H^{3/2}h_0^{3/2} \tag{5.36}$$

The error associated with the above simplification is less than 7% even for a

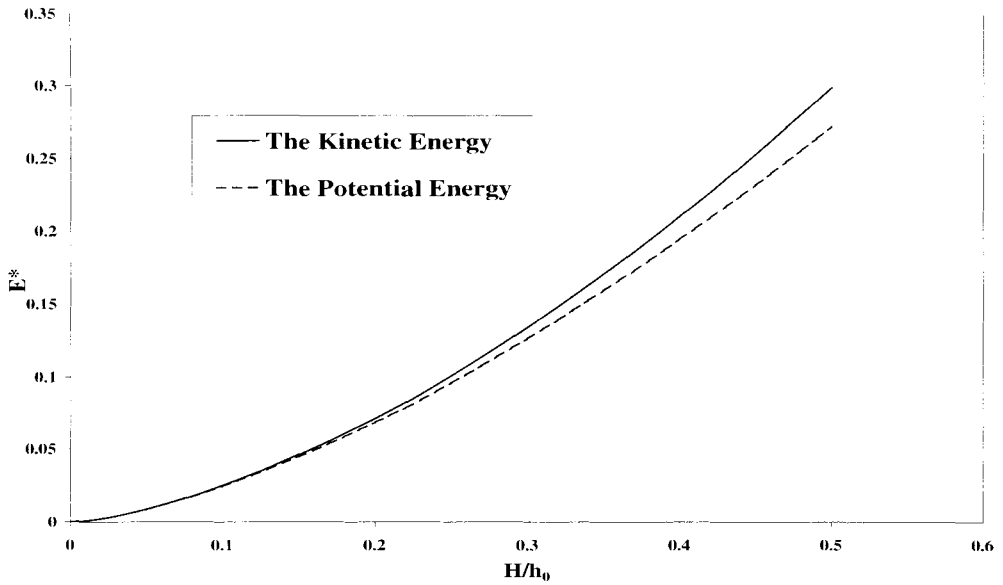

Figure 5.44: The potential and kinetic energy of solitary wave. The normalized energy is shown as function of incident wave height H/h_0. The solid line is the kinetic energy, the dashed line is the potential energy.

relatively large wave height of $H/h_0 = 0.40$.

The solitary wave will propagate towards and run up the slope. As the wave travels towards the slope, because of the non-linear effects, the wave height increases and therefore some of the kinetic energy is transformed into potential energy. Thus, the kinetic energy decreases and the potential energy increases slowly as the wave propagates up the slope. At the position of maximum run-up, the potential energy reaches a maximum while the kinetic energy is a minimum and has a value close to zero. This process was seen clearly in Figure 5.12 for non-breaking solitary wave run-up and Figure 5.38 for breaking solitary wave run-up and has been discussed previously. After the maximum run-up is reached the run-down process begins with

a decrease in the potential energy and a corresponding increase in kinetic energy.

During propagation a portion of the energy will be reflected from the slope and a portion of the energy is dissipated. The dissipation is caused by several mechanisms: friction at the bottom of the wave tank, friction at the free surface, i.e., between the air and the wave, and most important, wave breaking:

$$E_D = E_{FF} + E_{FB} + E_B \tag{5.37}$$

In Eq. 5.37 E_D is the total dissipated energy, E_{FF} is the energy dissipated by the free surface friction between air and water, E_{FB} is the energy dissipated by the bottom friction, and E_B is the energy dissipation associated with wave breaking.

Keulegan (1948) has analyzed the rate of loss of energy due to viscous shear with the laminar boundary layer beneath the solitary wave on a smooth surface, and found:

$$\begin{aligned} \frac{dE}{dt} &= -\frac{4}{\sqrt{3}}\rho g^{3/2} h_0^2 H^{1/2} \frac{dH}{dx} \\ &= \frac{4}{\pi^{3/2}}(\frac{4}{3})^{1/4} \rho \nu^{1/2} g^{5/4} H^{7/4} \end{aligned} \tag{5.38}$$

where in Eq. 5.38 the energy dissipation rate due to bottom friction was proportional to the attenuation in wave height dH/dx. Naheer (1978) also investigated the energy dissipation and viscous damping of solitary waves propagating in a constant depth over a rough bottom, and the viscous dissipation and attenuation were found to be small compared to the energy associated with the incident wave. Clearly, for breaking solitary wave run-up on the slope, the majority of energy dissipation is due to wave breaking. This is especially true in experiments where the wave tank bottom and the slope surface are smooth. For rough beaches and other conditions such dissipations probably cannot be neglected, and corresponding empirical formulae can be used in

the energy balance model to represent these. Nevertheless, in the following discussion the dissipation caused by friction will be omitted for simplicity. Therefore, assuming the energy dissipation is caused mainly by wave breaking, then in Eq. 5.37 $E_D \approx E_B$. Thus, the energy equation for the run-up process at an arbitrary location on the slope shoreward of breaking can be expressed as:

$$E_I = E_K + E_P + E_B + E_R \tag{5.39}$$

where E_K and E_P are the kinetic and potential energies, respectively, E_B is the energy dissipation associated with wave breaking, and E_R is the energy associated with the reflection.

The reflected wave associated with run-up mentioned in the literature usually refers to the reflected wave arising both from the reflected wave from the slope before the wave reaches the maximum run-up and the wave generated by the run-down process. However, the reflected wave used in the energy balance consideration here only refers to the wave which is reflected from the slope before the water sheet on the slope reaches the maximum run-up position. A time-history of the solitary wave run-up process is presented in Figure 5.45 (denoted as water time-history without eliminating the run-up tongue in the figure) for a wave gage located half of characteristic length of solitary wave ($L/2$) offshore of the toe of the slope. The initial wave height of the solitary wave is $H/h_0 = 0.28$, the slope of the beach is 1:15, and the water depth in the constant depth region before the slope is $h_0 = 30.48$ cm. The portion of the water surface time-history between line A and line B in the figure is the reflection used in this discussion, and the reflection associated with the run-down generated wave extended from line B to the end of the recording, i.e., $t^* > 20$. It can be seen that the specific reflected wave used in this discussion only comprises a small portion of the total reflected wave system. Therefore, the energy associated with it

is much smaller. A series of experiments were conducted in the lab to measure this portion of the energy which is labeled E_R in Figure 5.43.

Figure 5.46 shows the experimental arrangement used to measure the reflected wave energy. The difference between this setup and that used for measuring run-up discussed earlier lies in the arrangement of the slope. Instead of the relatively long slope used for wave run-up measurement, the slope used in the reflection measurement only extends from the wave tank bottom to the initial shoreline position. A collection box with water level lower than that in the wave tank is arranged shoreward of the end of the slope. Thus, when the incident solitary wave runs up the slope, the portion of the wave which would normally comprise the run-up tongue and hence the run-down tongue will flow over the end of the slope and be captured in the collection box. Therefore, only the reflected wave which is due to the wave-slope interaction, E_R, will be recorded by the offshore wave gage.

The measured water surface time-history from a wave gage using this experimental setup is also shown in Figure 5.45 (denoted as water time-history after eliminating the run-up tongue). The location of the wave gage was the same as that in regular run-up measurement. It can be seen clearly that the reflected wave from the slope is very small compared to the wave generated by the run-down from the slope. Another wave gage was located at the toe of the slope to measure the profile of the reflected wave and also the maximum height of the reflected wave height. Figure 5.47 shows this maximum height as function of incident wave height for solitary wave run-up. From Figure 5.47 we can see that even for a incident solitary wave with wave height $H/h_0 = 0.45$, the relative maximum reflected wave height before the run-down process is less than 0.03. For such a small wave, the linear wave theory is applicable to calculate the wave properties such as wave celerity, wave energy etc. For example, the time-history measurement can be converted into spatial measurement according

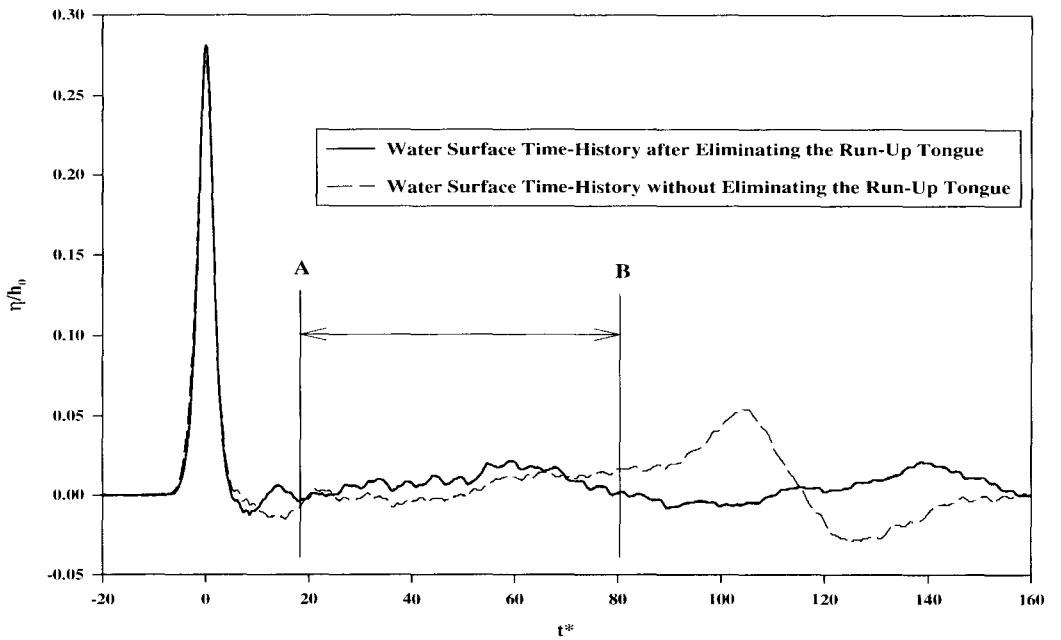

Figure 5.45: The experimental wave time-history for solitary wave run-up with $H/h_0 = 0.28$. The solid line is the normalized wave amplitude after eliminating of the run-up tongue, the dashed line is the wave amplitude obtained without eliminating the run-up tongue.

to linear theory, the wave energy including potential energy and kinetic energy can be computed by integrating this spatial wave signal over the wave record. i.e, Eqs. 5.6 and 5.7. By doing this, the energy associated with the reflection E_R can be obtained and it was found that $E_R \approx 0$ compared to the incident wave energy.

The kinetic energy E_K associated with the water movement at the time of maximum run-up is also very small. This kinetic energy comes from the wave energy associated with the run-up tongue on the slope. It was found from numerical simulations that the water particle velocity of the run-up tongue at the maximum run-up is very small. Grilli and Svendsen (1989) calculated the non-breaking run-up on a slope

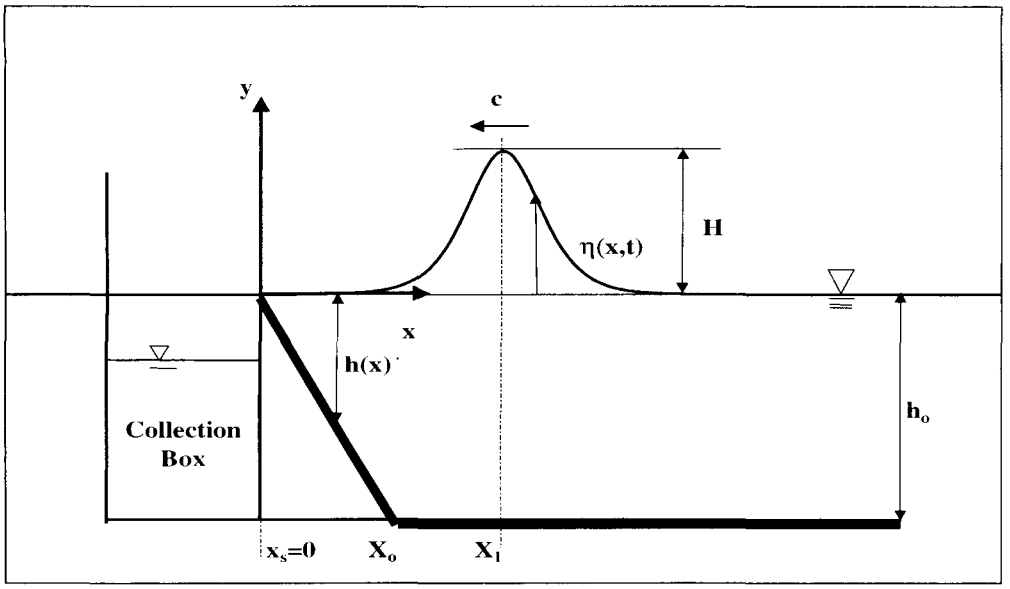

Figure 5.46: Sketch of the experimental setup used to measure the wave reflection

using the BEM method and found the kinetic energy in the run-up tongue at the time of the maximum run-up is almost equal to zero. The numerical results using the WENO scheme presented earlier, i.e., Figure 5.12, 5.13 and 5.38, also shows that the kinetic energy at the time of maximum run-up is very small. Therefore, the kinetic energy term in the energy conservation equation, Eq. 5.39, at the time of maximum run-up, is neglected, i.e., $E_K \approx 0$.

In the following discussion the remaining terms in equation 5.39, i.e., E_B and E_P are treated. From these discussions a simple and reasonably accurate prediction of the maximum run-up of breaking solitary waves is presented. This is contrasted to the numerical model, which although more accurate, is more difficult to apply.

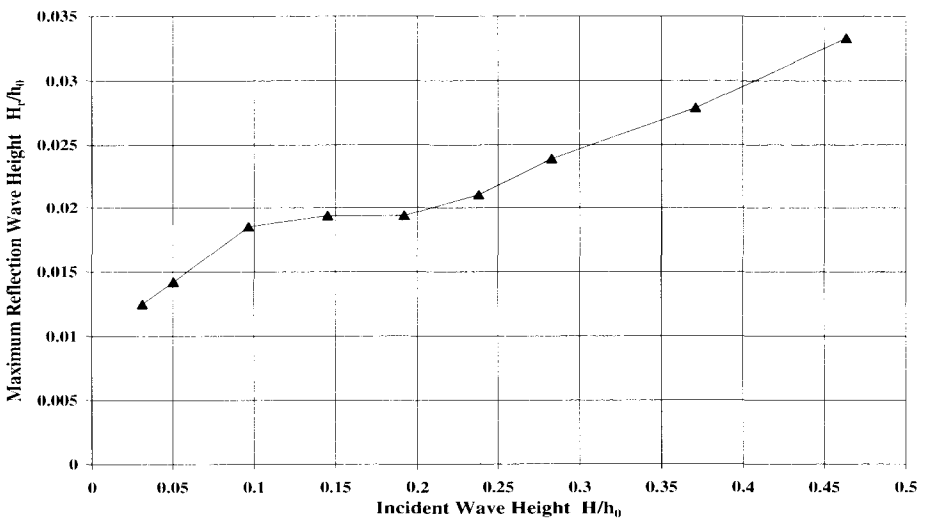

Figure 5.47: Maximum reflected wave height for breaking solitary wave run-up after eliminating the run-up tongue as a function of relative incident wave height

5.3.3.2 Potential Energy

If the potential energy, E_P in Eq. 5.39, can be modeled correctly, the energy loss caused by wave breaking can be obtained from the energy equation, or conversely, if the energy dissipation can be modeled, the potential energy can be obtained. In this section, the empirical formula which was obtained using the WENO numerical model presented earlier (Eq. 5.29) is used to model the dissipated energy due to wave breaking. Using dimensional analysis a relationship between the maximum run-up for a breaking solitary wave and the potential energy at the time of maximum run-up is proposed.

Dimensional analysis will be used as an aid to model the potential energy at the

time of maximum wave run-up, R. The dependent variables for this run-up process are grouped into three categories: (i) the incident wave parameters: the wave height H, the water depth in the constant depth region h_0, and the total volume of the wave V. (ii) the angle of the slope β and the maximum run-up of solitary wave on the slope R, and (iii) physical constants: the acceleration of gravity g and the density of the water, ρ. Writing this as an expression in functional form:

$$f(E_P, H, h_0, V, R, cot\beta, \rho, g) = 0 \tag{5.40}$$

where E_P is the potential energy at the time of maximum run-up.

Choosing the variables h_0, ρ and g as the independent physical variables, we obtain the following expression:

$$\frac{E_P}{\rho g h_0^3} = F(\frac{R}{h_0}, \frac{V}{h_0^2}, \frac{H}{h_0}, cot\beta) \tag{5.41}$$

(Only two-dimensional run-up is considered here and the width of the section is assumed to be unity and non-dimensional, thus, the dimensional parameters above such as the volume of the water are one order less in length scale.)

The relation among the non-dimensional variables in Eq. 5.41 can only be obtained from numerical simulations or experiments.

To calculate the potential energy at the time of the maximum run-up, the shape of the full run-up tongue has to be determined. Figure 5.48 shows profile of the run-up tongue shape at the time of maximum run-up determined experimentally for a solitary wave: $H/h_0 = 0.30$ on 1:15 slope. (These data were obtained using high-speed video.) As mentioned earlier, the experiments were repeated several times with the camera moved to new location to cover the full length of the run-up tongue.

There are some deviations in the data obtained from the two recordings probably due to a small variation in the generated waves for such set of data. These data were integrated numerically to get the potential energy for this example. To reduce the error associated with the numerical integration, the order of the numerical integration accuracy is chosen such that for a change in the integration greater than 1%, the order of the integration is increased by 1. It was found that fourth-order polynomial fitting is adequate for the numerical integration. The data of run-up tongue shape from Synolakis (1986) shown in Figure 5.30 were also used to calculate the potential energy at maximum run-up for the 1:19.85 slope. These two data sets were used to verify the potential energy obtained using the numerical WENO scheme. The results are shown in Figure 5.49 for 1:15 slope and Figure 5.50 for 1:19.85 slope. Agreement between the numerical results and the experiments is relatively good.

An assumed form of the functional relation described by Eq. 5.41 is taken as:

$$\frac{E_P}{\rho g h_0^3} = \alpha \frac{R}{h_0} \frac{V}{h_0^2} \tag{5.42}$$

the quantity α is a constant called the shape factor. In Eq. 5.42 , it has been assumed that the potential energy is independent of the slope angle $cot\beta$, and not directly related to the initial wave height H/h_0 except as it relates to the total volume of the wave, V.

Knowing E_P, R, and V, Eq. 5.42 can be solved for shape factor, α. Figure 5.51 shows the values of shape factor obtained from the numerical simulations. The results from three slopes ranging from 1:15 to a very gentle slope of 1:50 are shown. For $0.05 < H/h_0 < 0.5$ the shape factor, α, is about 0.12. Therefore, in the following discussion α is chosen to as 0.12.

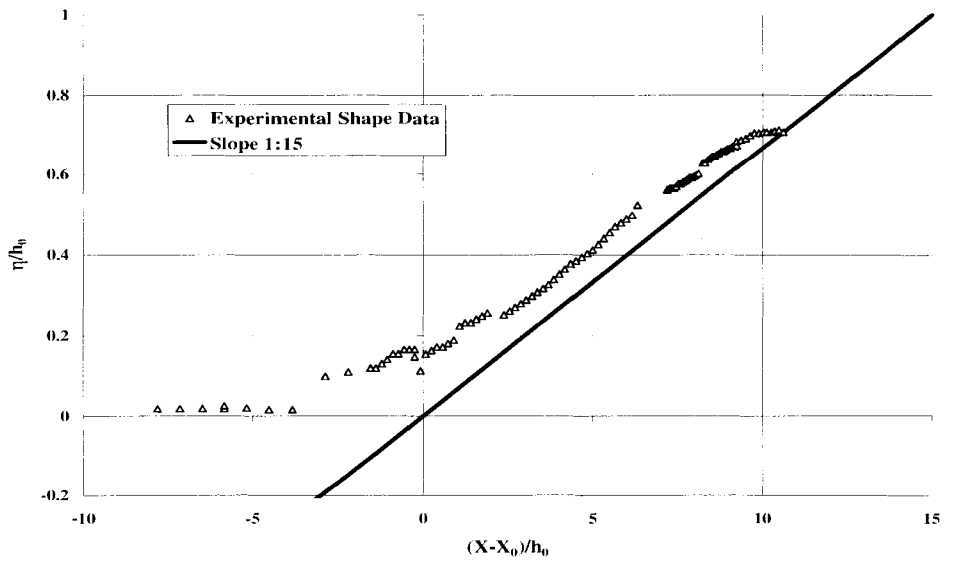

Figure 5.48: The shape of the run-up tongue of breaking solitary wave on 1:15 slope with wave height $H/h_0 = 0.30$

5.3.3.3 Prediction of Maximum Run-Up

Equation 5.29 presented in last section is used to model the energy dissipation due to wave breaking during the solitary wave run-up process. When Eq. 5.29 and the expression for the potential energy at the maximum run-up, i.e., Eq. 5.42 along with $\alpha = 0.12$ are substituted into the energy balance equation (Eq. 5.39), by doing some simple algebraic manipulations, the following expression for the maximum run-up of a breaking solitary wave can be obtained:

$$R = \alpha_1 \frac{E_I - E_B}{\alpha V}$$

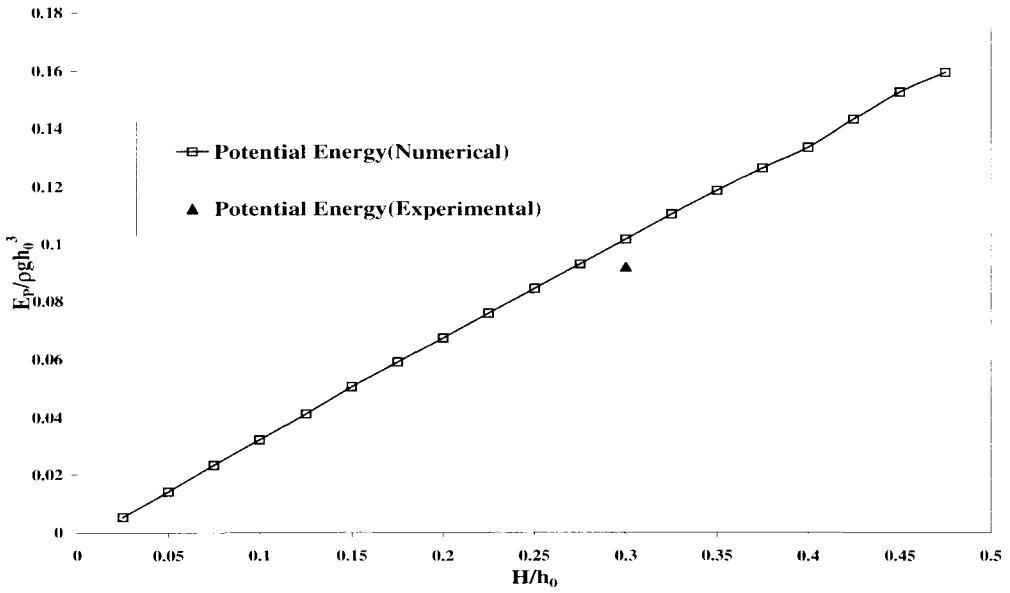

Figure 5.49: The normalized potential energy at maximum run-up for 1:15 slope as a function of relative incident wave height

$$\frac{R}{h_0} = \alpha_1 \frac{\frac{8}{3\sqrt{3}}(H/h_0)^{\frac{3}{2}} - 0.7(cot\beta)^{\frac{2}{5}}(H/h_0)^{\frac{5}{2}}}{\alpha[\frac{16}{3}H/h_0]^{\frac{1}{2}}} \tag{5.43}$$

where α_1 is a constant which slightly changes with slope and was found to best fit Eq. 5.43 to the data to be:

$$\alpha_1 = 1.11(cot\beta)^{-0.183} \tag{5.44}$$

Eq. 5.43 will be used to predict the maximum run-up of a breaking solitary wave based on energy conservation considerations and the results will be compared to both the numerical results from the WENO scheme and experimental results. It seems that Eqs. 5.43 and 5.44 derived from the energy balance model can predict the trend of the maximum run-up as function of incident wave height reasonably well.

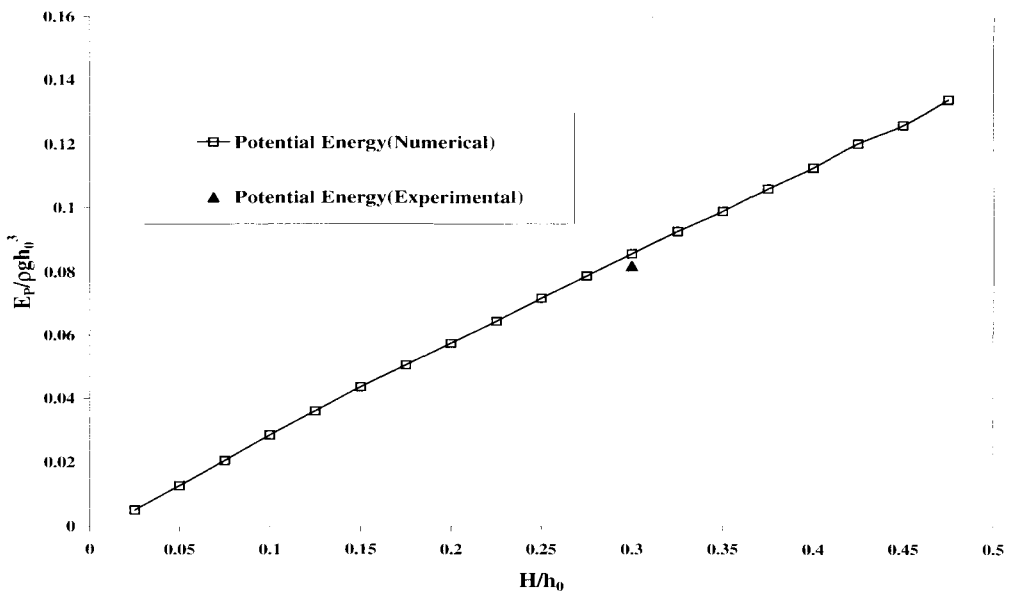

Figure 5.50: The normalized potential energy at maximum run-up for 1:19.85 slope as a function of relative incident wave height (Experiment from Synolakis (1986))

Figures 5.52, 5.53, 5.54 show the variation of the maximum run-up with incident wave height for 1:5.67 slope, 1:15 slope and 1:19.85 slope, respectively. It can be seen that Eq. 5.43 can model the maximum run-up for a wide range of incident wave height $0 < H/h_0 < 0.35$. For incident wave heights greater than 0.40, the energy dissipation formula, i.e., Eq. 5.41 appears to overestimate the energy dissipation, thus, the maximum run-up predicted by the energy balance model is somewhat less than that obtained from the numerical model.

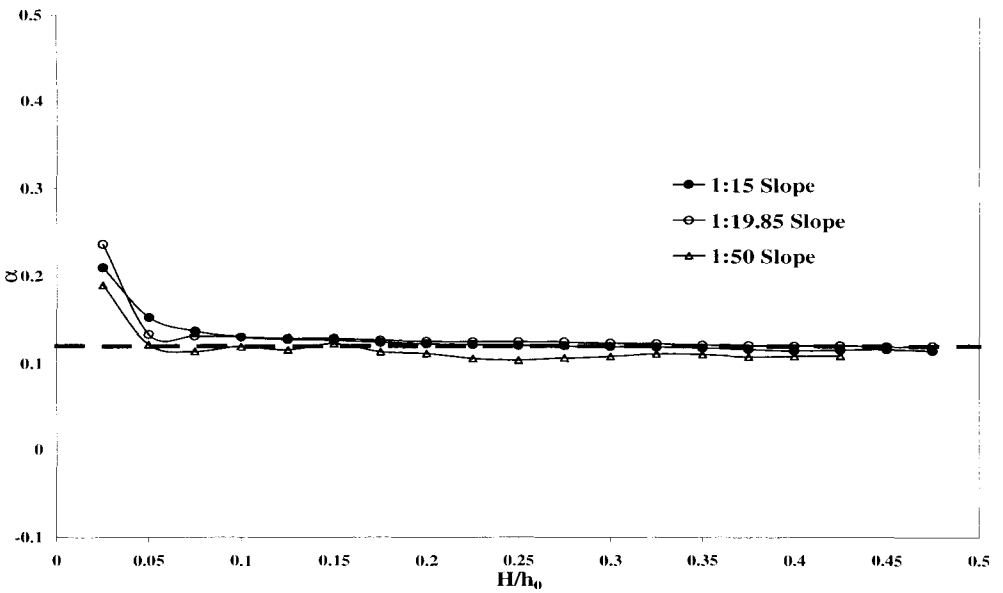

Figure 5.51: The shape factor of solitary wave run-up tongue at maximum run-up as a function of relative incident wave height. Numerical results

5.4 Breaking Solitary Wave Run-Up on Vertical Walls

In this section, the experimental and numerical results of breaking solitary wave run-up (splash-up) on a vertical wall positioned at different locations on a 1:19.85 slope are presented. (This section is taken from the paper by Li, Raichlen, and Lee (2000b)).

Splash-up resulting from the interaction between the wave and the wall usually consists of sheet flow for small relative wave heights, but for extreme waves it is composed of both sheet flow and spray and drops which break away from the splash-

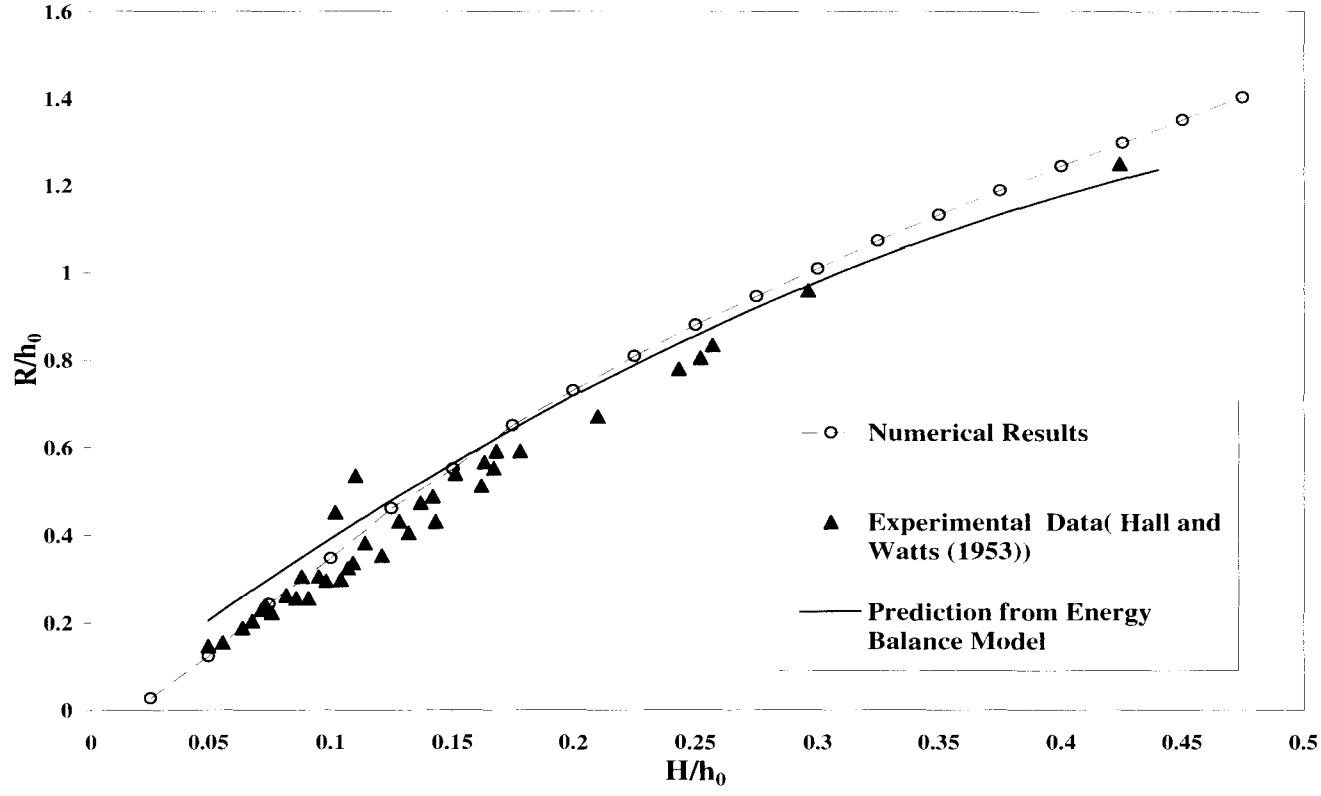

Figure 5.52: Prediction of maximum run-up of solitary wave run-up on 1:5.67 slope as a function of relative incident wave height. The solid line is the prediction from the Energy Balance Model, the dashed line with circles is the numerical results from WENO scheme, the triangles are the experimental data from Hall and Watts (1953)

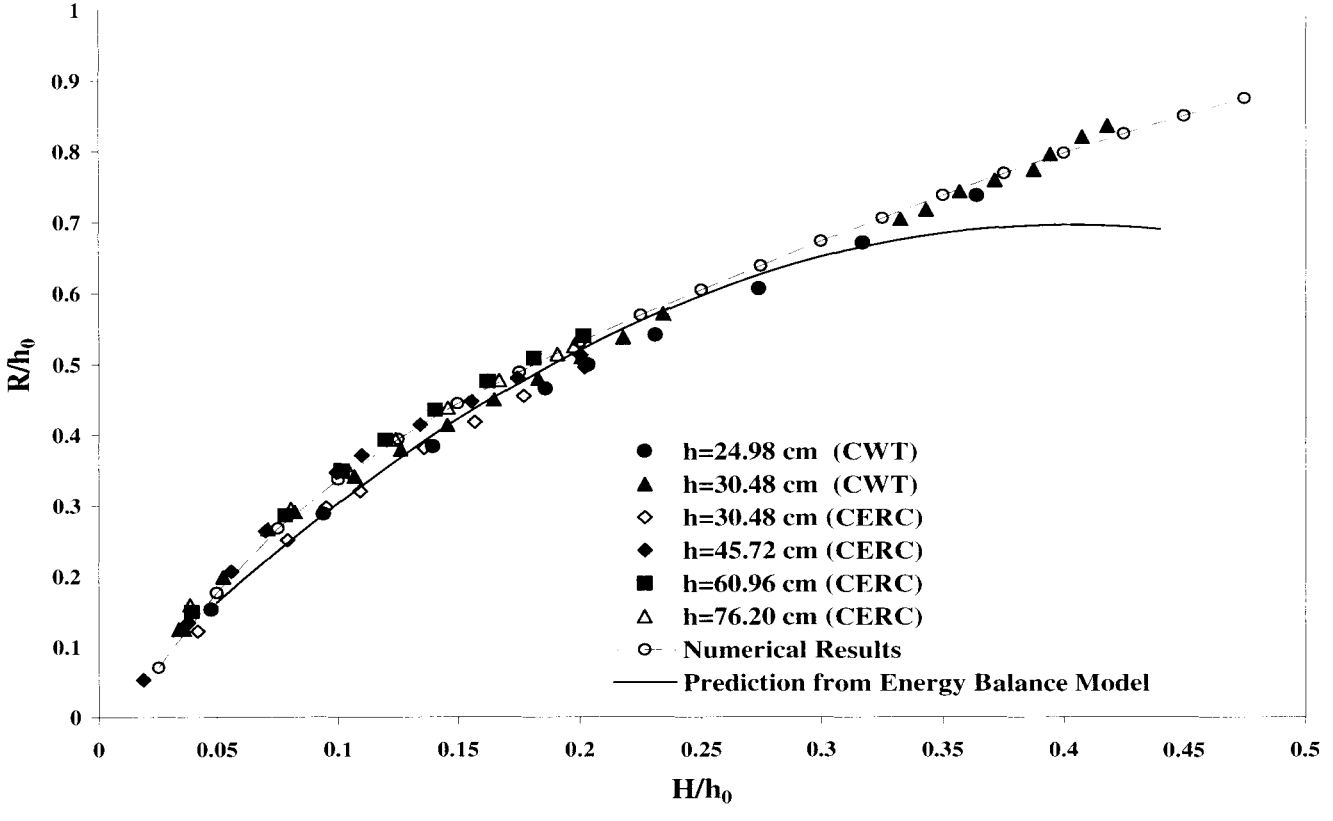

Figure 5.53: Prediction of maximum run-up of solitary wave run-up on 1:15 slope as a function of relative incident wave height. The solid line is the prediction from the Energy Balance Model, the dashed line with circles is the numerical results from WENO scheme, the symbols are the experimental data

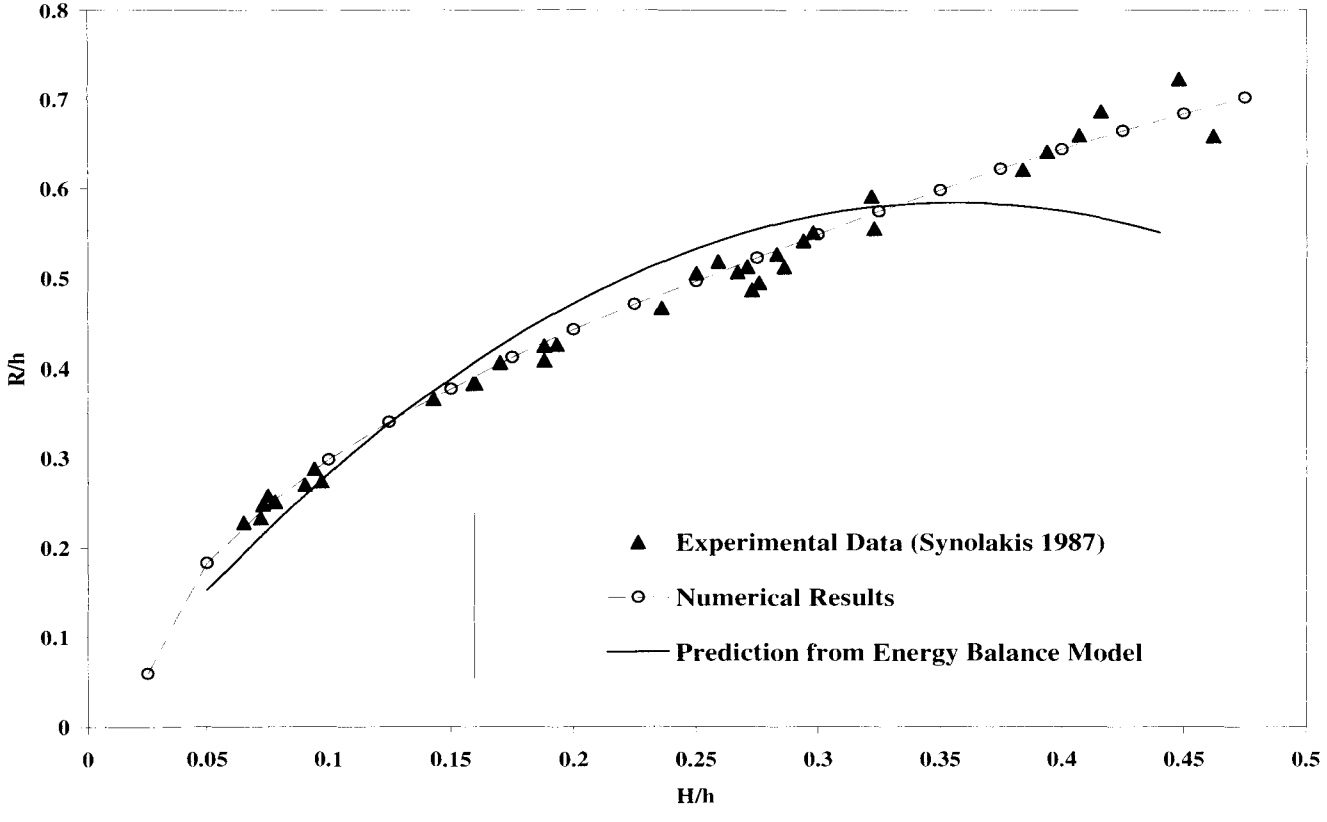

Figure 5.54: Prediction of maximum run-up of solitary wave run-up on 1:19.85 slope as a function of relative incident wave height. The solid line is the prediction from the Energy balance model, the dashed line with circles is the numerical results from WENO scheme, the triangles are the experimental data from Synolakis (1986)

up tongue and can travel significantly higher than would the sheet splash-up. The numerical results from the WENO scheme described in Chapter 4 was applied only to the sheet flow process. However, experimental data are presented for the spray and drops where applicable.

The experimental arrangement for the solitary wave splash-up on a vertical wall was shown in Figure 4.26. As mentioned earlier, experiments were conducted using a movable vertical wall mounted at various positions on a plane beach with a slope of 1:19.85. Therefore, for a solitary wave with a given relative wave height offshore, H/h_0, either a non-breaking, an incipient breaking, or a post-breaking (broken) wave can be caused to impinge on the wall. Data for three offshore relative wave heights are presented in Figure 5.55 where the abscissa is the ratio of the distance between the vertical wall and the original shoreline, i.e., x_w, to the offshore depth, h_0. Positive values indicate distances offshore of the shoreline and negative distances are shoreward of the shoreline. The ordinate, R/H, is the ratio of the maximum splash-up on the wall with respect to the original water surface, R, to the incident wave height, H. The position where breaking occurs for each of the three relative incident wave heights is indicated by the arrows on the abscissa. When the wall is at its most seaward location, i.e., $x_w/h_0 = 19.85$, the wall is located essentially at the shoreward extent of the constant depth portion of the tank. Thus, as would be expected, for a relative height of $H/h_0 = 0.10$ the splash-up relative to the incident wave height is about two from the theoretical analysis and experiments (see Byatt-Smith (1971) and Ramsden (1993)). For that wall location as the relative wave height offshore increases, the splash-up becomes greater than two due to increasing non-linear effects. As the wall is moved onshore, but to positions seaward of the location of wave breaking, the splash-up increases significantly. For example, for a relative offshore height of $H/h_0 = 0.43$ the splash-up on the wall increases by a factor of three as the wall is

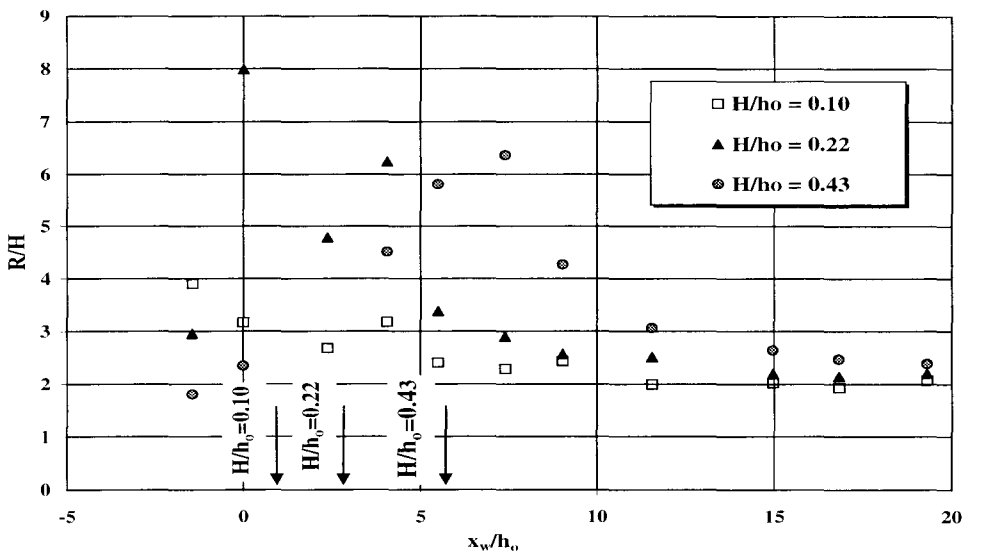

Figure 5.55: Variation of splash-up with the vertical wall location relative to the shoreline, bottom slope 1:19.85

moved from the toe of the slope to a location just seaward of wave breaking. It will be shown later that this increase is associated with the increasing slope of the front face of the wave as it shoals while propagating up the beach. However, if the wall is located some distance shoreward of the breaking location the relative splash-up decreases dramatically. This is due to the collapse of the wave shoreward of breaking with a resultant decrease in both the wave height and the slope of the front face of the wave compared to that when the wall is located near where the wave breaks.

The variation of the relative splash-up, R/H, with relative incident wave height, H/h_0, is presented in Figure 5.56 for eleven different wall locations varying from the toe of the sloping beach to shoreward of the shoreline. In upper portion of Figure 5.56

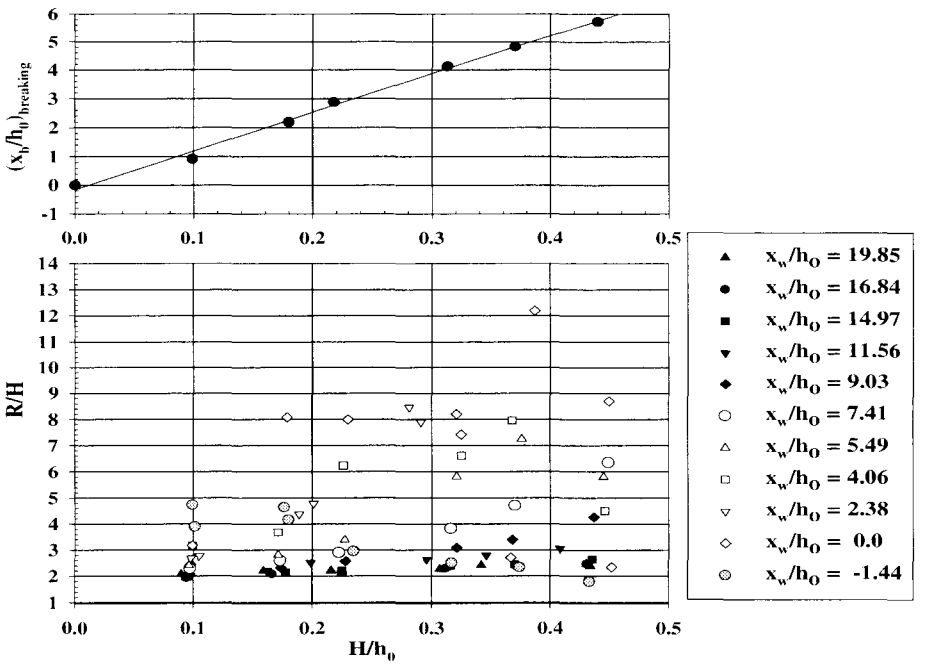

Figure 5.56: Variation of location of wave breaking and splash-up with relative incident wave height

the location of breaking is also shown as a function of relative incident wave height, H/h_0, with the ordinate expressed as x_b/h_0 at breaking, where x_b was denoted as the horizontal location of wave breaking point measured from the initial shoreline. For the limits of experiments, i.e., $0.1 < H/h_0 < 0.45$, it can be seen that the location of the breaking wave is: $1 < (x_b/h_0)_{breaking} < 6$, i.e., one to six depths offshore of the shoreline. Thus, referring to upper portion of Figure 5.56, for waves with a relative wave height of $H/h_0 \approx 0.1$, except for the two most shoreward locations of the wall, the splash-up is caused by non-breaking waves. In general, it appears that for each relative wave height, H/h_0, the further the wall is located offshore of the position of wave breaking the smaller the relative splash-up.

The maximum splash-up is presented in Figures 5.57 (a), (b), and (c) as a function of the relative incident wave height for three different wall locations: x_w/h_0=19.85, 9.03, and 0.0, respectively. The numerical results obtained using the WENO scheme described in Chapter 3 are also presented. The three cases shown correspond to: the toe of the slope, the original shoreline, and a location midway between these two. For the vertical wall located at the toe of the slope and at the mid-point, i.e., half-way between the toe of the slope and the original shoreline, the waves are not breaking before they impinge on the wall. However, for the wall located at the shoreline (x_w/h_0=0.0) the waves break seaward of the wall at different distances depending upon the incident wave heights, see upper portion of Figure 5.56. The numerical results are compared to the experiments for each case, and the agreement is reasonable for the experiments corresponding to the non-breaking waves. Theoretical results from Byatt-Smith (1971) for the case of a solitary wave propagating in a constant depth and impinging on a vertical wall are also shown in Figure 5.57 (a). These results agree well both with the experimental data and the numerical results of this study. For the larger incident waves and a wall location further up the slope the wave is either near breaking or breaking before impinging on the wall. In Figure 5.57 (b) where the wave shoals, but does not break before striking the wall, the numerical model agrees reasonably well with the experimental results. When the wave splash-up is composed of spray and drops one would not expect the numerical model to predict the maximum splash-up, as can be seen in Figure 5.57 (b) for $H/h_0 = 0.36$. In Figure 5.57 (c) agreement with the theory appears reasonable for a relative wave height of $H/h_0 = 0.1$ and for $H/h_0 > 0.36$. The former is a case of a wave of small amplitude breaking about one depth, i.e., h_0, seaward of the wall. The latter corresponds to waves which have broken some distance from the wall and impinge on the wall as a collapsed broken wave. In between these limits, i.e., for $0.1 < H/h_0 < 0.36$, the impingement is more violent and drops and spray are formed and agreement with

the theory would not be expected. It is in this region that the detailed kinematics of the wave at breaking must be important in defining the splash-up, and these details cannot be defined by the non-linear shallow water theory.

The splash-up of a wave on the vertical wall, R/H, is shown as a function of normalized time, $t^* = t\sqrt{g/h_0}$ in Figures 5.58 and 5.59 for two cases for a wall position of $x_w/h_0 = 11.56$: (i) a wave nearly breaking before reaching the vertical wall ($H/h_0 = 0.296$), and (ii) a wave which has broken already before reaching the wall ($H/h_0 = 0.374$). Favorable agreement is found between the results of the WENO numerical model and the experiments for the sheet splash-up showing that the numerical scheme can model both the waves shoaling but not breaking before impinging on a vertical wall and waves which break on the 1:19.85 slope and the splash-up process associated with broken waves impinging on the wall. In the latter case the wave breaks and then collapses as it propagates shoreward before striking the wall.

The experiments have suggested that the maximum local water particle acceleration of the incident wave at the time the wave just reaches the wall may be more important in defining the extent of the splash-up than the maximum water particle velocity at that instant. From the non-linear shallow water theory, the water particle acceleration is equivalent to the local wave slope as shown in the following:

$$\frac{Du}{Dt} = u_t + uu_x = -g\eta_x \tag{5.45}$$

Where Du/Dt is the water particle acceleration, and η_x represents the wave slope. Therefore, the maximum wave front slope at the instant that the wave reaches the vertical wall was chosen to represent the wave particle acceleration.

We use a length scale for the deforming and breaking wave which incorporates the maximum slope of the front face of the wave just as it impinges on the vertical

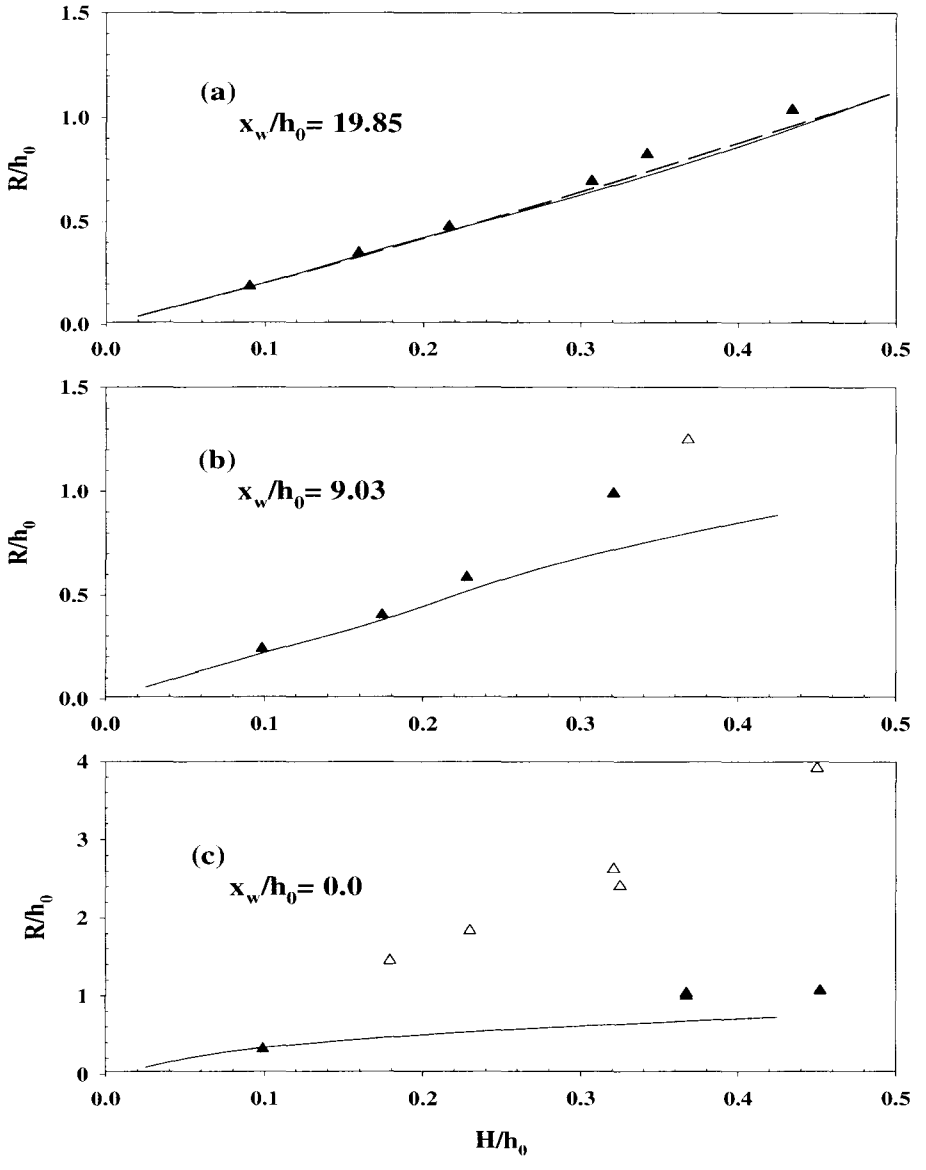

Figure 5.57: Variation of the splash-up with relative incident wave height for various wall locations. solid line is the present numerical results, dashed line is the theoretical results of Byatt-Smith (1971), Solid triangle is the solid sheet splash-up, hollow triangle is the drop and spray splash-up.

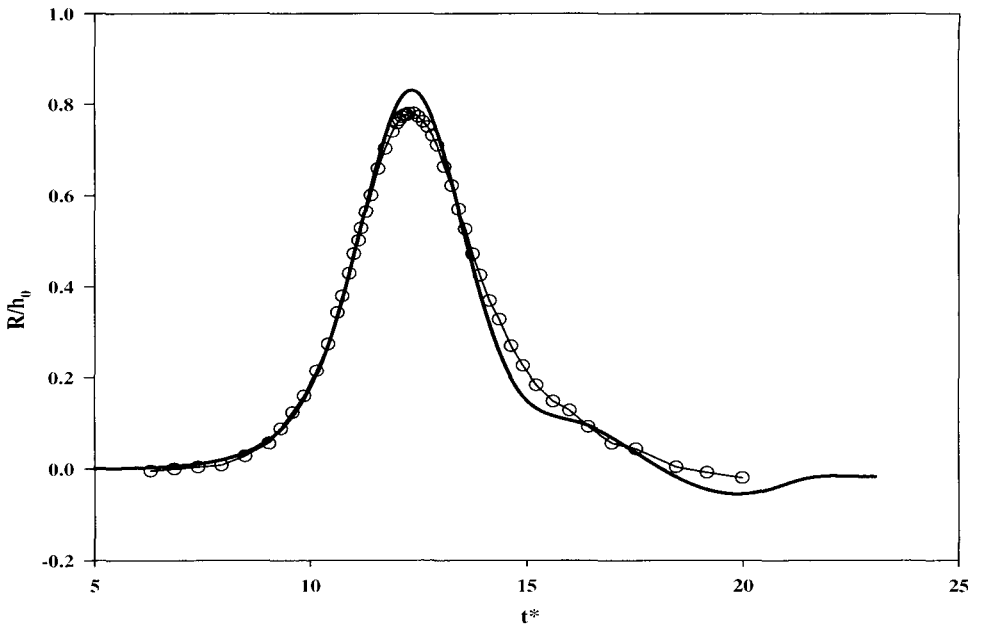

Figure 5.58: Variation of splash-up with time, $H/h_0 = 0.296$, $x_w/h_0 = 11.56$. Open circles with line with line are experiments, solid line is the numerical theory.

wall. (The use of this front face slope was first proposed by Hammack (1972) to define a more meaningful Ursell number for a breaking or broken long wave.) The length scale used is the ratio of the wave height to the maximum slope on the front face of the wave, i.e., $H/(|d\eta/dx|)_{max}$. The dramatic increase in the splash-up, as seen in Figure 5.55, as the wall location approaches the position on the sloping beach where the wave breaks is probably due to the increase in the slope of the front face of the wave as it shoals and then impinges on the wall. The variation of the ratio of the relative splash-up, R/H, with time that is normalized by using this length scale, $t[gH/|d\eta/dx|_{max}]^{1/2}$, as determined from experiments is presented in Figure 5.60 for a range of relative incident wave heights. All cases are for a wall position of $x_w/h_0 = 11.56$, and from Figure 5.56 it is seen that the wave impinging on the

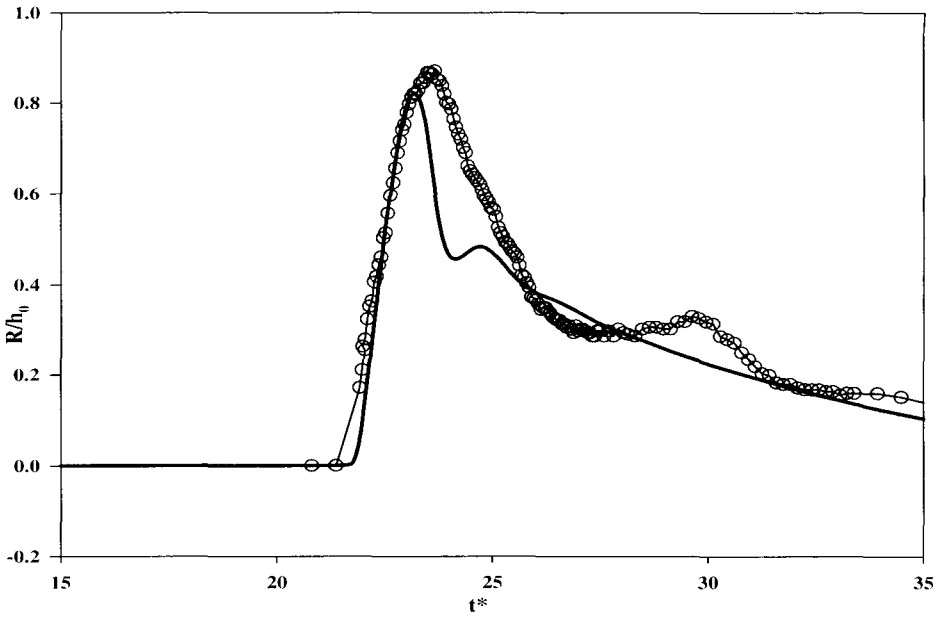

Figure 5.59: Variation of splash-up with time, $H/h_0 = 0.374$, $x_w/h_0 = 0.0$. Open circles are experiments, solid line is the numerical theory.

wall is unbroken for this wall location. The variation of the maximum splash-up with relative offshore wave height was also shown in Figure 5.56 for this location. The abscissal parameter appears to be reasonable in shifting the time-histories so that the non-dimensional times of the maxima are in nominal agreement.

The maximum splash-up on the wall, R/H, is shown in Figure 5.61 as a function of the maximum front face slope $|d\eta/dx|_{max}$ for various wall locations, x_w/h_0, and offshore relative wave heights, H/h_0. A well-defined linear fit to the data is seen independent of the wall location and the initial relative wave height:

$$\frac{R}{h_0} = 4.73|\frac{d\eta}{dx}|_{max} \tag{5.46}$$

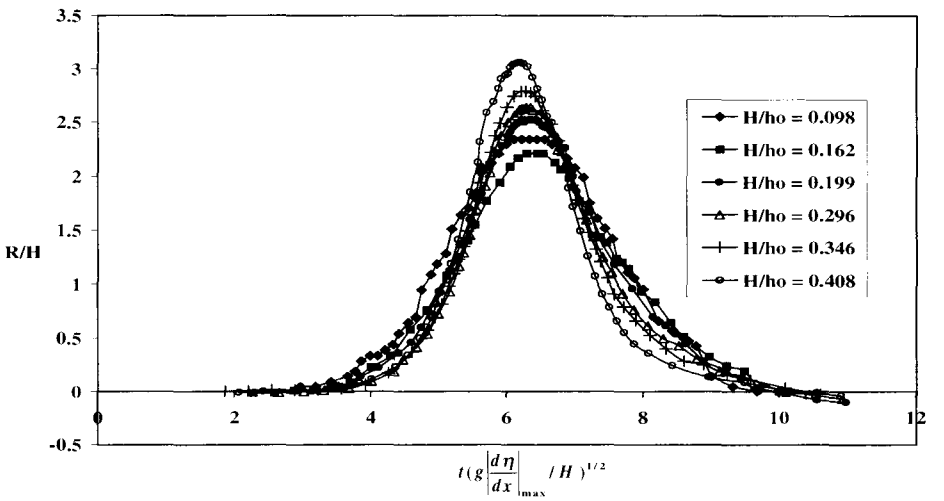

Figure 5.60: Splash-up time-history for solitary waves; wall location $x_w/h_0 = 11.56$

If the wave breaks on the slope just in front of the vertical wall, it appears that this relationship is violated and large splash-up occurs consisting of drops and spray along with a relatively ill-defined water sheet following the drops and spray. (This effect can be seen in Figure 5.61 for large water surface slopes.) Although the data still appear to follow the trend associated with smaller wave-face slopes, the data are scattered.

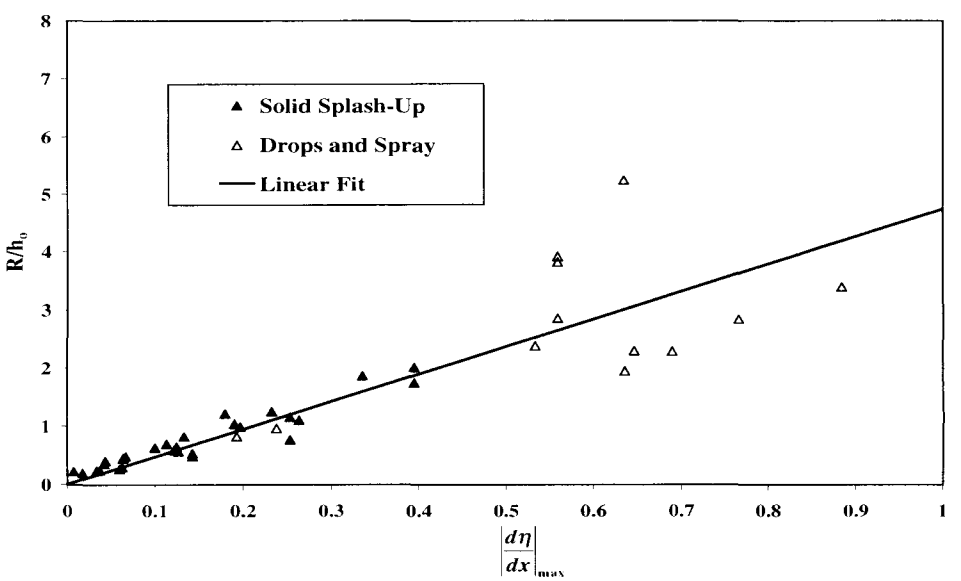

Figure 5.61: Maximum splash-up as a function of maximum slope of incident wave front face

Chapter 6 Conclusions

The objective of this study has been to investigate some aspects of solitary wave run-up on a smooth plane sloping beach.

The process of non-breaking solitary wave run-up was investigated theoretically by proposing a new higher order solution to the well-known shallow water equations. Experiments were performed in the laboratory to measure the surface profile, wave time-histories, water particle velocities, and maximum run-up. These experimental data were compared to the theoretical results and good agreement was found. The run-up of breaking solitary waves was studied experimentally and numerically. A finite-difference numerical model that solved the fully non-linear shallow water equations including a bore structure was developed and used to simulate the breaking solitary wave run-up. This numerical model was validated by the experimental measurements. A simple empirical formula used to predict the maximum run-up of breaking solitary wave run-up from energy conservation considerations was presented and discussed in this study. The special case of breaking solitary wave run-up on a gentle slope and then splash-up on a vertical wall at various locations with respect to the slope was also studied experimentally and numerically.

The following major conclusions were drawn and they are divided into categories corresponding to the main areas of this investigation:

6.1 Non-Breaking Solitary Wave Run-Up on Beaches

1. The non-linear theory developed herein agrees well with the experimental data corresponding to the run-up on a relatively steep slope (1:2.08) as well as on a more gentle slope (1:19.85). The agreement is good for both the water surface time-histories, the spatial water surface profiles, and the horizontal water particle velocities that were obtained at several locations during the run-up process.

2. The present non-linear theory provides a somewhat better prediction of various aspects of the run-up process than the approximate non-linear theory presented earlier by Synolakis (1986). The improvement in accuracy of this prediction from the present non-linear theory compared to the approximate non-linear theory is at the order of 10% based on the wave breaking limit chosen. This indicates that the assumptions made by Synolakis (1986) in his approximate non-linear theory are reasonably satisfactory for most engineering applications especially for small slopes where the breaking wave height is significantly less than that for steep slopes such as those investigated here.

3. A unique laser-photodiode camera experiment arrangement was developed in connection with this study to measure the time-history of the tip of the run-up tongue of a solitary wave, which was non-breaking, as it progressed up the slope. The results obtained with this run-up gage agreed well with other measurement and provided a simple and reliable way of measuring run-up time-histories.

6.2 Breaking Solitary Wave Run-Up on Beaches

6.2.1 Plunging Jet and Splash-Up

1. The jet generated by the plunging breaking wave has the trajectory of a simple free-falling jet with the horizontal velocity equal to the solitary wave celerity in the constant depth region.

2. The point where the plunging jet touched the slope determines the resulted splash-up. If the jet impinges on a dry slope, no splash-up occurs and the plunging breaker simply collapses. If the impingement point is located on the free surface ahead of the jet, splash-up including a reflected jet is formed which further increases the turbulence and energy dissipation associated with wave breaking.

3. Clockwise and counter-clockwise vortices may be generated by the impinging plunging jet and the reflected jet associated with the splash-up when the jet impinges on the front face of a breaking wave or on the still water surface.

4. The plunging jet kinematics generated by a breaking solitary wave are similar to those generated by breaking periodic waves.

6.2.2 Numerical Model

1. The numerical method developed in this study to predict the run-up of breaking waves provides a somewhat simple and reasonably good prediction of various aspects of the run-up process. The results agree well with the experimental data corresponding to the run-up on a relatively steep slope (1:2.08) as well as on a gentle slope (1:19.85).

2. The numerical method is stable, simple to implement and requires relatively small computational resources.

3. The numerical results for the "global parameters" of solitary wave run-up such as the maximum run-up and the wave profile agree reasonably well with the experiments for both wave breaking conditions, i.e., wave breaking with and without rigorous splash-up.

4. The detailed characteristics of wave breaking process such as plunging jet and splash-up cannot be described by the numerical model.

6.2.3 Energy Balance Model

1. The energy dissipation associated with wave breaking is estimated using the numerical model and this was verified by the experimental measurement of potential energy at maximum run-up, and the incident and reflected wave energy.

2. The reflected wave energy resulting from the wave-slope interaction for the slope investigated is negligibly small comparing to the incident wave energy associated with the solitary wave.

3. The fairly good agreement of the energy balance model with experiments indicates that the bore model which is used to describe energy dissipation is reasonable.

4. The energy balance model appears to be useful to predict the run-up of experimental plunging breaking solitary waves.

6.3 Breaking Solitary Wave Splash-Up on Vertical Walls

1. The position of the vertical wall on the slope is of critical importance to the maximum splash-up as it relates to the location of wave breaking.

2. The numerical approach proposed appears to predict the time-history of the sheet splash-up well both for non-breaking waves and for waves which break seaward of the wall location.

3. The maximum slope of the front face of the wave upon impingement of the wave on the wall is important in defining the maximum sheet splash-up as well as the trend for splash-up composed of drops and spray.

6.4 Future Research Considerations

Three possible future research directions can be recommended here:

1. The numerical model developed in this study has the potential to be extended to study three-dimensional breaking wave run-up.

2. It appears that plunging jet and the resulted splash-up are important to understand the wave breaking kinematics and the energy dissipation process. A numerical model, similar to that used by Lin, chang, and Liu (1999), solves the Navier-stokes equation and uses VOF method to advect free surface, could lead to promising results of jet and also the maximum run-up of solitary waves. This type of numerical model, if tested and validated by the experimental results, can provide a more accurate description of the wave breaking process.

3. To obtain more information about the wave breaking and run-up process, more experimental measurements such as water particle velocity measurements using digital particle imaging velocimetry (DPIV) have to be conducted.

Appendix

Experimental Data

Table A-1: Experimental Maximum Run-Up of Non-Breaking Solitary Waves

h_0(cm)	Wave Tank	$cot\beta$	H/h_0	R/h_0
21.51	CST	2.08	0.026	0.050
21.51	CST	2.08	0.063	0.148
21.51	CST	2.08	0.071	0.172
21.51	CST	2.08	0.089	0.221
21.51	CST	2.08	0.108	0.273
21.51	CST	2.08	0.113	0.304
21.51	CST	2.08	0.135	0.362
21.51	CST	2.08	0.147	0.415
21.51	CST	2.08	0.164	0.443
21.51	CST	2.08	0.174	0.496
21.51	CST	2.08	0.198	0.566
21.51	CST	2.08	0.201	0.575
21.51	CST	2.08	0.230	0.690
21.51	CST	2.08	0.236	0.694
21.51	CST	2.08	0.258	0.773
21.51	CST	2.08	0.271	0.846
21.51	CST	2.08	0.281	0.889
21.51	CST	2.08	0.288	0.889

h_0(cm)	Wave Tank	$cot\beta$	H/h_0	R/h_0
21.51	CST	2.08	0.307	0.974
21.51	CST	2.08	0.316	1.033
21.51	CST	2.08	0.322	1.075
21.51	CST	2.08	0.339	1.132

Table A-2: Experimental Maximum Run-Up of Breaking Solitary Waves

h_0(cm)	Wave Tank	$cot\beta$	H/h_0	R/h_0
24.98	CWT	15.0	0.048	0.152
24.98	CWT	15.0	0.094	0.288
24.98	CWT	15.0	0.140	0.384
24.98	CWT	15.0	0.186	0.467
24.98	CWT	15.0	0.203	0.500
24.98	CWT	15.0	0.231	0.542
24.98	CWT	15.0	0.274	0.607
24.98	CWT	15.0	0.317	0.672
24.98	CWT	15.0	0.364	0.739
30.48	CWT	15.0	0.036	0.125
30.48	CWT	15.0	0.034	0.125
30.48	CWT	15.0	0.053	0.198
30.48	CWT	15.0	0.071	0.267
30.48	CWT	15.0	0.082	0.291

h_0(cm)	Wave Tank	$cot\beta$	H/h_0	R/h_0
30.48	CWT	15.0	0.107	0.342
30.48	CWT	15.0	0.126	0.380
30.48	CWT	15.0	0.146	0.414
30.48	CWT	15.0	0.165	0.450
30.48	CWT	15.0	0.183	0.481
30.48	CWT	15.0	0.201	0.511
30.48	CWT	15.0	0.218	0.538
30.48	CWT	15.0	0.234	0.572
30.48	CWT	15.0	0.332	0.705
30.48	CWT	15.0	0.343	0.718
30.48	CWT	15.0	0.357	0.745
30.48	CWT	15.0	0.371	0.761
30.48	CWT	15.0	0.387	0.775
30.48	CWT	15.0	0.394	0.797
30.48	CWT	15.0	0.408	0.821
30.48	CWT	15.0	0.418	0.836
30.48	CERC	15.0	0.042	0.122
30.48	CERC	15.0	0.079	0.251
30.48	CERC	15.0	0.095	0.298
30.48	CERC	15.0	0.109	0.321
30.48	CERC	15.0	0.136	0.382
30.48	CERC	15.0	0.157	0.419
30.48	CERC	15.0	0.177	0.456

h_0(cm)	Wave Tank	$cot\beta$	H/h_0	R/h_0
30.48	CERC	15.0	0.202	0.497
45.72	CERC	15.0	0.019	0.053
45.72	CERC	15.0	0.038	0.134
45.72	CERC	15.0	0.056	0.206
45.72	CERC	15.0	0.070	0.264
45.72	CERC	15.0	0.099	0.347
45.72	CERC	15.0	0.110	0.372
45.72	CERC	15.0	0.134	0.415
45.72	CERC	15.0	0.156	0.448
45.72	CERC	15.0	0.174	0.482
45.72	CERC	15.0	0.200	0.514
60.96	CERC	15.0	0.040	0.150
60.96	CERC	15.0	0.078	0.287
60.96	CERC	15.0	0.102	0.350
60.96	CERC	15.0	0.102	0.351
60.96	CERC	15.0	0.120	0.394
60.96	CERC	15.0	0.141	0.436
60.96	CERC	15.0	0.162	0.477
60.96	CERC	15.0	0.181	0.510
60.96	CERC	15.0	0.202	0.541
76.20	CERC	15.0	0.039	0.159

h_0(cm)	Wave Tank	$cot\beta$	H/h_0	R/h_0
76.20	CERC	15.0	0.080	0.296
76.20	CERC	15.0	0.104	0.349
76.20	CERC	15.0	0.124	0.394
76.20	CERC	15.0	0.146	0.439
76.20	CERC	15.0	0.167	0.478
76.20	CERC	15.0	0.191	0.515
76.20	CERC	15.0	0.198	0.527

Bibliography

[1] Battjes, J. A. (1974) "Surf similarity." *Proceedings of the 14th Conference on Coastal Engineering*, ASCE, Vol. 1, 466-480.

[2] Battjes, J. A. (1988) "Surf-zone dynamics." *Annual Review of Fluid Mechanics*, Vol. 20, 257-293.

[3] Brennen, C. and Whitney, A. K. (1970) "Unsteady free surface flows; solutions employing the Lagrangian description of the motion." *Proceedings of the 8th Symposium Naval Hydrodynamics*, August 24-28, 117-145.

[4] Briggs, M. J., Synolakis, C. E., and Hughes, S. T. (1995) "Large scale three-dimensional laboratory measurements of tsunami inundation." Tsunami: Progress in Prediction, Disaster Prevention and Warning, Kluwer Academic Publishers, 129-149.

[5] Brocchini, M. (1998) "The run-up of weakly-two-dimensional solitary pulses." *Nonlinear Processes in Geophysics*, Vol. 5, 27-37.

[6] Byatt-Smith, J. G. B. (1971) "An integral equation for unsteady surface waves and a comment on the Boussinesq equation." *Journal of Fluid Mechanics*, Vol. 49, 625-633.

[7] Chanson, H. and Lee, J-F. (1997) "Plunging jet characteristics of plunging breakers." *Coastal Engineering*, Vol. 31, 125-141.

[8] Camfield, F. E. and Street, R. L. (1969) "Shoaling of solitary waves on small slopes." *Proceedings of ASCE*, WW95, 1-22.

[9] Carrier, G. F. and Greenspan, H. P. (1958) "Water waves of finite amplitude on a sloping beach." *Journal of Fluid Mechanics*, Vol. 4, 97-109.

[10] Carrier, G. F. (1966) "Gravity waves on water of variable depth." *Journal of Fluid Mechanics*, Vol. 24, 641-659.

[11] Dean, R. G. and Ursell, F. (1959) "Interaction of a fixed, semi-immersed circular cylinder with a train of surface waves." *Technical Report*, No. 37, Hydrodynamics Laboratory, Massachusetts Institute of Technology.

[12] Dodd, N. (1998) "Numerical model of wave run-up, overtopping, and regeneration." *Journal of Waterway, Port, Coastal, and Ocean Engineering*, Vol. 124, 73-81.

[13] Freeman, J. C. and Le Mehaute, B. (1964) "Wave breakers on a beach and surges on a dry bed." *Journal of Hydraulic Engineering*, ASCE, Vol. 90, No. 2, 187-216.

[14] Galvin, Jr. C. (1983) "Wave breaking in shallow water." Waves on Beaches and Resulting Sediment Transport (ed. Meyer, R. E.), Academic Press, 413-456.

[15] Goda, Y., Kishira, Y., and Kamiyama, Y. (1975) "Laboratory investigation on the overtopping rate of seawalls by irregular waves." *Report of Port and Harbor Research Institute*, Japan, Vol. 14, No. 4, 3-44.

[16] Goring, D. G. (1979) "Tsunami: the propagation of long waves onto a shelf." Ph.D. Thesis, California Institute of Technology.

[17] Grilli, S. T. and Svendsen, I. A (1989) "Computation of non-linear wave kinematics during propagation and run-up on a shelf." *Proceedings of the NATO Advanced Research Workshop on Water Wave Kinematics*, 387-413.

[18] Grilli, S. T., Svendsen, I. A., and Subramanya, R. (1997) "Breaking criterion and characteristics for solitary waves on slope." *Journal of Waterway, Port, Coastal, and Ocean Engineering*, Vol. 123, 102-112.

[19] Hall, J. V. and Watts, J. W. (1953) "Laboratory investigation of the vertical rise of solitary waves on impermeable slopes." *Technical Report*, Beach Erosion Board, US Army Corps of Engineering. Vol. 33.

[20] Hammack, J. L. (1972) "Tsunamis: a model of their generation and propagation." Report No. KH-R-28, W.M. Keck Laboratory of Hydraulic and Water Resources, California Institute of Technology.

[21] Harden, A., Engquist, B., Osher, S., and Chakravarthy, S., (1987) "Uniformly high order essentially non-oscillatory schemes." *Journal of Computational Physics*, Vol. 71, 231-303.

[22] Hibbert, S. and Peregrine, D. H. (1979) "Surf and runup on a beach: a uniform bore." *Journal of Fluid Mechanics*, Vol. 95, 323-345.

[23] Hirt, C. W. and Nichols, B. D. (1981) "Volume of fluid (VOF) method for the dynamics of free boundary." *Journal of Computational Physics*, Vol. 39, 201-225.

[24] Ho, D.V. and Meyer, R. E. (1962) "Climb of a bore on a beach." *Journal of Fluid Mechanics*, Vol. 14, 305-318.

[25] Ippen, A. T. and Kulin, G. (1955) "The Shoaling and breaking of the solitary wave." *Technical Report*, No. 15, Hydrodynamics Laboratory, Massachusetts Institute of Technology.

[26] Jiang, G. and Shu, C-W. (1996) "Efficient implementation of weighted ENO schemes." *Journal of Computational Physics*, Vol. 126, 202-228.

[27] Kanoglu, U., and Synolakis, C. E. (1998) "Long wave runup on piecewise linear topographies." *Journal of Fluid Mechanics*, Vol. 374, 1-28.

[28] Keller, J. B. and Keller, H. B. (1964) "Water wave run-up on a beach." *ONR Research Report*, Contract No. NONR-3828(00), Department of the Navy, Washington, D.C.

[29] Keulegan, G. H. (1948) "Gradual damping of solitary waves." *Journal of Research of the National Bureau of Standards*, Vol. 40, 487-501.

[30] Kobayashi, N. and Karjadi, E. A. (1994) "Surf-similarity parameter for breaking solitary wave runup." *Journal of Waterway, Port, Coastal, and Ocean Engineering*, Vol. 120, 645-650.

[31] Lamb, H. (1932) Hydrodynamics, Dover Publications.

[32] Lander, J. F. and Lockridge, P. A. (1989) "United States tsunamis 1890-1988." Pub. 41-2, U.S. Department of Commerce, National Oceanic and Atmosphere Administration, National Environmental Satellite, Data, and Information Service, National Geophysical Data Center.

[33] Li, Y. and Raichlen, F. (1998) "Breaking criterion and characteristics for solitary waves on slope (discussion)." *Journal of Waterway, Port, Coastal, and Ocean Engineering*, Vol. 124, 329-333.

[34] Li, Y. and Raichlen, F. (2000a) "Solitary wave run-up on plane slopes." accepted by *Journal of Waterway, Port, Coastal and Ocean Engineering*.

[35] Li, Y., Raichlen, F. and Lee, S. (2000b) "Physical and numerical model of splash-up of shoreline structures." accepted by 2000 ASME Fluid Engineering Division Summer Meeting, Boston, MA.

[36] Lin, P., Chang, K-A., and Liu, P. L-F. (1999) "Runup and run-down of solitary waves on sloping beaches." *Journal of Waterway, Port, Coastal, and Ocean Engineering*, Vol. 125, 247-255.

[37] Liu, P. L-F., Synolakis, C., and Yeh, H. H. (1991) "Report on the international workshop on long-wave run-up." *Journal of Fluid Mechanics*, Vol. 229, 675-688.

[38] Liu, P. L-F. and Cho, Y-S. (1994) "Integral equation model for wave propagation with bottom frictions." *Journal of Waterway, Port, Coastal, and Ocean Engineering*, Vol. 120, 594-608.

[39] Liu, P. L-F., Cho, Y-S., Briggs, M. J., Kanoglu, U., and Synolakis, C. E. "Runup of solitary waves on a circular island." *Journal of Fluid Mechanics*, Vol. 302, 259-285.

[40] Liu, X-D., Osher, S., and Chan, T. (1994) "Weighted essentially non-oscillatory schemes." *Journal of Computational Physics*, Vol. 115, 200-212.

[41] Mei, C. C. (1983) The Applied Dynamics of Ocean Surface Wave. Wiley Interscience.

[42] Miller, R. (1968) "Experimental determination of run-up of undular and fully developed bores." *Journal of Geophysical Research*, Vol. 73, No. 14, 4497-4510.

[43] Naheer, E. (1976) "Stability of bottom armoring under the attack of solitary waves." Ph.D. Thesis, California Institute of Technology.

[44] Naheer, E. (1978) "The damping of solitary waves." *International Journal of Hydraulic Research*, Vol. 16, 235-249.

[45] Papanicolaou, P. and Raichlen, F. (1987a) "Wave and bubble characteristics in the surf zone." *Proceedings of the NATO Advanced Research Workshop on Natural Mechanisms of Surface Generated Noise in the Ocean*, Lerici, Italy.

[46] Papanicolaou, P. and Raichlen, F. (1987b) "Wave characteristics in the surf zone." *Proceedings of Coastal Hydrodynamics Conference*, Univ. of Delaware, Newalk, Delaware.

[47] Pederson, G. and Gjevik, B. (1983) "Run-up of solitary waves." *Journal of Fluid Mechanics*, Vol. 135, 283-209.

[48] Peregrine, D. H. (1967) "Long waves on a beach." *Journal of Fluid Mechanics*, Vol. 27, 815-827.

[49] Peregrine, D. H. (1983) "Breaking waves on beaches." *Annual Review of Fluid Mechanics*, Vol. 15, 149-178.

[50] Ramsden, J. D. (1993) "Tsunamis: forces on a vertical wall caused by long waves, bore, and surges on a dry bed." Report No. KH-R-54, W. M. Keck Laboratory of Hydraulics and Water Resources, California Institute of Technology.

[51] Shen, M. C. and Meyer, R. E. (1963) "Climb of a bore on a beach, part 3: run-up." *Journal of Fluid Mechanics*, Vol. 16, 113-125.

[52] Shu, C-W. (1998) "Essentially non-oscillatory and weighted essentially non-oscillatory schemes for hyperbolic conservation laws." Advanced Numerical Approximation of Nonlinear Hyperbolic Equations (Ed. Quarteroni, A.), Springer, 329-432.

[53] Skjelbreia, J. E. (1987) "Observation of breaking waves on sloping bottoms by use of laser Doppler velocimetry." Report No. KH-R-48, W. M. Keck Laboratory of Hydraulics and Water Resources, California Institute of Technology.

[54] Spielvogel, L. Q. (1976) "Single wave run-up on sloping beaches." *Journal of Fluid Mechanics*, Vol. 74, 685-694.

[55] Stansby, P. K., Chegini, A., and Barnes, T. C. D. "The initial stages of dam-break flow." *Journal of Fluid Mechanics*, Vol. 370, 203-220.

[56] Stoker, J. J. (1957) Water Waves. Interscience Publishers Ltd.

[57] Synolakis, C. E. (1986) "The run-up of long waves." Ph.D. Thesis, California Institute of Technology.

[58] Synolakis, C. E. (1987) "The run-up of solitary waves." *Journal of Fluid Mechanics*. Vol. 185, 523-545.

[59] Synolakis, C. E. (1999) Personal communication.

[60] Tadepalli, S. and Synolakis, C. E. (1994) "The run-up of N-waves on sloping beaches." *Proceedings of the Royal Society of London: Series A - Mathematical Physical and Engineering Science*, A, Vol. 445, 99-112.

[61] Milne-Thomson, L. M. (1968) Theoretical Hydrodynamics, Macmillan Publication.

[62] Titov, V. V. and Synolakis, C. E. (1995) "Modeling of breaking and non-breaking long-wave evolution and run-up using VTCS-2." *Journal of Waterway, Port, Coastal, and Ocean Engineering*, ASCE, Vol. 121, 308-461.

[63] Tuck, E. O. and Hwang, L-S. (1972) "Long wave generation on a sloping beach." *Journal of Fluid Mechanics*, Vol. 51, 449-461.

[64] Waniewski, T., A. (1999) "Air entrainment by bow waves." Ph.D. Thesis, California Institute of Technology.

[65] Wiegel, R. L. (1955) "Parallel wire resistance wave meter." *Proceedings of the 1st Conference on Coastal Engineering Instruments*, 39-43.

[66] Wu, T. Y. (1979) "Tsunamis." *Proceedings of National Science Foundation Workshop*, Pasadena, 110-149.

[67] Yang, J. Y. and Hsu. C. A. "Computations of free-surface flows: 2-dimensional unsteady bore diffraction." *Journal of Hydraulic Research*, Vol. 31, 403-414.

[68] Yeh, H. H. (1991) "Tsunami bore runup." *Natural Hazards*, Vol. 4, 209-220.

[69] Zelt, J. A. (1986) "Tsunami: the response of harbors with sloping boundaries to long wave excitation." Report No. KH-R-47, W. M. Keck Laboratory of Hydraulics and Water Resources, California Institute of Technology.

[70] Zelt, J. A. and Raichlen, F. (1990) "A Lagrangian model for water-induced harbor oscillations." *Journal of Fluid Mechanics*, Vol. 213, 203-225.

[71] Zelt, J. A. (1991a) "The run-up of non-breaking and breaking solitary waves." *Coastal Engineering*, Vol. 15, No. 3, 205-246.

[72] Zelt, J.A. (1991b) "Overland flow from solitary waves." *Journal of Waterway, Port, Coastal, and Ocean Engineering*, ASCE, Vol. 117, 247-263.

[73] Zhang, J. E. (1996) "Run-up of ocean waves on beaches." Ph.D. Thesis, California Institute of Technology.